https://doi.org/10.15388/vu.thesis.1001
https://orcid.org/0009-0001-0770-7856

VILNIUS UNIVERSITY
CENTER FOR PHYSICAL SCIENCES AND TECHNOLOGY

Huma Amber

Advanced Materials for Electrochemical Water Splitting in Alkaline Media

DOCTORAL DISSERTATION

Natural Sciences,
Chemistry (N 003)

VILNIUS 2026

The dissertation was prepared between 2022 and 2026 at the Center for Physical Sciences and Technology.
The research was supported by the Research Council of Lithuania (Mobility funding – P-DAK-24-42, P-DAK-25-134, P-DAK-26-71, financial grant based on study results – P-DAP-25-239 and P-DAP-26-268, and LMT Student Summer Internship project P-SV3-25-715).

Academic Supervisor – Dr. Loreta Tamašauskaitė-Tamašiūnaitė (Center for Physical Sciences and Technology, Natural Sciences, Chemistry, N 003).

This doctoral dissertation will be defended in a public meeting of the Dissertation Defence Panel:

Chairman – Prof. Habil. Dr. Rimantas Ramanauskas (Center for Physical Sciences and Technology, Natural Sciences, Chemistry, N 003).
Members:
Prof. Dr. Ingrida Ancutienė (Kaunas University of Technology, Natural Sciences, Chemistry, N 003)
Prof. Habil. Dr. Gediminas Niaura (Center for Physical Sciences and Technology, Natural Sciences, Chemistry, N 003);
Prof. Dr. Biljana Šljukić Paunković (University of Belgrade (Serbia), Natural Sciences, Chemistry, N 003).
Dr. Rokas Žalnėravičius (Center for Physical Sciences and Technology, Natural Sciences, Chemistry, N 003),

The dissertation shall be defended at a public meeting of the Dissertation Defence Panel at 13 pm on 30 October 2026 in Meeting room E302 of the Center for Physical Sciences and Technology.
Address: Saulėtekio Ave. 3, Room No. 302, LT-10257 Vilnius, Lithuania
Tel. +37064515550; e-mail: info@ftmc.lt

https://doi.org/10.15388/vu.thesis.1001
https://orcid.org/0009-0001-0770-7856

VILNIAUS UNIVERSITETAS
FIZINIŲ IR TECHNOLOGIJOS MOKSLŲ CENTRAS

Huma Amber

Pažangios medžiagos, skirtos elektrocheminiam vandens skilimui šarminėje terpėje

DAKTARO DISERTACIJA

Gamtos mokslai,
Chemija (N 003)

VILNIUS 2026

Disertacija buvo parengta 2022–2026 m. Fizinių ir technologijų mokslų centre.
Tyrimą rėmė Lietuvos mokso taryba (parama išvykoms – P-DAK-24-42, P-DAK-25-134 ir P-DAK-26-71, parama už mokslinius pasiekimus – P-DAP-25-239 ir P-DAP-26-268 bei “SMT studentų vasara“ projektas P-SV3-25-715.

Mokslinė vadovė – dr. Loreta Tamašauskaitė-Tamašiūnaitė (Fizinių ir technologijos mokslų centras, gamtos mokslai, chemija, N 003).

Gynimo taryba:
Pirmininkas – prof. habil. dr. Rimantas Ramanauskas (Fizinių ir technologijos mokslų centras, gamtos mokslai, chemija, N 003).
Nariai:
prof. dr. Ingrida Ancutienė (Kauno technologijos universitetas, gamtos mokslai, chemija, N 003),
prof. habil. dr. Gediminas Niaura (Fizinių ir technologijos mokslų centras, gamtos mokslai, chemija, N 003),
prof. dr. Biljana Šljukić Paunković (Belgrado universitetas (Serbija), gamtos mokslai, chemija, N 003),
dr. Rokas Žalnėravičius (Fizinių ir technologijos mokslų centras, gamtos mokslai, chemija, N 003).

Disertacija ginama viešame Gynimo tarybos posėdyje 2026 m. spalio mėn. 30 d. 13 val. Fizinių ir technologijos mokslų centro posėdžių salėje E302 anglų kalba.
Adresas: Saulėtekio al. 3, E302; LT-10257 Vilnius, Lietuva
Tel. +37064515550; el. paštas: info@ftmc.lt

LIST OF ABBREVIATIONS

Ag/AgCl	Silver/Silver Chloride Electrode
CO_2	Carbon dioxide
CA	Chronoamperometry
CCUS	Carbon capture utilization and storage
CP	Chronopotentiometry
CV	Cyclic Voltammetry
Co	Cobalt
Cu	Copper
CVD	Chemical Vapor Deposition
CH_4	Methane
C_{dl}	Double layer capacitance (μF)
CPE_{dl}	Constant phase element of the double layer
C_{eff}	Effective capacitance
DI	Deionized water
DFT	Density Functional Theory
ECSA	Electrochemically active surface area
EIS	Electrochemical Impedance Spectroscopy
EDX	Energy-Dispersive X-ray Spectroscopy
E_a	Activation Energy
Fe	Iron
GHG	Greenhouse Gas
HER	Hydrogen Evolution Reaction
IEA	International Energy Agency
j	Current Density (mA cm^{-2})
KOH	Potassium Hydroxide
LSV	Linear Sweep Voltammetry
LSVs	Linear Sweep Voltammograms
MJ kg^{-1}	Megajoule per kilogram
Mt	Million Tonnes
NZE	Net Zero Emissions
OCP	Open Circuit Potential
OER	Oxygen Evolution Reaction
OWS	Overall Water Splitting
P2C	Power-to-Chemicals
P2G	Power-to-Gas
P2H	Power-to-Heat

P2L	Power-to-Liquid
P2P	Power-to-Power
P2X (PtX)	Power-to-X
Pd	Palladium
Pt	Platinum
P	Phosphorus
PVD	Physical Vapor Deposition
RHE	Reversible Hydrogen Electrode
Rs	Solution Resistance
Ra	Adsorption Resistance
Rct	Charge Transfer Resistance
Red	Reducing Agent
RuO_2	Ruthenium Dioxide
SEM	Scanning Electron Microscopy
SMR	Steam Methane Reforming
TMPs	Transition Metal Phosphides
TMs	Transition Metals
TOF	Turnover Frequency
XRD	X-ray Diffraction
η	Overpotential (mV)

PADĖKA/ACKNOWLEDGMENTS

The completion of this doctoral thesis marks the culmination of a significant academic and personal journey. I am deeply grateful to all those whose guidance, support, and kindness contributed to my doctoral experience and to the successful completion of this work.

First and foremost, I extend my deepest gratitude to my supervisor, **Dr. Loreta Tamašauskaitė-Tamašiūnaitė**, for her exceptional guidance, patience, encouragement, and unwavering support throughout my doctoral studies. I consider myself truly fortunate to have pursued my research under her supervision. Her expertise, thoughtful mentorship, and trust have been invaluable throughout this journey.

I sincerely thank **Prof. habil. Dr. Eugenijus Norkus** for the opportunity to contribute to his research project and for his valuable scientific guidance and encouragement. I am also deeply grateful to **Dr. Žita Šukackienė** for her scientific support and assistance, and to **Dr. Aldona Balčiūnaitė** for her continuous assistance, valuable advice, kindness, and scientific collaboration.

I sincerely thank **Dr. Ramūnas Levinas** and **Dr. Giedrius Stalnionis** for their assistance, cooperation, and contributions to my research. My heartfelt appreciation also goes to **PhD student Karina Vjūnova** for her valuable scientific collaboration and insightful discussions.

I extend my sincere appreciation to the **members of my Doctoral Committee** for their time, expertise, constructive observations, and valuable recommendations. I gratefully acknowledge the **Center for Physical Sciences and Technology (FTMC)** for providing a stimulating scientific environment, research facilities, and institutional support throughout my doctoral research.

I also sincerely thank the **Lietuvos Mokslo Taryba (LMT)** for the funding and support that enabled my participation in scientific conferences, academic activities, and research opportunities, contributing to my professional and scientific development.

Above all, my deepest gratitude goes to my parents, **Mr. and Mrs. Ashiq Hussain**, whose unconditional love, countless sacrifices, prayers, and unwavering faith in me have been the foundation of my achievements. I am equally grateful to my brothers, **Dr. Zeeshan Ashiq** and **Flight Lieutenant Usman Ashiq**, and my sister, **Dr. Aneeta Amber**, for their love, understanding, devotion, and constant presence.

Finally, I sincerely thank everyone who contributed, directly or indirectly, to my doctoral journey, especially **my best friend** for steadfast encouragement, understanding, and presence throughout these years. I carry with me not only the knowledge and experience gained throughout these years, but also the memories and meaningful connections formed along the way. To each of you, I offer my heartfelt thanks and sincere appreciation.

TABLE OF CONTENTS

PADĖKA/ACKNOWLEDGMENTS 7
INTRODUCTION 12
MAIN GOAL 13
TASKS 14
SCIENTIFIC NOVELTY 14
STATEMENTS OF DEFENSE 15
1. LITERATURE REVIEW 16
1.1. The Energy Transition 16
1.2. Hydrogen as an Energy Carrier 17
1.3. Global Hydrogen Production and Future Prospects 18
1.4. Hydrogen Production Methods 19
1.5. Fundamentals of Electrochemical Water Splitting 21
1.5.1. Hydrogen Evolution Reaction (HER) Mechanism 23
1.5.2. Oxygen Evolution Reaction (OER) Mechanism 24
1.6. Electrocatalysts for HER & OER 26
1.7. Fabrication Strategies for Electrocatalysts 30
1.7.1. Electroless Deposition 32
1.7.2. Galvanic Displacement 33
2. MATERIALS AND METHODS 35
2.1. Materials and Chemicals 35
2.2. Substrate Preparation 35
2.3. Fabrication of Co-P_x/Cu Catalysts 36
2.4. Fabrication of PdCoP/Cu and PdCoFeP/Cu Catalysts 37
2.5. Fabrication of PtCoP/Cu and PtCoFeP/Cu Catalysts 38
2.6. Characterization of the Synthesized Catalysts 39
2.7. Electrochemical Measurements 39
3. RESULTS AND DISCUSSION 42
3.1. Synthesis and Characterization of Co-P_x/Cu Catalysts 42

3.1.1. Studies of Co-P_x Coatings, Microstructure, and Morphology 42

3.1.2. Electrocatalytic Activity of Co-P_x/Cu Towards HER 44

3.1.3. Electrocatalytic Activity of Co-P_x/Cu Towards OER 47

3.1.4. Determination of Electrochemically Active Surface Areas..... 50

3.1.5. Investigation of the Stability of Co-P_x/Cu Catalysts 52

3.1.6. Investigation of Overall Water Splitting Performance with Co-P_x/Cu..... 53

3.2. Synthesis and Characterization of PdCoP/Cu and PdCoFeP/Cu Catalysts 56

3.2.1. Studies of the Unmodified and Pd-modified CoP and CoFeP Coatings, Microstructure, and Morphology Studies..... 56

3.2.2. Electrocatalytic Activity of the Unmodified and Pd-modified CoP and CoFeP Catalysts Towards HER..... 60

3.2.3. Electrocatalytic Activity of the Unmodified and Pd-modified CoP and CoFeP Catalysts Towards OER..... 65

3.2.4. Determination of Electrochemically Active Surface Areas..... 70

3.2.5. Investigation of the Stability of PdCoP/Cu and PdCoFeP/Cu Catalysts 72

3.2.6. Investigation of Overall Water Splitting by Employing the Unmodified and Pd-modified CoP and CoFeP Catalysts 73

3.3. Synthesis and Characterization of PtCoP/Cu and PtCoFeP/Cu Catalysts 75

3.3.1. Studies of Unmodified and Pt-modified CoP and CoFeP Coatings, Microstructure, and Morphology..... 75

3.3.2. Electrocatalytic Activity of Unmodified and Pt-modified CoP and CoFeP Catalysts Towards HER..... 77

3.3.3. Electrocatalytic Activity of Unmodified and Pt-modified CoP and CoFeP Catalysts Towards OER..... 81

3.3.4. Investigation of the Stability of PtCoP/Cu and PtCoFeP/Cu Catalysts 83

3.3.5. Investigation of Overall Water Splitting by Employing the Unmodified and Pt-modified CoP and CoFeP Catalysts 84

LIMITATIONS AND PROSPECTS FOR FURTHER IMPROVEMENT.. 87

CONCLUSIONS 88
SANTRAUKA LIETUVIŲ KALBA 90
ĮVADAS 90
DARBO TIKSLAS 91
DARBO UŽDAVINIAI 92
MOKSLINIS NAUJUMAS 92
GINAMIEJI TEIGINIAI 93
2. EKSPERIMENTO METODIKA 94
2.1. Pagrindo paruošimas 94
2.2. Co-P_x/Cu katalizatorių gamyba 94
2.3. PdCoP/Cu ir PdCoFeP/Cu katalizatorių gamyba 95
2.4. PtCoP/Cu ir PtCoFeP/Cu katalizatorių gamyba 95
2.5. Suformuotų katalizatorių charakterizavimas 96
2.6. Elektrocheminiai matavimai 96
3. REZULTATAI IR APTARIMAS 100
3.1. Co-P_x/Cu katalizatorių sintezė ir charakterizavimas 100
3.1.1. Co-P_x dangų, mikrostruktūros ir morfologijos tyrimai. 100
3.1.2. Elektrokatalizinis aktyvumas Co-P_x/Cu HER atžvilgiu 102
3.1.3. Elektrokatalizinis aktyvumas Co-P_x/Cu OER atžvilgiu 104
3.1.4. Elektrochemiškai 105
3.1.5. Vandens skaidymo proceso tyrimas, naudojant Co-P_x/Cu katalizatorius 108
3.2. PdCoP/Cu ir PdCoFeP/Cu katalizatorių sintezė ir charakterizavimas 110
3.2.1. Nemodifikuotų ir Pd-modifikuotų CoP ir CoFeP dangų, mikrostruktūros ir morfologijos tyrimai 110
3.2.2. Nemodifikuotų ir Pd-modifikuotų CoP/Cu ir CoFeP/Cu elektrokatalizinis aktyvumas HER atžvilgiu 114
3.2.3. Nemodifikuotų ir Pd-modifikuotų CoP/Cu ir CoFeP/Cu elektrokatalizinis aktyvumas OER atžvilgiu 119

3.2.4. Elektrochemiškai aktyvaus paviršiaus ploto nustatymas..... 122

3.2.5. PdCoP/Cu ir PdCoFeP/Cu katalizatorių stabilumo tyrimas 124

3.2.6. Vandens skilimo proceso tyrimas, naudojant nemodifikuotus ir Pd-modifikuotus CoP/Cu ir CoFeP/Cu katalizatorius 125

3.3. PtCoP/Cu ir PtCoFeP/Cu katalizatorių sintezė ir charakterizavimas .. 126

3.3.1. Nemodifikuotų ir Pt-modifikuotų CoP ir CoFeP dangų, mikrostruktūros ir morfologijos tyrimai 126

3.3.2. Nemodifikuotų ir Pt-modifikuotų CoP/Cu ir CoFeP/Cu elektrokatalizinis aktyvumas HER atžvilgiu 129

3.3.3. Nemodifikuotų ir Pt-modifikuotų CoP/Cu ir CoFeP/Cu elektrokatalizinis aktyvumas OER atžvilgiu 132

3.3.4. PtCoP/Cu ir PtCoFeP/Cu katalizatorių stabilumo tyrimas 134

3.3.5. Vandens skilimo proceso tyrimas, naudojant nemodifikuotus ir Pt-modifikuotus CoP/Cu ir CoFeP/Cu katalizatorius. 135

APRIBOJIMAI IR TOLESNIO TOBULINIMO PERSPEKTYVOS..... 138

IŠVADOS..... 139

REFERENCES 141

LIST OF PUBLICATIONS..... 158

LIST OF CONFERENCE PRESENTATIONS 159

LIST OF AWARDS 162

CURRICULUM VITAE 163

INTRODUCTION

The current global population is estimated to be around 7.5 billion, with predictions indicating a rise to 8.5 billion by the year 2030. This ongoing increase in population is a primary factor driving up global energy consumption [1, 2]. The majority of global energy production and usage is accounted for by fossil fuels, including coal, oil and natural gas. Moreover, the sustained combustion of these fuels has led to a substantial increase in carbon dioxide (CO_2) emissions into the atmosphere. The increase in atmospheric CO_2 levels has led to a series of environmental concerns, including global warming, acidic rain, ecosystem degradation, forest depletion and climatic change. Climate change has resulted in an increase in the frequency and intensity of severe weather conditions, including heat waves, floods, droughts, storms, rising sea levels, and a general increase in global temperatures [3]. Therefore, the sustainable development and utilization of energy sources have become imperative for the reduction of carbon emissions and the mitigation of climate change [4].

These environmental and energy-related challenges are prompting scientists to identify suitable solutions to address the world's energy problems [5, 6]. Over the past few decades, hydrogen has been identified as the most promising alternative, owing to its exceptionally high gravimetric energy density (120–140 MJ kg^{-1}), nearly three times larger than that of conventional fossil fuels such as natural gas, gasoline, and coal (50 MJ kg^{-1}) [7, 8].

Electrochemical water splitting is regarded as a prospective sustainable technology with the potential to produce high-purity hydrogen gas through two crucial half-reactions: the cathodic hydrogen evolution reaction (HER) and the anodic oxygen evolution reaction (OER) [9]. Currently, alkaline electrolysis of water is regarded as the most promising approach for large-scale green hydrogen production [10]. The current state-of-the-art OER catalysts include IrO_2 and RuO_2, and the most advanced HER catalyst is Pt/C [11, 12]. Moreover, the high cost, scarcity, and limited functionality of these catalysts have imposed significant limitations on the industrial production of hydrogen via electrochemical water splitting [13]. Therefore, it is imperative to develop a novel nonprecious metal bifunctional electrocatalyst that is both cost-effective and ultrastable, while maintaining optimal efficiency [14].

Transition-metal-based materials have garnered significant attention for their remarkable electrocatalytic activity. In particular, transition metal phosphides (TMPs) have attracted considerable interest from researchers due to their cost-effectiveness and superior electrical conductivity. Among them, cobalt phosphides are considered to be emerging transition metal

electrocatalysts owing to their excellent electrocatalytic performance, facile synthesis, and earth abundance [15, 16]. Despite these advantages, cobalt phosphide-based catalysts are still limited in terms of intrinsic conductivity and active-site exposure, which restricts their bifunctional performance in comparison to noble-metal benchmarks. This has prompted research into optimization approaches such as heteroatom doping, composite construction, conductive supports, and surface modification of catalysts with trace amounts of precious metals [17, 18]. However, most reported studies evaluate these strategies under standard laboratory conditions, whereas practical alkaline electrolyzers typically operate at elevated temperatures. Indeed, a significant gap still exists between laboratory testing conditions (room temperature) and the industrial operating environment (50–80°C) [19]. Therefore, it is critical to evaluate the electrocatalytic performance under such challenging operating conditions to ensure its effectiveness in real-world applications.

In this study, a facile, binder-free, scalable, and inexpensive method combining electroless deposition and galvanic displacement was developed to fabricate cobalt phosphide-based electrocatalysts on a Cu substrate. The influence of phosphorus content on the electrocatalytic performance of CoP was initially investigated. Furthermore, Fe was introduced into the cobalt phosphide framework to produce CoFeP. In addition, both CoP and CoFeP were modified with small amounts of Pd and Pt species via galvanic displacement to further enhance their electrocatalytic bifunctional performance. The activity of resulting electrocatalysts was evaluated for HER, OER, and OWS in 1 M KOH across 25–75 ^{o}C, indicating enhanced catalytic activity and long-term durability with reduced noble-metal utilization, thus substantiating their feasibility under industrially relevant conditions.

MAIN GOAL

Fabrication of the Co-P_x/Cu, CoFeP/Cu, PdCoP/Cu, PdCoFeP/Cu, PtCoP/Cu and PtCoFeP/Cu electrocatalysts by electroless deposition and galvanic displacement methods, characterization of composition, microstructure and surface morphology, and evaluation of electrocatalytic activity and stability towards the hydrogen evolution reaction (HER), oxygen evolution reaction (OER) and overall water splitting (OWS) in alkaline media under practical and industrial water splitting conditions.

TASKS

1. To synthesize Co-P_x/Cu and CoFeP/Cu electrocatalysts via electroless deposition, and to investigate the influence of phosphorus (P) content and iron (Fe) incorporation on their structure, morphology, and electrocatalytic performance.
2. To prepare PdCoP/Cu, PtCoP/Cu, PdCoFeP/Cu and PtCoFeP/Cu electrocatalysts through the galvanic displacement of CoP and CoFeP coatings with palladium (Pd) and platinum (Pt) species, then evaluate the impact of noble-metal modification on their electrocatalytic performance.
3. To characterize the crystal structure, microstructure, surface morphology, and elemental distribution of the synthesized electrocatalysts by X-ray diffraction (XRD), scanning electron microscopy (SEM), and energy-dispersive X-ray spectroscopy (EDS).
4. To assess the electrocatalytic activity of the prepared electrocatalysts for the HER and OER in alkaline media.
5. To determine the electrochemically active surface area (ECSA), reaction kinetics and electrochemical long-term stability of the developed electrocatalysts.
6. To evaluate the OWS performance of Co-P_x/Cu, CoFeP/Cu, PdCoP/Cu, PdCoFeP/Cu, PtCoP/Cu, and PtCoFeP/Cu electrocatalysts in an alkaline medium (1 M KOH) at 25 ^{o}C, and to assess the temperature-dependent OWS performance of PtCoP/Cu and PtCoFeP/Cu across the temperature range of 25–75 ^{o}C.

SCIENTIFIC NOVELTY

1. A straightforward and inexpensive fabrication approach, which integrates electroless deposition and galvanic displacement, was developed for the fabrication of Co-P_x/Cu, CoFeP/Cu, PdCoP/Cu, PdCoFeP/Cu, PtCoP/Cu, and PtCoFeP/Cu electrocatalysts for alkaline water splitting.
2. The effects of P, Fe, and surface modification with Pd and Pt species and the combination of them were thoroughly investigated on the structural, surface, and electrocatalytic properties of cobalt phosphide-based electrocatalysts.
3. The bifunctional electrocatalytic activity and stability of the cobalt phosphide-based electrocatalysts in both the HER and OER were significantly improved by surface modification with Pd and Pt species, prepared by the galvanic displacement method.

4. The OWS was successfully tested with the electrocatalysts PtCoP/Cu and PtCoFeP/Cu under industrially relevant operating temperatures (25–75 ^{o}C) to gain insight into their practical applicability for alkaline water electrolysis.
5. A facile, scalable and cost-effective approach for the fabrication of high-performance bifunctional electrocatalysts for efficient alkaline water electrolysis has been developed.

STATEMENTS OF DEFENSE

1. A straightforward and inexpensive combination of electroless deposition and galvanic displacement methods was employed for the successful fabrication of Co-P_x/Cu, CoFeP/Cu, PdCoP/Cu, PdCoFeP/Cu, PtCoP/Cu, and PtCoFeP/Cu electrocatalysts for alkaline water splitting applications.
2. It was established that the phosphorus content (P_x) in Co-P_x/Cu coatings plays a critical role in determining the surface morphology, ECSA, and electrocatalytic performance towards the HER and OER.
3. It was demonstrated that the addition of Fe to cobalt phosphide coatings further improves the catalytic activity and stability of the electrocatalysts by modifying their chemical composition and surface characteristics.
4. It was determined that surface modification of CoP- and CoFeP-based electrocatalysts with trace amounts of Pd and Pt through galvanic displacement significantly enhances the reaction kinetics, catalytic activity, and stability for both HER and OER.
5. The optimized CoP_{11}/Cu, PdCoFeP/Cu, and PtCoFeP/Cu electrocatalysts showed excellent OWS performance in alkaline media. The CoP_{11}/Cu- and PdCoFeP/Cu-based electrolyzers exhibited efficient OWS at 25 ^{o}C, while the PtCoFeP/Cu-based electrolyzer demonstrated exceptional performance at both lab-scale and industry-relevant operating temperatures (25–75 ^{o}C), signifying its feasibility for practical alkaline water electrolysis.

1. LITERATURE REVIEW

1.1. The Energy Transition

Since the industrial revolution, the economic and social evolution of nations has been strongly associated with the large-scale utilization of fossil fuels. This particular dependency has played a significant role in shaping the level of social welfare experienced by society today. However, a critical aspect has frequently been overlooked: environmental sustainability [20, 21]. In recent decades, the global population has grown substantially, resulting in increased energy demand. Consequently, there has been an increase in greenhouse gas (GHG) emissions, including carbon dioxide (CO_2). CO_2 is a known greenhouse gas, and its accelerated release due to human activities has played a significant role in the observed increase in average global surface temperatures. This gas serves to trap solar heat within the atmosphere, thereby increasing global temperatures. To address this issue, world leaders gathered in Paris in 2015 for the UN Climate Change Conference (COP21) to develop a strategic approach to tackle climate change. A primary objective of the Paris Agreement is to encourage a worldwide initiative to restrict the rise in global temperatures to 1.5 °C and to decrease emissions by 45% by 2030, with the ultimate goal of achieving net-zero emissions by 2050 [22].Currently, fossil fuels are the primary source of energy globally and the most significant contributors to rising GHG levels. Consequently, there has been an increasing emphasis on the development of power from renewable energy sources, such as solar and wind power, to mitigate dependence on fossil fuels. However, this approach is hindered by the intermittent nature of renewable energy and its incapacity to align energy supply with human demand in a consistent manner. In order to address the intermittent nature of renewable energy sources, it is crucial to establish energy storage systems that can accumulate excess electricity for future use. Among the several energy storage technologies, hydrogen stands out as a promising candidate, and in particular, water electrolysis is regarded as a promising technology. This method utilises surplus electricity to produce hydrogen. The stored hydrogen can be utilised in a variety of applications, such as in the chemical industry (as a feedstock), energy systems, steel manufacturing (as a reducing agent), transport, urban heating, and in the production of ammonia, which is employed in fertilizers. Furthermore, oxygen, a byproduct of water electrolysis, can be used in the healthcare sector or for industrial applications [23]. In order to meet the EU climate change targets set for the year 2050, hydrogen produced through electrolysis will play an essential role in the decarbonization process [22].

1.2. Hydrogen as an Energy Carrier

Hydrogen, the lightest and most plentiful element, constitutes around 90% of the known universe. Among all traditional fuels, it exhibits the highest energy content per unit of weight, approximately three times greater than that of gasoline. Moreover, in comparison with hydrocarbons, hydrogen presents a low energy density by volume despite exhibiting high energy density by weight. This suggests that, to accommodate the same energy, significantly larger tanks are required for hydrogen storage [24]. In contrast to coal or natural gas, hydrogen is a form of energy carrier and not a source of energy. This indicates that energy derived from solar, wind, or nuclear power, for instance, can be preserved in the form of hydrogen and transferred to where it is required. The hydrogen can then be converted back into heat, electricity, or other forms of energy that are useful to society.

This concept is known as "Power-to-X" (P2X), where "X" refers to the specific application or energy form into which the hydrogen is converted, and "Power" signifies the energy stored in hydrogen [23]. It has recently been determined that "white hydrogen", a natural form of hydrogen, is constantly produced deeply within the Earth. This finding has garnered significant attention due to its potential as a sustainable hydrogen source. Despite this, green hydrogen derived from water electrolysis using renewable energy sources is regarded as the most promising approach for achieving large-scale decarbonisation [25].

The concept of "Power-to-X" (abbreviated as PtX or P2X) is of significance as it facilitates the integration of renewable energy into industries such as heavy manufacturing, transportation, and aviation, which are challenging in terms of direct electrification. Figure 1 illustrates the major Power-to-X routes and their respective applications. The following examples are provided to demonstrate these pathways [26, 27]:

1. Power-to-Power (P2P): The use of fuel cell devices facilitates the reversible conversion of hydrogen into electrical energy. This is of particular significance in ensuring grid stability, maintaining equilibrium between supply and demand of renewable energy, and serving as a reliable source of emergency power when required.
2. Power-to-Gas (P2G): The production of gaseous fuels, including synthetic methane (CH_4), from hydrogen is a viable option.
3. The Power-to-Liquid (P2L): This process uses hydrogen to generate synthetic kerosene or methanol, two liquid hydrocarbons that are essential for various industries, particularly aviation, which requires liquid fuels with a high energy content.

4. The Power-to-Chemicals (P2C): The process of employing hydrogen in the production of chemical products, including ammonia (NH_3), a fundamental component of fertilisers.
5. Power-to-Heat (P2H): The process of producing heat for industrial applications or district heating systems by burning hydrogen or utilising it in fuel cells.

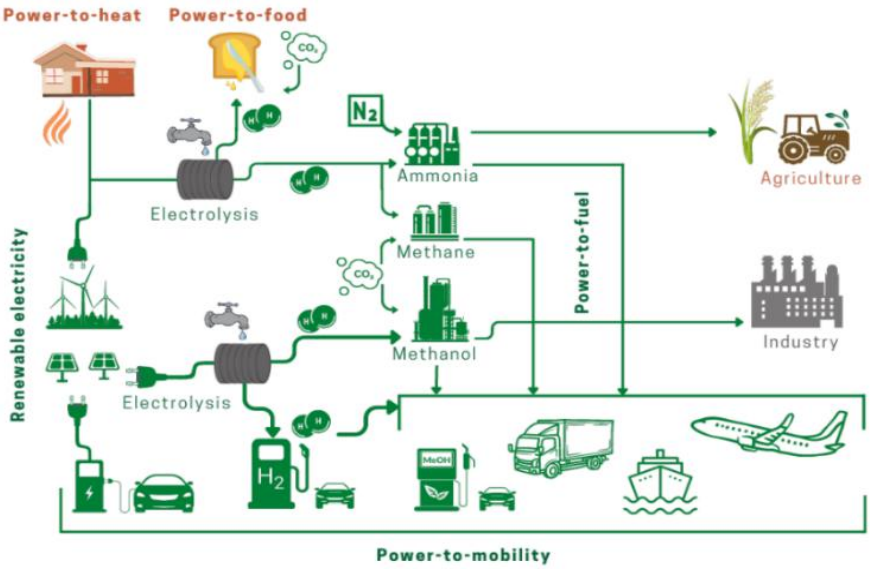

Figure 1. Schematic illustration of the Power-to-X (PtX) concept. Reprinted under the Creative Commons CC BY license from Ref. [26].

1.3. Global Hydrogen Production and Future Prospects

The global production of hydrogen has exhibited a steady upward movement in recent years, predominantly driven by growing industrial demand and the emerging recognition of hydrogen as a pivotal element in the future of low-carbon energy systems [28]. The International Energy Agency (IEA) has reported an increase in global hydrogen production, from approximately 90 Mt in 2020 to nearly 100 Mt in 2024, with continued growth expected in 2025. As shown in Figure 2, the global hydrogen industry is still dependent on fossil fuels for production. Coal and natural gas remain the predominant sources of hydrogen production worldwide, with low-emission hydrogen, derived through water electrolysis and enhanced by carbon capture, utilisation, and storage (CCUS) techniques, contributing a relatively minor share to the overall output. Moreover, the figure also highlights considerable regional inconsistencies in hydrogen production, with China emerging as the

leading global producer, followed by North America, the Middle East, Europe, and India [29, 30]. Despite the increased investment in clean hydrogen production technologies, the implementation of low-emission hydrogen initiatives has proceeded at a more gradual pace than initially predicted. According to the IEA Global Hydrogen Review 2025, the potential for low-emission hydrogen projects is estimated to reach approximately 37 million tonnes per annum by 2030, in comparison to an earlier estimate of 49 million tonnes per annum. However, it is anticipated that hydrogen will play a pivotal role in achieving global decarbonisation goals and facilitating the energy transition towards a sustainable and low-carbon energy economy. To accelerate the large-scale adoption of low-emission and green hydrogen in the coming decades, continued technological advancements, supportive policy frameworks, and further investments in renewable electricity generation and electrolyser technologies will be required [30].

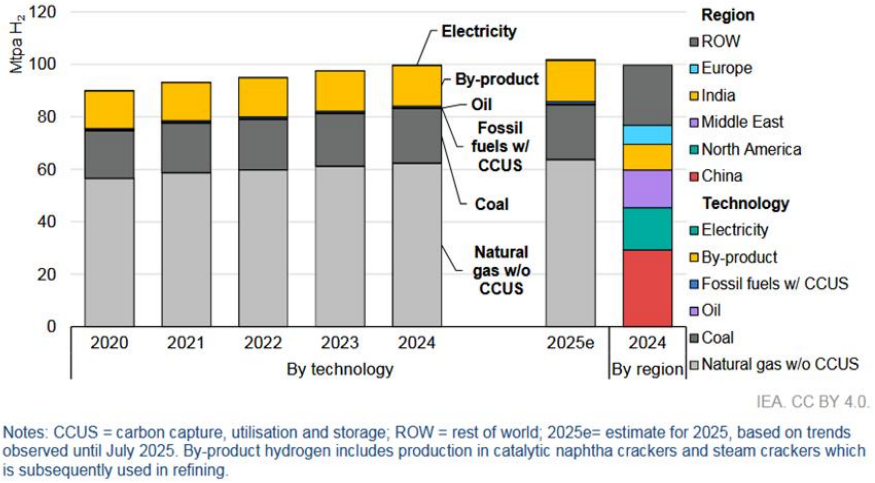

Notes: CCUS = carbon capture, utilisation and storage; ROW = rest of world; 2025e= estimate for 2025, based on trends observed until July 2025. By-product hydrogen includes production in catalytic naphtha crackers and steam crackers which is subsequently used in refining.

Figure 2. Global hydrogen production by technology and by region in 2020-2025. Reprinted under the Creative Commons CC BY license from Ref. [30].

1.4. Hydrogen Production Methods

The production of hydrogen is a crucial aspect that has a significant impact on the development of sustainable hydrogen energy. Despite hydrogen's colorless nature, its sources and synthesis techniques are identified by various color codes. As illustrated in Figure 3, the Hydrogen colour code is represented by H_2-bulletin [31].

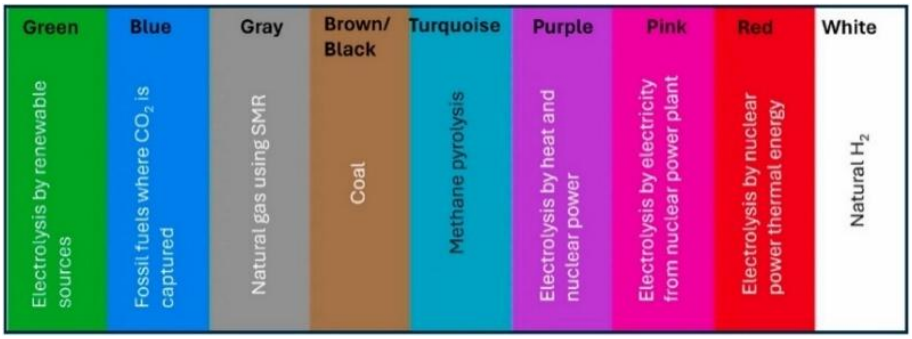

Figure 3. Hydrogen color code from Ref. [31].

The production of green hydrogen involves the electrolysis of water using renewable electricity without the emission of CO_2. The production of blue hydrogen, derived from fossil fuels, results in a net-zero carbon footprint due to its capacity to absorb and store CO_2 in the subsurface. When steam methane reforming is employed to produce grey hydrogen from fossil fuels, CO_2 is released into the environment. The process of coal combustion results in the production of hydrogen in the form of black or brown carbon, which, in turn, releases carbon monoxide and carbon dioxide into the atmosphere. Methane pyrolysis is a process that is employed to recover turquoise hydrogen while eliminating solid carbon. Purple hydrogen relies on the use of heat and nuclear power for water electrolysis. Red hydrogen is obtained through the high-temperature catalytic breakdown of water, using thermal energy from nuclear power sources. Meanwhile, pink hydrogen is derived from electricity produced by nuclear power plants. Natural hydrogen is known as white hydrogen.

This color code has been developed to assist consumers in better understanding the environmental implications of their energy consumption. Furthermore, it provides governments with a way to impose carbon fees on energy sources utilized [32]. There are several methods employed in the production of hydrogen. These methods vary in terms of efficiency, environmental impact, and scalability, and include steam methane reforming, electrolysis, and photoelectrochemical processes. The production of hydrogen plays a significant role in the advancement of a cleaner and more sustainable energy system [31]. As indicated in Figure 4, there are several methods for producing hydrogen.

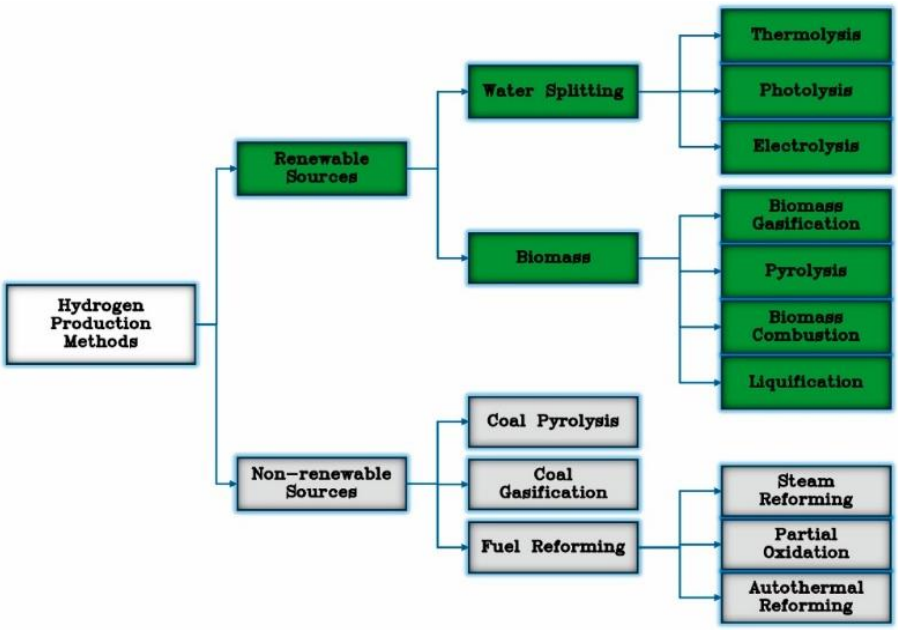

Figure 4. Hydrogen production methods from Ref. [31].

1.5. Fundamentals of Electrochemical Water Splitting

Water, the most abundant source of hydrogen, can be dissociated into oxygen and hydrogen when sufficient energy is supplied. Electrochemical water splitting is a highly effective and ecologically sustainable technology for converting electricity into hydrogen of the highest purity from water. This process involves two electrochemical half-reactions: the anodic oxygen evolution reaction (OER) and the cathodic hydrogen evolution reaction (HER), which convert water into oxygen and hydrogen, respectively. The electrochemical water-splitting process is schematically illustrated in Figure 5. Furthermore, the practical efficiency of water splitting is often hampered by the sluggish reaction kinetics of both HER and OER, resulting in significant overpotentials. Thermodynamically, overall water splitting necessitates a Gibbs free energy (ΔG) of approximately 237.2 kJ mol^{-1}, which corresponds to a standard potential of 1.23 V versus the reversible hydrogen electrode (RHE) [34,35]. In practical electrolysis systems, however, higher potentials are required to achieve efficient water splitting. This excess potential, denoted here as overpotential (η), is a critical factor in overcoming the intrinsic activation barriers during the electrode reaction.

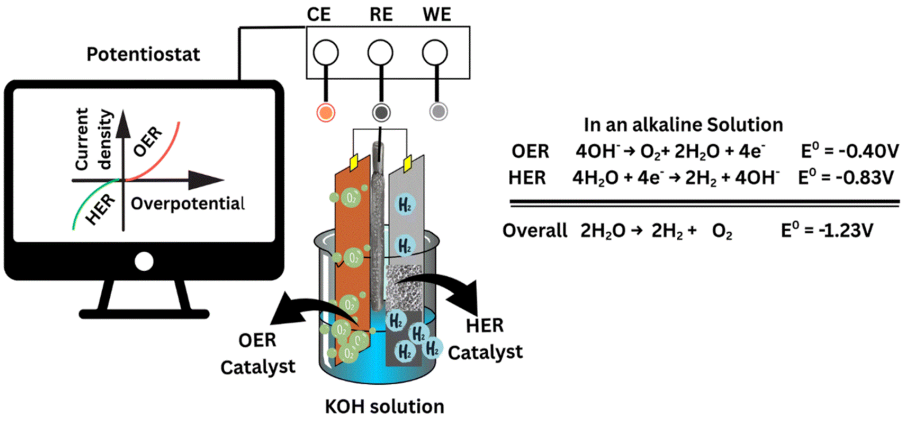

Figure 5. A three-electrode setup for electrocatalytic water splitting from Ref. [33].

Then, the applied potential for the two half-cell reactions of water splitting can be represented as follows [36]:

$$E_{HER} = E^0_{HER} + iR + \eta_{HER} \quad (1)$$

$$E_{OER} = E^0_{OER} + iR + \eta_{OER} \quad (2)$$

where iR represents the ohmic potential drop, η denotes the overpotential, E^0_{HER} = 0 V, and E^0_{OER} = 1.23 V. Another important parameter for evaluating the activity of an electrocatalyst is the Tafel slope, which can be calculated using the following equation: $\eta = b \log(j/j_0)$, wherein b is the Tafel slope, j represents the current density, and j_0 refers to the exchange current density. A smaller Tafel slope (b) indicates a more rapid increase in current density with overpotential, suggesting that electrode kinetics may be more efficient. Moreover, the Tafel slope is correlated with the reaction mechanism, which can be applied to derive the rate-limiting step in the HER and OER [37].

To be economically attractive, it is preferred to conduct both half-reactions of water splitting in the same electrolyte. Therefore, the development of bifunctional electrocatalysts has emerged as an important research direction. These catalysts can simplify the design and manufacture of water-splitting electrolyzers, effectively reduce the overpotentials associated with both HER and OER, and thereby improve overall water-splitting efficiency and lower the cost of practical applications [38].

1.5.1. Hydrogen Evolution Reaction (HER) Mechanism

Regardless of the pH conditions, a specific reaction mechanism is followed by the HER, which is one of the half-reactions of electrochemical splitting of water (Figure 6).

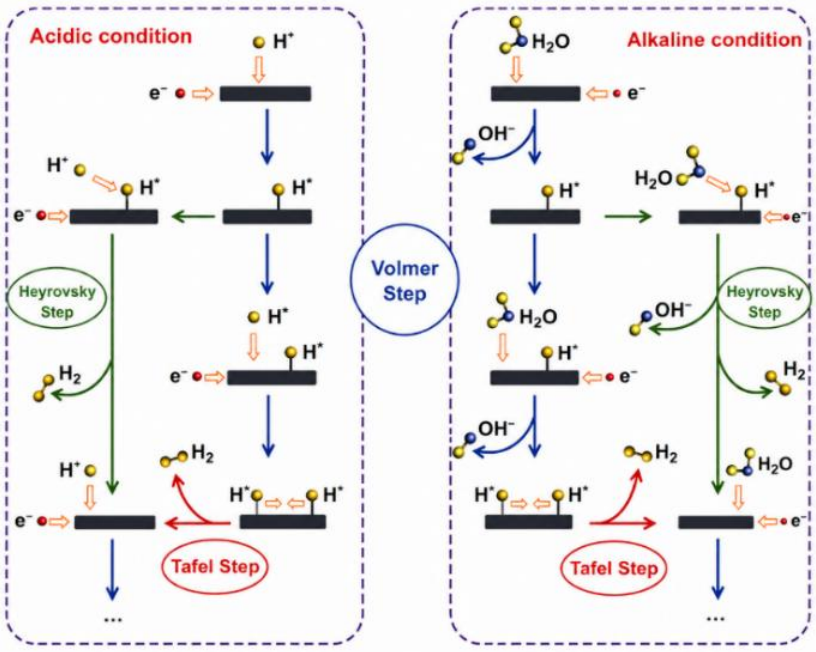

Figure 6. HER pathways in alkaline and acidic environments from Ref. [39].

The mechanism of cathodic HER in electrocatalytic water splitting comprises three principal steps: Volmer, Heyrovsky, and Tafel reactions. The initial Volmer phase involves proton reduction on the electrode surface (M), which results in the formation of H_2 intermediates (H*).

Stage 1: Adsorption of H_2 gas electrochemically (Volmer step)

$$H_3O^+ + M + e^- \rightarrow H^* + H_2O \quad \text{under acidic conditions} \quad (3)$$

$$H_2O + M + e^- \rightarrow H^* + OH \quad \text{under alkaline environments} \quad (4)$$

The Tafel or Heyrovsky phases, or both, are used to generate H_2 once H^* has occurred on the electrode surface. In the process of desorption, the surface coverage of H^* is identified as the rate-determining step [40]. The Tafel step is representative of a rate-determining step that takes place when the surface

coverage of H^* is significant. Nearby H^* intermediates are capable of undergoing a reaction that results in the formation of H_2 at this specific point. The rate-determining process in electrochemical desorption is crucial for the poor surface coverage of H^*, since the adsorbed H^* intermediate undergoes the Heyrovsky reaction with the electron and proton to produce H_2 [41].

Stage 2: Steps of chemical desorption (Tafel step)

$$H^* + H^* \rightarrow H_2 \quad (5)$$

From the desorption steps, electrochemically (Heyrovsky step)

$$H_3O^+ + e^- + H^* \rightarrow H_2 + H_2O \quad \text{under acidic conditions} \quad (6)$$

$$H_2O + e^- + H^* \rightarrow H_2 + OH^- \quad \text{under an alkaline environment} \quad (7)$$

Ideally, a HER catalyst would exhibit a binding energy that exceeds the minimal threshold yet does not exceed the optimal level, thereby ensuring that the intermediates' binding is neither overly weak nor excessively strong. To ensure efficient charge transfer and optimal H_2 desorption, the binding energy between the intermediates and electrocatalysts is a pivotal factor [41,42].

1.5.2. Oxygen Evolution Reaction (OER) Mechanism

The OER involves more proton and electron exchanges; therefore, it requires a greater overpotential. Despite the numerous theories that have been proposed to explain the mechanisms of OER, there is a general consensus among researchers that an electrochemical oxidation step is a critical component of the reaction pathway [43]. In addition, the interpretation of the general strategy is complicated by the tendency of oxygen to form on metal oxide surfaces rather than on bare metal. When designing an OER employing metal electrocatalysts, it is imperative to consider the concept of the 4-step proton-coupled electron transfer pathways. Under acidic conditions, water molecules act as the reactant, and the OER proceeds through the following four-step mechanism:

$$M + H_2O \rightarrow M{-}OH^* + H^+ + e^- \quad (8)$$

$$M{-}OH^* \rightarrow M{-}O^* + H^+ + e^- \quad (9)$$

$$M{-}O^* + H_2O \rightarrow M{-}OOH^* + H^+ + e^- \quad (10)$$

$$M{-}OOH^{*} \rightarrow M + O_2 + H^{+} + e^{-} \quad (11)$$

Accordingly, the surface active site of the electrocatalyst is denoted by M, while the adsorbed intermediates are represented by an asterisk (*). The majority of transition-metal (TM) oxides exhibit unreliability in oxidation potential within acidic environments, irrespective of the underlying pathway. This phenomenon is predominantly attributed to first-principles analysis from DFT [44]. To develop a comprehensive understanding of the OER mechanism on transition-metal-based electrocatalysts, it is imperative to elucidate the reaction mechanism that occurs under alkaline environments (Figure 7).

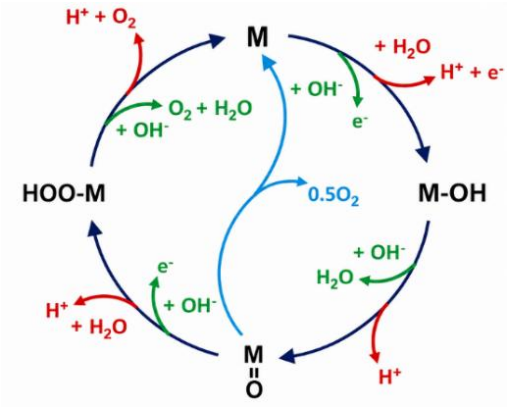

Figure 7. OER approach in acidic (green route) and alkaline (red route) environments. Two neighboring oxo (M–O) intermediates directly react to create O_2, as shown by the light blue line, and the development of a peroxide (M–OH) intermediate is shown by the black line, which represents the OER from Ref. [39].

Conversely, under alkaline conditions, hydroxide ions (OH^{-}) directly participate in the reaction pathway, and the OER mechanism can be represented by the following reactions:

$$M + OH^{-} \rightarrow M{-}OH^{*} + e^{-} \quad (12)$$

$$M{-}OH^{*} + OH^{-} \rightarrow M{-}O^{*} + H_2O + e^{-} \quad (13)$$

$$M{-}O^{*} + OH^{-} \rightarrow M{-}OOH^{*} + e^{-} \quad (14)$$

$$M{-}OOH^{*} + OH^{-} \rightarrow M + O_2 + H_2O + e^{-} \quad (15)$$

The oxidation of OH^- ions result in the formation of $M–OH^*$, representing the initial stage of the oxygen evolution reaction (OER). In the initial stage, the proton is removed from the structured $M–OH^*$ species, resulting in the transformation to $M–O^*$. In the subsequent stage of the reaction, $M–O^*$ merges with the OH ion to produce $M–OOH^*$. Subsequently, the $M–OOH^*$ species reacts with the OH^-, yielding O_2 and the initial active site. As demonstrated in Figure 7, the OER process constitutes a continuous cycle that initiates with the adsorption of OH^- and terminates with the evolution of O_2. Various criteria may be employed to assess the activity of the catalyst, including the overpotential, onset potential, Tafel slope, electrochemical surface area (ECSA), specific activity, turnover frequency, and Faradaic efficiency. A number of these properties may be dependent on one another or may only be assessed in specific systems. In order to evaluate the performance of generic water splitting systems in a consistent manner, this assessment employs the overpotential required to attain 10 mA cm^{-2}, in conjunction with the Tafel slope [39].

1.6. Electrocatalysts for HER & OER

An efficient water splitting process demands electrocatalysts that exhibit high efficiency, stability, and corrosion resistance. Various catalysts have been synthesized to enhance the reaction rate and reduce the overpotential for HER and OER. Currently, noble metals and noble metal oxides, including Pt [45, 46], RuO_2 [47], and IrO_2 [48], are regarded as the most effective catalysts for both HER and OER. However, Pt/C exhibits excellent HER activity in both acidic and basic electrolytes. Conversely, IrO_2 and RuO_2 demonstrate effective OER activity only in basic electrolytes [49–52]. However, their large-scale commercial application is significantly restricted by the limited availability and high cost of these precious metals. Consequently, a strong research focus has emerged on developing low-cost, high-efficiency, non-precious electrocatalysts, which serve as an alternative to precious-metal-based materials and exhibit high activity towards OER and HER [53–57].

Among the numerous non-precious electrocatalysts, cobalt-based materials have received significant attention for their applications in the hydrogen evolution reaction (HER), oxygen evolution reaction (OER), and overall water splitting. This attention is attributed to their abundance on Earth, cost-effectiveness, and favourable electrochemical properties. As demonstrated in Figure 8, cobalt-based electrocatalysts exist in multiple forms, including metallic Co, nitrides, phosphides, sulfides, and mixed metal

oxides. These have been thoroughly investigated for water-splitting applications. The catalytic efficacy of these materials is significantly influenced by several factors, including their structural characteristics, electrical conductivity, the presence of active sites, intrinsic activity, and stability. Therefore, a comprehensive understanding of the structure-activity relation and catalytic mechanisms of Co-based electrocatalysts is imperative for the optimal design of effective and durable water-splitting systems [58].

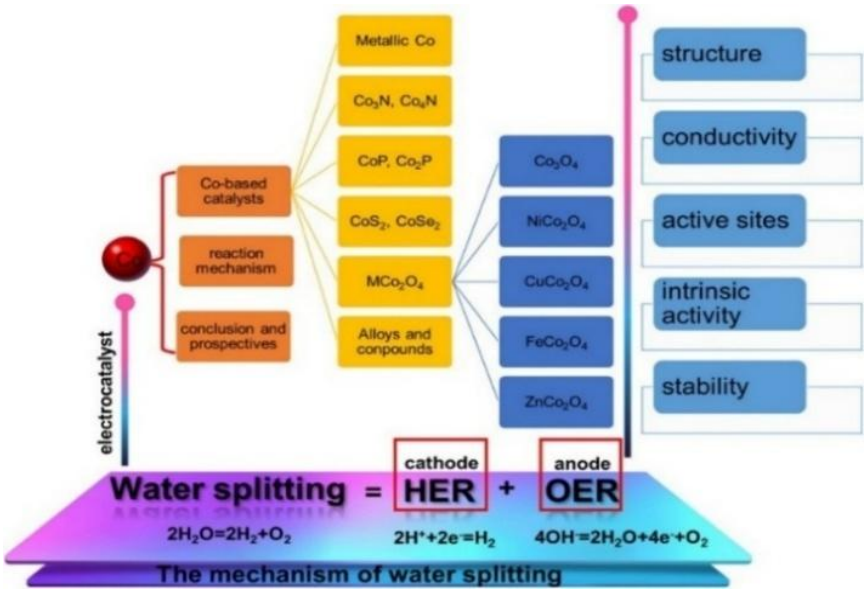

Figure 8. Outline of Co-based catalysts. Schematic summarizing the application of Co-based electrocatalysts to water splitting showing the structure, conductivity, active sites, intrinsic activity, and stability of the different types of Co-based catalysts from Ref. [58].

Currently, transition metal-based materials (TMs) have been extensively studied as potential alternatives to precious metal-based electrocatalysts due to their competitive electrochemical performance and high abundance [59–61]. Among these TMs, sulfides [62–64], borides [65], (oxy)hydroxides [66–68], and phosphides [69,70] have attracted considerable attention. Transition metal phosphides (TMPs) possess excellent electrochemical properties for water electrolysis. Researchers have highlighted transition-metal phosphides (TMPs) such as Co-P [71,72], Fe-P [73], Ni-P [74,75], and Mo-P [76,77] as highly attractive catalysts due to the favourable redox properties, cost-effectiveness, and high electrocatalytic activity.

The main cause of their exceptional electrocatalytic activities is attributed to the incorporation of phosphorus (P) atoms. Due to the high electronegativity of P atoms, the formation of metal-phosphide complexes occurs, resulting in the transfer of electrons from metal atoms to P atoms and the subsequent adjustment of the electronic structure. Furthermore, the presence of P atoms on the surface of catalysts has been shown to increase defect levels, thereby enhancing the adsorption capability of the active site for reaction intermediates [78]. Although several single transition metallic phosphides have been reported to possess good electrocatalytic performance, the majority of these are limited to a single half-reaction process (HER or OER) and exhibit a slight decrease in efficiency at high overpotential [79]. The addition of one more transition metal to the single metallic phosphide composition is a viable method to broaden the range of applications and enhance electrochemical performance. The synergistic effects of bimetal catalysts promote an optimal electron distribution, resulting in enhanced catalytic performance compared to single TMPs [80–85].

As a category of transition metal phosphide, CoP has attracted significant attention and has emerged as a widely used electrocatalyst [86,87], but its OER performance requires further enhancement to achieve efficient overall water splitting. Currently, the lower activity of OER active sites and the slower electron transfer rate of CoP can be enhanced by modifying the composition and morphology of the material [71]. For example, the addition of metal Fe as a promoter to CoP results in the formation of binary phosphides to produce efficient and stable electrocatalysts, which has been documented in the literature [88–91]. Despite the remarkable progress achieved with bimetallic phosphides, their catalytic performance remains significantly inferior to that of the Pt-based catalysts under practical operating conditions. Therefore, further improvements are still required in the catalytic activity and stability of TMPs to facilitate the large-scale application of hydrogen production by water electrolysis.

Platinum (Pt) is regarded as an ideal material for the HER due to its moderate metal-hydrogen (M-H) bonding strength and favourable reaction kinetics over a broad range. However, the practical application of Pt in electrochemical reactions has been significantly restricted by its scarcity, high cost, and limited utilisation efficiency. The current challenge is to enhance the utilisation efficiency of Pt-based catalysts through rational design. For this purpose, a variety of strategies have been developed, including interfacial engineering [92, 93], morphology control, ultralow precious-metal modification [94–96], and the formation of heterostructures [97–100]. These

strategies focus on promoting charge transfer, moderating the electronic structure, and reducing the adsorption energy of different intermediates (such as *H_2O, *OH, and *H) in the electrocatalytic process, and thus enhance the catalytic OWS performance. Notably, the intrinsically high HER activity of precious metals (e.g., Pt, Ir, and Ru), combined with ultralow precious-metal modification of transition-metal composites, can result in a substantial increase in HER performance and, consequently, an exceptional OWS performance of electrocatalysts. Cheng et al. proposed a method to improve the HER and OER properties of $NiCo_2O_4$ through the application of Pt doping and subsequently applied it to the efficient electrolysis of water. Pt doping not only increases the intrinsic HER activity of Pt-$NiCo_2O_4$ but also enhances its OER performance through a synergistic effect between Pt and $NiCo_2O_4$. The electrolyzer that is assembled with Pt-$NiCo_2O_4$ needs a voltage of only 1.62 V to achieve 10 mA cm^{-2} [101]. However, additional research is necessary to explore the low Pt modification techniques that could enhance the OWS performance of transition metal-based electrocatalysts.

In addition to Pt-based catalysts, Pd has been identified as a potential alternative for the HER, because it is closely located in the volcano plot between hydrogen chemisorption energy and exchange current. Moreover, the greater hydrogen affinity of Pd restricts its HER activity, which is typically 30–40 times lower than that of Pt. In order to attain a moderate hydrogen binding strength, the alloying of Pd with transition metals (e.g. Fe, Co, and Cu) has been extensively employed, thereby facilitating the modulation of the electronic structure via synergistic and ligand effects. This suggests that bimetallic Pd–M catalysts, such as Pd–Fe, Pd–Cu, and Pd–Co, exhibit greater HER activity in comparison to pure Pd. Furthermore, light-atom dopants (e.g., N, H, and P) and the presence of Pd hydrides (PdH_x) have been shown to weaken hydrogen adsorption and promote hydrogen generation.

Furthermore, Pd-based alloys have been shown to exhibit excellent activity and high current density, a phenomenon attributed to their ability to absorb a significant amount of hydrogen from electrolytes, thereby enhancing their HER activity [102]. Specifically, among Pd-based catalysts, effective strategies for improving HER performance include the precise control of doping concentration and the employment of supporting materials, which have been shown to enhance HER activity, primarily by increasing the accessible active surface area [103]. For instance, Zhong et al. examined the electrocatalytic behaviour of PdCo-based catalysts in acidic, alkaline, and neutral electrolytes. Their PdCo@N–C/rGO catalyst exhibited excellent HER performance across all three media, with low overpotentials and notable long-term stability [104].

1.7. Fabrication Strategies for Electrocatalysts

As illustrated in Figure 9, a variety of fabrication methods can be utilised to produce electrodes for electrochemical water splitting.



Figure 9. Overview of advanced fabrication and interface-engineering strategies employed for the synthesis of electrocatalysts from Ref. [105].

These methods are designed to optimise electrocatalytic activity and decrease production expenses. In addition to fabrication methods, a range of modification techniques can be employed to improve the efficiency of the prepared catalysts. These approaches comprise heteroatom doping, defect engineering, nano-size modulation, construction of heterostructures, and the formation of bimetallic systems. The efficacy of the catalytic materials can be enhanced by implementing these modifications [105].

The selection of an optimal fabrication strategy is imperative in determining the morphology, composition, active site density, and long-term stability of electrocatalysts. In recent years, a variety of metal film deposition and surface engineering techniques have been developed, facilitating the

fabrication of coatings with controlled morphology, thickness, composition, and surface properties.

As demonstrated in Figure 10, these techniques consist of physical vapor deposition (PVD), chemical vapor deposition (CVD), electrospraying, metal powder coating, electroplating, and electroless plating.

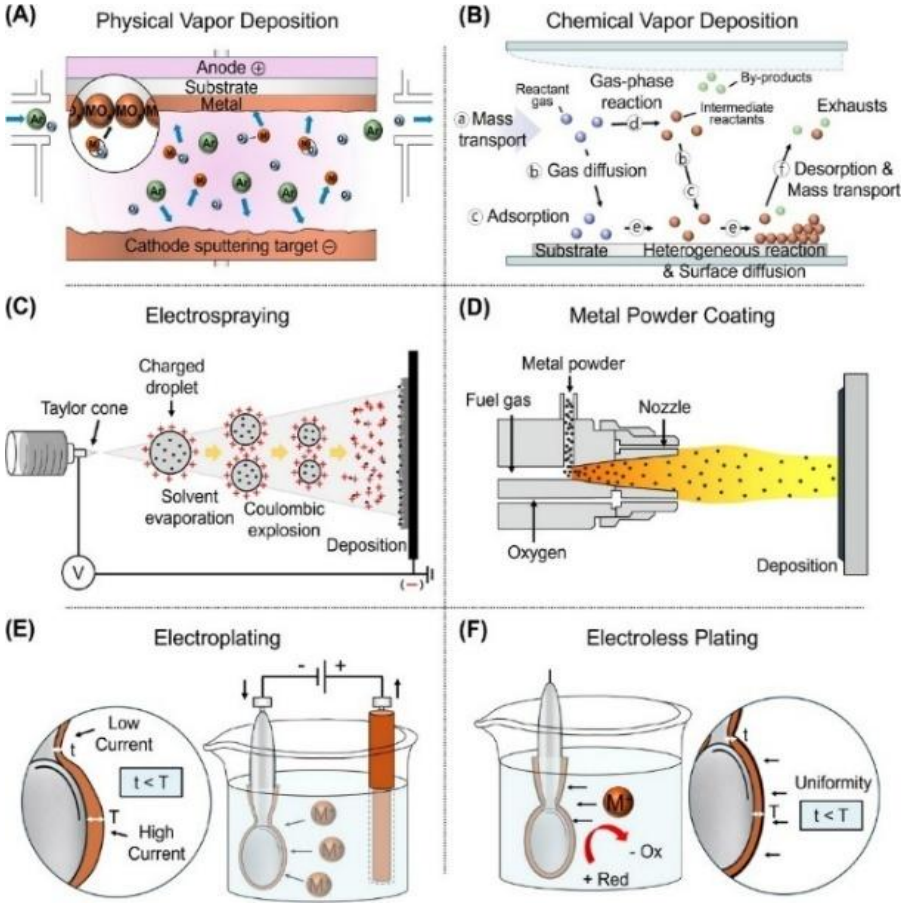

Figure 10. Comparison of commonly used coating and deposition techniques, including PVD, CVD, electrospraying, metal powder coating, electroplating, and electroless plating from Ref. [106].

Each approach has its own set of advantages and limitations, which are dependent on the specific application, the characteristics of the substrate, and the production parameters. Among these methods, electroless deposition has garnered considerable attention due to its simplicity, affordability, and capacity to generate uniform coatings without the requirement of an external power source [106].

1.7.1. Electroless Deposition

Electroless deposition, also known as an autocatalytic chemical reduction process, offers a simple, environmentally friendly, cost-effective, energy-saving, and highly efficient method for directly producing metal and alloy nanoparticles on metallic or nonmetallic substrate surfaces using electrochemical redox reactions in aqueous acidic, neutral, or alkaline solution baths. The difference in reduction potential between the metal ions in the solution bath and the substrate material drives a spontaneous redox reaction, resulting in the formation of a coating on the substrate [107]. In electroless deposition, the reaction is catalyzed by employing a suitable reducing agent, which supplies the electrons required for the reduction reaction, and metal is deposited over the substrate. The overall reaction can be represented as [108]:

$$\text{Metal ion } (M^+) + \text{Reducing agent (Red)} \rightarrow \text{Metal deposited} + \text{Oxidized product (Ox)} \quad (16)$$

There are two reactions involved in electroless deposition:

$$\text{Metal deposition: } M^+ + e^- \rightarrow M \quad (16a)$$

$$\text{Oxidation: Red} + H_2O \rightarrow \text{Ox} + H^+ + e^- \quad (16b)$$

where M represents the metal, e^- is the electron, Red is the reducing agent, and Ox is the oxidized product. Electroless deposition is typically carried out under mild heating conditions (50–80 ^oC) for several minutes to several hours, depending on the desired mass loading. The thickness of electroless coatings can reach up to 10–200 μm. The schematic illustration of the electroless deposition technique is shown in Figure 11. Compared with electroplating, electroless deposition offers several advantages, including the possibility of producing coatings with uniform thickness, depositing material even in deep recesses, the ability to produce very thin layers, excellent step coverage, and independence from the size, shape, or conductivity of the substrate [108, 109].

Additionally, the composition of the as-deposited coatings can be finely tuned by adjusting the deposition conditions and the concentration of metal salts in the solution bath. One of the major advantages of electroless deposition is its ability to coat substrates with complex geometries, making it highly attractive for surface coating and the fabrication of advanced electrocatalytic materials. However, controlling the reactions and the size of the deposited particles can be challenging due to the thermodynamically spontaneous nature of the deposition process [110, 111].

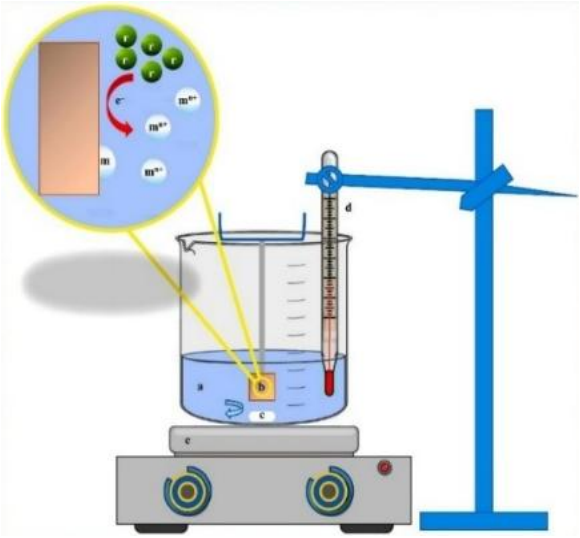

Figure 11. Schematic illustration of electroless deposition technique (a: solution bath, b: substrate, c: magnetic stirrer, d: thermometer, e: hot plate, m: metal, and r: reducing agent from Ref. [107].

1.7.2. Galvanic Displacement

Galvanic displacement is defined as the process of spontaneous replacement of a metal's (M) surface layers by a more noble metal when the former is immersed in a solution containing the latter in ionic form. The reaction is facilitated by the equilibrium potential difference between the two metal/metal ion redox couples. The following reaction is thermodynamically favoured and can take place spontaneously when a metal, M (e.g., Cu, Fe, Co, Ni, Al, etc.), is immersed in a solution which contains ions of a more noble metal, M_{noble}^{n+} (e.g., Pt, Au, Pd, Ag, Ru, Ir, Rh, Os, etc.):

$$M_{noble}^{n+} + n/m\ M \rightarrow M_{noble} + n/m\ M^{m+} \quad (17)$$

Consequently, this reaction results in the partial or complete dissolution of M as M^{m+} ions, and the deposition of M_{noble} in metallic form, which occurs either on surface sites of remaining M or on top of already deposited M_{noble} atoms. As demonstrated in Figure 12, the initial step involves the deposition of a metal layer by electrodeposition or electroless deposition. Following this, a more noble metal is then introduced through the process of galvanic replacement.

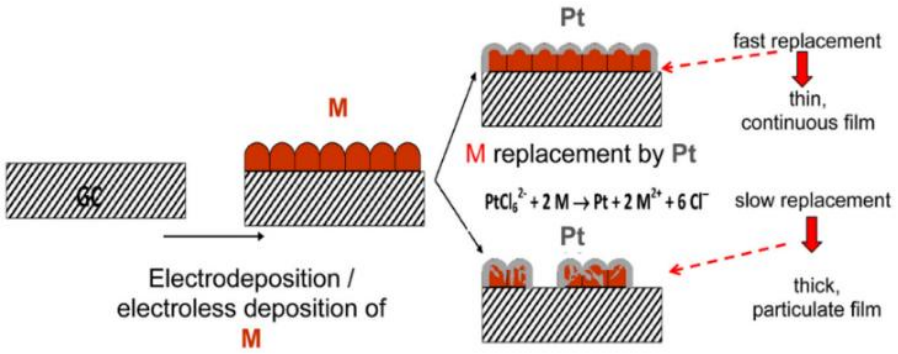

Figure 12. Schematic illustration showing the morphology of Pt(M) deposits produced by galvanic replacement of continuous M layers on a smooth glassy carbon (GC) substrate. Fast replacement results in a continuous Pt(M) layer (top part), while slow replacement leads to particulate Pt(M) deposits (bottom part from Ref. [112].

The resultant bimetallic material may exhibit a noble-rich shell and an M-rich core, potentially leading to a reduction in noble metal loading and the modification of its properties by the underlying metal M [112]. This process is referred to as immersion plating [113] in the plating industry and galvanic replacement in materials chemistry [114].

2. MATERIALS AND METHODS

2.1. Materials and Chemicals

The following materials and reagents used for the experiments conducted in this work are listed below:

- Hydrochloric acid, HCl (35–38%, Chempur, Piekary Śląskie, Poland);
- Potassium hydroxide, KOH (98.8%, Chempur, Piekary Śląskie, Poland);
- Sodium hydroxide, NaOH (98.8 %, Chempur);
- Cobalt(II) sulfate, $CoSO_4 \cdot 7H_2O$ (99.5%, Chempur, Piekary Śląskie, Poland);
- Iron(II) sulfate heptahydrate, $FeSO_4 \cdot 7H_2O$ (99.0 %, PENTA, Czech Republic);
- Sodium hypophosphite, $NaH_2PO_2 \cdot H_2O$ (97%, Alfa Aesar, Kandel, Germany);
- Glycine, $C_2H_5O_2N$ (99%, Chempur, Piekary Śląskie, Poland);
- Palladium (II) chloride, $PdCl_2$ (59.5%, Thermo Fisher Scientific, Horsham, UK);
- Cu sheets (99%, Goodfellow Cambridge Limited, Huntingdon, England);
- Calcium magnesium oxide, known as “Vienna Lime” (50–100%, Kremer Pigments GmbH & Co. KG, Aichstetten, Germany);
- Hexachloroplatinic acid, H_2PtCl_6 (99.95%, Sigma-Aldrich).

The chemicals utilized in this study were of analytical grade, and no additional purification was performed. The electrolytes were prepared by using deionized water obtained from a Millipore Milli-Q Ultra system, which exhibited a resistivity of 18.2 MΩ.cm or higher.

2.2. Substrate Preparation

Before electrode fabrication, copper substrates were precisely cut from a Cu sheet into dimensions of 1 × 1 cm for electrochemical measurements and structural characterization.

1. Pretreatment: The Cu substrate was pretreated with calcium magnesium oxide, following which rinsed with deionized water (DI).
2. Cleaning: The pretreated substrate was immersed in a solution of $HCl:H_2O$ (1:1, *v/v*) for 1 min at a temperature of 25 ^oC to remove any residual inorganic impurities from the surface, and then rinsed with DI water.

3. Activation: Subsequently, the cleaned Cu substrate was subjected to activation by means of immersion in a 0.5 g L^{-1} $PdCl_2$ solution for 1 min at 25 °C. Following this, the substrate was thoroughly rinsed with DI water before further processing.

2.3. Fabrication of Co-P_x/Cu Catalysts

The Co-P_x/Cu catalysts were fabricated via an electroless deposition process on a pretreated Cu substrate. The chemical composition of the electroless plating bath, as well as the deposition parameters utilized for the synthesis of the Co-P_x/Cu electrodes, are presented schematically in Figure 13. The pretreated Cu substrate was immersed in a freshly prepared electroless plating bath containing 0.1 M $CoSO_4$, 0.6 M glycine (NH_2CH_2COOH), and NaH_2PO_2 concentrations of 0.25, 0.5, 0.75, 2.5, and 4.5 M. The pH of the plating solution was precisely adjusted to 11 using a NaOH solution. The plating bath operated at a temperature of 80 °C for 10 min.

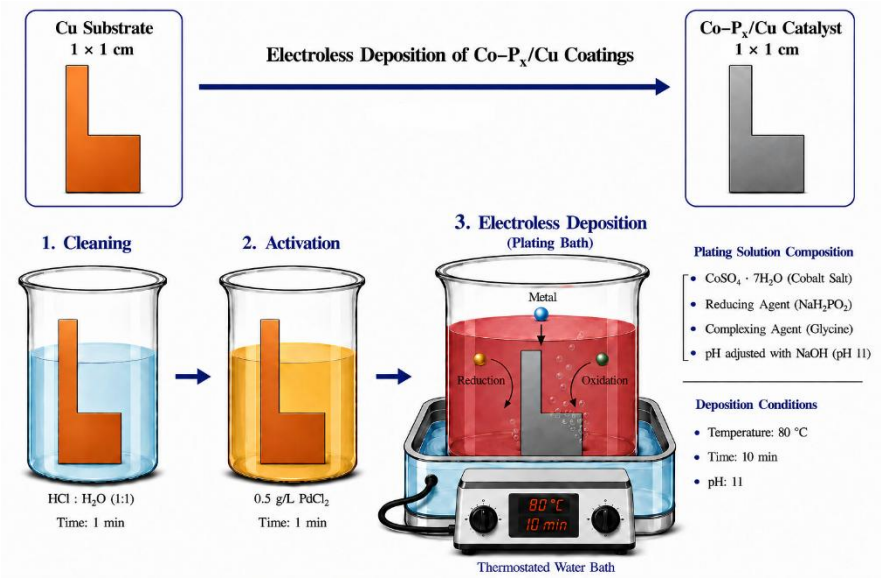

Figure 13. Schematic representation of the electroless deposition process for the fabrication of Co-P_x/Cu catalysts investigated in this research. The schematic illustration was generated by the author using ChatGPT (GPT-5.6 Luna).

Preliminary experiments were conducted to optimize the deposition parameters. In these experiments, the bath pH, temperature, deposition time, and NaH_2PO_2 concentration were varied systematically. From these

experiments, the optimal conditions for obtaining uniform and adherent Co-P_x coatings on the Cu substrate were determined to be pH 11, 80 ^oC and 10 min. The concentration of NaH_2PO_2 was varied to control the amount of phosphorus in the coating and to investigate its effect on the catalyst properties. NaH_2PO_2 was utilized as both the reducing agent and the phosphorus source, while glycine was employed as a complexing agent for Co^{2+} ions. By varying the NaH_2PO_2 concentration, Co-P_x/Cu electrodes with different phosphorus contents (x = 0.4, 1.6, 5, 8, and 11) were successfully obtained. After the deposition process, the obtained Co-P_x/Cu sample was carefully removed, thoroughly rinsed with DI water, air-dried, and used without further treatment.

2.4. Fabrication of PdCoP/Cu and PdCoFeP/Cu Catalysts

The Cu substrates, prepared according to the procedure outlined in Section 2.2, were used for the electroless deposition of CoP and CoFeP coatings. The fabrication of CoP/Cu involved the immersion of a pretreated and Pd-activated Cu substrate in an electroless plating bath containing 0.1 M $CoSO_4$, 0.6 M glycine, and 0.75 M NaH_2PO_2 (pH = 11). Deposition was performed at a temperature of 60 ^oC for 30 min. These conditions were chosen from preliminary optimization experiments where the bath composition, pH, deposition temperature and deposition time were varied to get uniform and adherent CoP and CoFeP coatings on the Cu substrate. The CoFeP/Cu catalyst was synthesised under identical deposition conditions, with the addition of 0.01 M $FeSO_4$ to the plating bath. The resulting coatings were thoroughly rinsed with DI water and air-dried at room temperature.

The Pd species were deposited on the as-prepared CoP and CoFeP coatings via a galvanic displacement process. The CoP/Cu and CoFeP/Cu electrodes were immersed in a 1 mmol L^{-1} $PdCl_2$ solution for 1 minute at 25 ^oC to facilitate the deposition of Pd species on the catalyst surface. The deposition conditions for Pd were selected on the basis of preliminary experiments aimed at identifying the optimal conditions for the control of surface modification without compromising the underlying CoP and CoFeP coatings. Then, the samples were rinsed thoroughly with DI water and dried at ambient temperature.

2.5. Fabrication of PtCoP/Cu and PtCoFeP/Cu Catalysts

The Cu substrates, prepared as outlined in Section 2.2, were used for the deposition of the CoP and CoFeP coatings. Briefly, Pd-activated Cu substrates were immersed in an electroless plating bath comprising 0.1 M $CoSO_4$, 1.5 M NaH_2PO_2, and 0.6 M glycine (pH = 10.5) for 30 min at 80 °C. The CoFeP/Cu catalyst was prepared under identical experimental conditions, incorporating 0.01 M $FeSO_4$ into the plating bath. The conditions of the depositions were determined in a preliminary optimization experiment by varying the composition of the bath, pH, temperature and deposition time to obtain uniform and adherent CoP and CoFeP coatings on the Cu substrate. The resulting coatings were thoroughly rinsed with DI water and air-dried at room temperature.

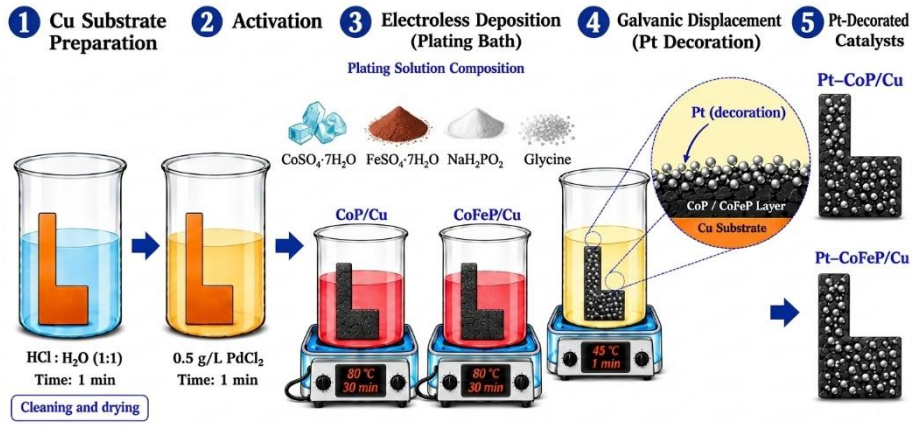

Figure 14. Schematic representation of the fabrication process of PtCoP/Cu and PtCoFeP/Cu electrocatalysts via electroless deposition followed by galvanic replacement investigated in this research. The schematic illustration was generated by the author using ChatGPT (GPT-5.6 Luna).

A schematic illustration of the fabrication process is presented in Figure 14. Thereafter, Pt species were deposited onto the surface of the as-prepared CoP/Cu and CoFeP/Cu electrodes via a galvanic displacement method. To achieve this, the deposited electrodes were immersed in a 1 mmol L^{-1} H_2PtCl_6 solution at 45 °C for 1 min. The deposition conditions for Pt were selected on the basis of preliminary experiments aimed at identifying the optimal conditions for the control of surface modification without compromising the underlying CoP and CoFeP coatings. The samples were

then rinsed thoroughly with DI water and dried at room temperature before further characterization and electrochemical investigations.

2.6. Characterization of the Synthesized Catalysts

A TM4000Plus scanning electron microscope with an AZetecOne detector (Hitachi, Tokyo, Japan) was used for the characterization of the surface morphology and elemental distribution of the Co-P_x/Cu catalysts.

An FEI Helios Nanolab 650 (Hillsboro, OR, USA) dual beam system with an energy dispersive X-ray (EDX) spectrometer INCA Energy 350 (Oxford Instruments, Abingdon, Oxfordshire, UK) and an X-Max 20 mm^2 (Oxford Instruments, Abingdon, Oxfordshire, UK) detector was used to observe the surface morphology of the CoP, CoFeP, PdCoP/Cu, PdCoFeP/Cu, PtCoP/Cu, and PtCoFeP/Cu catalysts via scanning electron microscopy.

X-ray diffraction patterns were recorded using an X-ray diffractometer D2 Phaser using CuK_α radiation (Bruker, Karlsruhe, Germany). A step-scan mode was used in a 2θ range from 10° to 100° with a step length of 0.04^o and a counting time of 1 s per step. For XRD measurements, the CoP, CoFeP, PdCoP, and PdCoFeP catalysts were deposited on the glass surface.

2.7. Electrochemical Measurements

The electrocatalytic activities of the prepared catalysts towards the HER and OER were evaluated via linear sweep voltammetry (LSV). This was conducted using a PGSTAT100 potentiostat/galvanostat (Metrohm Autolab B. V., Utrecht, The Netherlands) with a standard three-electrode electrochemical cell setup. The fabricated catalysts with geometric areas of 2 cm^2 were employed as working electrodes. A Pt sheet was used as a counter electrode, and an Ag/AgCl (3 M KCl) electrode was used as a reference. All the reported potential values reported in this study were converted to the reversible hydrogen electrode (RHE) scale using the following equation:

$$E_{RHE} = E_{measured} + 0.059 \cdot pH + E_{Ag/AgCl\ (3\ M\ KCl)} \quad (18)$$

where $E_{Ag/AgCl\ (3\ M\ KCl))} = 0.210$ V. In the case of Co-P_x/Cu catalysts, all the exhibited potentials were corrected using $E_{corr} = E_{RHE} - iR$, where R was determined via electrochemical impedance spectroscopy (EIS).

HER and OER linear sweep voltammograms (LSVs) were recorded in an N_2–saturated 1 M KOH solution at room temperature from the open circuit potential (OCP) to –0.432 V or –0.5 V (vs. RHE) and from the OCP to

1.840 V or 2.1 V (vs. RHE), respectively, at a potential scan rate of 2 or 5 mV s^{-1}. To evaluate the long-term stability of the fabricated catalysts, the chronoamperometric curves were recorded at a constant potential of –0.26 V in 1.0 M KOH solution for 10 h or 15 h, while chronopotentiometric curves were recorded at a constant current density of ±10 mA cm^{-2} at 25 °C for 10 h or 15 h.

The accelerated degradation test (ADT) was performed for 1000 cycles at a constant scan rate of 400 mV s^{-1}, after which the stable polarization curves were recorded at 2 mV s^{-1} for comparison with the initial curve.

The HER and OER current densities presented in this study have been scaled to the geometric area of the catalysts. Tafel slopes were determined from the following Equation (19) [115]:

$$\eta = b \cdot \log j/j_0 \quad (19)$$

where η is the overpotential; b is the Tafel slope; j is the experimental current density, and j_0 is the exchange current density. The plot of η versus log j represents the Tafel slope. In alkaline media, the HER process involves three main steps, as shown in Equations (20)–(22) [115]:

$$* + H_2O + e^- \leftrightarrow {}^*H_{ads} + OH^- \text{ (Volmer step, 120 mV dec}^{-1}\text{)} \quad (20)$$

$${}^*H_{ads} + e^- + H_2O \leftrightarrow H_2 + OH^- + * \text{ (Heyrovsky step, 40 mV dec}^{-1}\text{)} \quad (21)$$

$$2\ {}^*H_{ads} \leftrightarrow H_2 + * \text{ (Tafel step, 30 mV dec}^{-1}\text{)} \quad (22)$$

H_{ads} denotes the H_2 adsorbed to the metal sites, where * represents the metal sites.

To evaluate the ECSA of the catalysts, the double layer capacitance (C_{dl}) was determined by recording the CVs at various scan rates under the non-faradaic region, followed by the calculation of the slope of the curve obtained by plotting the difference in the anodic and cathodic current against the scan rate [123–125]. From the CVs, the charging current, I_c, of the electrodes at each scan rate was determined via Equation (23):

$$I_c\ [A] = (I_{anodic} - I_{cathodic})_{OCP.} \quad (23)$$

The C_{dl} values were evaluated by plotting a graph of the charging current vs. the scan rate and calculating the slope, as shown by Equation (24):

$$\text{Slope} = C_{dl}\ [F] = \Delta I_C\ [A]/\Delta v\ [V\ s^{-1}]. \quad (24)$$

Then, the ECSA values were calculated using the specific capacitance (C_s) of 40 μF cm^{-2} [116–118] and Equation (25):

$$\text{ECSA } [\text{cm}^2] = C_{dl}\ [\mu\text{F}]/C_s\ [\mu\text{F cm}^{-2}]. \quad (25)$$

A two-electrode water electrolysis cell was constructed using two of the same prepared electrodes as the anode and the cathode. The energy efficiency of the cell was calculated using the following Equation (26):

$$\eta_{\text{electrolyzer}} = E_{\text{th}}/V_{\text{e at } j}, \quad (26)$$

where E_{th} = 1.23 V; $V_{\text{e at } j}$ is the input voltage required to drive the electrolysis at the current density of interest. The energy efficiency calculated in this study was obtained at j = 10 mA cm^{-2}. Furthermore, the overall water splitting (OWS) performance of the assembled electrolyzer was investigated in 1.0 M KOH over the temperature range of 25–75 ºC, representing industrially relevant operating conditions, to evaluate the effect of temperature on the electrochemical performance of the cell.

The turnover frequency (TOF) value was calculated using the following Equation (27) [119]:

$$\text{TOF} = j \times \text{A/m} \times \text{F} \times \text{n}, \quad (27)$$

where j is the current density at an overpotential of 400 and 120 mV for OER and HER, respectively; A is the geometric surface area of the electrode; F is the Faraday constant (96,485 C mol^{-1}); m is the number of electrons transferred in the OER is 4 and 2 for HER, and n is the number of moles of all metal ions calculated from the ICP-OES results.

To determine E_a, the current values from the LSVs at different temperatures at potentials of –0.40 V (vs. RHE) for the HER and 1.8 V (vs. RHE) for the OER were extracted from the LSV profiles presented in Figures 24 and 27. The data were plotted as log(i) against 1/T, resulting in a straight line with a gradient of $-E_a/2.3\text{R}$. E_a was calculated using the slope of this line according to Equation (28):

$$\partial \log i/\partial(1/\text{T}) = -E_a/2.3\text{R} \quad (28)$$

where i is the current (mA), T is the temperature (K), and R is the gas constant (8.314 J mol^{-1} K^{-1}) [120].

Electrochemical impedance spectroscopy (EIS) spectra were obtained on a Zahner Zennium potentiostat in the 10 kHz–50 mHz frequency range, with a 10 mV perturbation amplitude. Measurements were carried out potentiostatically at –0.2 V (vs. RHE) in 1 M KOH using the same three-electrode configuration. Equivalent circuit fitting was used to calculate double-layer capacitance and charge transfer resistance values.

3. RESULTS AND DISCUSSION

3.1. Synthesis and Characterization of Co-P_x/Cu Catalysts

3.1.1. Studies of Co-P_x Coatings, Microstructure, and Morphology

The surface morphology of the coatings was examined using scanning electron microscopy (SEM). Figure 15 shows the SEM images of the prepared Co-P_x catalysts with different P contents (a–e). The surface morphology of the Co-P_x was observed to be compact, smooth, and free of cracks, where the Co particles appeared to be uniformly distributed. A typical globular morphology consisting of smaller nodules can be seen in the top side views of the Co-P_x catalysts in Figure 15c. As the concentration of P increased on the catalyst, the formation of nodular structures was observed, which subsequently covered the surface of the substrate (Figure 15c,d). The corresponding EDX spectra of all the samples confirm the presence of Co and P in the coatings (Fig. 15 a′–e′). The composition of the coating elements deposited onto the Cu substrate surface was determined via EDX analysis, and the results of which are presented in Table 1.

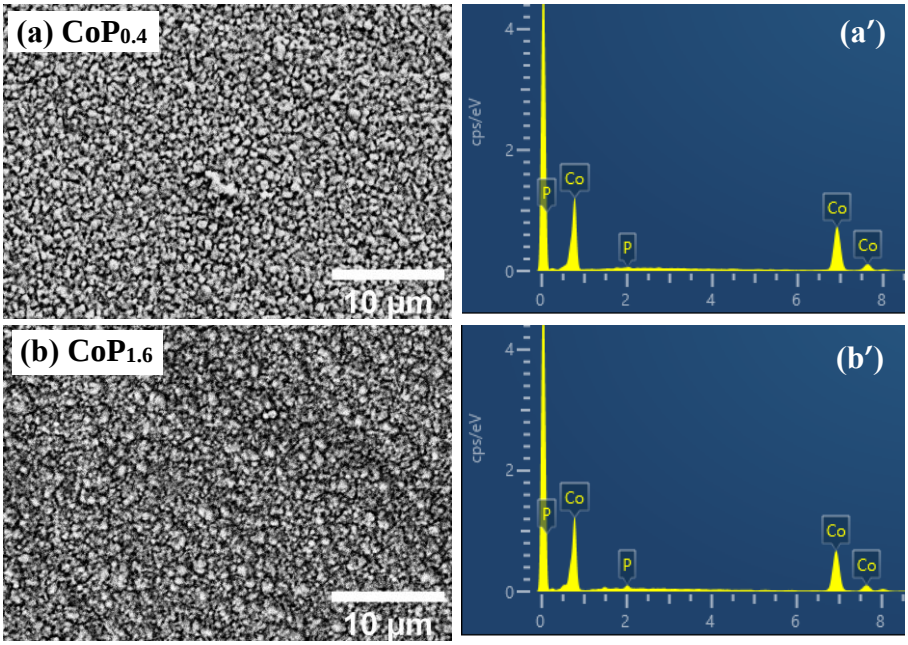

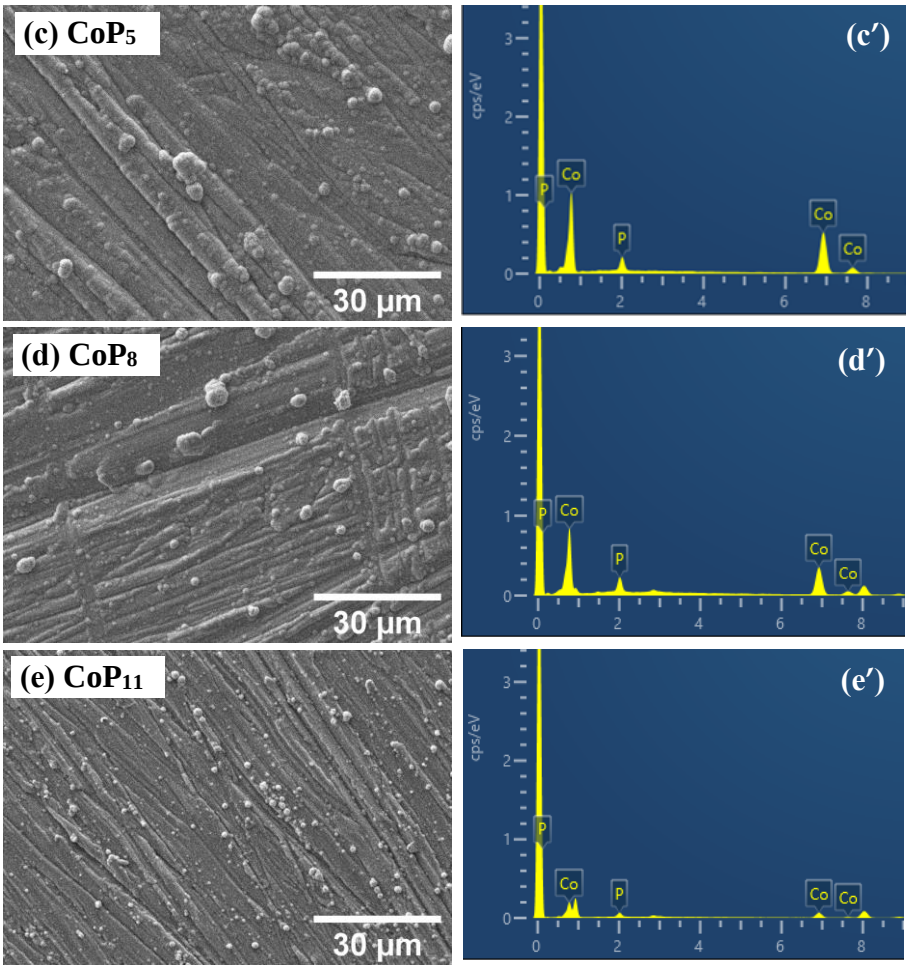

Figure 15. SEM views of Co-P_x coatings with P content of 0.4 (a), 1.6 (b), 5 (c), 8 (d), and 11 (e) wt% deposited on Cu surface. (a′–e′) The corresponding EDX spectra.

Table 1. Composition of CoP_x coatings deposited on Cu surface via EDX analysis.

Sample	Element, wt%	
	Co	P
$CoP_{0.4}$/Cu	99.62	0.38
$CoP_{1.6}$/Cu	98.45	1.55
CoP_5/Cu	95.13	4.87
CoP_8/Cu	92.02	7.98
CoP_{11}/Cu	88.87	11.13

It can be observed that the fabricated Co-P_x/Cu electrocatalysts exhibited a Co content of approximately 99.62–88.87 wt% and a P content of approximately 0.38–11.13 wt%. The P content in the prepared catalysts was gradually enhanced with an increase in the NaH_2PO_2 concentration from 0.25 M to 4.5 M in the plating bath.

3.1.2. Electrocatalytic Activity of Co-P_x/Cu Towards HER

The electrocatalytic performance of the prepared catalysts for the HER was investigated by recording LSVs in 1.0 M KOH solution at a potential scan rate of 2 mV s^{-1} at room temperature (Figure 16). The summarized data for the HER obtained on the Co-P_x/Cu catalysts are shown in Table 2.

Table 2. Summarized parameters for the HER on Co-P_x/Cu catalysts in alkaline media.

Sample	E_{onset}, V at $j = -1$ mA cm^{-2}	η_{10} *, mV	Tafel Slope, mV dec^{-1}
Co-$P_{0.4}$/Cu	–0.210	253.9	50.3
Co-$P_{1.6}$/Cu	–0.186	218.2	43.9
Co-P_5/Cu	–0.114	165.9	48.1
Co-P_8/Cu	–0.071	107.6	34.1
Co-P_{11}/Cu	–0.067	98.9	29.4

* Overpotential at 10 mA cm^{-2}.

As can be seen in Figure 16a, the catalyst activity in the HER depends on the P content of the catalyst. The Co-P coating with the highest amount of 11 wt% P exhibited the lowest overpotential value of 98.9 mV in the HER, obtaining a current density of 10 mA cm^{-2}, compared to the Co-P coatings with 8 wt% (107.6 mV), 5 wt% (165.9 mV), 1.6 wt% (218.2 mV), and 0.4 wt% (253.9 mV) P (Figure 16c). At 10 mA cm^{-2}, Co-P_{11}/Cu has a lower overpotential than other Co-P-based and advanced noble metal catalysts (Table 3). This suggests that higher P content improves HER activity.

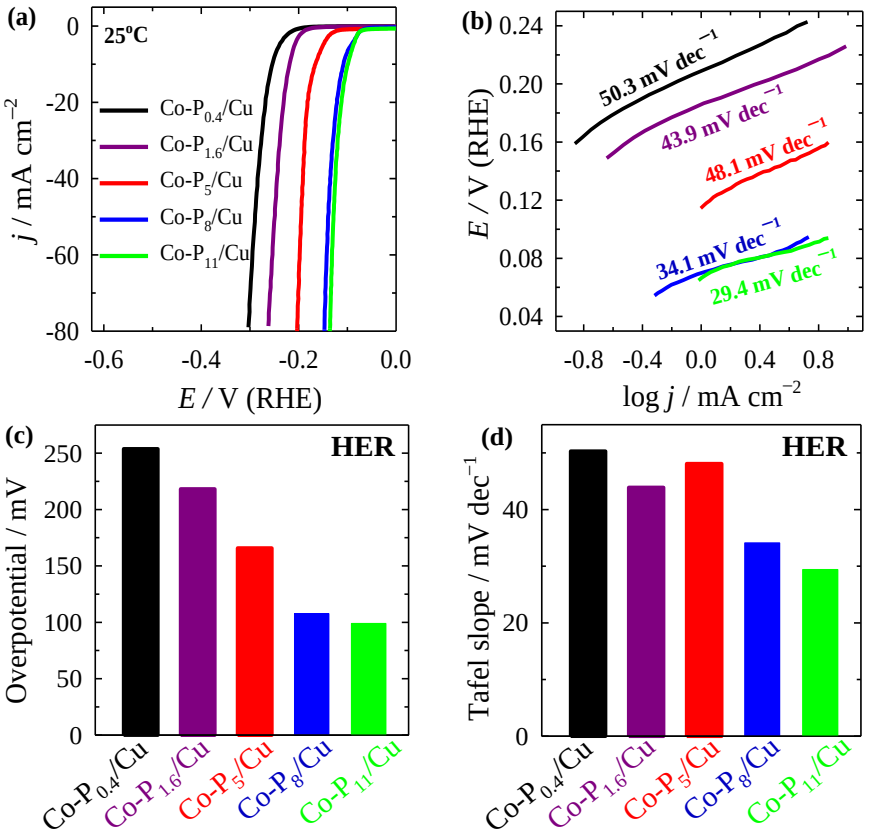

Figure 16. (a) HER polarization curves (iR-corrected) of the Co-P_x/Cu catalyst in N_2-saturated 1 M KOH solution at a potential scan rate of 2 mV s^{-1}. (b) The corresponding Tafel slopes. Bar columns of the corresponding overpotentials at 10 mA cm^{-2} (c) and Tafel slopes (d).

While the obtained overpotential value of 98.9 mV is higher than those for various Pt-based catalysts (from 13.5 to 50 mV) [124–127], Co-P/NF (65 mV) [123], Fe-CoP/Ti (78 mV) [135], Ni-Co-P/NF (85 mV) [133], and Co-P-B/CC MPs (87 mV) [149], it is lower compared to other overpotential values obtained for various Co-based catalysts (Table 3). The reaction kinetics and mechanism of the as-prepared catalysts can be evaluated based on Tafel slopes. The plot of overpotential (η) versus log j represents the Tafel slope (Figure 16d).

Table 3. Comparison of HER performance of Co-P_x with some previously reported Co-P-based and most advanced noble metal catalysts.

Catalyst	η_{10}, mV at $j = -10$ mA cm^{-2}	Tafel Slope, mV dec^{-1}	Electrolyte	Ref.
Co-P_{11}/Cu	98.9	29.4	1 M KOH	This work
Co-P_8/Cu	107.6	34.1	1 M KOH	This work
Fe-codoped CoP/RGO	145	60	1 M KOH	[121]
CoP/RGO	272	134	1 M KOH	[121]
Al-doped CoP/RGO	206	106	1 M KOH	[121]
Fe-doped CoP/RGO	208	107	1 M KOH	[121]
CoP hollow polyhedron	159	59	1 M KOH	[122]
Co–B/NF	103	98.3	1 M KOH	[123]
Co–P/NF	65	59.7	1 M KOH	[123]
Pt/C on GCE	50	108	1 M KOH	[124]
Pt/C (20 wt% Pt/XC-72) on NF	30	49	1 M KOH	[125]
Pt/C	–	108	1 M KOH	[125]
Ni-Co-P	44	52	1 M KOH	[126]
20 wt% Pt/C	13.5	58.9	1 M KOH	[127]
Ni/iP	130	58.5	1 M KOH	[128]
V-doped CoP	235	86.1	1 M KOH	[129]
MoP/NF	114	54.6	1 M KOH	[130]
NiFeLDH@NiCoP/NF	120	88.2	1 M KOH	[131]
NiCoP/NF	185	124.4	1 M KOH	[131]
CoP Nanoparticle	170	66	1 M KOH	[132]
Ni-Co-P/NF	85	46	1 M KOH	[133]
FeP NAs/CC	218	146	1 M KOH	[134]
Fe–CoP/Ti	78	75	1 M KOH	[135]
CoP NS	207	124.5	1 M KOH	[136]
CoP NS/C	111	70.9	1 M KOH	[136]
S:CoP NPs	175	71	1 M KOH	[137]
CoP NPs	216	90	1 M KOH	[137]
CoP-MNA/Ni Foam	150	51	1 M KOH	[138]
CoP@BCN	215	52	1 M KOH	[139]
$(Co_xNi_{1-x})_2P$	180	63	1 M KOH	[140]
f-CoP/CoP_2/Al_2O_3	138	73	1 M KOH	[141]

CoP nanowires	147	69	1 M KOH	[142]
Co_2P	247	86.3	1 M KOH	[143]
Ni-Co-P	150	60.6	1 M KOH	[144]
Co/NBC	117	146	1 M KOH	[145]
Co-P/N-doped carbon matrices	154	51	1 M KOH	[146]
CoP/PNC	165	70	1 M KOH	[147]
Co-P-2	188	–	1 M KOH	[148]
Co-P-B/CC MPs	87	69.2	1 M KOH	[111]

The calculated Tafel slopes were in the range of ca. 29.4 to 50.3 mV dec^{-1}, indicating that the HER might occur through the Volmer–Heyrovsky mechanism, in which water molecules or H_2 adsorbs onto an electrode to generate MH_{ads} species.

3.1.3. Electrocatalytic Activity of Co-P_x/Cu Towards OER

The activity of the Co-P_x/Cu catalysts in the OER was also evaluated. The obtained data are given in Figure 17 and Table 4.

Table 4. Electrochemical performance of Co-P_x/Cu catalysts for OER in alkaline media.

Sample	E_{onset}, V at j = 1 mA cm^{-2}	η_{onset}, mV	E, V at j = 10 mA cm^{-2}	η_{10} *, mV	Tafel Slope, mV dec^{-1}
Co-$P_{0.4}$/Cu	1.590	360	1.664	434	73.0
Co-$P_{1.6}$/Cu	1.589	359	1.664	434	74.3
Co-P_5/Cu	1.569	339	1.630	400	61.7
Co-P_8/Cu	1.544	314	1.608	378	66.4
Co-P_{11}/Cu	1.574	344	1.643	413	73.9

* Overpotential at 10 mA cm^{-2}.

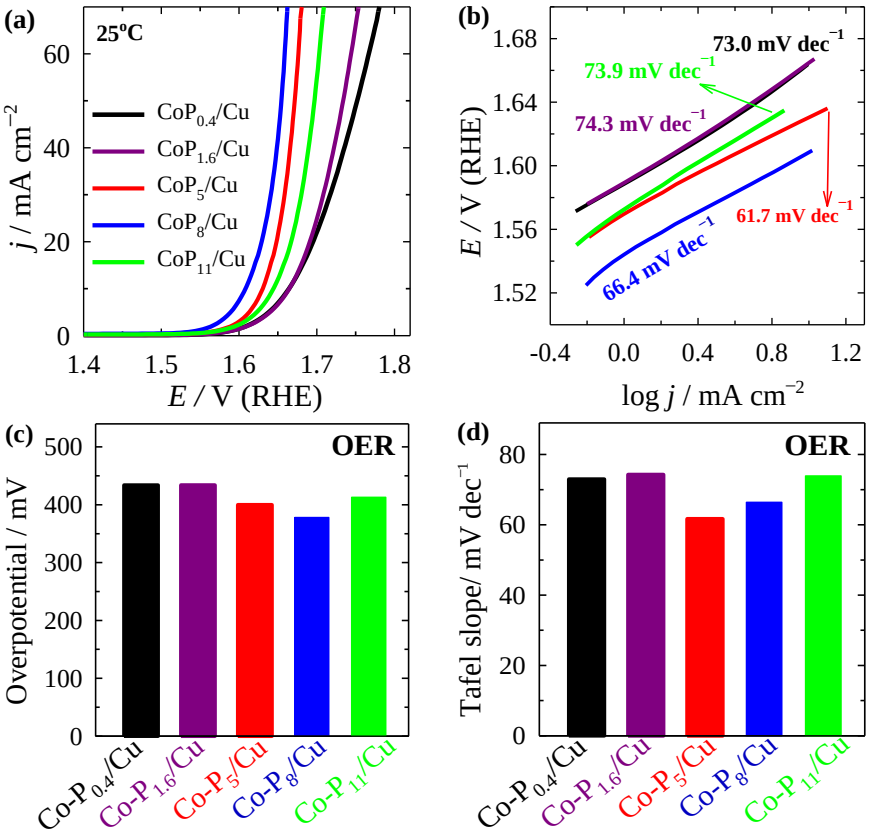

Figure 17. (a) OER polarization curves (iR-corrected) of the Co-P_x/Cu catalyst in N_2–saturated 1 M KOH solution at a potential scan rate of 2 mV s^{-1}. (b) The corresponding Tafel slopes. Bar columns of the corresponding overpotentials at 10 mA cm^{-2} (c) and Tafel slopes (d).

As can be seen from the LSVs recorded for the Co-P_x/Cu catalysts with different P contents in a 1 M KOH solution, the lowest OER overpotential (378 mV) was observed for the Co-P_x coating with 8 wt% P, obtaining a current density of 10 mA cm^{-2}, as compared to the Co-P coatings with 0.4 wt% P (434 mV), 1.6 wt% P (434 mV), 5 wt% P (400 mV), and 11 wt% P (413 mV). In comparison with some previously reported Co-P-based and most advanced noble metal catalysts at 10 mA cm^{-2}, the overpotential of Co-P_8/Cu is lower than that of the majority of the other catalysts (Table 5).

Table 5. Comparison of the OER performance of Co-P_x with some previously reported Co-P-based and most advanced noble metal catalysts.

Catalyst	η_{10}, mV at j = 10 mA cm^{-2}	Tafel Slope, mV dec^{-1}	Electrolyte	Ref.
Co-P_8/Cu	378	66.4	1 M KOH	This work
Co-P_5/Cu	400	61.7	1 M KOH	This work
CoP hollow polyhedron	400	57	1 M KOH	[122]
RuO_2 on NF	290	81	1 M KOH	[124]
RuO_2/CF	360	164	1 M KOH	[126]
IrO_2 commercial	339	94.5	1 M KOH	[127]
V-doped CoP/GCE	340	95.7	1 M KOH	[129]
CoP nanosheet	361	69.5	1 M KOH	[136]
CoP NPs@NF	320	102	1 M KOH	[137]
S:CoP/NF	300	82	1 M KOH	[137]
CoP-MNA/Ni Foam	390	65	1 M KOH	[138]
CoP nanowires	326	80	1 M KOH	[142]
CoP nanoparticles	340	99	1 M KOH	[149]
Co_2P nanorods	310	61.0	1 M KOH	[150]
CoPi/PCDs	350	-	1 M KOH	[151]
Ir/C	254	71.9	1 M KOH	[151]
Mo-CoP/CC	305	56	1 M KOH	[152]
Co-P film	350	47	1 M KOH	[125]
Co phosphide/Co phosphate thin film (PCPTF)	300	65	1 M KOH	[153]
Reduced mesoporous Co_3O_4 nanowires	400	72	1 M KOH	[154]
CL-$Co_2P_2O_7$@C nanohybrids	397	70	1 M KOH	[155]
$Co_2P_2O_7$ nanostructure	490	86	1 M KOH	[155]
$Co(PO_3)_2$ nanosheets	574	106	1 M KOH	[155]

Co–Fe–P–O	267	30	1 M KOH	[156]
CoSi-P	309	121	1 M KOH	[157]
Co_2B	360	45	1 M KOH	[158]
Co-Mn oxyphosphide	370	52	1 M KOH	[159]
NiCoP Nanoboxes	370	115	1 M KOH	[160]
O-CoP/GCE	310	59.9	1 M KOH	[161]
Mn-CoP	288	77.2	1 M KOH	[162]
SnPi@CoP–Ni_5P_4/NCF	364	52	1 M KOH	[163]
Ni-P	300	64	1 M KOH	[164]
Hydrous cobalt phosphate thin films	292	98	1 M KOH	[165]

This indicates that an optimal P content exists for OER activity. The Tafel slope of the Co-P/Cu catalysts ranged from 61.7 to 73.9 mV dec^{-1}, indicating superior OER kinetics (Table 4). The comparison of the OER performances achieved in this study on the Co-P_5/Cu and Co-P_8/Cu catalysts, as well as on the recently reported high-performance catalysts (Table 5), shows that the obtained overpotential values of 378 and 400 mV for the CoP_8/Cu and CoP_5/Cu catalysts are higher compared to RuO_2 on NF (290 mV) [124], RuO_2/CF catalyst (360 mV) [126], Ir/C (254 mV) [151], IrO_2 commercial (339 mV) [127], Mn-CoP (288 mV) [162], CoSi-P (309 mV) [157], CoP (300 mV) [153], and CoP film (350 mV) [125], but lower compared to overpotential values for CoP-MNA/Ni foam (390 mV] [138], CoP hollow polyhedron (400 mV) [122], reduced mesoporous Co_3O_4 nanowires (400 mV) [154], and $Co_2P_2O_7$ (490 mV) [155]. These results show that Co-P_x/Cu catalysts with higher amounts of P (8 and 11 wt%) lead to simultaneous improvements in both HER and OER activities, suggesting that these catalysts have potential as a highly efficient overall water splitting catalysts.

3.1.4. Determination of Electrochemically Active Surface Areas

The electrochemically active surface areas (ECSAs) of the Co-P_x/Cu catalysts with P content of 5, 8, and 11 wt% were determined from measurements of the electrochemical double-layer capacitance (C_{dl}). The CV curves were recorded at different scan rates in the non-faradaic region (Figure 18a–c), which was followed by the calculation of the slope of the curve obtained by

plotting the difference in the anodic and cathodic current versus the scan rate (Figure 18d).

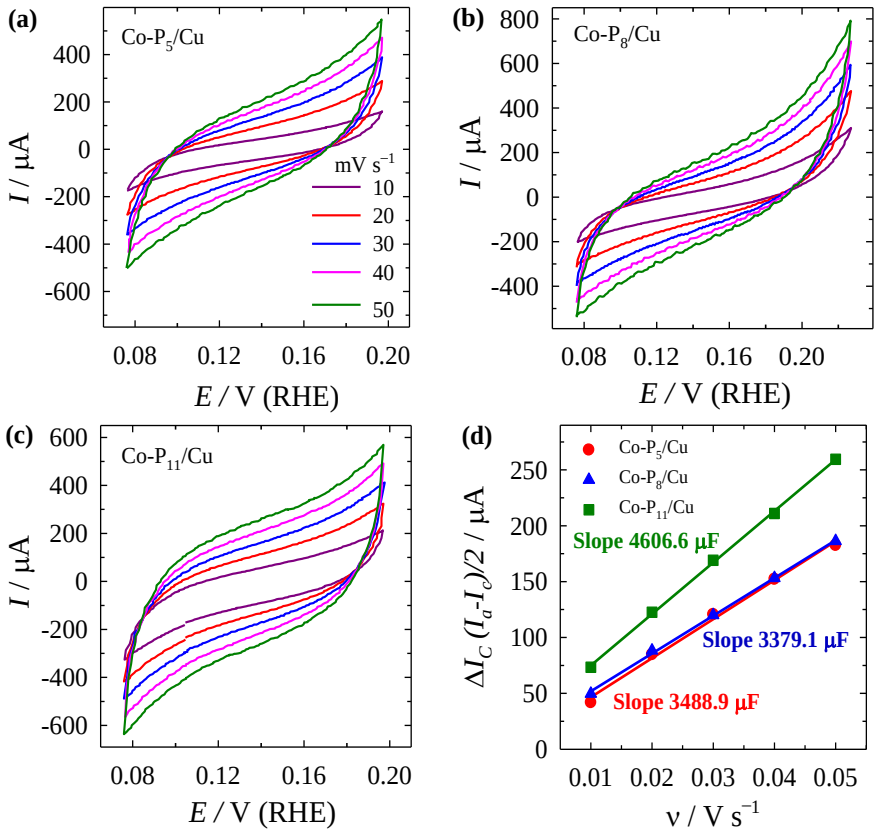

Figure 18. CVs of (a) Co-P/Cu (5 wt% P), (b) Co-P/Cu (8 wt%), and (c) Co-P/Cu (11 wt%) in N_2-saturated 1 M KOH in the non-faradaic potential region at different scan rates. (d) Capacitive current as a function of scan rate.

The C_{dl} was found to be 3488.9, 3379.1, and 4606.6 μF for Co-P_5/Cu, Co-P_8/Cu, and Co-P_{11}/Cu (Figure 18d), whereas the calculated ECSA values were 87.2, 84.5, and 115.6 cm^2 for Co-P_5/Cu, Co-P_8/Cu, and Co-P_{11}/Cu, respectively. Notably, the C_{dl}-derived ECSA has been observed to represent an electrochemically accessible surface area, which can be influenced by both the accessible surface area and the characteristics of the electrolyte/electrode interface. In alkaline media, OH^--containing species have been observed to interact with CoP surfaces, resulting in changes to surface composition and morphology. CoP undergoes electrochemical surface reconstruction in an alkaline electrolyte, including the formation of $Co(OH)_x$ species on the CoP surface, thereby modifying surface/interfacial properties and catalytic

behaviour [166]. Furthermore, the adsorption of OH^- and the subsequent formation of oxygen-containing surface species have been observed to play a role in the surface reconstruction of CoP-based catalysts in alkaline electrochemical environments [167]. Such adsorption and surface-reconstruction mechanisms may have a significant impact on the structural integrity of the electrical double layer. Consequently, this may affect the experimentally determined C_{dl}. Hence, the C_{dl}-derived ECSA measurements should be regarded as comparative metrics of the electrochemically accessible surface characteristics, instead of being interpreted as a direct quantitative representation of the number of catalytically active sites.

The ECSA of Co-P_{11}/Cu being higher than that of Co-P_8/Cu and Co-P_5/Cu is due to the higher number of active sites, which contributes to the higher HER electrocatalytic activity. Notably, the catalyst with 11 wt% P did not achieve the lowest OER overpotential, suggesting that factors beyond active site availability are influencing OER performance. Other factors, such as electronic structure and conductivity, also significantly influence catalyst performance. In this case, the catalyst with 8 wt% P performed best for the OER despite having a lower ECSA than the 11 wt% P catalyst.

3.1.5. Investigation of the Stability of Co-P_x/Cu Catalysts

Additionally, the Co-P_{11}/Cu catalyst was investigated using an accelerated degradation test (ADT) by recording 1000 cycles at a higher scan rate of 400 mV s^{-1} in N_2-saturated 1 M KOH solution. The inset in Figure 19 shows the initial LSV and the LSV after 1000 cycles recorded at 2 mV s^{-1}. A slight decrease was observed in the performance after 1000 cycles at a current density of 10 mA cm^{-2}, indicating the high stability of the catalyst in the HER (the inset of Figure 19). Moreover, the SEM images show that the surface morphology is well maintained; the catalyst does not separate from the substrate after the ADT, indicating good adhesion (shown in the insets of Figure 19). Additionally, after the ADT, the chronoamperometric curve was recorded at a constant potential of –0.26 V for 15 h on the Co-P_{11}/Cu catalyst (Figure 19). The Co-P/Cu catalyst containing 11 wt% P possessed excellent stability, accompanied by two increases in the current density over the 15 h of operation. This can be attributed to changes in the catalyst's structure, composition, or morphology during the stability test.

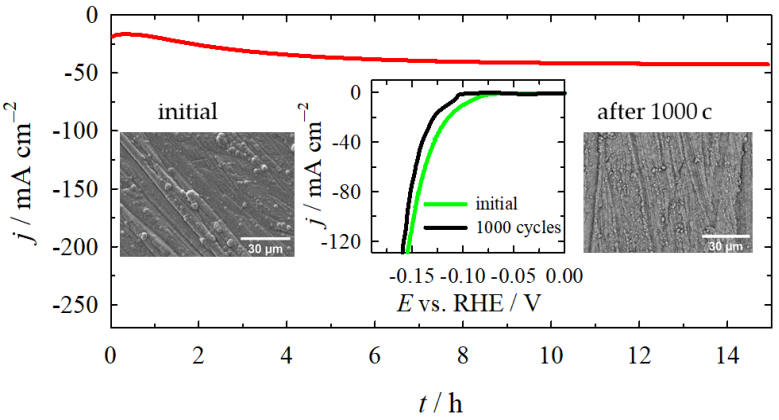

Figure 19. Chronoamperometric curve of the Co-P_{11}/Cu catalyst in N_2-saturated 1 M KOH solution at a constant potential of –0.26 V for 15 h (red line). The insets show the initial LSV and the LSV after the 1000th cycle recorded at 2 mV s^{-1}, and the corresponding SEM images of the initial and after the 1000th cycle test of the same catalyst.

Moreover, the increase in activity after the stability test may include contributions from active sites other than pristine CoP. CoP may transform into more active phases, including cobalt oxides, hydroxides, mixed metal phosphates, or CoP nanoparticles with altered surface states, which are known active catalysts for the OER/HER. These new phases are often more catalytically active than pristine CoP.

3.1.6. Investigation of Overall Water Splitting Performance with Co-P_x/Cu

To confirm the bifunctional activity of the Co-P_x/Cu catalysts for overall water splitting, both cathodic (HER) (Figure 16a) and anodic (OER) (Figure 17a) polarization curves (*i*R-corrected) were replotted and are shown in Figure 20a. The potential difference ($\Delta\eta_{10}$) between the HER and OER had a current density of ±10 mA cm^{-2} (η^{10}_{OER}–η^{10}_{HER}) for the Co-P/Cu catalysts with 5, 8, and 11 wt% P, representing an expected full-cell potential window. The calculated values of the full-cell potential $\Delta\eta_{10}$ delivered from the corresponding HER and OER polarization curves are 1.80 V for Co-P_5/Cu, 1.72 V for Co-P_8/Cu, and 1.74 V for Co-P_{11}/Cu (Figure 20a). The obtained values suggest the potential application of the catalysts for a practical overall water splitting (OWS) device in an alkaline electrolyte, employing the same electrode materials as both the anode and the cathode.

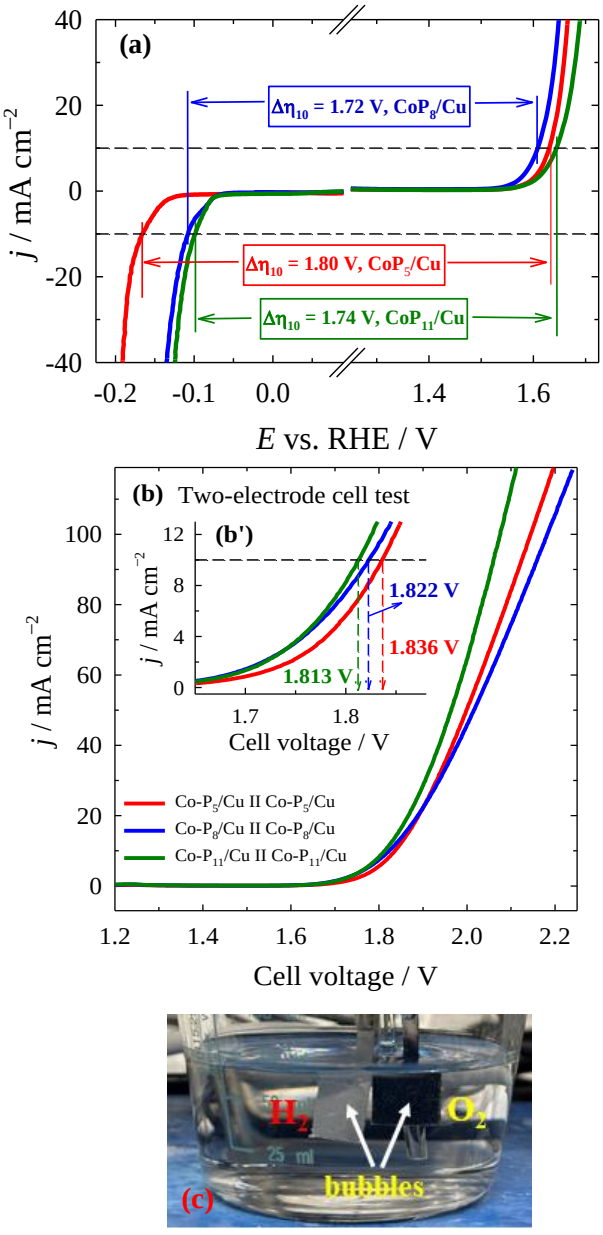

Figure 20. (a) The predicted bifunctional activity of Co-P/Cu catalysts: values of the full-cell potential $\Delta\eta_{10}$ calculated from the difference between the overpotential values (η_{10}) at ±10 mA cm^{-2}, obtained from the corresponding HER and OER LSVs in Figures 16a and 17a. (b) LSVs for different Co-P$_x$/Cu catalysts as both anode and cathode electrocatalytic water splitting in 1 M KOH solution, and the inset (b′) presents the corresponding LSVs at lower current densities. (c) Photograph of OWS on Co-P$_x$/Cu as cathode and anode.

The overall catalytic performance in a two-electrode alkaline electrolyzer cell configuration using the same catalysts as both the anode and the cathode, Co-P_5/Cu‖Co-P_5/Cu, Co-P_8/Cu‖Co-P_8/Cu, and Co-P_{11}/Cu‖Co-P_{11}/Cu, is presented in Figure 20b. The developed Co-P_5/Cu, Co-P_8/Cu, and Co-P_{11}/Cu electrodes exhibit cell potentials of 1.836 V, 1.822 V, and 1.813 V, respectively, at 10 mA cm^{-2} (Figure 20b), which are comparable to cell potential values for CoP/rGO-400‖CoP/rGO-400 (1.70 V) [168], Co-P/NC/CC‖Co-P/NC/CC (1.77 V) [169], Co-P/NC-CC‖Co-P/NC-CC (1.95 V) [169], and $Co(OH)_2$@NCNTs@NF‖ $Co(OH)_2$@NCNTs@NF (1.72 V) [171], as well as for Pt/C‖IrO_2 (1.71 V) [172], Pt/C‖Pt/C (1.83 V) [173], and others reported in the literature (Table 6).

Table 6. Comparison with various electrocatalysts for overall water splitting.

Catalyst	Cell Voltage, V	Electrolyte	Ref.
Co-P_{11}/Cu	1.81	1 M KOH	This work
CoP/rGO-400	1.70	1 M KOH	[168]
Co-P/NC/CC	1.77	1 M KOH	[169]
Co-P/NC-CC	1.95	1 M KOH	[169]
$Co(OH)_2$@NCNTs@NF	1.72	1 M KOH	[171]
Pt/C‖IrO_2	1.71	1 M KOH	[172]
Pt/C‖Pt/C	1.83	1 M KOH	[173]
Hydrous cobalt phosphate thin films	1.80	1 M KOH	[165]
CoP@PNC-DoS	1.74	1 M KOH	[170]
S:CoP NPs	1.72	1 M KOH	[137]
Co phosphide/Co phosphate thin film (PCPTF)	1.92	1 M KOH	[153]

The calculated energy efficiencies of the Co-P_5/Cu, Co-P_8/Cu, and Co-P_{11}/Cu cells are 66.49%, 67.03%, and 67.29%, respectively. The obtained catalysts seem to be suitable candidates for practical overall water splitting applications. The turnover frequency (TOF) is an important indicator for determining the intrinsic activity of the catalysts, which was calculated to evaluate the intrinsic HER and OER performance of the prepared Co-P/Cu catalysts at an overpotential of 120 and 400 mV, respectively. The TOF value of Co-P_8/Cu catalyst was observed to be 12.08 s^{-1} at an overpotential of 400 mV, which significantly outperformed that of Co-P_{11}/Cu (2.99 s^{-1}), Co-P_5/Cu 1.91 s^{-1}), Co-$P_{1.6}$/Cu (0.83 s^{-1}), and Co-$P_{0.4}$/Cu (0.29 s^{-1}), indicating the high intrinsic properties of this catalyst. The calculated TOF values for

HER show that the highest values were obtained for the Co-P/Cu catalysts with higher amounts of P at 8 and 11 wt%. The TOF value of the Co-P_8/Cu catalyst was observed as 56.61 s^{-1} at an overpotential of 120 mV, followed by Co-P_{11}/Cu (19.16 s^{-1}), Co-P_5/Cu (13.38 s^{-1}), Co-$P_{1.6}$/Cu (5.83 s^{-1}), and Co-$P_{0.4}$/Cu (1.86 s^{-1}).

3.2. Synthesis and Characterization of PdCoP/Cu and PdCoFeP/Cu Catalysts

3.2.1. Studies of the Unmodified and Pd-modified CoP and CoFeP Coatings, Microstructure, and Morphology Studies

Scanning electron microscopy (SEM) and energy-dispersive X-ray analysis (EDX) were employed to investigate the surface morphology and composition of the coatings. Figure 21 illustrates the SEM images of the fabricated Co-based coatings with different compositions such as CoP (a), CoFeP (b), PdCoP (c), and PdCoFeP (d). The presence of Pd, Co, Fe, and P in the coatings is confirmed by the corresponding EDX spectra of all the samples (Figure 21 a′–d′). The results of the EDX are outlined in Table 7, which shows that the fabricated CoP, CoFeP, PdCoP, and PdCoFeP electrocatalysts demonstrated Pd contents ranging from 3.54 to 8.36 at%, Co contents ranging from 64.08 to 90.22 at%, Fe contents ranging from 9.96 to 12.49 at%, and P contents ranging from 6.26 to 15.07 at%. SEM analysis demonstrates distinct morphological variations induced by compositional modifications in the electrolessly deposited coatings.

The CoP coating exhibited a compact and relatively homogeneous surface composition, characterized by densely packed grains [174,115], indicative of stable nucleation and uniform growth (Figure 21a). It is noteworthy that incorporating Fe into the CoFeP structure results in a significant structural transformation, creating a porous and heterogeneous morphology [120]. This substantial modification underscores the considerable impact of Fe on nucleation kinetics, surface energy, and phosphorus incorporation during electroless deposition (Figure 21b). Adding Pd to CoP leads to the surface becoming rougher and more fragmented. This is characterized by the presence of finer clusters and increased grain boundaries, indicative of an enhanced nucleation density. The PdCoFeP coating exhibits the most irregular and nanostructured surface, characterized by textured characteristics and fine crystallites (Figure 21c,d). This observation indicates a synergistic effect of Pd and Fe in inducing high nucleation rates and complex growth pathways. The obtained results demonstrate the extreme sensitivity of electroless

deposition processes to even minor compositional variations, which can dramatically alter the resulting microstructure.

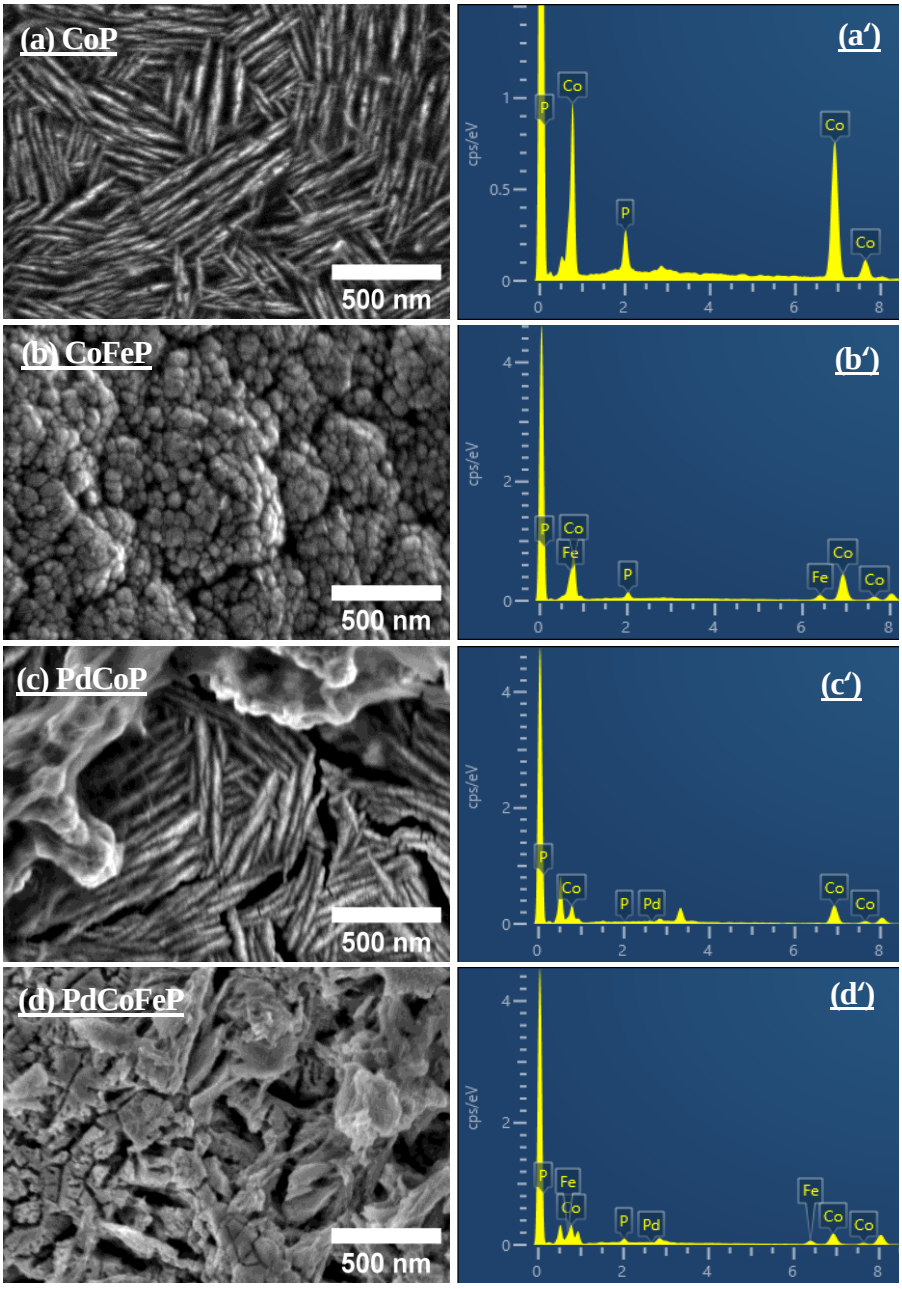

Figure 21. SEM images of CoP (a), CoFeP (b), PdCoP (c), and PdCoFeP (d) deposited on the Cu surface. (a′–d′) EDX spectra corresponding to the aforementioned SEM images.

Table 7. Composition of coatings deposited on the Cu surface determined by EDX analysis.

Sample	Element, at%			
	Pd	Co	Fe	P
CoP	-	90.22	-	9.78
CoFeP	-	83.78	9.96	6.26
PdCoP	3.54	83.72	-	12.74
PdCoFeP	8.36	64.08	12.49	15.07

Figure 22a shows the XRD pattern of the CoP catalyst. The diffraction patterns of the CoP revealed crystalline phases associated with orthorhombic CoP and metallic Co. The CoP peaks were detected at approximately 2θ of 45.1° and 48.1 °. These peaks corresponded to the (021) and (121) planes, respectively, and matched with COD file No. 9,008,928 (a = 5.59900 Å, b = 5.07600 Å, c = 3.28100 Å). The 2θ peaks at approximately 41.7°, 44.9°, 47.7°, 62.9°, 76.2°, 84.9 ° and 93.1° corresponded to the metallic Co phase (COD No. 1512501, a—2.49680 Å, b = 2.49680 Å, c = 4.03081 Å), which were indexed to the (100), (002), (101), (102), (110), (103) and (112) crystal planes, respectively. Following the incorporation of Fe into the CoP structure, the resulting CoFeP coating exhibits diffraction peaks at 2θ values of 44.97°, 65.48° and 82.96°, corresponding to the crystal planes of (110), (200), (211) and (220), respectively, of a CoFe-type solid solution phase (COD 1524319) (Figure 22b). Compared with pure CoP, a slight shift in peak positions is observed, confirming the successful incorporation of Fe atoms into the CoP lattice and the formation of a CoFeP alloy-like structure. Reflections corresponding to metallic Co (COD 1512501) and metallic Fe (COD 1512555) are also detected (Figure 22b). Introducing Fe induces lattice distortion and modifies the crystal structure, which could enhance electronic conductivity and catalytic active site density. For PdCoP (Figure 22c), the additional reflections observed at 2θ = 40.24°, 46.80°, 68.34°, 82.39° and 86.93° correspond to the (111), (200), (220), (311) and (222) crystallographic planes of face-centered cubic Pd (COD 1011105), respectively, which confirms the presence of palladium on the surface. Reflections assigned to metallic Co (COD 1512501) are also detected. Incorporating Pd does not significantly alter the CoP crystal structure, as the main CoP peaks remain unchanged after Pd deposition. However, the slight broadening and reduction in intensity of the CoP peaks compared to pure CoP suggest the occurrence of surface modification and possible lattice strain due to Pd deposition.

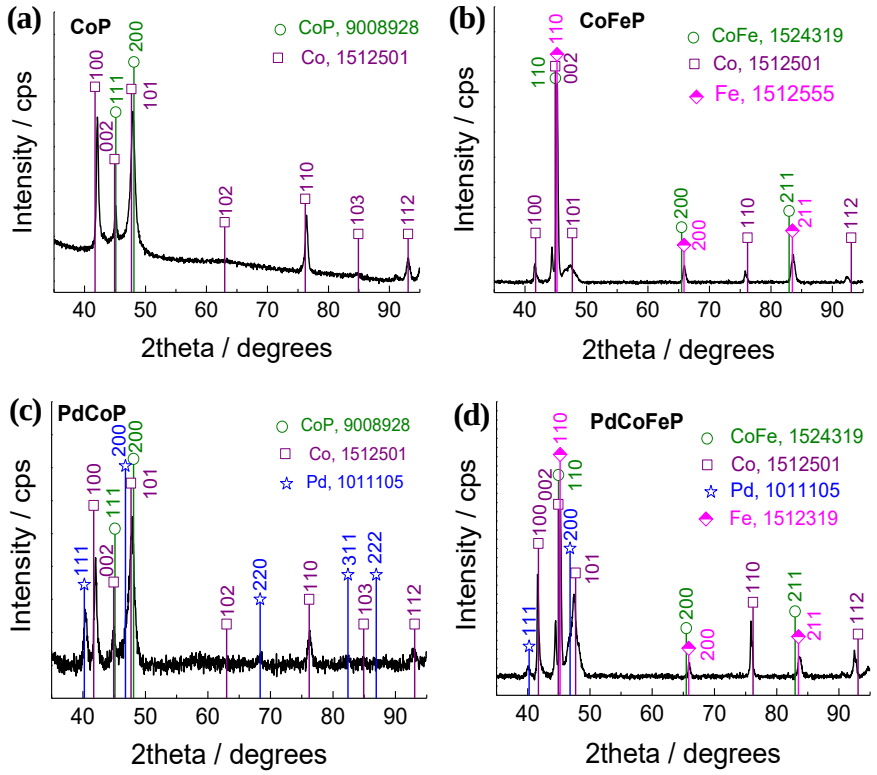

Figure 22. XRD patterns of CoP (a), CoFeP (b), PdCoP (c), and PdCoFeP (d) deposited on the glass surface. Peak positions are indicated according to Crystallography Open Database (COD) data cards: Co—1512501; CoP—9008928; Fe—1512319; CoFe—1524319; Pd—1011105.

The presence of both CoP and Pd peaks indicates the formation of a bimetallic heterostructure (Pd–CoP) rather than a new intermetallic compound. Figure 22d shows the XRD pattern of PdCoFeP, which exhibits diffraction peaks corresponding to the CoFe phase (COD 1524319), metallic Co (COD 1512501), metallic Fe (COD 1512555), and Pd (COD 1011105). These results confirm the successful deposition of Pd crystallites onto the CoFeP surface via galvanic displacement, with no alteration in the original CoFeP crystal structure. The structural evolution from CoP to CoFeP and subsequently to PdCoP and PdCoFeP demonstrates a clear progression in crystal structure and surface composition. The CoP coating exhibits well-defined peaks corresponding to orthorhombic CoP, indicating high crystallinity with a small amount of residual metallic Co. After introducing Fe, the diffraction peaks undergo a slight shift and broadening, confirming the successful incorporation of Fe into the CoP lattice to form a CoFeP alloy-like structure. This Fe substitution introduces lattice distortion, enhancing

electronic conductivity and potentially creating more catalytically active sites. Following Pd deposition via galvanic displacement, the characteristic CoP or CoFe peaks remain largely unchanged, indicating that Pd incorporation does not disturb the bulk CoP or CoFeP structures. However, new reflections assigned to fcc Pd appear, verifying the formation of Pd nanoparticles on the CoP or CoFeP surfaces. The sequential modification in the order CoP → CoFeP → PdCoP → PdCoFeP leads to a progressive structural and compositional evolution. Fe alloying alters the bulk crystal lattice, while Pd addition tunes the surface composition and introduces additional active sites. This synergistic structural tuning is expected to improve the electronic structures, surface reactivities, and catalytic performances of the PdCoP and PdCoFeP composite catalysts.

3.2.2. Electrocatalytic Activity of the Unmodified and Pd-modified CoP and CoFeP Catalysts Towards HER

The electrocatalytic performances of the prepared catalysts for the HER were investigated by recording linear sweep voltammograms (LSVs) in 1.0 M KOH solution at a potential scan rate of 5 mV s^{-1} at room temperature (Figure 23a). Summarized parameters for HER on the investigated catalysts in alkaline media at 25° C are given in Table 8. The corresponding overpotential values at 10, 20, 50, and 100 mA cm^{-2} are given in Figure 23b. Among the catalysts investigated, the CoP catalyst exhibited the lowest overpotential value of 239 mV for the HER compared to CoFeP (245 mV), PdCoP (250 mV), and PdCoFeP (259 mV), attaining a current density of 10 mA cm^{-2} at 25 °C (Figure 23a and Table 8). However, a higher current density is delivered on PdCoFeP, indicating that more efficient hydrogen generation occurs under higher load conditions. Moreover, the overpotential of PdCoFeP at 100 mV cm^{-2} is 385 mV, which is smaller than those of PdCoP (420 mV), CoFeP (428 mV), and CoP (458 mV) (Figure 23b). These improvements are attributed to the synergistic interactions between Co, Fe, P, and Pd, which enhance electron transfer and facilitate HER kinetics. Figure 23c displays the plots of η versus log j for each catalyst. The Tafel slopes calculated were within a range of approximately 76 to 83 mV dec^{-1} (Table 8), whereas the CoFeP and PdCoP catalysts had the lowest Tafel slope (ca. 76 mV dec^{-1}) relative to CoP (78.1 mV dec^{-1}) and PdCoFeP (82.8 mV dec^{-1}) (Figure 23c). This finding indicates that the HER may occur through the Volmer–Heyrovsky mechanism, in which water molecules or H_2 adsorbs onto an electrode to generate MH_{ads} species.

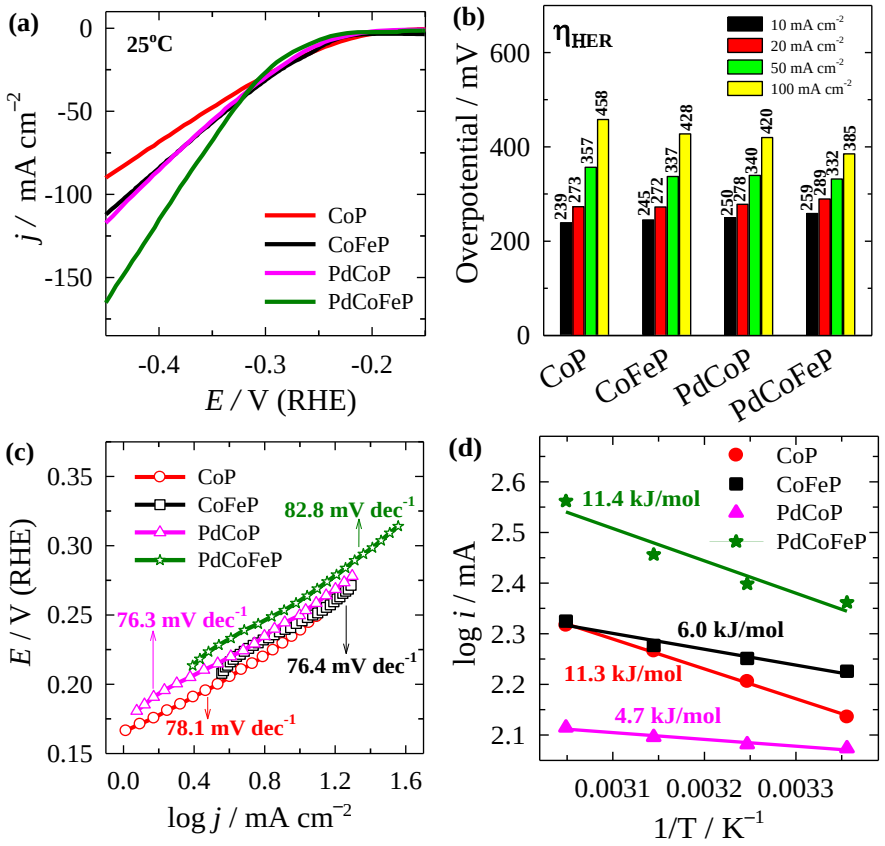

Figure 23. (a) HER polarization curves in an N_2-saturated 1 M KOH solution at a potential scan rate of 5 mV s^{-1} and a temperature of 25 °C. (b) Bar columns of the corresponding overpotentials at current densities of 10, 20, 50 and 100 mA cm^{-2}. (c,d) The corresponding Tafel slopes and Arrhenius plots of the current at –0.40 V versus RHE for each catalyst.

Table 8. Summarized parameters for HER on the investigated catalysts in alkaline media.

Sample	E_{onset} *, V	η_{10} **, mV	Tafel Slope, mV dec^{-1}	E_a, kJ mol^{-1}
CoP	0.166	239	78.1	11.3
CoFeP	0.188	245	76.4	6.0
PdCoP	0.171	250	76.3	4.7
PdCoFeP	0.213	259	82.8	11.4

* Potential at –1 mA cm^{-2}, ** Overpotential at 10 mA cm^{-2}.

The activation energy (E_a) is a critical factor in evaluating the performance of the catalyst. This energy can be estimated by employing the

LSV curves at varying temperatures. The obtained HER LSVs for each catalyst at temperatures from 25 to 55 ºC are shown in Figure 24 and Table 9.

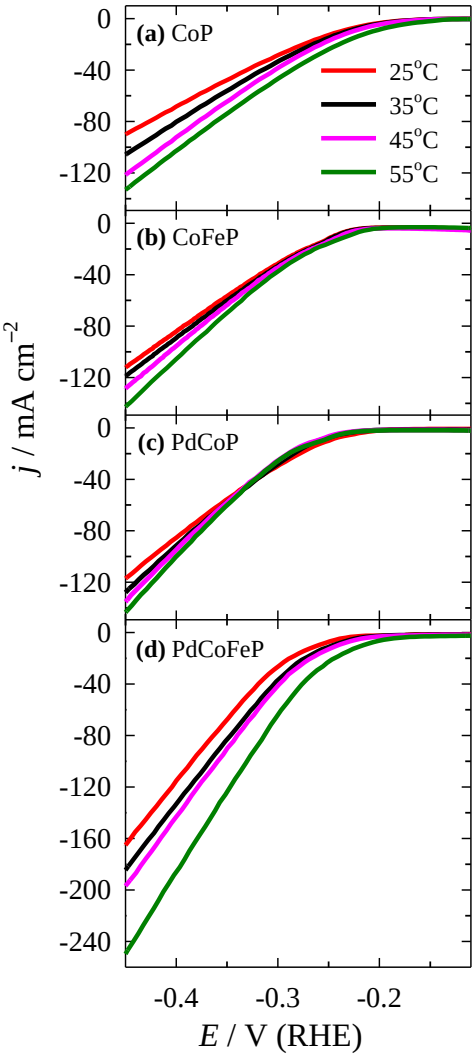

Figure 24. HER Polarization curves recorded on CoP (a), CoFeP (b), PdCoP (c), and PdCoFeP (d) catalysts in N_2–saturated 1 M KOH solution at a potential scan rate of 5 mV s^{-1} and a temperature range from 25 to 55°C.

The results obtained outline that the HER activity of the CoP, CoFeP, PdCoP, and PdCoFeP catalysts is enhanced as the electrolyte temperature increases, whereas the overpotentials required to achieve the current density of 10 mA cm^{-2} decrease with the increase in temperature for each catalyst

(Table 9). Furthermore, the obtained Tafel slope values range from approximately 72 to 94 mV dec^{-1}.

Table 9. Electrochemical performance of catalysts for the HER in alkaline media.

Sample	T, °C	η_{onset*}, mV	η_{10**}, mV	Tafel slope, mV dec^{-1}
CoP/Cu	25	166.4	239.0	78.1
	35	161.5	232.0	75.5
	45	227.1	227.1	72.8
	55	137.9	206.5	72.2
CoFeP/Cu	25	188.1	244.8	76.4
	35	188.1	243.9	74.7
	45	188.7	238.6	74.0
	55	166.1	231.8	79.2
PdCoP/Cu	25	171.3	249.7	76.3
	35	158.5	258.6	76.7
	45	171.0	260.8	78.4
	55	175.8	256.4	78.9
PdCoFeP/Cu	25	213.4	258.6	82.8
	35	168.2	256.0	82.3
	45	122.1	241.0	85.1
	55	107.5	223.5	93.5

* Values at 1 mA cm^{-2}, ** Values at 10 mA cm^{-2}.

These results indicate that the HER kinetic process is closely related to temperature. For determining E_a, the current values at different temperatures recorded on the catalysts at –0.40 V (vs. RHE) were extracted from the LSV profiles (Figure 24). The data were plotted as log(i) against 1/T for the CoP, CoFeP, PdCoP, and PdCoFeP catalysts and are shown in Figure 23d. The E_a was calculated using the slope of the obtained straight lines for each catalyst from the Arrhenius equation [120]. It was determined that the PdCoP, CoFeP, CoP, and PdCoFeP catalysts had E_a values of 4.7, 6.0, 11.3, and 11.4 kJ mol^{-1}, respectively (Figure 23d).

The obtained E_a values were significantly lower against Pt/C (20 wt%) benchmark, which were reported as follows: benchmark—16 kJ mol^{-1} [103]; Pd_{100}—20.86 kJ mol^{-1} [103]; Pd_5Co_{95}—21.75 kJ mol^{-1} [103]; Pd/C—31 kJ mol^{-1} [103]; CoO_x—29.79 kJ mol^{-1} [175]. The low activation energies implied that a small reaction kinetic barrier is required for the reaction

to proceed efficiently. The reduction in E_a can be explained through several factors related to the catalyst's composition, electronic structure, and morphological properties. Incorporating of Fe and subsequent modification with Pd crystallites reduces the E_a of CoP due to the synergistic interactions between Fe, Co, and Pd. These interactions are crucial because they enhance electron transfer and facilitate the kinetics of the HER.

EIS spectra were obtained on the PdCoFeP and CoFeP samples to investigate the influence of modification with Pd on HER activity. The Nyquist plots shown in Figure 25 are characterized by a broad semicircle, while at low frequencies (1.5–0.5 Hz), a small but pronounced inductive response emerges as Z_{im} values become positive.

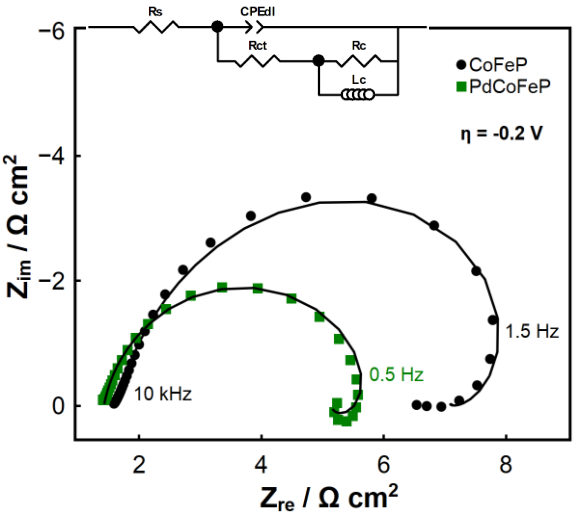

Figure 25. Nyquist plots of the CoFeP and PdCoFeP catalysts, obtained at –0.2 V vs. RHE. Solid lines represent fits to the equivalent circuits shown in the inset.

This phenomenon typically signals the slow relaxation of adsorbates in multistep reactions such as corrosion or electrocatalysis [176], suggesting that the electrode surface may undergo some restructuring or phase transformation during operation. Therefore, the impedance spectra were fitted to an equivalent circuit model that included an inductive element to account for the low-frequency inductive response [177]. The constant phase element (CPE_{dl}) values were recalculated into effective capacitance C_{eff} via Brug et al.'s formula [178], and the obtained values for CoFeP and PdCoFeP were 3.5 mF cm^{-2} and 7.4 mF cm^{-2}, respectively. Additionally, the associated charge transfer resistance (R_{ct}) of CoFeP (5.5 Ω cm^2) was two times larger than that of the more electrochemically active PdCoFeP (3.7 Ω cm^2). These

observations correspond well to the HER activity results presented in Figure 23. The palladium-decorated film exhibits better HER activity because it has a significantly larger electrochemically active surface area and faster HER kinetics, as demonstrated by the larger C_{eff} and lower R_{ct} values.

3.2.3. Electrocatalytic Activity of the Unmodified and Pd-modified CoP and CoFeP Catalysts Towards OER

The activity of the Co-based catalysts in the OER was also evaluated. The obtained data are given in Table 10 and Figure 26. In addition, the LSV was recorded on the Cu substrate for comparison. Higher OER current densities were obtained on the CoP, CoFeP, and Pd-modified CoP and CoFeP catalysts compared to the Cu substrate (Figure 26a), indicating that they demonstrated high activity during the OER. As shown by the LSVs recorded for the aforementioned catalysts in a 1 M KOH solution, the lowest OER overpotential of 396 mV was observed for the Pd-modified CoP and CoFeP, achieving a current density of 10 mA cm^{-2}, compared to the unmodified CoP (431 mV) and CoFeP (435 mV), and Cu (645 mV) (Table 10).

Table 10. Electrochemical performance of the investigated catalysts for OER in alkaline media at 25 °C.

Sample	E_{onset} *, V	η_{onset}, mV	E **, V	η_{10} **, mV	Tafel Slope, mV dec^{-1}	E_a, kJ mol^{-1}
CoP	1.5205	290	1.6607	431	120.3	20.7
CoFeP	1.5846	355	1.6650	435	74.5	21.2
PdCoP	1.5426	313	1.6255	396	77.8	12.2
PdCoFeP	1.5577	328	1.6256	396	70.5	11.8
Cu	1.7638	534	1.8750	645	-	-

* Values at 1 mA cm^{-2}, ** Values at 10 mA cm^{-2}.

Lower Tafel slope values (in the range of 70.5 to 77.8 mV dec^{-1}) were obtained for PdCoFeP, CoFeP, and PdCoP catalysts compared to the CoP catalyst (120.3 mV dec^{-1}). These results indicated superior OER kinetics (Table 10). Higher current density values for OER were obtained on the Pd-modified CoP and CoFeP catalysts compared to the unmodified CoP and CoFeP catalysts (Figure 26b).

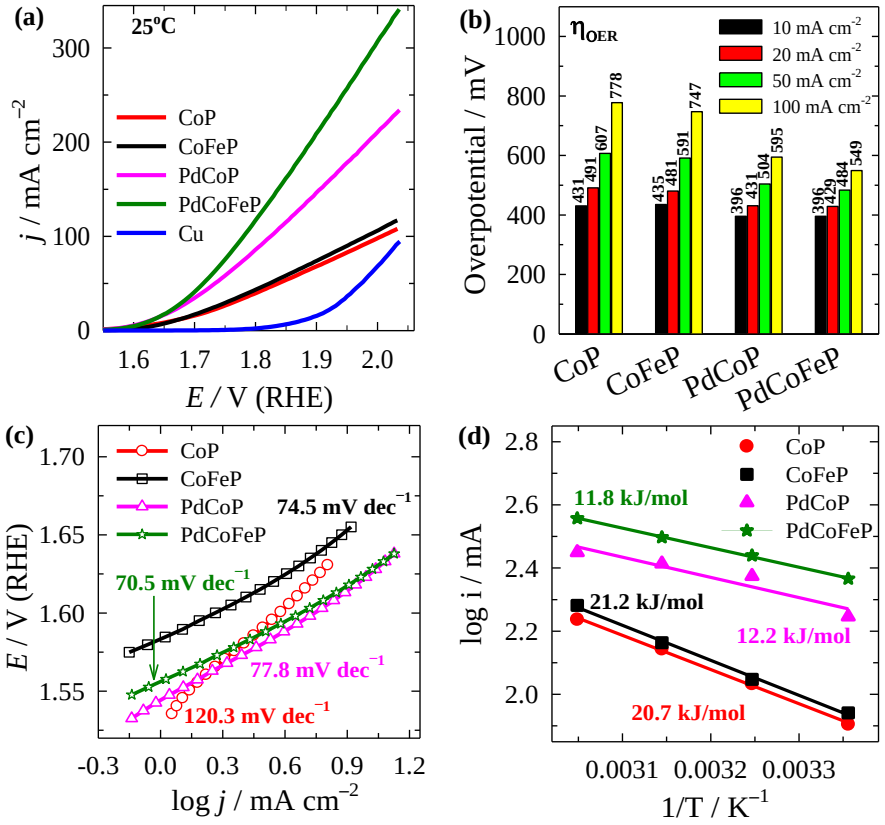

Figure 26. (a) OER polarization curves in an N_2-saturated 1 M KOH solution at a potential scan rate of 5 mV s^{-1} and a temperature of 25 °C. (b) Bar columns of the corresponding overpotentials at 10, 20, 50 and 100 mA cm^{-2}. (c,d) The corresponding Tafel slopes and Arrhenius plots of the current at 1.8 V versus RHE for each catalyst.

The overpotential of PdCoFeP at 100 mA cm^{-2} is 549 mV, which is smaller than those of PdCoP (595 mV), CoFeP (747 mV), and CoP (778 mV). The obtained OER LSVs for each catalyst at temperatures ranging from 25 to 55 °C are shown in Table 11 and Figure 27. The OER activity of the CoP, CoFeP, PdCoP, and PdCoFeP catalysts also increases as the temperature of electrolyte increases. An increase in temperature for each catalyst also results in a decrease in the overpotential values, which need to attain 10 mA cm^{-2} (Table 11).

Table 11. Electrochemical performance of catalysts for OER in alkaline media.

Sample	T, °C	E_{onset}*, V	η_{onset}, mV	E**, V	η_{10}**, mV	Tafel slope, mV dec^{-1}
CoP/Cu	25	1.5205	290.5	1.6607	430.7	120.2
	35	1.5003	270.3	1.6256	395.6	101.5
	45	1.4953	265.3	1.5954	365.5	96.3
	55	1.4802	250.2	1.5729	342.9	95.2
CoFeP/Cu	25	1.5846	354.65	1.6650	435.00	74.5
	35	1.5797	349.73	1.6501	420.08	72.9
	45	1.5603	330.26	1.6306	400.60	71.5
	55	1.5417	311.71	1.5994	369.45	59.6
PdCoP/Cu	25	1.5426	312.6	1.6255	395.5	77.8
	35	1.5224	292.4	1.5979	367.9	75.8
	45	1.5224	292.4	1.5954	365.4	74.9
	55	1.5174	287.4	1.5904	360.4	76.8
PdCoFeP/Cu	25	1.5577	327.7	1.6256	395.6	70.5
	35	1.5426	312.6	1.6080	378.0	69.5
	45	1.5325	302.5	1.5979	367.9	65.2
	55	1.5175	287.5	1.5803	350.3	65.1

* Values at 1 mA cm^{-2}, ** Values at 10 mA cm^{-2}.

The obtained Tafel slope values, which also decrease with the increase in temperature for each catalyst, range from approximately 120 to 95 mV dec^{-1} for CoP, from 74 to 60 mV dec^{-1} for CoFeP, from 78 to 77 mV dec^{-1} for PdCoP, and from 70 to 65 mV dec^{-1} for PdCoFeP at a temperature from 25 and 55 °C, respectively (Table 11).

To determine E_a for the OER, the current value and temperature value of the catalysts at 1.8 V (vs. RHE) were extracted from the LSV profiles (Figure 27). The PdCoFeP, PdCoP, CoP, and CoFeP catalysts have E_a values of 11.8, 12.2, 20.7 and 21.2 kJ mol^{-1}, respectively (Figure 26d). In addition, the PdCoFeP has the lowest activation energy, i.e., 11.8 kJ mol^{-1}, implying that it has the smallest reaction kinetic barrier. A comparison of the OER performances of the investigated catalysts with those of previously reported Co-P-based and most advanced noble-metal catalysts is shown in Table 12.

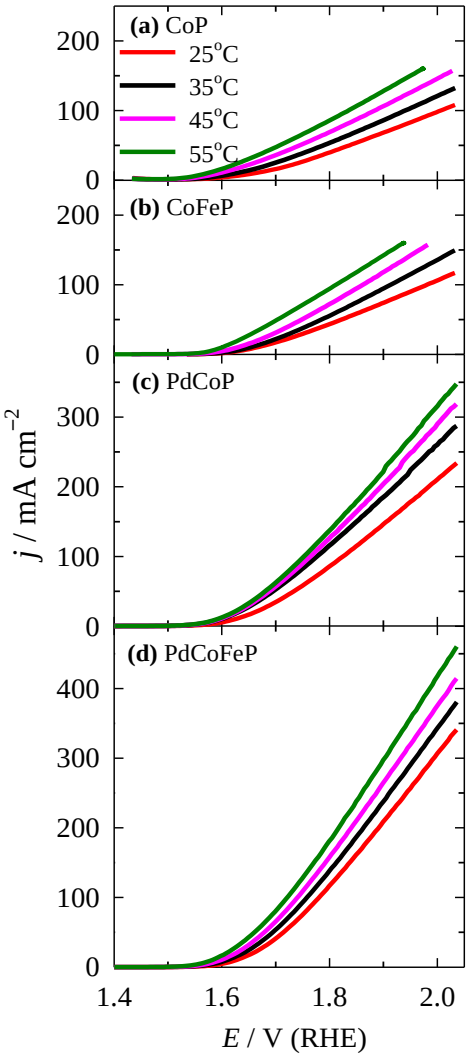

Figure 27. OER Polarization curves recorded on CoP (a), CoFeP (b), PdCoP (c), and PdCoFeP (d) catalysts in an N_2-saturated 1 M KOH solution at a potential scan rate of 5 mV s^{-1} and a temperature range from 25 to 55°C.

Table 12. Comparison of OER performance of the investigated catalysts with some previously reported Co-P-based and most advanced noble–metal catalysts.

Catalyst	η_{10} *, mV	Tafel Slope, mV dec^{-1}	Electrolyte	Ref.
PdCoFeP	396	70.5	1 M KOH	This study
PdCoP	396	77.8	1 M KOH	This study
CoO_x	423	42	1 M KOH	[179]
$Co_2P_2O_7$	490	86	1 M KOH	[180]
$Co(PO_3)_2$ nanosheets	574	106	1 M KOH	[180]
CoP hollow polyhedron	400	57	1 M KOH	[122]
Reduced mesoporous Co_3O_4 nanowires	400	72	1 M KOH	[154]
CoP-MNA/Ni foam	390	65	1 M KOH	[138]
CoSi-P	309	121	1 M KOH	[181]
CoP	300	65	1 M KOH	[153]
Mn-CoP	288	77.2	1 M KOH	[182]
RuO_2/CF	360	164	1 M KOH	[126]
RuO_2 on NF	290	81	1 M KOH	[124]
IrO_2 commercial	339	94.5	1 M KOH	[127]
Ir/C	254	71.9	1 M KOH	[151]
$Ni_{0.3}Co_2Fe$-P	290	-	1 M KOH	[183]
Co_2Fe-P	367	-	1 M KOH	[183]
CuO@FeCoP/CF	240	-	1 M KOH	[184]
Mo-CoP@C	280	53.1	1 M KOH	[185]
CoFe@Co_2C@Co-0.2/NF	246	-	1 M KOH	[186]
CoP	350	47	1 M KOH	[125]

* Values at 10 mA cm^{-2}.

The obtained overpotential values of 396 mV for the PdCoP/Cu and PdCoFeP/Cu catalysts are lower compared to CoO_x (423 mV) [179], $Co_2P_2O_7$ (490 mV) [180], CoP hollow polyhedron (400 mV) [122], and reduced mesoporous Co_3O_4 nanowires (400 mV) [154] but higher compared to the overpotential values for CoP-MNA/Ni foam (390 mV) [138], CoP film (350 mV) [206], CoSi-P (309 mV) [181], CoP (300 mV) [153], Mn-CoP (288 mV) [182], RuO_2/CF catalyst (360 mV) [126], RuO_2 on

NF (290 mV) [124], IrO_2 commercial (339 mV) [127], Ir/C (254 mV) [151], $Ni_{0.3}Co_2Fe$-P (290 mV) [183], Co_2Fe-P (367 mV) [183], CuO@FeCoP/CF (240 mV) [184], Mo-CoP@C (280 mV) [185], and CoFe@Co_2C@Co-0.2/NF (246 mV) [186].

3.2.4. Determination of Electrochemically Active Surface Areas

The electrochemically active surface areas (ECSAs) of the unmodified and Pd-modified CoP and CoFeP catalysts were determined from the measurements of the electrochemical double-layer capacitance (C_{dl}). The CV curves were recorded at different scan rates in the non-Faradaic region (Figure 28a–d), which was followed by calculating the slope of the curve obtained by plotting the differences in the anodic and cathodic current versus the scan rate (Figure 28e). The C_{dl} was 2458.5, 11,652.2, 10,858.9 and 56,291.2 μF for CoP, CoFeP, PdCoP and PdCoFeP (Figure 28e), whereas the calculated ECSA values were 61.5, 291.3, 271.5 and 1407.3 cm^2 for CoP, CoFeP, PdCoP and PdCoFeP, respectively. The high ECSA of PdCoFeP was due to the higher number of active sites, which contributed to the higher OER electrocatalytic activity. The incorporation of Fe into the CoP coating, followed by its modification with Pd crystallites, allowed it to achieve the lowest OER overpotential, Tafel slope, and E_a, which suggests that factors beyond active site availability influence OER performance. A similar observation has been made for CoFeP-based OER electrocatalysts, where variations in ECSA alone could not account for the differences in OER activity. Instead, it was suggested that the catalytic performance is also influenced by the synergistic interaction between the Co and Fe sites, as well as their electronic and charge-transfer properties [187]. Other factors, such as electronic structure and conductivity, as well as a high ECSA, also significantly influence catalyst performance. The catalyst with 8.36 at% Pd had the best activity during the OER.

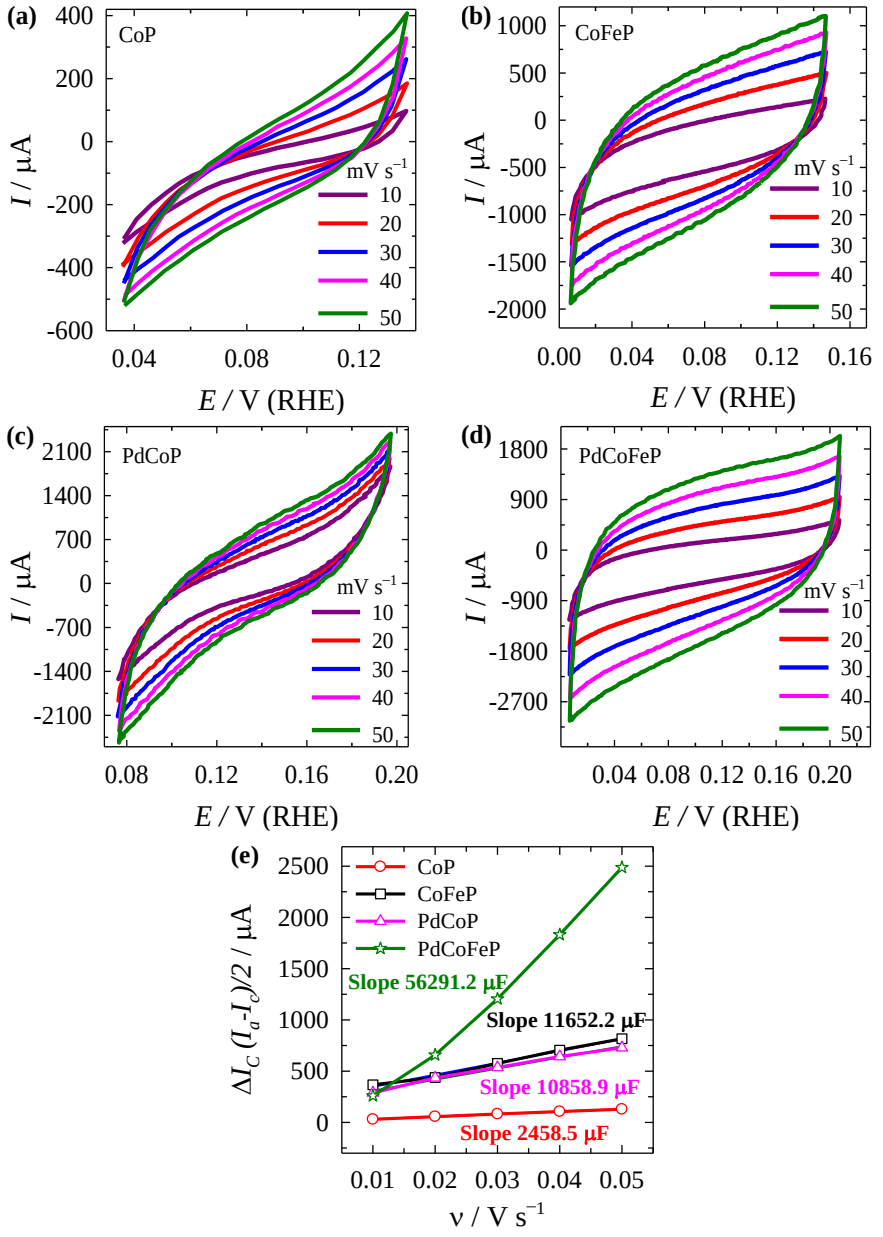

Figure 28. CVs of (a) CoP, (b) CoFeP, (c) PdCoP and (d) PdCoFeP in an N_2–saturated 1 M KOH solution in the non-Faradaic potential region at different scan rates (10–50 mV s^{-1}). (e) The capacitive current as a function of the scan rate.

3.2.5. Investigation of the Stability of PdCoP/Cu and PdCoFeP/Cu Catalysts

Additionally, the stabilities of the most promising Pd-modified CoP and CoFeP catalysts were investigated using chronoamperometry by recording the chronoamperometric curves at a constant potential of –0.26 V for 10 h on the PdCoP and PdCoFeP catalysts (Figure 29). The PdCoFeP/Cu catalyst possessed excellent stability, with current retention of 96.02% over 10 h compared to the PdCoP/Cu catalyst. Figure 30 shows the chronopotentiometric curves recorded on the PdCoP (a) and PdCoFeP (b) catalysts in a 1 M KOH solution at a constant current density of –10 mA cm^{-2} and 25 ºC. It is evident that the potential required to attain –10 mA cm^{-2} slightly increased from –0.1945 V to –0.2131 V for PdCoP (Figure 30a) and from –0.1551 V to –0.1740 V for PdFeCoP (Figure 30b) over 10 h, demonstrating the good stability of both catalysts.

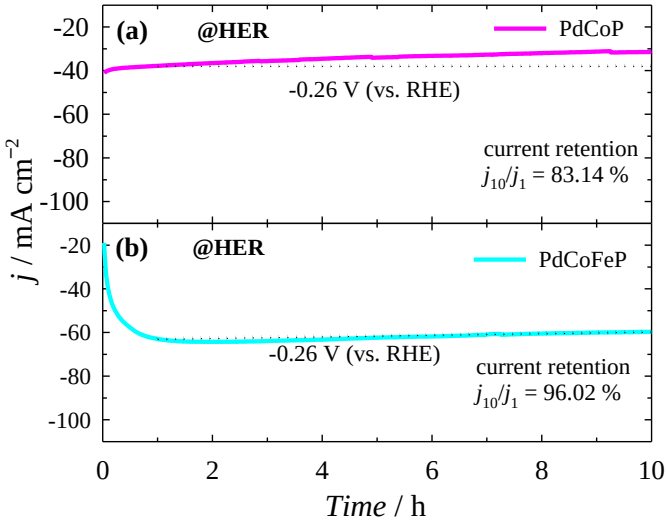

Figure 29. The CA curves of the investigated PdCoP (a) and PdCoFeP (b) catalysts in a 1 M KOH solution at 25 ºC and a potential value of –0.26 V (vs. RHE).

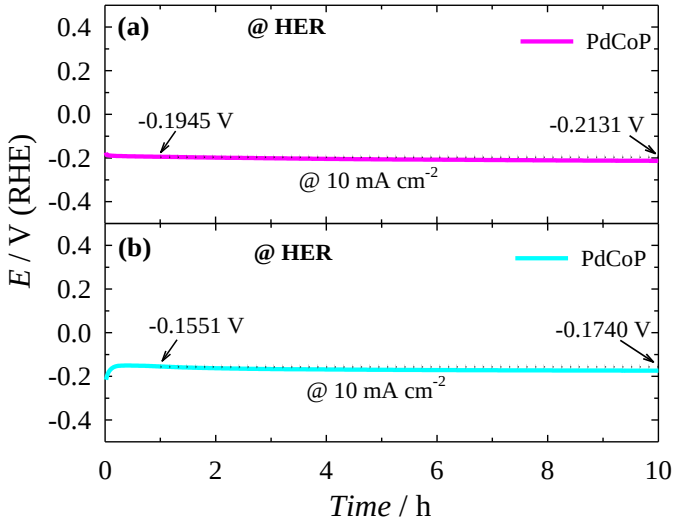

Figure 30. The CP curves of the investigated PdCoP (a) and PdCoFeP (b) catalysts in a 1 M KOH solution at a constant current density of –10 mA cm^{-2} and 25 ºC.

3.2.6. Investigation of Overall Water Splitting by Employing the Unmodified and Pd-modified CoP and CoFeP Catalysts

To confirm the bifunctional activity of the unmodified and Pd-modified CoP and CoFeP catalysts, a two-electrode water electrolysis cell was constructed using two of the same investigated catalysts as the anode and the cathode. Figure 31 shows the overall catalytic performance of a two-electrode alkaline electrolyzer cell configuration using the same catalysts for both the anode and the cathode: CoP‖CoP, CoFeP‖CoFeP, PdCoP‖PdCoP, and PdCoFeP‖PdFeCoP. The developed CoP, CoFeP, PdCoP and PdFeCoP electrodes exhibited cell potentials of 1.86 V, 1.81 V, 1.78 V and 1.69 V, respectively, at 10 mA cm^{-2} (Figure 31), comparable to the cell potential values recorded for other studies reported in the literature (Table 13). The energy efficiencies of the cells were calculated. The energy efficiencies of the CoP, CoFeP, PdCoP and PdCoFeP cells were 66.13%, 67.96%, 69.10%, and 72.78%, respectively. These catalysts appear to be promising candidates for practical overall water splitting applications.

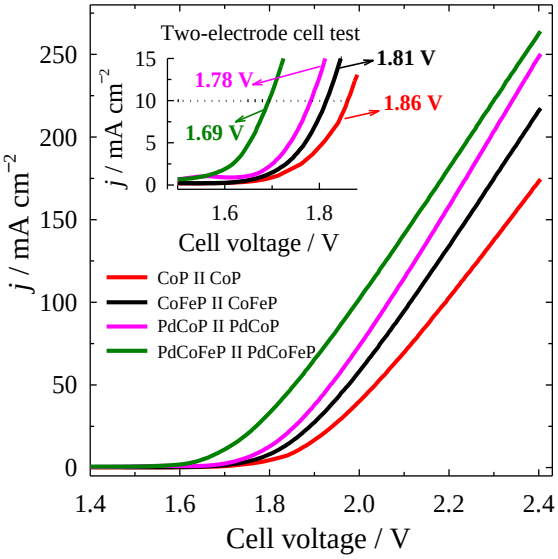

Figure 31. The polarization curves of the CoP, CoFeP, PdCoP, and PdCoFeP catalysts used as both an anode and a cathode for overall water splitting performance in the two-electrode setup at a scan rate of 5 mV s^{-1}.

Table 13. Comparison with various electrocatalysts for overall water splitting.

Anode II Cathode	Cell Voltage, V	Electrolyte	Ref.
PdCoFeP‖PdCoFeP	1.69	1 M KOH	This study
PdCoP‖PdCoP	1.78	1 M KOH	This study
Pt/C‖IrO_2	1.71	1 M KOH	[188]
Pt/C‖Pt/C	1.83	1 M KOH	[188]
CoP/rGO-400‖CoP/rGO-400	1.70	1 M KOH	[188]
$Co(OH)_2$@NCNTs@NF‖ $Co(OH)_2$@NCNTs@NF	1.72	1 M KOH	[189]
Co-P/NC/CC‖Co-P/NC/CC	1.77	1 M KOH	[190]
Co-P/NC-CC‖Co-P/NC-CC	1.95	1 M KOH	[190]

3.3. Synthesis and Characterization of PtCoP/Cu and PtCoFeP/Cu Catalysts

3.3.1. Studies of Unmodified and Pt-modified CoP and CoFeP Coatings, Microstructure, and Morphology

Scanning electron microscopy (SEM) and energy-dispersive X-ray spectroscopy (EDX) analysis were conducted to investigate the surface morphology and elemental composition of the electrolessly deposited coatings. Figure 32 shows the SEM images and EDX spectra of the Co-based coatings with different compositions, including CoP (a), CoFeP (b), PtCoP (c), and PtCoFeP (d), fabricated on a Cu substrate.

The presence of Pt, Co, Fe, and P in the coatings is confirmed by the corresponding EDX spectra of all the samples (Fig. 32 a′–d′). The results of the EDX are outlined in Table 14, which shows that the fabricated CoP, CoFeP, PtCoP, and PtCoFeP electrocatalysts demonstrated Pt contents ranging from 0.18 to 5.96 at%, Co contents ranging from 61.06 to 90.72 at%, Fe contents ranging from 10.31 to 13.33 at%, and P contents ranging from 6.18 to 22.66 at%. These results thus confirm the effective compositional modification after Fe incorporation and subsequent Pt surface modification.

SEM analysis demonstrated that distinct morphological variations occurred as a result of compositional modifications to the coatings. The CoP coating exhibited a compact flake-like morphology composed of crystallites of a leaf-like shape that were densely interconnected and uniformly covered the Cu substrate (Figure 32a). It was observed that the coating surface exhibited a relatively homogeneous and compact morphology, with moderate roughness, suggesting uniform nucleation and stable lateral crystalline growth during the electroless deposition process.

Conversely, the CoFeP coating (Figure 32b) demonstrated a rough cauliflower-like granular morphology, consisting of aggregated nanosized grains and porous microclusters distributed across the surface. The incorporation of Fe resulted in significant variations in deposition rates and growth behaviour, leading to enhanced surface roughness, a more refined grain distribution, as well as a distinctly heterogeneous porous structure. Following the incorporation of Pt, the PtCoP coating (Figure 32c) exhibited the development of relatively larger polyhedral and facet-like micrograins, accompanied by well-defined grain boundaries and localised microcracks. It was found that the surface became comparatively rough and dense as a result of Pt-induced particle adhesion and crystal formation, thus indicating effective surface reconstruction of the CoP coating.

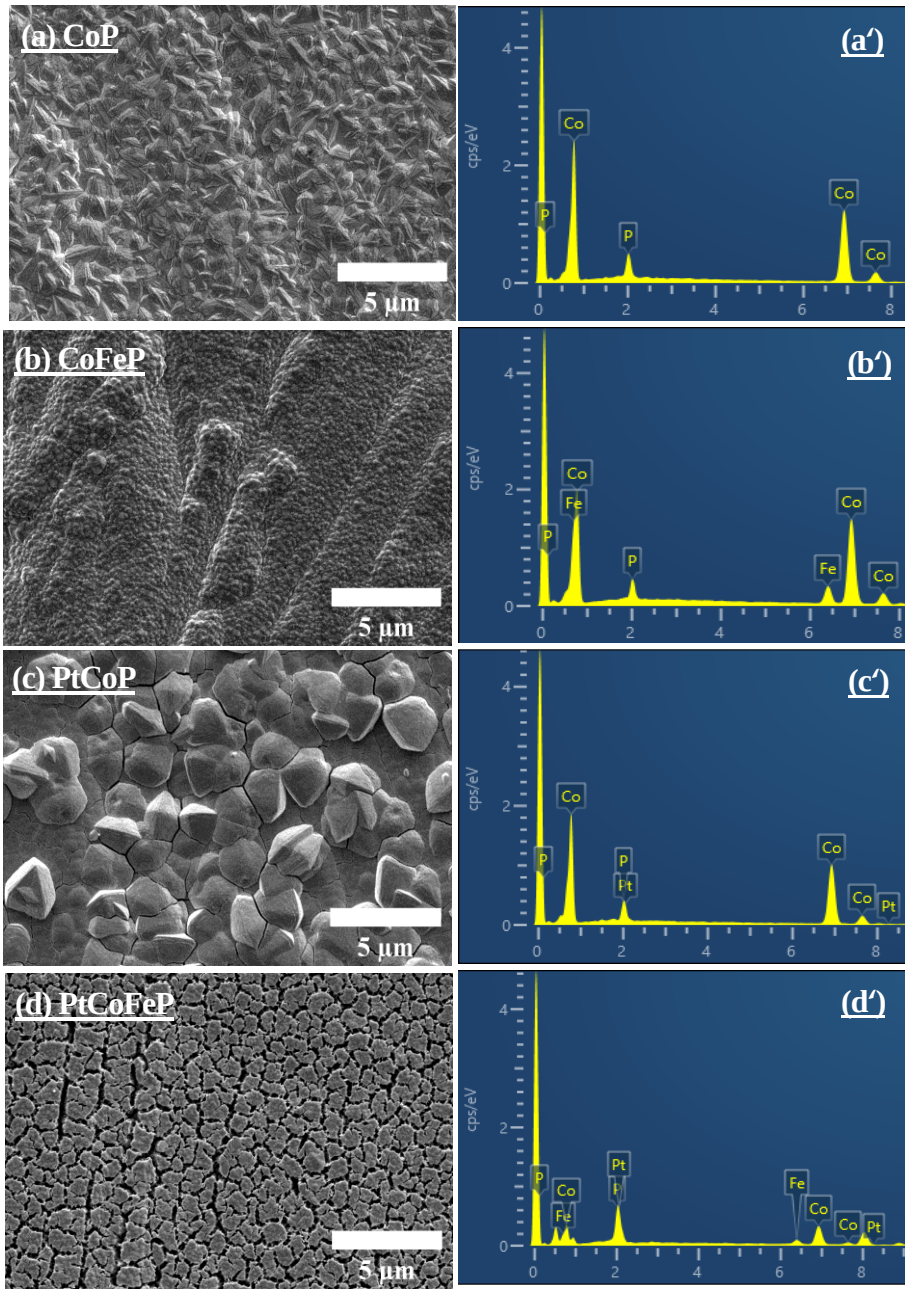

Figure 32. SEM images of CoP (a), CoFeP (b), PtCoP (c), and PtCoFeP (d) deposited on the Cu surface. (a′–d′) EDX spectra corresponding to the aforementioned SEM images.

Table 14. Elemental composition of coatings deposited on the Cu surface determined by EDX analysis.

Sample	Element, at%			
	Pt	**Co**	**Fe**	**P**
CoP	–	90.72	–	9.28
CoFeP	–	80.49	13.33	6.18
PtCoP	0.18	90.34	–	9.48
PtCoFeP	5.96	61.06	10.31	22.66

Among all samples, the PtCoFeP coating (Figure 32d) showed the most distinct and textured morphology, composed of uniformly distributed nodular nanoparticles connected in a porous network structure. The synergistic effect of Fe and Pt surface modification enhanced nucleation and grain refinement during deposition, resulting in significant modification of the surface texture and microstructure of the coating. The results obtained demonstrate the significant impact of compositional variations on the morphological evolution of electrolessly deposited coatings.

3.3.2. Electrocatalytic Activity of Unmodified and Pt-modified CoP and CoFeP Catalysts Towards HER

The electrocatalytic performances of the prepared catalysts towards the HER were investigated by recording linear sweep voltammograms (LSVs) in 1 M KOH solution at a scan rate of 5 mV s^{-1} at 25 °C, and the resulting polarization curves are presented in Figure 33a. Summarized parameters for HER on the investigated catalysts in alkaline media at 25 °C are given in Table 15. The corresponding overpotential values at current densities of 10, 20, 50, and 100 mA cm^{-2} are presented in Figure 33c. Among the catalysts investigated, the PtCoP electrocatalyst exhibited superior HER activity, requiring the lowest overpotential of 46 mV to achieve a current density of 10 mA cm^{-2}, followed by PtCoFeP (66 mV), CoP (102 mV), and CoFeP (132 mV) as illustrated in Figures 33a and 33c. The reproducibility of the HER performance of the most efficient PtCoP/Cu catalyst was subjected to further evaluation using three independent electrodes.

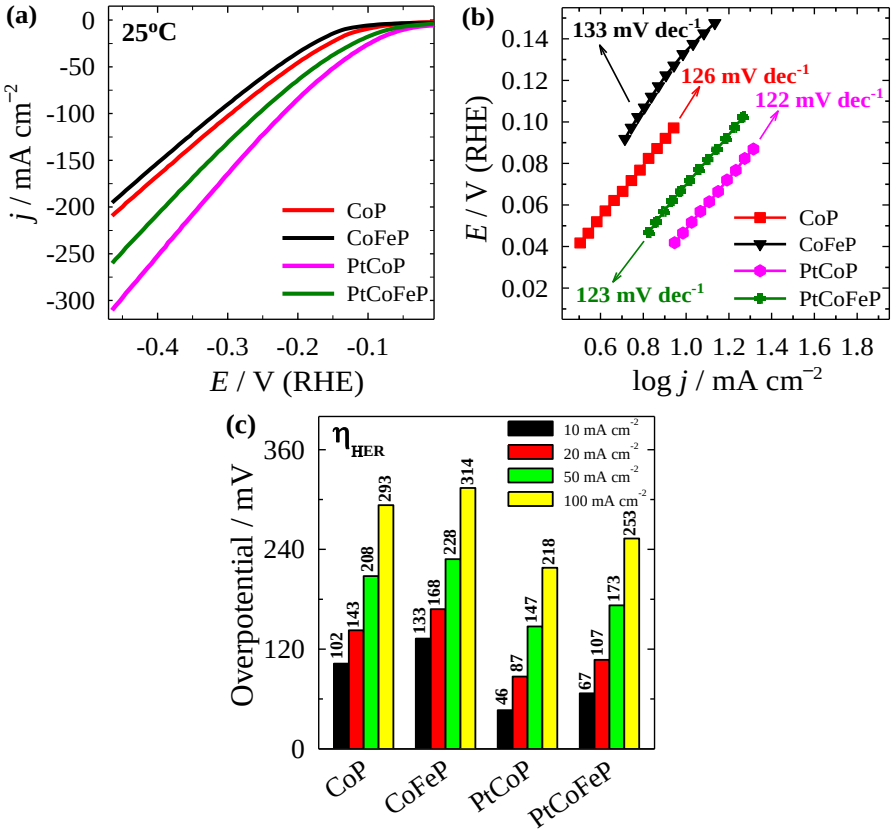

Figure 33. (a) HER polarization curves in an N_2–saturated 1 M KOH solution at a potential scan rate of 5 mV s^{-1} and a temperature of 25 ºC. (b) The corresponding Tafel slopes. (c) Bar columns of the corresponding overpotentials at current densities of 10, 20, 50 and 100 mA cm^{-2}.

The overpotential at 10 mA cm^{-2} and the Tafel slope were determined to be 46.57 ± 0.46 mV and 123.87 ± 1.00 mV dec^{-1}, respectively (n = 3). In addition, at a current density of 100 mA cm^{-2}, PtCoP exhibited the lowest overpotential of 217 mV in comparison with PtCoFeP (253 mV), CoP (293 mV), and CoFeP (313 mV), thus confirming its superior catalytic performance over the entire current density range. The lower overpotential of PtCoP is evidence of its enhanced catalytic activity towards hydrogen evolution in alkaline media. Moreover, the Pt-modified catalysts exhibited consistently lower overpotentials in comparison to their unmodified counterparts, thus confirming the crucial role of Pt incorporation in enhancing HER kinetics and boosting overall catalytic efficiency.

Table 15. Summarized parameters for HER on the investigated catalysts in alkaline media.

Sample	E_{onset} *, V	η_{10} **, mV	Tafel Slope, mV dec^{-1}
CoP	0.064	102	126
CoFeP	0.069	133	133
PtCoP	0.084	46	122
PtCoFeP	0.049	67	123

* Potential at –1 mA cm^{-2}, ** Overpotential at 10 mA cm^{-2}.

The HER kinetics of the synthesised catalysts were further investigated using the relevant Tafel plots, as shown in Figure 33b. The Tafel slope, which is determined by the correlation between overpotential (η) and logarithmic current density (log j), offers significant insights into the reaction kinetics and potential HER mechanism. The Tafel slope values that were calculated were 126, 133, 122, and 123 mV dec^{-1} for CoP, CoFeP, PtCoP, and PtCoFeP, respectively. Among the catalysts that were investigated, PtCoP exhibited the lowest Tafel slope, followed closely by PtCoFeP. This finding indicates more favourable HER kinetics and improved charge-transfer characteristics after Pt modification. The lower Tafel slopes of the Pt-modified catalysts in comparison with CoP and CoFeP provide further evidence of the favourable role of Pt in facilitating the HER. The Tafel slope values obtained, ranging from 122 to 133 mV dec^{-1}, suggest that the HER may proceed via a Volmer–Heyrovsky mechanism in alkaline media.

To gain further insight into the effect of Pt incorporation on the HER performance of the CoP, CoFeP, PtCoP, and PtCoFeP catalysts, electrochemical impedance spectroscopy (EIS) measurements were performed. The Nyquist plots of impedances obtained at –150 mV are shown in Figure 34. In this potential region, all spectra are comprised of an indistinct high frequency signal, followed by a wide semicircle at intermediate to low frequencies, which is determined by hydrogen adsorption [191]. In accordance with LSV results, the largest impedance magnitude (i.e., lowest HER current at this overpotential) is observed for the CoFeP catalyst, followed by CoP. The Pt-modified catalysts have significantly lower impedance magnitudes, as evidenced by the Nyquist plots shown in the inset of Figure 34. The spectra were fitted to an equivalent circuit comprised of two RC elements connected in parallel, often used in the literature for adsorption-based reactions such as HER [191].

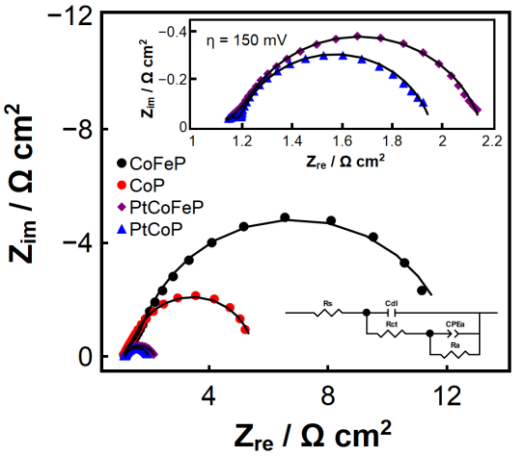

Figure 34. Nyquist plots obtained at –150 mV vs RHE for different films. Inset shows a magnified view of the EIS spectra of Pd-containing films.

Here, C_{dl} and R_{ct} are the double-layer capacitance and charge transfer resistance, and C_a and R_a are the hydrogen adsorption pseudocapacitance and related resistance. The obtained values are shown in Table 16, where it is apparent that the Pd-modified films exhibit ~10 times lower R_{ct} values, signalling much faster HER kinetics.

Table 16. EIS fitting parameters of CoP, CoFeP, PtCoP, and PtCoFeP electrocatalysts for HER.

Catalyst	C_{dl}, mF cm^{-2}	R_{ct}, Ω cm^2	C_a, mF cm^{-2}	R_a, Ω cm^2
CoP	1.47	0.94	2.01	3.44
CoFeP	1.00	1.01	1.88	9.98
PtCoP	1.13	0.075	16.8	0.77
PtCoFeP	1.95	0.095	5.20	0.93

In addition, R_a decreases strongly with Pd incorporation (from ~10 – 3.44 Ω cm^2 to 0.93 – 0.77 Ω cm^2), indicating faster relaxation of adsorbed H* intermediates. For PtCoP in particular, the high C_a value of 16.8 mF cm^{-2} is most likely attributable to the increased number of active sites for hydrogen adsorption/desorption. Overall, the EIS results confirm the beneficial effect of Pd incorporation for HER, and reveal that the best-performing PtCoP catalyst has the lowest charge transfer resistance, optimal hydrogen bonding strength for adsorption/desorption, and the largest hydrogen adsorption pseudocapacitance, which suggests a large number of active HER sites.

3.3.3. Electrocatalytic Activity of Unmodified and Pt-modified CoP and CoFeP Catalysts Towards OER

The electrocatalytic performance of the catalysts towards the oxygen evolution reaction (OER) was also evaluated, and the corresponding polarization curves are presented in Figure 35a. The summarized data are shown in Table 17.

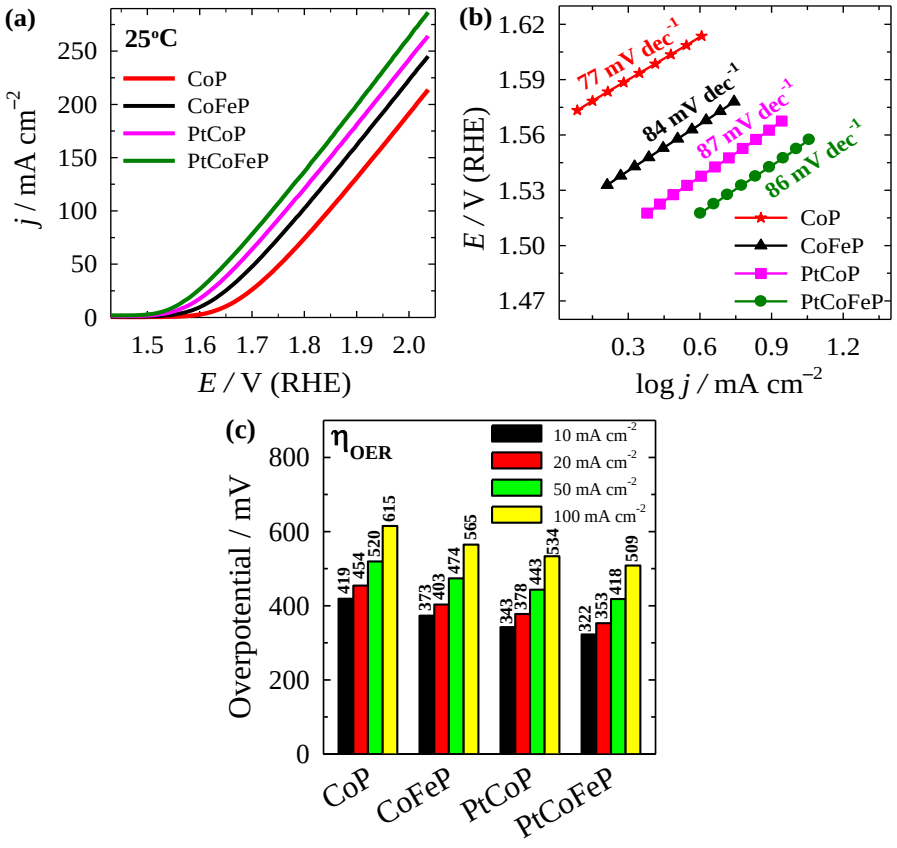

Figure 35. (a) OER polarization curves in an N_2–saturated 1 M KOH solution at a potential scan rate of 5 mV s^{-1} and a temperature of 25 °C (b) The corresponding Tafel slopes. (c) Bar columns of the corresponding overpotentials at current densities of 10, 20, 50 and 100 mA cm^{-2}.

As demonstrated by the LSVs recorded for the CoP, CoFeP, PtCoP, and PtCoFeP catalysts in a 1 M KOH solution at 25 °C, PtCoFeP exhibited the most significant OER activity among all the samples investigated. The overpotential values required to achieve current densities of 10, 20, 50, and 100 mA cm^{-2} are presented in Figure 35c.

Table 17. Electrochemical performance of the investigated catalysts for OER in alkaline media at 25 °C.

Sample	E_{onset} *, V	η_{10} **, mV	Tafel Slope, mV dec^{-1}
CoP	1.568	419	77
CoFeP	1.513	373	84
PtCoP	1.447	343	87
PtCoFeP	1.437	322	86

* Potential at –1 mA cm^{-2}, ** Overpotential at 10 mA cm^{-2}.

Among the catalysts investigated, PtCoFeP was found to require the lowest overpotential of 322 mV to attain a current density of 10 mA cm^{-2}, followed by PtCoP (343 mV), CoFeP (373 mV), and CoP (419 mV). In addition, at a current density of 100 mA cm^{-2}, PtCoFeP demonstrated the lowest overpotential of 509 mV in comparison with PtCoP (534 mV), CoFeP (565 mV), and CoP (615 mV), thus indicating its enhanced OER performance across the entire current density range. The lower overpotentials exhibited by PtCoFeP consistently demonstrate the favourable effect of Fe addition and consequent Pt surface modification in improving OER kinetics and overall electrocatalytic performance in alkaline media. The enhanced activity exhibited by PtCoFeP at both low and high current densities further suggests its remarkable capacity to facilitate rapid oxygen evolution under feasible operating conditions.

The OER kinetic behaviour of the catalysts was further investigated by means of the corresponding Tafel plots (see Figure 35b). The calculated Tafel slope values were 77, 84, 87, and 86 mV dec^{-1} for CoP, CoFeP, PtCoP, and PtCoFeP, respectively. However, despite exhibiting the lowest Tafel slope, CoP required significantly higher overpotentials to achieve the desired current densities. Meanwhile, PtCoFeP exhibited the lowest overpotential values over the range of current densities investigated, suggesting superior OER activity. The reproducibility of the OER performance of the best-performing PtCoFeP/Cu catalyst was subjected to further evaluation using three independent electrodes. The overpotential at 10 mA cm^{-2} and the Tafel slope were determined to be 327.42 ± 4.96 mV and 74.17 ± 12.32 mV dec^{-1}, respectively (n = 3). The Tafel slope values obtained from the experimental data suggest that the OER proceeds via a multi-step proton-coupled electron transfer process involving oxygen-containing intermediates. The superior OER performance of PtCoFeP may be attributed to its surface morphology and composition. Furthermore, the combined effects of Pt, Co, Fe, and P may

promote charge transfer and improve OER kinetics, thus contributing to the enhanced OER catalytic activity of PtCoFeP in alkaline media.

3.3.4. Investigation of the Stability of PtCoP/Cu and PtCoFeP/Cu Catalysts

The long-term stability of the PtCoP and PtCoFeP electrocatalysts toward the HER was evaluated using chronopotentiometry at a constant current density of –10 mA cm^{-2} for 15 hours in a 1 M KOH solution at 25 °C. The corresponding results are shown in Figure 36.

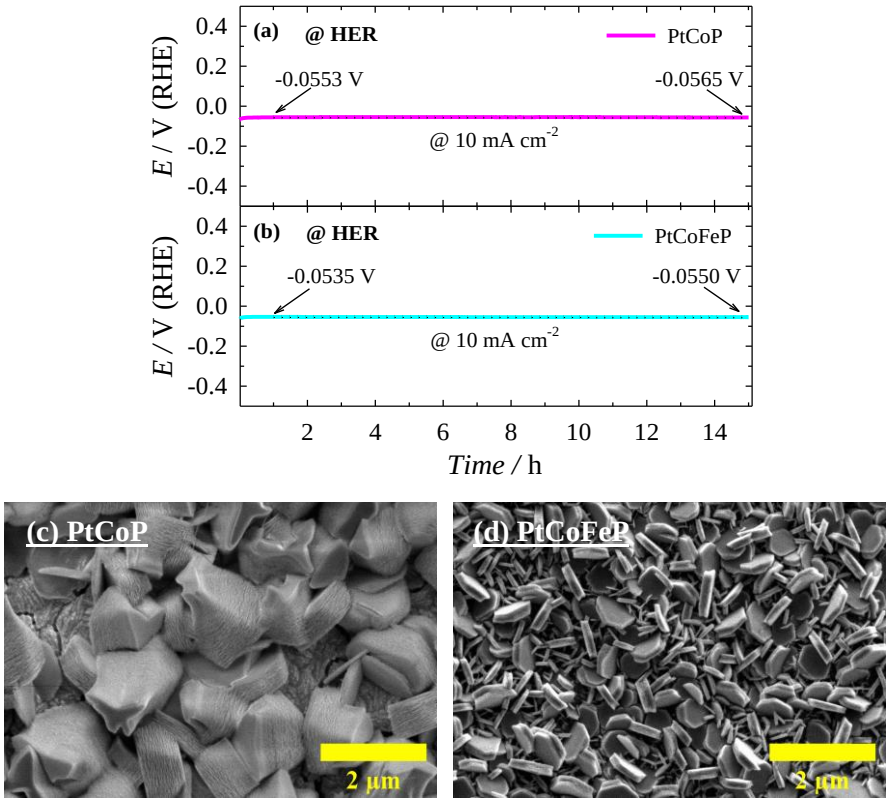

Figure 36. The CP curves of the investigated PtCoP (a) and PtCoFeP (b) catalysts in a 1 M KOH solution at a constant current density of 10 mA cm^{-2} and 25 °C. Post-SEM analysis images of Pt-CoP (c) and Pt-CoFeP (d) after stability test.

Notably, the required potential to maintain 10 mA cm^{-2} remained almost constant throughout the 15 hour stability test. Figure 36a shows that the PtCoP catalyst maintained excellent operational stability with only a minor potential shift from –0.0553 to –0.0565 V (vs. RHE). Similarly, as shown in Figure 36b, the PtCoFeP catalyst demonstrated significant durability, maintaining a

relatively constant potential throughout the measurement interval, with only slight variation from –0.0535 to –0.0550 V (vs RHE).

To further investigate the morphological preservation of the catalysts following prolonged HER operation, a SEM analysis was performed after the 15 h chronopotentiometric test. As shown in Figure 36c,d, the post-stability SEM images revealed that both PtCoP and PtCoFeP maintained their initial surface morphologies, with no evident signs of surface degradation or structural deterioration. Despite a slight surface reconstruction being observed, the overall morphological characteristics remained largely stable. Despite minute surface reconstruction, the overall morphology of both catalysts exhibited remarkable retention following extended electrolysis.

3.3.5. Investigation of Overall Water Splitting by Employing the Unmodified and Pt-modified CoP and CoFeP Catalysts

Encouraged by the superior HER and OER electrocatalytic performances of the prepared catalysts, the bifunctional electrocatalytic activity of the unmodified and Pt-modified CoP and CoFeP catalysts was investigated via overall water splitting (OWS) in a two-electrode water electrolysis cell under an alkaline environment that employed the same catalyst for both the anode and cathode (Fig. 37). Figure 37a shows the overall catalytic performance of a two-electrode alkaline electrolyzer cell configuration using the same catalysts for both the anode and the cathode: CoP‖CoP, CoFeP‖CoFeP, PtCoP‖PtCoP, and PtCoFeP‖PtFeCoP. The overall performance of water splitting is significantly influenced by the composition of the catalyst.

Among the investigated electrodes, the PtCoFeP‖PtCoFeP electrolyzer demonstrated excellent performance, requiring a cell voltage of only 1.628 V to achieve a current density of 10 mA cm^{-2}. In comparison, PtCoP‖PtCoP, CoFeP‖CoFeP, and CoP‖CoP requiring cell voltages of 1.658, 1.714, and 1.779 V, respectively. A notable decrease in cell voltage was observed in the PtCoFeP‖PtCoFeP system, indicating the favorable impact of Fe addition and Pt surface modification on the efficiency of overall water splitting. This enhanced bifunctional electrocatalytic performance can be primarily attributed to the synergy among Pt, Co, Fe, and P, which facilitates both hydrogen and oxygen evolution reactions by promoting charge transfer.

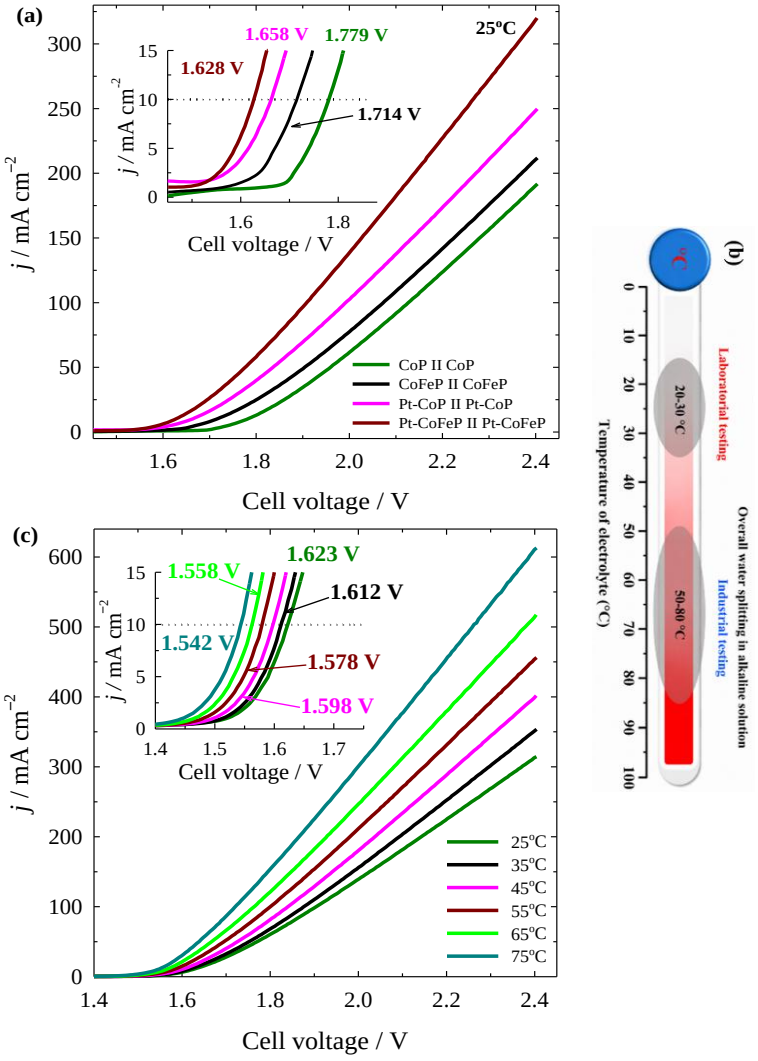

Figure 37. Polarization curves for overall water splitting recorded in the two-electrode setup employing the same catalysts as both anode and cathode at the scan rate of 5 mV s^{-1} (a). Difference between laboratory and industrial testing temperature (b). Polarization curves employing PtCoP as the cathode and PtCoFeP as the anode at different temperatures (25–75 ºC) (c).

As summarized in Table 18, the PtCoFeP‖PtCoFeP electrolyzer exhibited a cell voltage of 1.628 V at 10 mA cm^{-2}, outperforming several previously reported bifunctional electrocatalysts. As indicated in Figure 37b, a significant gap exists between laboratory testing and industrial applications of water electrolysis.

Table 18. Comparison with various electrocatalysts for overall water splitting.

Anode II Cathode	Cell Voltage, V	Electrolyte	Ref.
PtCoFeP‖PtCoFeP	1.63	1 M KOH	This study
PtCoP‖PtCoP	1.66	1 M KOH	This study
CoFeP‖CoFeP	1.71	1 M KOH	This study
CoP‖CoP	1.78	1 M KOH	This study
Pt/C‖IrO_2	1.71	1 M KOH	[188]
Pt/C‖Pt/C	1.83	1 M KOH	[188]
Co-P/NC-CC‖Co-P/NC-CC	1.95	1 M KOH	[190]
CoMoP nanofibers ‖ CoMoP nanofibers	1.75	1 M KOH	[192]
Pt-Co/Fe LDH‖Pt-Co/Fe LDH	1.66	1 M KOH	[193]
Pt-Ni Fe LDH‖ Pt-Ni Fe LDH	1.68	1 M KOH	[194]
FePx@Fe‖FePx@Fe	1.88	1 M KOH	[195]
Pt/NiW/NF‖ Pt/NiW/NF	1.76	1 M KOH	[196]
PtCoeFeCo PBAs‖PtCoeFeCo PBAs	1.68	1 M KOH	[197]

The laboratory temperature is typically maintained between 20 and 30 °C. In practical applications, the overall water-splitting performance is usually achieved at 50–80 °C to reduce the required voltage. In order to bridge the gap between laboratory and industrial conditions, the electrochemical behaviour of a water splitting electrolyzer is evaluated at an industrial temperature. The influence of temperature on electrolysis performance was evaluated through the investigation of a two-electrode electrolyzer comprising PtCoP as the cathode and PtCoFeP as the anode at temperatures ranging from 25 to 75 °C. Within a specific temperature range, the polarization curves of PtCoP‖PtCoFeP are presented in Figure 37c. It has been observed that the voltage of water splitting at the same current density undergoes a gradual decline as the reaction temperature is increased. The PtCoP‖PtCoFeP device exhibits a remarkable voltage requirement of 1.623, 1.612, 1.598, 1.578, 1.558 and 1.542V at 25, 35, 45, 55, 65 and 75 °C, respectively, to attain a current density of 10 mA cm^{-2}. The findings indicate that the PtCoP‖PtCoFeP electrolyzer exhibits considerable potential for application in the industrial domain of water electrolysis.

LIMITATIONS AND PROSPECTS FOR FURTHER IMPROVEMENT

Despite the demonstrated good electrocatalytic activity and stability of the synthesized CoP_x/Cu, CoFeP/Cu, PdCoP/Cu, PdCoFeP/Cu, PtCoP/Cu, and PtCoFeP/Cu electrocatalysts towards HER, OER, and overall water splitting, there are several limitations that require further investigation. Non-noble-metal CoP_x/Cu and CoFeP/Cu electrocatalysts still exhibit comparatively higher overpotentials, particularly for the OER, in comparison with Pt-modified electrocatalysts, suggesting the potential for enhancement of their catalytic performance. Furthermore, despite the introduction of Pt and Pd in relatively small amounts, the employment of precious metals remains a constraint for large-scale implementation due to their high cost and scarcity. Further enhancement may be achieved through optimization of the Co/Fe/P composition and modulation of surface morphology to improve the quantity and availability of active sites, while reducing the amount of noble metals via controlled surface modification. Furthermore, despite the good stability exhibited under the investigated conditions in this study, it is considered beneficial to conduct longer-term durability tests at elevated temperatures and higher current densities in order to evaluate their practical viability. Such optimization has the potential to enhance the overall catalytic performance, durability, and cost-effectiveness of the developed electrocatalysts.

CONCLUSIONS

1. The successful development of the CoP_x/Cu (0.4–11 wt% P), CoFeP/Cu, PdCoP/Cu, PdCoFeP/Cu, PtCoP/Cu, and PtCoFeP/Cu electrocatalysts in this study was achieved through a straightforward method combining electroless deposition and galvanic displacement. These electrocatalysts demonstrated superior performance for the HER, OER, and OWS in alkaline media. The HER and OER catalytic activities were assessed in a three-electrode cell using 1 M KOH, while the OWS performance was evaluated in a two-electrode electrolyzer under both laboratory-scale conditions and industrially relevant temperatures (25–75 ºC).
2. The phosphorus content was identified as a crucial factor influencing the electrocatalytic performance of cobalt phosphide coatings. Among the CoP_x catalysts, CoP_{11}/Cu showed the most promising HER activity, with an overpotential of 98.9 mV at 10 mA cm^{-2}, while CoP_8/Cu exhibited the most effective OER performance, requiring 378 mV at 10 mA cm^{-2} in 1 M KOH.
3. The electrocatalytic activity of CoP and CoFeP catalysts was significantly improved by surface modification with a small amount of Pd through galvanic displacement. Among the Pd-modified catalysts, PdCoP/Cu demonstrated the most favourable HER performance, exhibiting an overpotential of 250 mV at 10 mA cm^{-2}. Moreover, PdCoP/Cu and PdCoFeP/Cu exhibited enhanced OER activity, requiring an overpotential of 396 mV at 10 mA cm^{-2} in 1 M KOH. The incorporation of Fe into the coatings resulted in enhanced catalytic activity and stability, attributable to the modification of coating composition and surface characteristics.
4. It was demonstrated that surface modification of CoP and CoFeP catalysts with a small amount of Pt via galvanic displacement resulted in the enhancement of electrocatalytic performance. PtCoP/Cu demonstrated remarkable HER activity, exhibiting an overpotential of merely 46 mV at 10 mA cm^{-2}, while PtCoFeP/Cu evidenced superior OER performance, with an overpotential of 322 mV at 10 mA cm^{-2}, thereby substantiating the synergistic influence of Fe incorporation and Pt modification on the electrocatalytic performance.
5. It is notable that the OWS performance exhibited a progressive enhancement from the CoP_{11}/Cu-based electrolyzer (1.81 V at 10 mA cm^{-2}) to the PdCoFeP/Cu-based electrolyzer (1.69 V at 10 mA cm^{-2}) at 25 °C. Among all the assembled electrolyzers, it was found that the $PtCoFeP_{(+)} \parallel PtCoP_{(-)}$ configuration demonstrated the outstanding OWS performance, requiring a low voltage of only 1.63 V at 25 °C and 1.54 V

at 75 °C to achieve 10 mA cm^{-2} in 1 M KOH, thus indicating its remarkable potential for practical application in industrial alkaline water electrolysis at relevant operating temperatures.

6. Electrochemical stability under alkaline conditions was demonstrated by the developed CoP_{11}/Cu, PdCoP/Cu, PdCoFeP/Cu, PtCoP/Cu, and PtCoFeP/Cu electrocatalysts. Chronopotentiometry revealed potential shifts of 18.6 mV and 18.9 mV at a current density of 10 mA cm^{-2} for PdCoP/Cu and PdCoFeP/Cu, respectively, after 10 hours, respectively. Meanwhile, PtCoP/Cu and PtCoFeP/Cu exhibited shifts of only 1.2 mV and 1.5 mV, respectively, at a current density of 10 mA cm^{-2} after 15 hours. Furthermore, PdCoFeP/Cu demonstrated a remarkable retention of 96.02% of its initial current, whereas CoP_{11}/Cu exhibited consistent operation throughout 15 hours at a constant potential of –0.26 V. Additionally, CoP_{11}/Cu demonstrated high stability following 1,000 cycles of accelerated degradation testing.
7. The electrochemically active surface area (ECSA) of the optimized CoP_{11}/Cu and PdCoFeP/Cu electrocatalysts was 115.6 and 1407.3 cm^2, respectively. The high ECSA values suggest that the number of electrochemically accessible active sites might be higher, potentially leading to higher HER and OER electrocatalytic activity.
8. In summary, electroless deposition and galvanic displacement can be regarded as a facile, cost-effective, and scalable method for the production of highly efficient cobalt phosphide-based electrocatalysts. These materials have the potential to serve as efficient candidates for hydrogen production via alkaline water electrolysis, particularly under industrial operating conditions.

SANTRAUKA LIETUVIŲ KALBA

ĮVADAS

Manoma, kad šiuo metu pasaulio gyventojų skaičius siekia apie 7,5 milijardų, o prognozės rodo, kad iki 2030 m. jis išaugs iki 8,5 milijardų. Šis nuolatinis gyventojų skaičiaus augimas yra pagrindinis veiksnys, didinantis pasaulinį energijos suvartojimą. Didžiąją dalį pasaulinės energijos gamybos ir suvartojimo sudaro iškastinis kuras, įskaitant anglį, naftą ir gamtines dujas. Be to, nuolatinis šių kuro rūšių deginimas lėmė žymų anglies dioksido (CO_2) išmetimo į atmosferą padidėjimą, o tai labai prisideda prie visuotinio atšilimo ir klimato kaitos. Todėl tvarus energijos šaltinių vystymas ir naudojimas tapo būtini siekiant sumažinti anglies dioksido išmetimus ir sušvelninti klimato kaitos padarinius.

Todėl šie su aplinka ir energetika susiję iššūkiai skatina mokslininkus ieškoti tinkamų sprendimų pasaulio energetikos problemoms spręsti. Per pastaruosius kelis dešimtmečius vandenilis buvo pripažintas perspektyviausia alternatyva dėl savo didelio gravimetrinio energijos tankio (120–140 MJ/kg), kuris yra beveik tris kartus didesnis nei tradicinių iškastinių kuro rūšių, įskaitant gamtines dujas, benziną ir anglį (50 MJ/kg).

Elektrocheminis vandens skilimas (vandens elektrolizė) – perspektyvi tvari technologija, leidžianti išgauti ypač švarias vandenilio dujas, vykstant dviems reakcijoms: katodinei vandenilio išsiskyrimo reakcijai (HER) ir anodinei deguonies išsiskyrimo reakcijai (OER). Šiuo metu šarminė vandens elektrolizė laikoma perspektyviausiu būdu didelio masto ekologiško vandenilio gamybai.

Šiuo metu pažangiausi OER katalizatoriai yra IrO_2 ir RuO_2, o pažangiausias HER katalizatorius – Pt/C. Be to, šių katalizatorių didelė kaina, retumas ir ribotas funkcionalumas smarkiai riboja pramoninę vandenilio gamybą elektrocheminio vandens skilimo būdu. Todėl būtina sukurti naują netauriųjų metalų bifunkcinį elektrokatalizatorių, kuris būtų ekonomiškas ir itin stabilus, tuo pačiu išlaikydamas optimalų efektyvumą.

Medžiagos, kurių pagrindą sudaro pereinamieji metalai, ypač pereinamųjų metalų fosfidai (TMP), sulaukė didelio mokslininkų susidomėjimo dėl savo išskirtinio elektrokatalizinio aktyvumo, jų ekonomiškumo ir puikių elektrinio laidumo savybių. Tarp jų kobalto fosfidai laikomi naujos kartos pereinamųjų metalų elektrokatalizatoriais dėl puikių elektrokatalizinių savybių, paprastos jų gavimo sintezės ir gausaus paplitimo gamtoje. Nepaisant šių privalumų, kobalto fosfidų pagrindu pagamintų katalizatorių savitasis elektrinis laidumas ir aktyviųjų centrų prieinamumas vis

dar yra riboti, todėl, palyginti su tauriųjų metalų etaloniniais katalizatoriais, jų bifunkcinės katalizinės savybės yra prastesnės. Tai paskatino tyrimus, skirtus optimizavimo strategijoms, tokioms kaip heteroatomų įterpimas, kompozitų kūrimas, laidžių nešiklio medžiagų naudojimas ir katalizatorių paviršiaus modifikavimas nedideliais tauriųjų metalų kiekiais. Tačiau daugumoje paskelbtų tyrimų šios strategijos vertinamos standartinėmis laboratorinėmis sąlygomis, nors praktikoje šarminiai elektrolizeriai paprastai veikia aukštesnėje temperatūroje. Iš tiesų, vis dar egzistuoja didelis atotrūkis tarp laboratorinių bandymų sąlygų (kambario temperatūra) ir pramoninės eksploatacijos aplinkos (50–80 °C). Todėl labai svarbu įvertinti katalizatorių elektrokatalizinį našumą tokiomis sudėtingomis eksploatavimo sąlygomis, siekiant užtikrinti jų veiksmingumą realiomis taikymo sąlygomis.

Šiame tyrime buvo sukurtas paprastas, be rišiklių, lengvai pritaikomas ir nebrangus metodas, apjungiantis cheminį metalų nusodinimą ir galvaninį pakeitimą bei skirtas kobaltio fosfido pagrindu pagamintiems elektrokatalizatoriams ant Cu pagrindo formuoti. Iš pradžių buvo tiriama fosforo kiekio įtaka CoP elektrokatalizinėms savybėms. Be to, į kobalto fosfido struktūrą buvo įterpta Fe, siekiant suformuoti CoFeP. Be to, tiek CoP, tiek CoFeP buvo modifikuoti nedideliais Pd ir Pt kiekiais galvaninio pakeitimo būdu, siekiant dar labiau pagerinti jų bifunkcines elektrokatalizines savybes. Gautų elektrokatalizatorių aktyvumas buvo įvertintas HER, OER ir OWS procesams 1 M KOH tirpale 25–75 °C temperatūroje. Nustatyta, kad suformuoti katalizatoriai pasižymi padidintu katalizinu aktyvumu ir ilgalaikiu stabilumu, naudojant nedidelius tauriųjų metalų kiekius. Tai patvirtina šių elektrokatalizatorių pritaikomumą pramoniniu požiūriu aktualiomis eksploatavimo sąlygomis.

DARBO TIKSLAS

Co-P_x/Cu, CoFeP/Cu, PdCoP/Cu, PdCoFeP/Cu, PtCoP/Cu ir PtCoFeP/Cu elektrokatalizatorių formavimas, naudojant cheminį metalų nusodinimo ir galvaninio pakeitimo metodus, jų sudėties, mikrostruktūros ir paviršiaus morfologijos charakterizavimas bei elektrokatalizinio aktyvumo ir stabilumo įvertinimas vandenilio išsiskyrimo reakcijai (HER), deguonies išsiskyrimo reakcijai (OER) ir bendram vandens skilimo procesui (OWS) šarminėje terpėje (1 M KOH) praktinėmis ir pramoninėmis vandens skilimo sąlygomis.

DARBO UŽDAVINIAI

1. Susintetinti Co-P_x/Cu ir CoFeP/Cu elektrokatalizatorius, taikant cheminį metalų nusodinimo metodą ir ištirti fosforo (P) kiekio bei geležies (Fe) įterpimo įtaką jų struktūrai, morfologijai ir elektrokatalizinėms savybėms.
2. Suformuoti PdCoP/Cu, PtCoP/Cu, PdCoFeP/Cu ir PtCoFeP/Cu elektrokatalizatorius galvaninio pakeitimo būdu, pakeičiant CoP ir CoFeP dangas paladžio (Pd) ir platinos (Pt) daleles, ir įvertinti tauriųjų metalų modifikacijos įtaką jų elektrokatalizinėms savybėms.
3. Apibūdinti susintetintų elektrokatalizatorių kristalinę struktūrą, mikrostruktūrą, paviršiaus morfologiją ir elementų pasiskirstymą, taikant rentgeno spindulių difrakciją (XRD), skenuojančią elektronų mikroskopiją (SEM) ir energijos dispersinę rentgeno spektroskopiją (EDS).
4. Įvertinti suformuotų elektrokatalizatorių elektrokatalizinį aktyvumą HER ir OER reakcijoms šarminėje terpėje.
5. Nustatyti sukurtų elektrokatalizatorių elektrochemiškai aktyvų paviršiaus plotą (ECSA), reakcijos kinetiką ir elektrocheminį ilgalaikį stabilumą.
6. Įvertinti Co-P_x/Cu, CoFeP/Cu, PdCoP/Cu, PdCoFeP/Cu, PtCoP/Cu ir PtCoFeP/Cu elektrokatalizatorių efektyvumą OWS procesui šarminėje terpėje (1 M KOH), esant 25 °C temperatūrai, bei įvertinti PtCoP/Cu ir PtCoFeP/Cu elektrokatalizatorių efektyvumo priklausomybę OWS procesui nuo temperatūros 25–75 °C temperatūrų intervale.

MOKSLINIS NAUJUMAS

1. Buvo sukurtas paprastas ir nebrangus Co-P_x/Cu, CoFeP/Cu, PdCoP/Cu, PdCoFeP/Cu, PtCoP/Cu ir PtCoFeP/Cu elektrokatalizatorių, skirtų šarminiam vandens skilimui, gamybos metodas, apimantis cheminio metalų nusodinimo ir galvaninio pakeitimo metodus.
2. Buvo išsamiai ištirti P, Fe bei paviršiaus modifikavimo Pd ir Pt dalelėmis įtaka kobalto fosfido pagrindu pagamintų elektrokatalizatorių struktūrinėms, paviršiaus ir elektrokatalizinėms savybėms.
3. Kobalto fosfido pagrindu pagamintų elektrokatalizatorių bifunkcinis elektrokatalizinis aktyvumas ir stabilumas tiek HER, tiek OER procesuose buvo žymiai pagerintas, modifikuojant jų paviršių Pd ir Pt dalelėmis galvaninio pakeitimo metodu.
4. OWS procesas buvo sėkmingai išbandytas, naudojant PtCoP/Cu ir PtCoFeP/Cu elektrokatalizatorius pramonėje aktualiose darbinėse

temperatūrose (25–75 °C), siekiant įvertinti jų praktinį pritaikomumą šarminėje vandens elektrolizėje.

5. Paprastas, lengvai pritaikomas ir ekonomiškas metodas buvo sukurtas aukštos kokybės bifunkcinių elektrokatalizatorių, skirtų efektyviai šarminės vandens elektrolizei, formavimui.

GINAMIEJI TEIGINIAI

1. Nesudėtingi ir ekonomiški cheminio metalų nusodinimo bei galvaninio pakeitimo metodai buvo sėkmingai pritaikyti Co-P_x/Cu, CoFeP/Cu, PdCoP/Cu, PdCoFeP/Cu, PtCoP/Cu ir PtCoFeP/Cu elektrokatalizatorių, skirtų šarminiam vandens skilimui, formavimui.
2. Buvo nustatyta, kad fosforo (P_x) kiekis Co-P_x/Cu dangose ženkliai įtakoja paviršiaus morfologiją, ECSA ir elektrokatalizinį efektyvumą HER ir OER reakcijoms.
3. Buvo įrodyta, kad Fe įtraukimas į kobalto fosfido dangas dar labiau padidina elektrokatalizatorių katalizinį aktyvumą ir stabilumą, modifikuodamas jų cheminę sudėtį ir paviršiaus savybes.
4. Buvo nustatyta, kad CoP ir CoFeP pagrindu pagamintų elektrokatalizatorių paviršiaus modifikavimas, nusodinant nedidelius Pd ir Pt kiekius galvaninio pakeitimo būdu, žymiai pagerina reakcijos kinetiką, katalizinį aktyvumą ir stabilumą tiek HER, tiek OER atžvilgiu.
5. Optimizuoti CoP_{11}/Cu, PdCoFeP/Cu ir PtCoFeP/Cu elektrokatalizatoriai pasižymi puikiu efektyvumu OWS procesui šarminėje terpėje. CoP_{11}/Cu ir PdCoFeP/Cu pagrindu sukurti elektrolizeriai užtikrino efektyvų OWS procesą 25 °C temperatūroje, o PtCoFeP/Cu pagrindu sukurti elektrolizeriai pademonstravo išskirtinius veikimo rodiklius tiek laboratorinio masto, tiek pramoniniu požiūriu aktualiose eksploatavimo temperatūrose (25–75 °C), patvirtindami jų tinkamumą praktiniam šarminiam vandens elektrolizės procesui.

2. EKSPERIMENTO METODIKA

2.1. Pagrindo paruošimas

Prieš pradedant gaminti elektrodus, iš vario lakšto buvo tiksliai išpjauti 1 × 1 cm dydžio vario substratai, skirti elektrocheminiams matavimams ir struktūriniam charakterizavimui.

1. Priešapdorojimas: vario pagrindas buvo apdorotas kalcio ir magnio oksidu, po to nuplautas dejonizuotu vandeniu (DI).
2. Paviršiaus valymas: paruoštas vario pagrindas 1 minutę buvo panardintas į HCl:H_2O (1:1, tūrio santykiu) tirpalą 25 ^oC temperatūroje, siekiant pašalinti bet kokias neorganinių priemaišų liekanas nuo paviršiaus, o po to nuplautas dejonizuotu vandeniu.
3. Aktyvacija: po valymo Cu pagrindas buvo aktyvuotas, 1 minutę panardinant jį į 0,5 g/l $PdCl_2$ tirpalą 25 ^oC temperatūroje. Po to aktyvuotas Cu pagrindas prieš tolesnį apdorojimą buvo kruopščiai nuplautas dejonizuotu vandeniu.

2.2. Co-P_x/Cu katalizatorių gamyba

Co-P_x/Cu katalizatoriai buvo pagaminti taikant cheminio metalų nusodinimo metodą ant Pd aktyvuoto Cu pagrindo (Pd/Cu). Pd/Cu elektrodas buvo panardintas į ką tik paruoštą cheminio nusodinimo vonią, kurioje buvo 0,1 M $CoSO_4$, 0,6 M glicino (NH_2CH_2COOH) ir 0,25, 0,5, 0,75, 2,5 bei 4,5 M NaH_2PO_2 tirpalas. Dengimo tirpalo pH buvo tiksliai sureguliuotas iki pH 11, naudojant NaOH tirpalą. Dengimo vonia veikė 80 ^oC temperatūroje 10 min. Siekiant optimizuoti nusodinimo parametrus, buvo atlikti preliminarūs eksperimentai. Šių eksperimentų metu sistemingai keisti parametrai: vonios pH, temperatūra, nusodinimo trukmė ir NaH_2PO_2 koncentracija. Remiantis šių eksperimentų rezultatais, nustatyta, kad optimalios sąlygos, leidžiančios gauti vienodą ir gerai sukibusią Co-P_x dangą ant Cu pagrindo, yra pH 11, 80 ^oC ir trukmė 10 min. NaH_2PO_2 koncentracija buvo keičiama, siekiant kontroliuoti fosforo kiekį dangoje ir ištirti jo poveikį katalizatoriaus savybėms. NaH_2PO_2 buvo naudojamas kaip reduktorius ir fosforo šaltinis, o glicinas – kaip Co^{2+} jonų kompleksadarys. Keičiant NaH_2PO_2 koncentraciją, pavyko gauti Co-P_x/Cu elektrodus su skirtingu fosforo kiekiu (x = 0,4; 1,6; 5; 8 ir 11). Po nusodinimo proceso gautas Co-P_x/Cu mėginys buvo atsargiai išimtas, kruopščiai nuplautas dejonizuotu vandeniu, išdžiovintas ore ir naudotas be jokio papildomo apdorojimo.

2.3. PdCoP/Cu ir PdCoFeP/Cu katalizatorių gamyba

CoP ir CoFeP dangos buvo nusodintos ant Pd/Cu elektrodo cheminio metalų nusodinimo būdu. Pd/Cu elektrodas buvo panardintas į cheminio nusodinimo vonią, kurioje buvo 0,1 M $CoSO_4$, 0,6 M glicino ir 0,75 M NaH_2PO_2 (pH = 11) tirpalas. Nusodinimo procesas vyko 60 °C temperatūroje 30 min. Šios sąlygos buvo parinktos remiantis preliminariais optimizavimo eksperimentais, kurių metu buvo keičiama vonios sudėtis, pH, nusodinimo temperatūra ir trukmė, siekiant gauti vienodas ir gerai sukibusias CoP ir CoFeP dangas ant Cu pagrindo. CoFeP/Cu katalizatorius buvo suformuotas identiškomis nusodinimo sąlygomis, į nusodinimo vonią įdedant papildomai 0,01 M $FeSO_4$. Gauti elektrodai buvo kruopščiai nuplauti deionizuotu vandeniu ir išdžiovinti kambario temperatūroje. Pd kristalitai buvo nusodinti ant CoP/Cu ir CoFeP/Cu elektrodų galvaninio pakeitimo būdu. CoP/Cu ir CoFeP/Cu elektrodai buvo panardinti į 1 mmol L^{-1} $PdCl_2$ tirpalą 1 minutę 25 ^oC temperatūroje, siekiant nusodinti Pd kristalitus ant katalizatoriaus paviršiaus. Pd nusodinimo sąlygos buvo parinktos, remiantis preliminariais eksperimentais, kurių tikslas buvo nustatyti optimalias sąlygas paviršiaus modifikavimui kontroliuoti, nepažeidžiant po juo esančių CoP ir CoFeP dangų. Po modifikavimo mėginiai buvo kruopščiai nuplauti dejonizuotu vandeniu ir išdžiovinti kambario temperatūroje.

2.4. PtCoP/Cu ir PtCoFeP/Cu katalizatorių gamyba

Siekiant suformuoti CoP/Cu ir CoFeP/Cu elektrodus, Pd/Cu elektrodai buvo panardinami į cheminio nusodinimo vonią, sudarytą iš 0,1 M $CoSO_4$, 1,5 M NaH_2PO_2 ir 0,6 M glicino (pH = 10,5), 30 minučių 80 ^oC temperatūroje. CoFeP/Cu katalizatorius buvo pagamintas identiškomis eksperimentinėmis sąlygomis, į nusodinimo vonią įdedant 0,01 M $FeSO_4$. Nusodinimo sąlygos buvo nustatytos preliminariame optimizavimo eksperimente, keičiant vonios sudėtį, pH, temperatūrą ir nusodinimo trukmę, siekiant gauti vienodas ir gerai sukibusias CoP ir CoFeP dangas ant Cu pagrindo. Gauti elektrodai buvo kruopščiai nuplauti dejonizuotu vandeniu ir išdžiovinti kambario temperatūroje.

Vėliau, naudojant galvaninio pakeitimo metodą, platinos (Pt) nanodalelės buvo nusodintos ant paruoštų CoP/Cu ir CoFeP/Cu elektrodų paviršiaus. CoP/Cu ir CoFeP/Cu elektrodai buvo panardinti į 1 mmol L^{-1} H_2PtCl_6 tirpalą, kurio temperatūra buvo 45 °C, ir palikti 1 minutę. Pt nusodinimo sąlygos buvo parinktos remiantis preliminariais eksperimentais, kurių tikslas buvo nustatyti optimalias sąlygas paviršiaus modifikavimui kontroliuoti, nepažeidžiant po

juo esančių CoP ir CoFeP dangų. Po to mėginiai buvo kruopščiai nuplauti dejonizuotu vandeniu ir išdžiovinti kambario temperatūroje prieš atliekant tolesnius charakterizavimo ir elektrocheminius tyrimus.

2.5. Suformuotų katalizatorių charakterizavimas

Co-P_x/Cu katalizatorių paviršiaus morfologijai ir elementų pasiskirstymui tirti buvo naudojamas skenuojamasis elektronų mikroskopas TM4000Plus su AZetecOne detektoriumi (Hitachi, Tokijas, Japonija). CoP, CoFeP, PdCoP/Cu, PdCoFeP/Cu, PtCoP/Cu ir PtCoFeP/Cu katalizatorių paviršiaus morfologijai stebėti taip pat buvo naudojamas skenuojamasis elektronų mikroskopas FE-SEM-FIB HELIOS NanoLab 650 (FEI) su rentgeno spindulių energijų spektrometru (Oxford Instruments).

Rentgeno difrakcijos rentgenogramos buvo užregistruotos, naudojant rentgeno spindulių difraktometrą D2 Phaser su CuKα spinduliuote (Bruker, Karlsruhe, Vokietija). Buvo naudojamas žingsninio skleidimo režimas 2θ intervale nuo 10° iki 100°, žingsnio ilgis – $0{,}04^o$, o skaičiavimo trukmė – 1 s per žingsnį. XRD matavimams atlikti CoP, CoFeP, PdCoP ir PdCoFeP katalizatoriai buvo užnešti ant stiklo paviršiaus.

2.6. Elektrocheminiai matavimai

Paruoštų katalizatorių elektrokatalizinis aktyvumas HER ir OER reakcijoms buvo įvertintas, taikant linijinio skleidimo voltamperometriją (LSV). Tyrimas buvo atliktas, naudojant potenciostatą/galvanostatą PGSTAT100 (Metrohm Autolab B. V., Utrechtas, Nyderlandai) su standartine trijų elektrodų elektrochemine cele. Kaip darbiniai elektrodai buvo naudojami pagaminti katalizatoriai, kurių geometrinis plotas buvo 2 cm^2. Pagalbiniu elektrodu naudota Pt skarda, o palyginamuoju – Ag/AgCl (3 M KCl) elektrodas. Visos šiame tyrime pateiktos elektrodo potencialo vertės buvo perskaičiuotos į grįžtamojo vandenilio elektrodo (RHE) skalę pagal šią lygtį:

$$E_{\mathrm{RHE}} = E_{\text{išmatuotas}} + 0{,}059 \cdot \mathrm{pH} + E_{\mathrm{Ag/AgCl\ (3\ M\ KCl)}} \qquad (1)$$

kur $E_{\mathrm{Ag/AgCl\ (3\ M\ KCl)}} = 0{,}210$ V. Co-P_x/Cu kataliztorių atveju visi matuoti potencialai buvo pakoreguoti pagal formulę $E_{\mathrm{corr}} = E_{\mathrm{RHE}} - iR$, kur R buvo nustatyta, naudojant elektrocheminės impedanso spektroskopijos (EIS) metodą.

Linijinio skleidimo voltamogramos (LSVs) buvo registruojamos N_2 prisotintame 1 M KOH tirpale, HER atveju matuojant atitinkamai nuo atviros grandinės potencialo (OCP) iki maždaug −0,432 V ar −0,5 V (RHE), o OER

atveju – nuo OCP iki maždaug 1,840 V ar 2,1 V (RHE), esant 2 ar 5 mV s^{-1} skleidimo greičiui, jei nenurodyta kitaip.

Siekiant įvertinti pagamintų katalizatorių ilgalaikį stabilumą, buvo registruojamos chronoamperometrinės kreivės ant tiriamų katalizatorių 1,0 M KOH tirpale, esant pastoviam −0,26 V potencialui 10 val. ar 15 val. Pagreitintos degradacijos stabilumo eksperimentai (ADT) buvo atlikti, užrašant 1000 ciklų, esant 400 mV s^{-1} skleidimo greičiui, o po to buvo užregistruota poliarizacijos kreivė, esant 2 mV s^{-1} greičiui ir palyginta su pradine kreive.

Šiame darbe pateiktos HER ir OER srovės tankio vertės buvo perskaičiuotos pagal katalizatorių geometrinį plotą, jei nenurodyta kitaip. Tafelio nuolydžiai buvo apskaičiuoti pagal šią lygtį (2) [115]:

$$\eta = b \cdot \log j/j_0 \quad (2)$$

kur η – elektrodo viršįtampis (V arba mV); b – Tafelio nuolydis; j – eksperimentinis srovės tankis (mA cm^{-2}), o j_0 – mainų srovės tankis. η ir log j priklausomybės grafikas atspindi Tafelio nuolydį. HER procesas šarminėse terpėse susideda iš trijų pagrindinių etapų, kaip parodyta lygtyse (3)–(5) [115]:

$$* + H_2O + e^- \leftrightarrow {}^*H_{ads} + OH^- \text{ (Volmer step, 120 mV dec}^{-1}\text{)} \quad (3)$$

$${}^*H_{ads} + e^- + H_2O \leftrightarrow H_2 + OH^- + * \text{ (Heyrovsky step, 40 mV dec}^{-1}\text{)} \quad (4)$$

$$2\ {}^*H_{ads} \leftrightarrow H_2 + * \text{ (Tafel step, 30 mV dec}^{-1}\text{)} \quad (5)$$

H_{ads} žymi prie metalinių vietų adsorbuotą H_2, kur * žymi metalines vietas. Siekiant įvertinti katalizatorių ECSA, buvo nustatyta dvigubo sluoksnio talpa (C_{dl}), užrašant CV kreives nefaradėjiniame potencialų intervale, esant įvairiems skleidimo greičiams. Buvo atidedamos priklausomybės anodinės ir katodinės srovės skirtumo verčių nuo skleidimo greičio [116–118]. Remiantis CV kreivėmis, elektrodų įkrovimo srovė I_c, gauta esant skirtingiems skleidimo greičiams, buvo nustatyta pagal lygtį (6):

$$I_c\ [A] = (I_{anodic} - I_{cathodic})_{OCP.} \quad (6)$$

C_{dl} vertės buvo įvertintos, nubraižant įkrovimo srovės priklausomybę nuo skleidimo greičio bei apskaičiuojant nuolydį pagal lygtį (7):

$$\text{Nuolydis} = C_{dl}\ [\text{F}] = \Delta I_C\ [\text{A}]/\Delta\nu\ [\text{V s}^{-1}]. \quad (7)$$

Tada ECSA vertės buvo apskaičiuotos naudojant savitąją talpą (C_s) 40 μF cm^{-2} [116–118] ir lygtį (8):

$$\text{ECSA}\ [\text{cm}^2] = C_{dl}\ [\mu\text{F}]/C_s\ [\mu\text{F cm}^{-2}]. \quad (8)$$

Buvo sukonstruotas vandens elektrolizeris, naudojant du vienodus paruoštus elektrodus kaip anodą ir katodą. Elektrolizerio energijos naudingumas buvo apskaičiuotas pagal šią lygtį (9):

$$\eta_{\text{electrolizerio}} = E_{th}/V_{e\ \text{at}\ j}, \quad (9)$$

kur E_{th} = 1,23 V; V_e yra įėjimo įtampa, reikalinga elektrolizei vykdyti prie tiriamos srovės tankio (j) vertės. Šiame tyrime apskaičiuotas energijos efektyvumas buvo gautas, esant j = 10 mA cm^{-2}. Be to, vandens skilimo (OWS) procesas buvo tiriamas, naudojant elektrolizerio prototipą ir integruojant jame PtCoP/Cu ir PtCoFeP/Cu elektrokatalizatorius anodu ir katodu. Elektrolizerio našumas buvo tiriamas 1,0 M KOH tirpale 25–75 ºC temperatūrų intervale, atitinkančiame pramonines eksploatavimo sąlygas, siekiant įvertinti temperatūros poveikį elektrolizerio elektrocheminiam našumui.

Apyvartos dažnio (TOF) vertė buvo apskaičiuota naudojant šią lygtį (10) [119]:

$$\text{TOF} = j \times \text{A/m} \times \text{F} \times \text{n}, \quad (10)$$

kur j – srovės tankis, esant 400 ir 120 mV viršįtampio potencialams atitinkamai OER ir HER procesams; A – elektrodo geometrinis paviršiaus plotas; F – Faradėjaus konstanta (96 485 C mol^{-1}); m –elektronų skaičius, kuris OER atveju yra 4, o HER atveju – 2, o n – visų metalų jonų molių skaičius, apskaičiuotas pagal ICP-OES rezultatus.

Siekiant nustatyti E_a, iš užrašytų LSV kreivių buvo išskirtos srovės vertės, gautos skirtingose temperatūrose ir esant −0,40 V (RHE) potencialui HER atveju ir 1,8 V (RHE) potencialui OER atveju. Duomenys buvo pavaizduoti grafike kaip log(i) priklausomybė nuo 1/T. Tiesės nuolydis yra lygus $-E_a$/2,3R. E_a buvo apskaičiuota, naudojant šios tiesės nuolydį pagal lygtį (11):

$$\partial \log i/\partial(1/\text{T}) = -E_a/2.3\text{R} \quad (11)$$

kur i – srovė (mA), T – temperatūra (K), o R – dujų konstanta (8,314 J mol^{-1} K^{-1}) [120].

Elektrocheminės impedanso spektroskopijos (EIS) spektrai buvo gauti, naudojant Zahner Zennium potenciostatą 10 kHz–50 mHz dažnių diapazone, esant 10 mV trikdžio amplitudei. Matavimai buvo atliekami potenciostatiškai, esant −0,2 V (RHE) 1 M KOH tirpale, naudojant tą pačią trijų elektrodų celę. Dvigubo sluoksnio talpos ir krūvio perdavimo varžos vertės buvo apskaičiuotos, taikant ekvivalentinės grandinės modelį.

3. REZULTATAI IR APTARIMAS

3.1. Co-P_x/Cu katalizatorių sintezė ir charakterizavimas

3.1.1. Co-P_x dangų, mikrostruktūros ir morfologijos tyrimai.

Dangų paviršiaus morfologija buvo tirta, naudojant skenuojančią elektronų mikroskopiją (SEM). 1 paveiksle pateikti paruoštų Co-P_x katalizatorių su skirtingu P kiekiu SEM vaizdai (a–e). Pastebėta, kad Co-P_x paviršiaus morfologija yra kompaktiška, lygi ir be įtrūkimų, o Co dalelės atrodo tolygiai pasiskirsčiusios. 1c paveiksle pateiktuose Co-P_x katalizatorių vaizduose iš viršaus matoma tipiška sferinė morfologija, susidedanti iš mažesnių mazgelių.

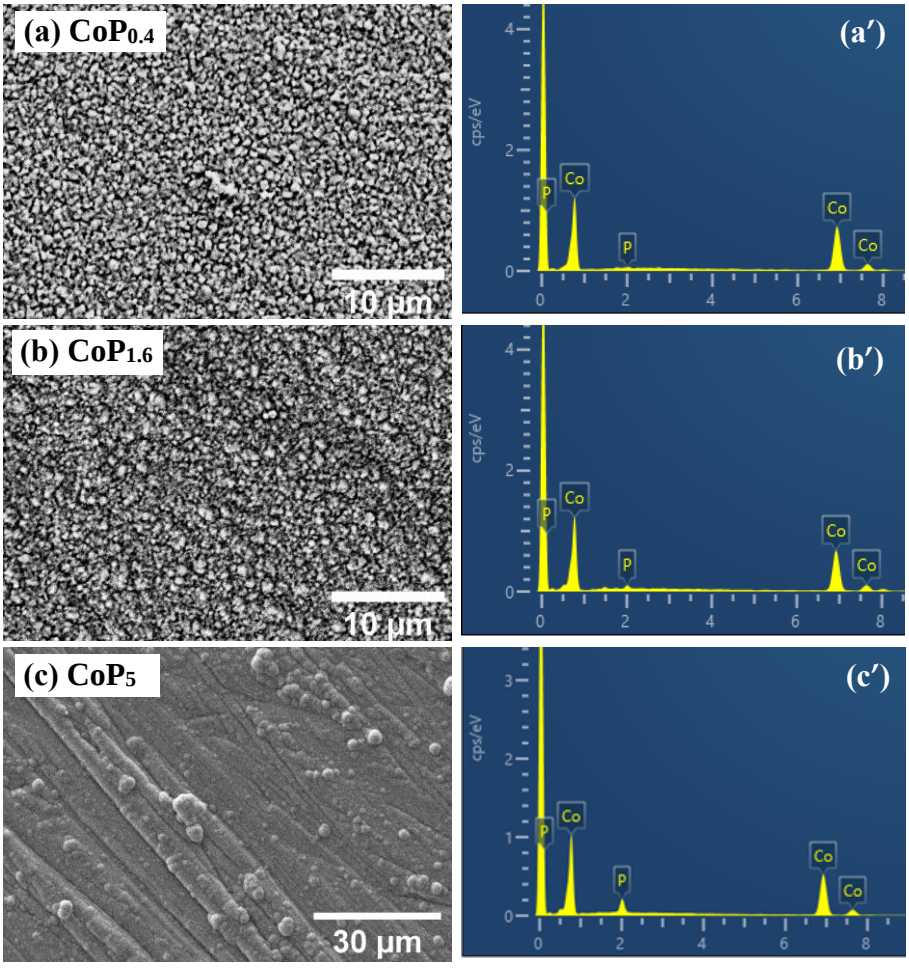

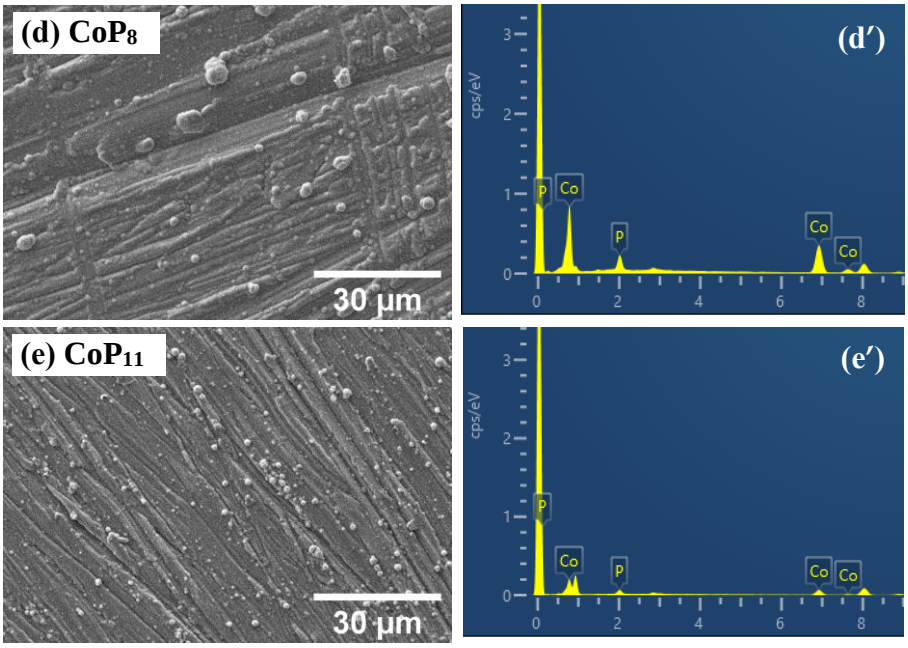

1 pav. SEM vaizdai Co-P_x dangų, kurių P kiekis sudaro 0,4 (a), 1,6 (b), 5 (c), 8 (d) ir 11 (e) masės proc., nusodintų ant Cu paviršiaus. (a′–e′) Atitinkami EDX spektrai.

Didėjant P koncentracijai katalizatoriuje, buvo pastebėtas mazgelių struktūrų susidarymas, padengiantis Cu pagrindo paviršių (1c, d paveikslai). Nusodintų dangų ant Cu pagrindo paviršiaus elementinė sudėtis buvo nustatyta, atliekant EDX analizę, o jos rezultatai pateikiami 1 lentelėje.

1 lentelė. CoP_x dangų, nusodintų ant Cu paviršiaus, sudėtis, nustatyta naudojant EDX analizę.

Pavyzdys	Elementas, masės%	
	Co	P
$CoP_{0.4}$/Cu	99,62	0,38
$CoP_{1.6}$/Cu	98,45	1,55
CoP_5/Cu	95,13	4,87
CoP_8/Cu	92,02	7,98
CoP_{11}/Cu	88,87	11,13

Visų mėginių atitinkami EDX spektrai patvirtina, kad dangose yra Co ir P. Matyti, kad pagamintų Co-P_x/Cu elektrokatalizatorių Co kiekis sudarė maždaug 99,62–88,87 masės proc., o P kiekis – maždaug 0,38–11,13 masės

proc. P kiekis pagamintuose katalizatoriuose palaipsniui didėjo, didėjant NaH_2PO_2 koncentracijai dengimo vonioje nuo 0,25 M iki 4,5 M.

3.1.2. Elektrokatalizinis aktyvumas Co-P_x/Cu HER atžvilgiu

Paruoštų Co-P_x/Cu katalizatorių elektrokatalizinės savybės buvo tiriamos, registruojant LSV kreives 1,0 M KOH tirpale, esant 2 mV s^{-1} potencialo skleidimo greičiui kambario temperatūroje (2 pav.). 2 lentelėje pateikiami apibendrinti Co-P_x/Cu katalizatorių HER duomenys. Kaip matyti iš 2a paveikslo, katalizatoriaus aktyvumas HER procese priklauso nuo katalizatoriaus P kiekio. Co-P danga, kurioje buvo didžiausias P kiekis – 11 masės proc., HER procese parodė mažiausią viršįtampio (η) potencialo vertę – 98,9 mV, pasiekdama 10 mA cm^{-2} srovės tankį, palyginti su Co-P dangomis, kurių P kiekis buvo 8 masės proc. (107,6 mV), 5 mas. % (165,9 mV), 1,6 mas. % (218,2 mV) ir 0,4 mas. % (253,9 mV) P (2c pav.). Paruoštų katalizatorių reakcijos kinetiką ir mechanizmą galima įvertinti, remiantis Tafelio nuolydžiais. Iš η priklausomybės nuo log(j) gauti Tafelio nuolydžiai pateikti 2d pav. Apskaičiuoti Tafelio nuolydžiai svyravo nuo maždaug 29,4 iki 50,3 mV dec^{-1}, o tai rodo, kad HER gali vykti pagal Volmerio–Heyrovskio mechanizmą, kurio metu vandens molekulės arba H_2 adsorbuojasi ant elektrodo, sukurdamos MH_{ads} junginius.

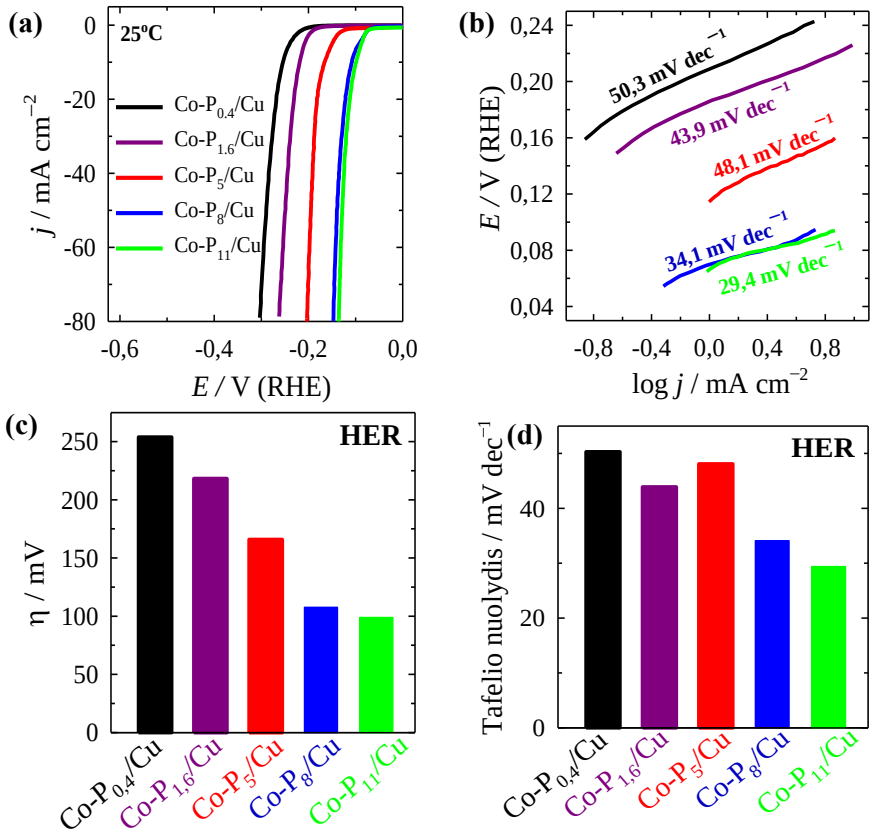

2 pav. (a) Co-P_x/Cu katalizatorių HER poliarizacijos kreivės (koreguotos pagal *i*R) N_2 prisotintame 1 M KOH tirpale, esant 2 mV s^{-1} potencialo skleidimo greičiui. (b) Atitinkami Tafelio nuolydžiai. Stulpelinės diagramos, atspindinčios atitinkamus viršįtampius, esant –10 mA cm^{-2} (c) ir Tafelio nuolydžius (d).

2 lentelė. Apibendrinti Co-P_x/Cu katalizatorių HER parametrai šarminėje terpėje.

Pavyzdys	**$E_{pradžios}$, V, kai j = -1 mA cm^{-2}**	**η_{10} *, mV**	**Tafelio nuolydis, mV dec^{-1}**
Co-$P_{0,4}$/Cu	-0,210	253,9	50,3
Co-$P_{1,6}$/Cu	-0,186	218,2	43,9
Co-P_5/Cu	-0,114	165,9	48,1
Co-P_8/Cu	-0,071	107,6	34,1
Co-P_{11}/Cu	-0,067	98,9	29,4

* Viršįtampio potencialas, esant –10 mA cm^{-2}.

3.1.3. Elektrokatalizinis aktyvumas Co-P_x/Cu OER atžvilgiu

Taip pat buvo įvertintas Co-P_x/Cu katalizatorių aktyvumas OER procese. Gauti duomenys pateikiami 3 paveiksle ir 4 lentelėje.

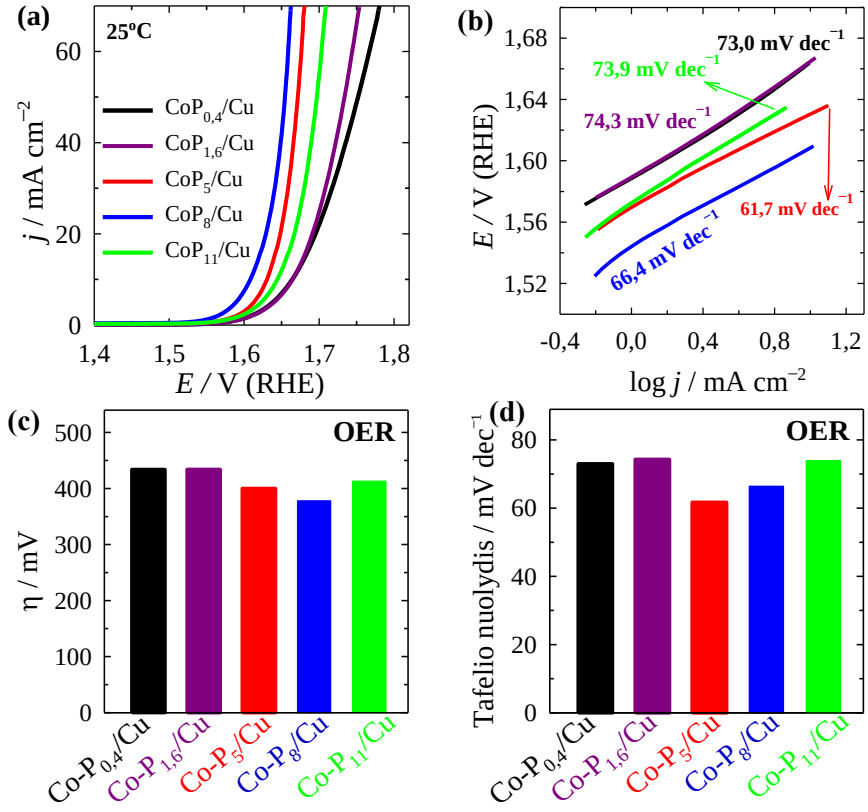

3 pav. (a) Co-P_x/Cu katalizatoriaus OER poliarizacijos kreivės (koreguotos pagal iR) N_2 prisotintame 1 M KOH tirpale, esant 2 mV s^{-1} potencialo skleidimo greičiui. (b) Atitinkami Tafelio nuolydžiai. Stulpelinės diagramos, atspindinčios atitinkamus viršįtampio potencialus, esant 10 mA cm^{-2} (c) ir Tafelio nuolydžius (d).

Kaip matyti iš LSV kreivių, užregistruotų ant Co-P_x/Cu katalizatorių su skirtingu P kiekiu 1 M KOH tirpale, esant srovės tankiui 10 mA cm^{-2}, mažiausias OER viršįtampio potencialas (378 mV) buvo užfiksuotas Co-P_x dangai, kurios sudėtyje buvo 8 masės % P, lyginant su Co-P dangomis, kuriose P kiekis buvo 0,4 masės proc. (434 mV), 1,6 masės proc. (434 mV), 5 masės proc. (400 mV) ir 11 masės proc. (413 mV).

4 lentelė. Co-P_x/Cu katalizatorių elektrocheminės savybės, taikant juos OER šarminėje terpėje.

Pavyzdys	$E_{pradžios}$, V, kai j = 1 mA cm^{-2}	$\eta_{pradžios}$, mV	E, V, kai j = 10 mA cm^{-2}	η_{10} *, mV	Tafelio nuolydis, mV dec^{-1}
Co-$P_{0,4}$/Cu	1,590	360	1,664	434	73,0
Co-$P_{1,6}$/Cu	1,589	359	1,664	434	74,3
Co-P_5/Cu	1,569	339	1,630	400	61,7
Co-P_8/Cu	1,544	314	1,608	378	66,4
Co-P_{11}/Cu	1,574	344	1,643	413	73,9

* Viršįtampio potencialas, esant 10 mA cm^{-2}.

Palyginti su kai kuriais anksčiau aprašytais Co-P pagrindu pagamintais ir pažangiausiais tauriųjų metalų katalizatoriais, esant 10 mA cm^{-2} srovės tankiui, Co-P_8/Cu viršįtampio potencialas yra mažesnis nei daugumos kitų katalizatorių (5 lentelė). Tai rodo, kad OER aktyvumui egzistuoja optimalus P kiekis. Co-P/Cu katalizatorių Tafelio nuolydis svyravo nuo 61,7 iki 73,9 mV dec^{-1}, o tai rodo puikią OER kinetiką (4 lentelė). Šie rezultatai rodo, kad Co-P_x/Cu katalizatoriai, kuriuose yra didesnis P kiekis (8 ir 11 % masės), leidžia vienu metu padidinti tiek HER, tiek OER aktyvumą, todėl šie katalizatoriai turi potencialą tapti labai efektyviais bendro vandens skilimo katalizatoriais.

3.1.4. Elektrochemiškai aktyvaus paviršiaus ploto nustatymas

Co-P_x/Cu katalizatorių, kurių P kiekis sudarė 5, 8 ir 11 % masės, elektrochemiškai aktyvūs paviršiaus plotai (ECSA) buvo nustatyti, remiantis elektrocheminės dvigubo sluoksnio talpos (C_{dl}) matavimais. CV kreivės buvo registruojamos, esant skirtingiems elektrodo potencialo skleidimo greičiams nefaradėjinėje potencialų srityje (4a–c pav.). Po to buvo apskaičiuotas kreivės nuolydis, nubrėžus anodinės ir katodinės srovės skirtumo priklausomybę nuo skleidimo greičio (4d pav.).

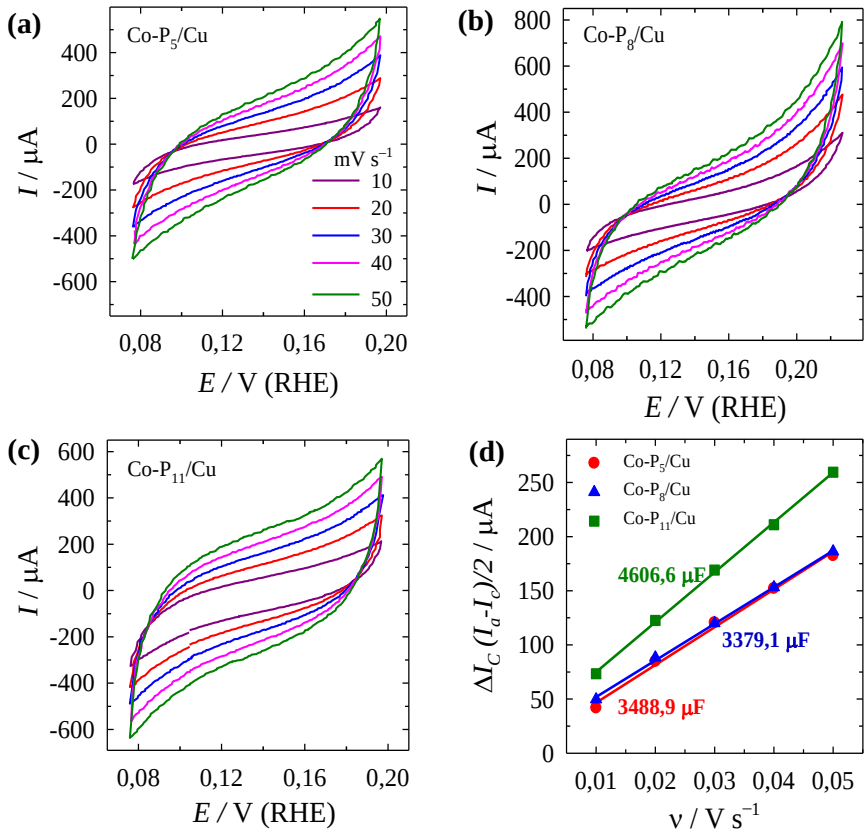

4 pav. (a) Co-P_5/Cu, (b) Co-P_8/Cu ir (c) Co-P_{11}/Cu CV kreivės N_2 prisotintame 1 M KOH tirpale nefaradėjinėje potencialo verčių srityje, esant skirtingiems skleidimo greičiams. (d) Įkrovimo srovės priklausomybė nuo skleidimo greičio.

Nustatyta, kad C_{dl} vertės buvo 3488,9, 3379,1, ir 4606,6 µF atitinkamai Co-P_5/Cu, Co-P_8/Cu ir Co-P_{11}/Cu katalizatorių atveju (4d pav.), o apskaičiuotos ECSA vertės buvo atitinkamai 87,2, 84,5 ir 115,6 cm^2 atitinkamai Co-P_5/Cu, Co-P_8/Cu ir Co-P_{11}/Cu katalizatorių atveju. Tai, kad Co-P_{11}/Cu ECSA vertė yra didesnė nei Co-P_8/Cu ir Co-P_5/Cu, lemia didesnį aktyviųjų vietų skaičių, kuris prisideda prie didesnio katalizatoriaus elektrokatalizinio aktyvumo HER. Pažymėtina, kad katalizatorius su 11 % masės P nepasiekė mažiausio OER viršįtampio potencialo, o tai rodo, kad OER charakteristikas lemia ne tik aktyviųjų vietų skaičius. Kiti veiksniai, tokie kaip elektroninė struktūra ir laidumas, taip pat turi įtakos katalizatoriaus efektyviam veikimui. Šiuo atveju katalizatorius su 8 % masės P pasirodė geriausiai OER atžvilgiu, nors jo ECSA buvo mažesnis nei katalizatoriaus su 11 % masės P. Be to, Co-P_{11}/Cu

katalizatorius buvo tiriamas, taikant pagreitintos degradacijos stabilumo eksperimentą (ADT), užregistruojant 1000 ciklų, esant didesniam skleidimo greičiui (400 mV s^{-1}) N_2 prisotintame 1 M KOH tirpale. 5 paveikslo įterptiniame grafike pateikta pradinė LSV kreivė ir LSV kreivė po 1000 ciklų, užregistruota, esant 2 mV s^{-1} greičiui. Po 1000 ciklų, esant 10 mA cm^{-2} srovės tankiui, buvo pastebėtas nežymus aktyvumo sumažėjimas, o tai rodo aukštą katalizatoriaus stabilumą HER procesui (19 paveikslo įterptinis grafikas). Be to, SEM vaizdai rodo, kad paviršiaus morfologija išlieka nepakitusi; po ADT katalizatorius neatsiskiria nuo pagrindo, kas rodo gerą sukibimą (5 pav.). Be to, po ADT matavimų chronoamperometrinė kreivė buvo registruojama, esant pastoviam –0,26 V potencialui 15 val. ant Co-P_{11}/Cu katalizatoriaus (5 pav.).

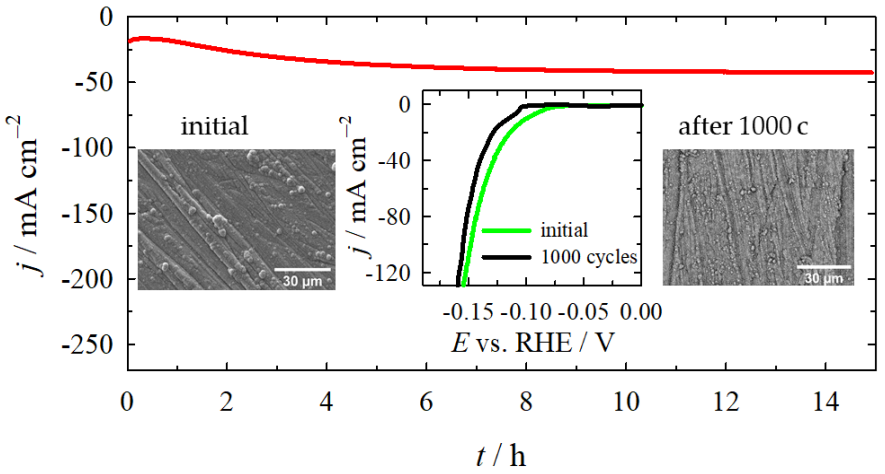

5 pav. Co-P_{11}/Cu katalizatoriaus chronoamperometrinė kreivė N_2 prisotintame 1 M KOH tirpale, esant pastoviam –0,26 V potencialui 15 val. (raudona linija). Įterptiniuose paveikslėliuose pateikta pradinė LSV kreivė ir LSV kreivė po 1000-ojo ciklo, užregistruotos esant 2 mV s^{-1} greičiui, bei atitinkami to paties katalizatoriaus pradinio ir po 1000-ojo ciklo bandymo SEM vaizdai.

Co-P/Cu katalizatorius, kurio sudėtyje yra 11 % masės P, pasižymėjo puikiu stabilumu, o per 15 valandų veikimo srovės tankis padidėjo du kartus. Tai galima priskirti katalizatoriaus struktūros, sudėties ar morfologijos pokyčiams stabilumo bandymo metu. Be to, aktyvumo padidėjimas po stabilumo bandymo gali būti susijęs su kitų aktyviųjų vietų, nei gryno CoP, indėliu. CoP gali transformuotis į aktyvesnes fazes, įskaitant kobalto oksidus, hidroksidus, mišrius metalų fosfatus arba CoP nanodaleles su pasikeitusiomis

paviršiaus būsenomis, kurie yra žinomi aktyvūs OER/HER katalizatoriai. Šios naujos fazės dažnai yra kataliziškai aktyvesnės nei grynasis CoP.

3.1.5. Vandens skaidymo proceso tyrimas, naudojant Co-P_x/Cu katalizatorius

Siekiant patvirtinti Co-P_x/Cu katalizatorių bifunkcinį aktyvumą bendram vandens skilimo procesui, 6a pav. pateiktos išmatuotos katodinės (HER) (2a pav.) ir anodinės (OER) (3a pav.) poliarizacijos kreivės (koreguotos pagal *i*R). Potencialų skirtumas ($\Delta\eta_{10}$) tarp HER ir OER, esant srovės tankiui ±10 mA cm^{-2} (η_{10}OER−η_{10}HER) Co-P/Cu katalizatoriams su 5, 8 ir 11 masės proc. P, parodo prognozuojamas viršįtampio vertes. Iš atitinkamų HER ir OER poliarizacijos kreivių apskaičiuotos viršįtampio potencialo $\Delta\eta_{10}$ vertės yra 1,80 V Co-P_5/Cu atveju, 1,72 V Co-P_8/Cu atveju ir 1,74 V Co-P_{11}/Cu atveju (6a pav.). Gautos vertės rodo, kad šiuos katalizatorius būtų galima pritaikyti praktiniame bendro vandens skilimo (OWS) įrenginyje šarminėje elektrolitinėje terpėje, naudojant tas pačias elektrodų medžiagas tiek anodu, tiek katodu. Bendras katalizinis našumas dviejų elektrodų šarminiame elektrolizeryje, kuriame tiek anodu, tiek katodu naudojami tie patys katalizatoriai – Co-P_5/Cu‖Co-P_5/Cu, Co-P_8/Cu‖Co-P_8/Cu ir Co-P_{11}/Cu‖Co-P_{11}/Cu – pateiktas 6b paveiksle. Integruoti Co-P_5/Cu, Co-P_8/Cu ir Co-P_{11}/Cu elektrodai rodo atitinkamai 1,836 V, 1,822 V ir 1,813 V elektrolizerių įtampas, esant 10 mA cm^{-2} (6b pav.).

Apskaičiuotas Co-P_5/Cu, Co-P_8/Cu ir Co-P_{11}/Cu elektrolizerių energijos efektyvumas yra atitinkamai 66,49 %, 67,03 % ir 67,29 %. Atrodo, kad gauti katalizatoriai yra tinkami kandidatai jų panaudojimui vandens elektrolizei.

Apyvartos dažnis (TOF) yra svarbus rodiklis, leidžiantis nustatyti katalizatorių savitąjį aktyvumą. Jis buvo apskaičiuotas, siekiant įvertinti paruoštų Co-P/Cu katalizatorių savitąjį HER ir OER našumą, esant atitinkamai 120 ir 400 mV viršįtampio potencialui. Nustatyta, kad Co-P_8/Cu katalizatoriaus TOF vertė, esant 400 mV viršįtampio potencialui, buvo 12,08 s^{-1}, o tai žymiai pranoko Co-P_{11}/Cu (2,99 s^{-1}), Co-P_5/Cu (1,91 s^{-1}), Co-$P_{1,6}$/Cu (0,83 s^{-1}) ir Co-$P_{0,4}$/Cu (0,29 s^{-1}). Tai patvirtina šio katalizatoriaus efektyvumą OER. Apskaičiuotos TOF vertės HER rodo, kad didžiausios vertės buvo gautos Co-P/Cu katalizatoriams, turintiems didesnį P kiekį – 8 ir 11 % masės.

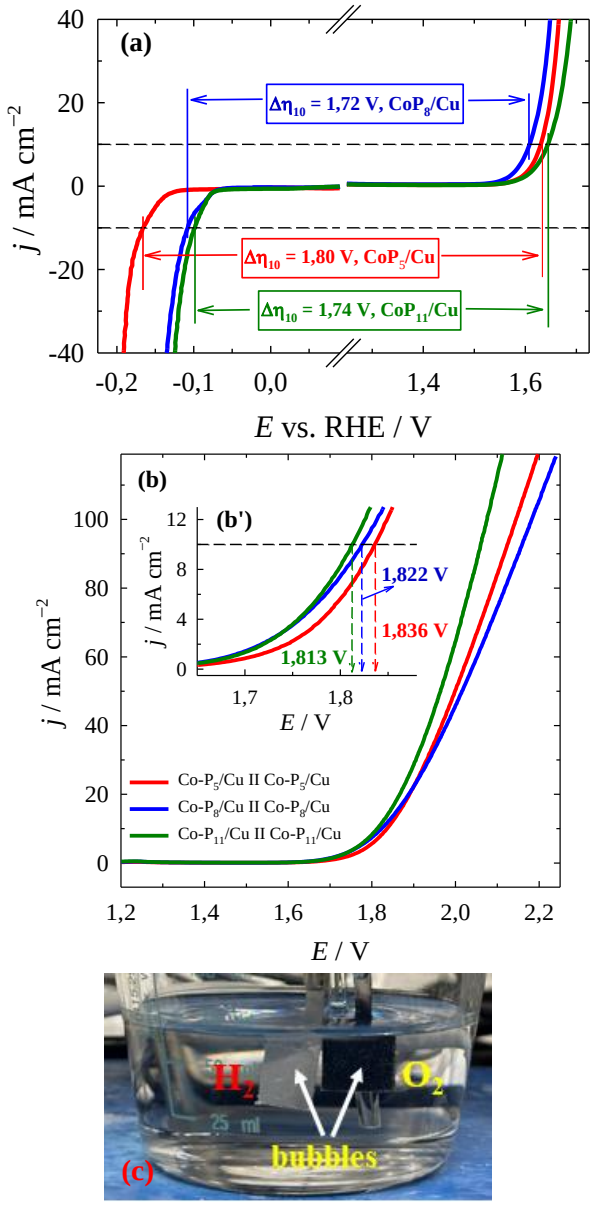

6 pav. (a) Prognozuojamas Co-P/Cu katalizatorių bifunkcinis aktyvumas: viršįtampio potencialo $\Delta\eta_{10}$ vertės, apskaičiuotos pagal viršįtampio verčių (η_{10}) skirtumą esant ±10 mA cm^{-2}, gautas iš atitinkamų HER ir OER LSV kreivių, pateiktų 2a ir 3a pav. (b) Įvairių Co-P_x/Cu katalizatorių LSV kreivės, naudojant juos kaip anodo ir katodo elektrokatalizatorius vandens skilimui 1 M KOH tirpale; įterptiniame paveiksle (b') pateiktos atitinkamos LSV kreivės esant mažesniems srovės tankiams. (c) OWS proceso nuotrauka, kurioje Co-P_x/Cu naudojamas kaip katodas ir anodas.

Co-P_8/Cu katalizatoriaus TOF vertė, esant 120 mV viršįtampio potencialui, buvo 56,61 s^{-1}, po jo sekė Co-P_{11}/Cu (19,16 s^{-1}), Co-P_5/Cu (13,38 s^{-1}), Co-$P_{1,6}$/Cu (5,83 s^{-1}), ir Co-$P_{0,4}$/Cu (1,86 s^{-1}).

3.2. PdCoP/Cu ir PdCoFeP/Cu katalizatorių sintezė ir charakterizavimas

3.2.1. Nemodifikuotų ir Pd-modifikuotų CoP ir CoFeP dangų, mikrostruktūros ir morfologijos tyrimai

Siekiant ištirti dangų paviršiaus morfologiją ir sudėtį, buvo panaudota skenuojamoji elektronų mikroskopija (SEM) ir energijos dispersinė rentgeno analizė (EDX). 7 paveiksle pateikti pagamintų Co pagrindu pagamintų dangų, turinčių skirtingą sudėtį, pvz., CoP (a), CoFeP (b), PdCoP (c) ir PdCoFeP (d), SEM vaizdai. Pd, Co, Fe ir P buvimas dangose patvirtintas atitinkamais visų mėginių EDX spektrais. EDX rezultatai pateikti 5 lentelėje, iš kurios matyti, kad pagamintų CoP, CoFeP, PdCoP ir PdCoFeP elektrokatalizatorių Pd kiekis svyruoja nuo 3,54 iki 8,36 at%, Co kiekis – nuo 64,08 iki 90,22 at%, Fe kiekis – nuo 9,96 iki 12,49 at%, o P kiekis – nuo 6,26 iki 15,07 at%.

5 lentelė. EDX analize nustatyta CoP, CoFeP, PdCoP ir PdCoFeP dangų, nusodintų ant Cu paviršiaus, sudėtis.

Pavyzdys	**Elementas, at%**			
	Pd	**Co**	**Fe**	**P**
CoP	–	90,22	–	9,78
CoFeP	–	83,78	9,96	6,26
PdCoP	3,54	83,72	–	12,74
PdCoFeP	8,36	64,08	12,49	15,07

SEM analizė rodo aiškius morfologinius skirtumus, kuriuos lemia cheminio nusodinimo dangų sudėties pokyčiai. CoP danga pasižymėjo kompaktiška ir palyginti homogeniška paviršiaus sudėtimi, kuriai būdingi tankiai susikaupusios granulės [74, 75], kas rodo stabilų branduolių susidarymą ir tolygų augimą (7a pav.). Verta paminėti, kad Fe įtraukimas į CoFeP struktūrą sukelia reikšmingą struktūrinį pokytį, dėl kurio susidaro akytas ir nevienalytis paviršius [76]. Šis esminis pokytis pabrėžia didelį Fe poveikį branduolių susidarymo kinetikai, paviršiaus energijai ir fosforo įterpimui cheminio nusodinimo metu (7b pav.). Į CoP dangą įterpus Pd, paviršius tampa grubesnis ir labiau suskaidytas.

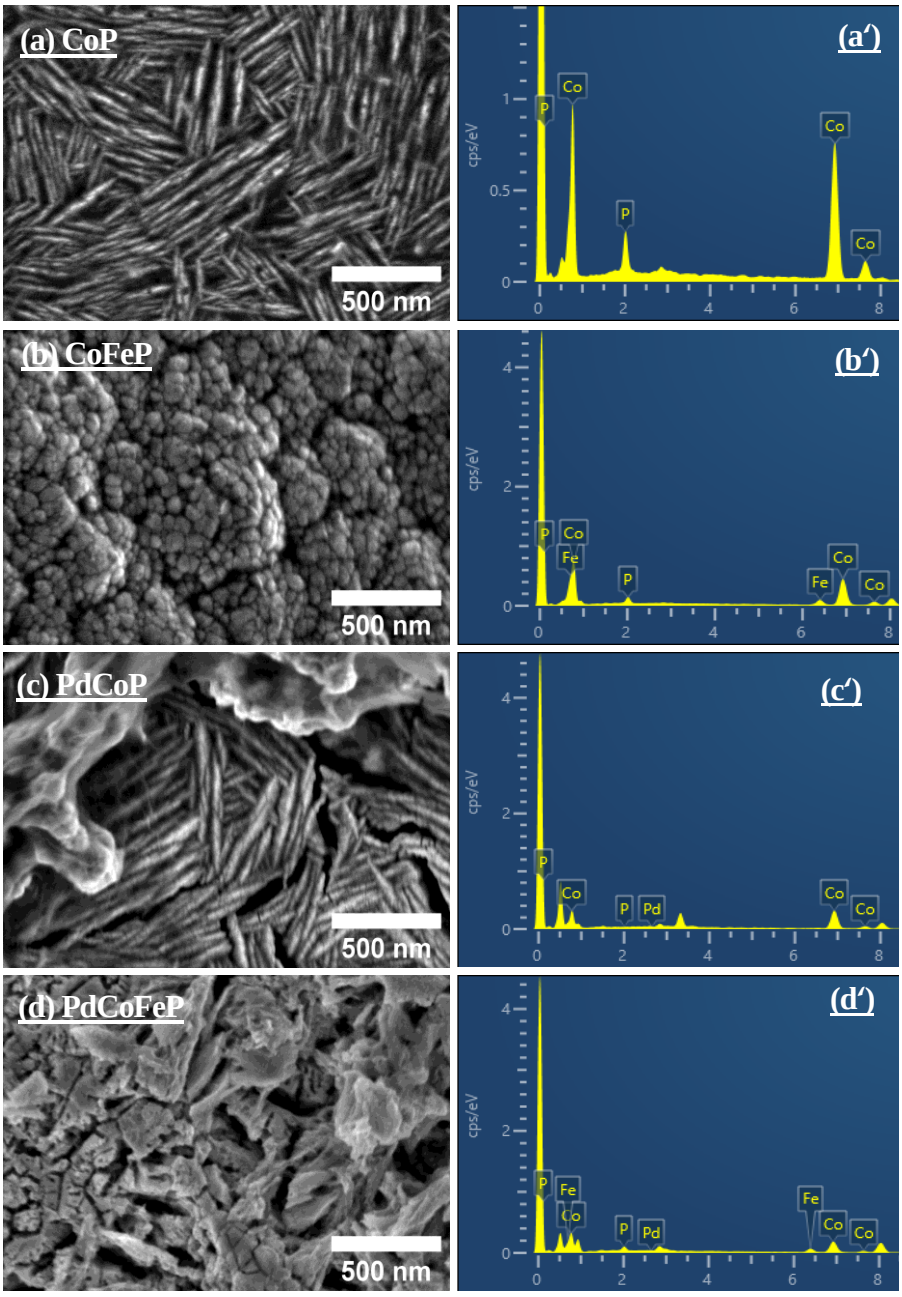

7 pav. SEM vaizdai CoP (a), CoFeP (b), PdCoP (c) ir PdCoFeP (d), nusodintų ant Cu paviršiaus. (a′–d′) EDX spektrai, atitinkantys minėtus SEM vaizdus.

Tai pasireiškia smulkesnių sankaupų buvimu ir padidėjusiu grūdelių ribų skaičiumi, kas rodo padidėjusį branduolių susidarymo tankį. PdCoFeP danga pasižymi labiausiai nereguliariu ir nanostruktūruotu paviršiumi, kuriam būdingos tekstūrinės savybės ir smulkūs kristalitai (7c, d pav.). Tai rodo sinergetinį Pd ir Fe poveikį, skatinantį didelius kristalizacijos greičius ir sudėtingus augimo kelius. Gauti rezultatai rodo, kad cheminio nusodinimo procesai yra ypač jautrūs net menkiausiems sudėties pokyčiams, kurie gali drastiškai pakeisti galutinę mikrostruktūrą.

8a paveiksle pateiktas CoP katalizatoriaus XRD rentgenograma, kurioje išryškėja difrakcinės smailės, susijusios su ortorombiniu CoP ir metaliniu Co.

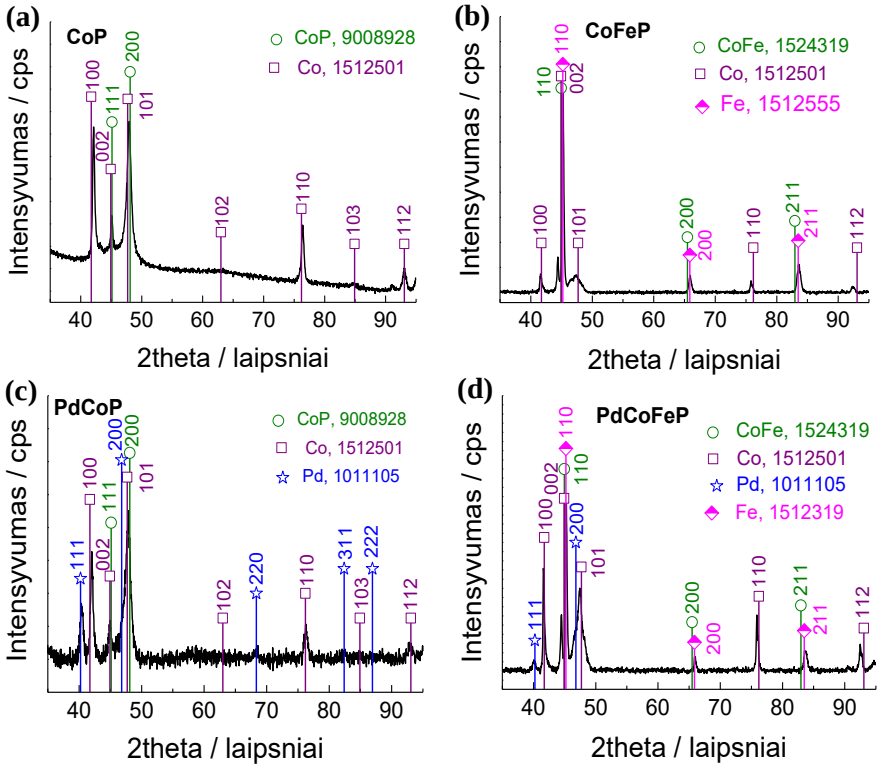

8 pav. XRD rentgenogramos CoP (a), CoFeP (b), PdCoP (c) ir PdCoFeP (d) dangų, nusodintų ant stiklo paviršiaus. Smailių padėtys nurodytos remiantis „Crystallography Open Database (COD)“ duomenų kortelėmis: Co—1512501; CoP—9008928; Fe – 1512319; CoFe – 1524319; Pd – 1011105.

Rentgenogramoje esančios smailės ties maždaug 2θ vertėse 45,1° ir 48,1° yra siejamos su CoP kristalinėmis (021) ir (121) plokštumomis remiantis COD

kortelės Nr. 9008928 duomenimis (a = 5,59900 Å, b = 5,07600 Å, c = 3,28100 Å). 2θ smailės, esančios maždaug ties 41,7°, 44,9°, 47,7°, 62,9°, 76,2°, 84,9° ir 93,1° kampais, atitinka metalinę Co fazę (COD Nr. 1512501, a — 2,49680 Å, b = 2,49680 Å, c = 4,03081 Å), kurią galima susieti atitinkamai su (100), (002), (101), (102), (110), (103) ir (112) kristalinėmis plokštumomis. Įterpus Fe į CoP struktūrą, gauta CoFeP danga rodo difrakcijos smailes, esant 2θ vertėms 44,97°, 65,48° ir 82,96°, atitinkančioms (110), (200), (211) ir (220) kristalines plokštumas (COD 1524319) (8b pav.). Palyginti su grynu CoP, pastebimas nežymus smailių padėčių poslinkis, patvirtinantis sėkmingą Fe atomų įterpimą į CoP gardelę ir CoFeP lydinio tipo struktūros susidarymą. Taip pat aptikti atspindžiai, atitinkantys metalines Co (COD 1512501) ir Fe struktūras (COD 1512555) (8b pav.). Fe įterpimas sukelia gardelės iškraipymą ir keičia kristalinę struktūrą, o tai galėtų padidinti elektroninį laidumą ir katalizinį aktyvumą.

PdCoP atveju (8c pav.) papildomi atspindžiai, stebimi esant 2θ = 40,24°, 46,80°, 68,34°, 82,39° ir 86,93°, atitinka atitinkamai (111), (200), (220), (311) ir (222) kristalografines plokštumas, siejamas su kubine Pd kristaline struktūra (COD 1011105) ir patvirtina paladžio buvimą paviršiuje.

Taip pat aptinkamos smailės, priskiriamos metaliniam Co (COD 1512501). Pd įterpimas iš esmės nekeičia CoP kristalinės struktūros, nes pagrindinės CoP smailės po Pd nusėdimo išlieka nepakitusios. Tačiau, palyginti su grynu CoP, nežymus CoP smailių išsiplėtimas ir intensyvumo sumažėjimas rodo, kad dėl Pd nusėdimo įvyko paviršiaus modifikacija ir galimas gardelės deformavimas. Tiek CoP, tiek Pd smailių buvimas rodo, kad susiformavo bimetalinė heterostruktūra (Pd–CoP), o ne naujas intermetalinis junginys.

8d paveiksle pateikta PdCoFeP XRD rentgenograma, kurioje matomos smailės, atitinkančios CoFe fazę (COD 1524319), metalinį Co (COD 1512501), metalinę Fe (COD 1512555) ir Pd (COD 1011105). Šie rezultatai patvirtina sėkmingą Pd kristalitų nusodinimą ant CoFeP paviršiaus galvaninio pakeitimo būdu, nekeičiant pradinės CoFeP kristalinės struktūros.

Struktūrinė evoliucija nuo CoP iki CoFeP, o vėliau iki PdCoP ir PdCoFeP rodo aiškią kristalinės struktūros ir paviršiaus sudėties raidą. CoP danga pasižymi aiškiai apibrėžtomis smailėmis, atitinkančiomis ortorombinį CoP, o tai rodo aukštą kristališkumą su nedideliu metalinio Co kiekiu. Įvedus Fe, difrakcijos smailės šiek tiek pasislenka ir išplatėja, kas patvirtina sėkmingą Fe įterpimą į CoP gardelę, kuriant CoFeP lydinio tipo struktūrą. Šis Fe pakeitimas sukelia gardelės iškraipymą, galimai padidindamas elektroninį laidumą ir potencialiai sukurdamas daugiau kataliziškai aktyvių vietų. Po Pd nusodinimo galvaninio pakeitimo būdu būdingos CoP arba CoFe smailės išlieka beveik

nepakitusios. Tai rodo, kad Pd įtraukimas nepakeičia pagrindinių CoP arba CoFeP struktūrų. Tačiau atsiranda naujos smailės, priskiriamos kubinei (fcc) Pd struktūrai, patvirtinančios Pd nanodalelių susidarymą ant CoP arba CoFeP paviršių. Eilės tvarka atliekamas modifikavimas CoP → CoFeP → PdCoP → PdCoFeP lemia laipsnišką struktūrinę ir sudėties evoliuciją. Fe lydinys keičia tūrinį kristalinį tinklą, o Pd pridėjimas reguliuoja paviršiaus sudėtį ir sukuria papildomų aktyviųjų vietų. Tikimasi, kad šis sinergetinis struktūrinis reguliavimas pagerins PdCoP ir PdCoFeP kompozicinių katalizatorių elektronines struktūras, paviršiaus reaktyvumą ir katalizinį efektyvumą.

3.2.2. Nemodifikuotų ir Pd-modifikuotų CoP/Cu ir CoFeP/Cu elektrokatalizinis aktyvumas HER atžvilgiu

Paruoštų HER katalizatorių elektrokatalizinės savybės buvo tiriamos registruojant LSVs ant tiriamų katalizatorių 1,0 M KOH tirpale, esant 5 $mV \cdot s^{-1}$ potencialo skleidimo greičiui kambario temperatūroje (9a pav.). Apibendrinti HER parametrai, gauti naudojant tiriamus katalizatorius šarminėje terpėje 25 °C temperatūroje, pateikti 6 lentelėje. Atitinkamos viršįtampio potencialo vertės esant 10, 20, 50 ir 100 mA cm^{-2} srovės tankiui pateiktos 9b paveiksle. Iš tirtų katalizatorių CoP katalizatorius parodė mažiausią HER viršįtampio potencialo vertę – 239 mV, palyginti su CoFeP (245 mV), PdCoP (250 mV) ir PdCoFeP (259 mV), pasiekdamas 10 mA cm^{-2} srovės tankį 25 °C temperatūroje (9a paveikslas ir 6 lentelė). Tačiau PdCoFeP užtikrina didesnį srovės tankį, o tai rodo, kad didesnės apkrovos sąlygomis vandenilis generuojamas efektyviau. Be to, PdCoFeP viršįtampio potencialas esant 100 mV cm^{-2} yra 385 mV, o tai yra mažiau nei PdCoP (420 mV), CoFeP (428 mV) ir CoP (458 mV) atveju (9b pav.).

6 lentelė. HER parametrų apibendrinimas tiriamuose katalizatoriuose šarminėje terpėje.

Pavyzdys	$E_{\text{pradžios}}$ ***, V**	η_{10} ****, mV**	**Tafelio nuolydis, mV dec^{-1}**	E_a, **kJ mol^{-1}**
CoP	0,166	239	78,1	11,3
CoFeP	0,188	245	76,4	6,0
PdCoP	0,171	250	76,3	4,7
PdCoFeP	0,213	259	82,8	11.4

* Potencialas, esant -1 mA cm^{-2},

** Viršįtampio potencialas, esant 10 mA cm^{-2}.

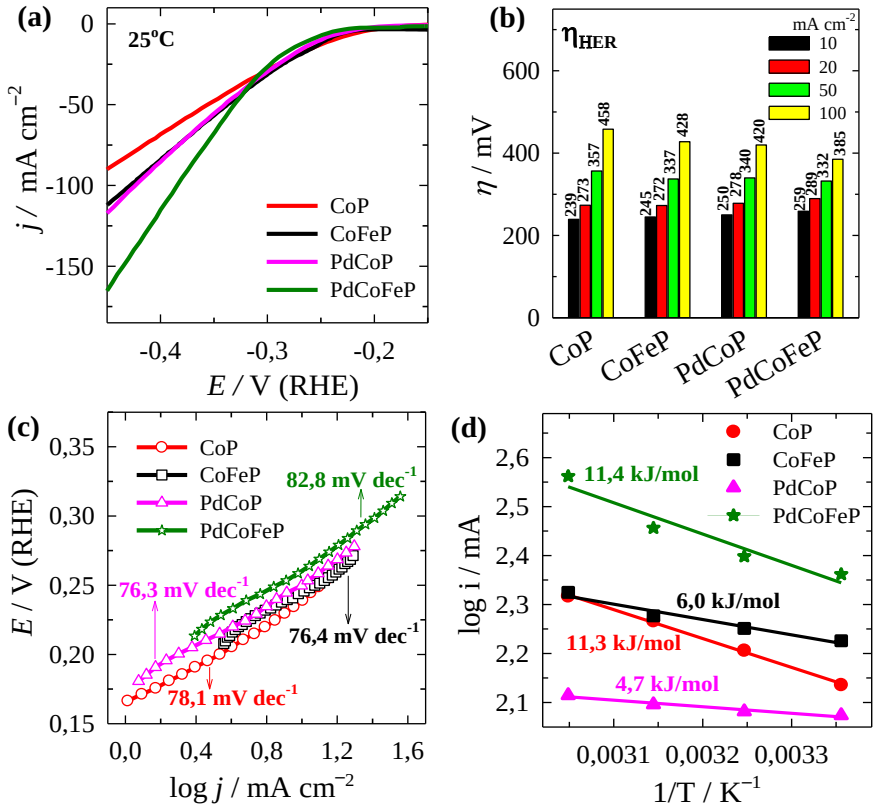

9 pav. (a) HER poliarizacijos kreivės N_2 prisotintame 1 M KOH tirpale, esant 5 mV s^{-1} potencialo skleidimo greičiui ir 25 °C temperatūrai. (b) Stulpelinės diagramos viršįtampio potencialų verčių, esant 10, 20, 50 ir 100 mA cm^{-2} srovės tankiams. (c, d) Atitinkami Tafelio nuolydžiai ir Arrhenius priklausomybės, vaizduojančios log(*i*) priklausomybę nuo 1/T, esant −0,40 V priklausomai nuo RHE kiekvienam katalizatoriui.

Šie patobulinimai priskiriami sinergetinėms Co, Fe, P ir Pd sąveikoms, kurios sustiprina elektronų perdavimą ir palengvina HER kinetiką. 9c paveiksle pateikti kiekvieno katalizatoriaus η ir log(j) priklausomybės grafikai. Apskaičiuoti Tafelio nuolydžiai svyravo nuo maždaug 76 iki 83 mV dec^{-1} (6 lentelė), o CoFeP ir PdCoP katalizatoriai turėjo mažiausią Tafelio nuolydį (maždaug 76 mV dec^{-1}), palyginti su CoP (78,1 mV dec^{-1}) ir PdCoFeP (82,8 mV dec^{-1}) (9c pav.). Šis rezultatas rodo, kad HER gali vykti pagal Volmerio–Heyrovskio mechanizmą, kurio metu vandens molekulės arba H_2 adsorbuojasi ant elektrodo, susidarydamos MH_{ads} junginius.

Aktyvacijos energija (E_a) yra kritinis veiksnys vertinant katalizatoriaus veikimą. Šią energiją galima įvertinti naudojant LSV kreives esant

skirtingoms temperatūroms. Kiekvieno katalizatoriaus HER LSV kreivės, gautos esant 25–55 °C temperatūrai, pateiktos 10 pav. ir 7 lentelėje.

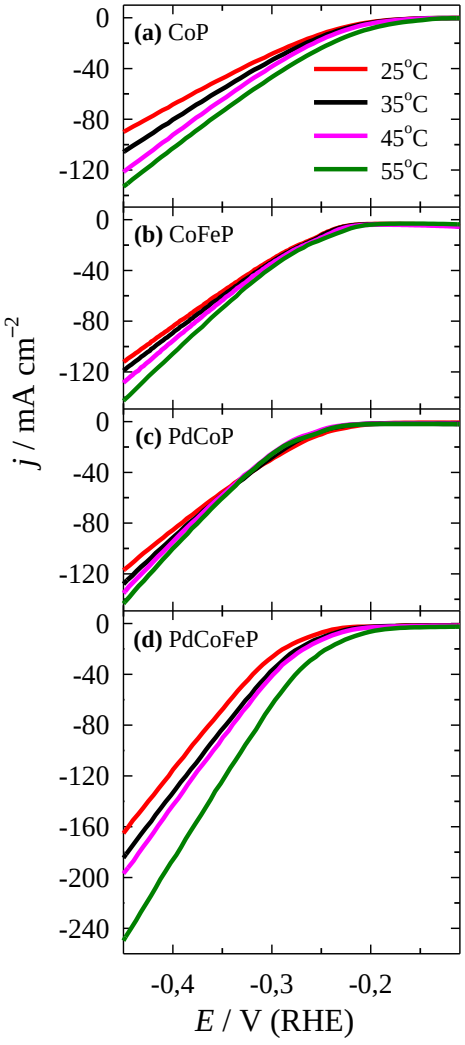

10 pav. HER poliarizacijos kreivės, užregistruotos ant CoP (a), CoFeP (b), PdCoP (c) ir PdCoFeP (d) katalizatorių N_2 prisotintame 1 M KOH tirpale, esant 5 mV s^{-1} potencialo skleidimo greičiui ir temperatūros intervale nuo 25 iki 55 °C.

Gauti rezultatai rodo, kad CoP, CoFeP, PdCoP ir PdCoFeP katalizatorių HER aktyvumas didėja, didėjant elektrolito temperatūrai, o viršįtampiai, reikalingi pasiekti 10 mA cm^{-2} srovės tankį, mažėja didėjant temperatūrai kiekvienam katalizatoriui (7 lentelė).

7 lentelė. HER katalizatorių elektrocheminės savybės šarminėje terpėje.

Pavyzdys	T, °C	$\eta_{\text{pradžios}*}$, mV	η_{10**}, mV	Tafelio nuolydis, mV dec^{-1}
CoP/Cu	25	166,4	239,0	78,1
	35	161,5	232,0	75,5
	45	227,1	227,1	72,8
	55	137,9	206,5	72,2
CoFeP/Cu	25	188,1	244,8	76,4
	35	188,1	243,9	74,7
	45	188,7	238,6	74,0
	55	166,1	231,8	79,2
PdCoP/Cu	25	171,3	249,7	76,3
	35	158,5	258,6	76,7
	45	171,0	260,8	78,4
	55	175,8	256,4	78,9
PdCoFeP/Cu	25	213,4	258,6	82,8
	35	168,2	256,0	82,3
	45	122,1	241,0	85,1
	55	107,5	223,5	93,5

* Vertės, esant 1 mA cm^{-2}, ** Vertės, esant 10 mA cm^{-2}.

Be to, gautos Tafelio nuolydžio vertės svyruoja nuo maždaug 72 iki 94 mV dec^{-1}. Šie rezultatai rodo, kad HER kinetinis procesas yra glaudžiai susijęs su temperatūra. Norint nustatyti E_a, iš LSV profilių buvo išskirtos srovės vertės skirtingose temperatūrose, užregistruotos ant katalizatorių esant −0,40 V (RHE) (10 pav.). Duomenys buvo pavaizduoti grafike kaip log(i) priklausomybė nuo 1/T CoP, CoFeP, PdCoP ir PdCoFeP katalizatoriams ir pateikiami 9d paveiksle. E_a buvo apskaičiuota naudojant kiekvieno katalizatoriaus gautų tiesių linijų nuolydį pagal Arrhenius lygtį [120]. Nustatyta, kad PdCoP, CoFeP, CoP ir PdCoFeP katalizatorių E_a vertės buvo atitinkamai 4,7, 6,0, 11,3 ir 11,4 kJ mol^{-1} (9d pav.). Gautos E_a vertės buvo žymiai mažesnės, palyginti su etalonu Pt/C (20 mas. %) katalizatoriumi, kurio duomenys pateikti taip: etalonas – 16 kJ mol^{-1} [103]; Pd_{100} – 20,86 kJ mol^{-1} [103]; Pd_5Co_{95} – 21,75 kJ mol^{-1} [103]; Pd/C – 31 kJ mol^{-1} [103]; CoO_x – 29,79 kJ mol^{-1} [175]. Mažos aktyvacijos energijos reiškė, kad reakcijai efektyviai vykti reikalingas nedidelis reakcijos kinetinis barjeras. E_a sumažėjimą galima paaiškinti keliais veiksniais, susijusiais su katalizatoriaus sudėtimi, elektronine struktūra ir morfologinėmis savybėmis. Fe įterpimas ir vėlesnis modifikavimas Pd kristalitais sumažina CoP E_a dėl sinergetinių

sąveikų tarp Fe, Co ir Pd. Šios sąveikos yra labai svarbios, nes jos sustiprina elektronų perdavimą ir palengvina HER kinetiką.

EIS spektrai buvo išmatuoti, naudojant PdCoFeP ir CoFeP mėginius, siekiant ištirti Pd modifikacijos įtaką HER aktyvumui. 11 paveiksle pateikti Nyquisto grafikai pasižymi plačiu pusapskritimu, o žemų dažnių srityje (1,5–0,5 Hz) atsiranda nedidelis, bet ryškus indukcinis atsakas, kai Z_{im} vertės tampa teigiamos.

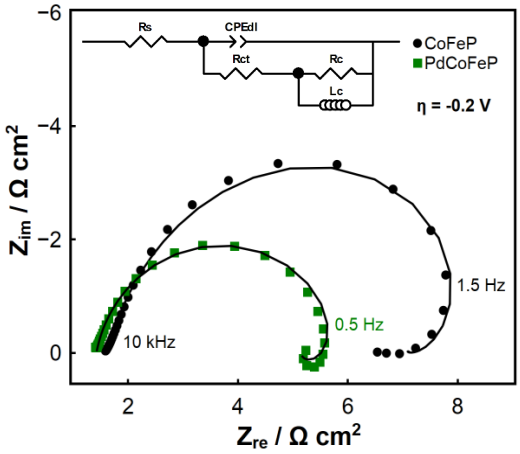

11 pav. CoFeP ir PdCoFeP katalizatorių Nyquisto diagramos, gautos esant −0,2 V (palyginti su RHE). Ištisinės linijos atspindi ekvivalentiškų grandinių, pavaizduotų įterptiniame paveikslėlyje, aproksimacijas.

Šis reiškinys paprastai rodo lėtą adsorbatų relaksaciją daugiapakopėse reakcijose, pavyzdžiui, korozijoje ar elektrokatalizėje [176], o tai leidžia manyti, kad elektrodų paviršius veikimo metu gali patirti tam tikrą restruktūrizaciją arba fazinį virsmą. Todėl impedanso spektrai buvo pritaikyti ekvivalentinės grandinės modeliui, į kurį buvo įtrauktas indukcinis elementas, siekiant atsižvelgti į žemo dažnio indukcinį atsaką [177]. Pastoviosios fazės elemento (CPE_{dl}) vertės buvo perskaičiuotos į efektyviąją talpą C_{eff} pagal Brug ir kt. formulę [178], o gautos CoFeP ir PdCoFeP vertės buvo atitinkamai 3,5 mF cm^{-2} ir 7,4 mF cm^{-2}. Be to, CoFeP krūvio perdavimo varža (R_{ct}) (5,5 Ω cm^2) buvo du kartus didesnė nei elektrochemiškai aktyvesnio PdCoFeP (3,7 Ω cm^2). Šie pastebėjimai gerai atitinka 9 paveiksle pateiktus HER aktyvumo rezultatus. Paladžiu modifikuota danga pasižymi geresniu HER aktyvumu, nes turi žymiai didesnį elektrochemiškai aktyvų paviršiaus plotą ir spartesnę HER kinetiką, kaip rodo didesnės C_{eff} ir mažesnės R_{ct} vertės.

3.2.3. Nemodifikuotų ir Pd-modifikuotų CoP/Cu ir CoFeP/Cu elektrokatalizinis aktyvumas OER atžvilgiu

Taip pat buvo įvertintas Co pagrindu pagamintų katalizatorių aktyvumas OER procese. Gauti duomenys pateikiami 12 paveiksle ir 8 lentelėje.

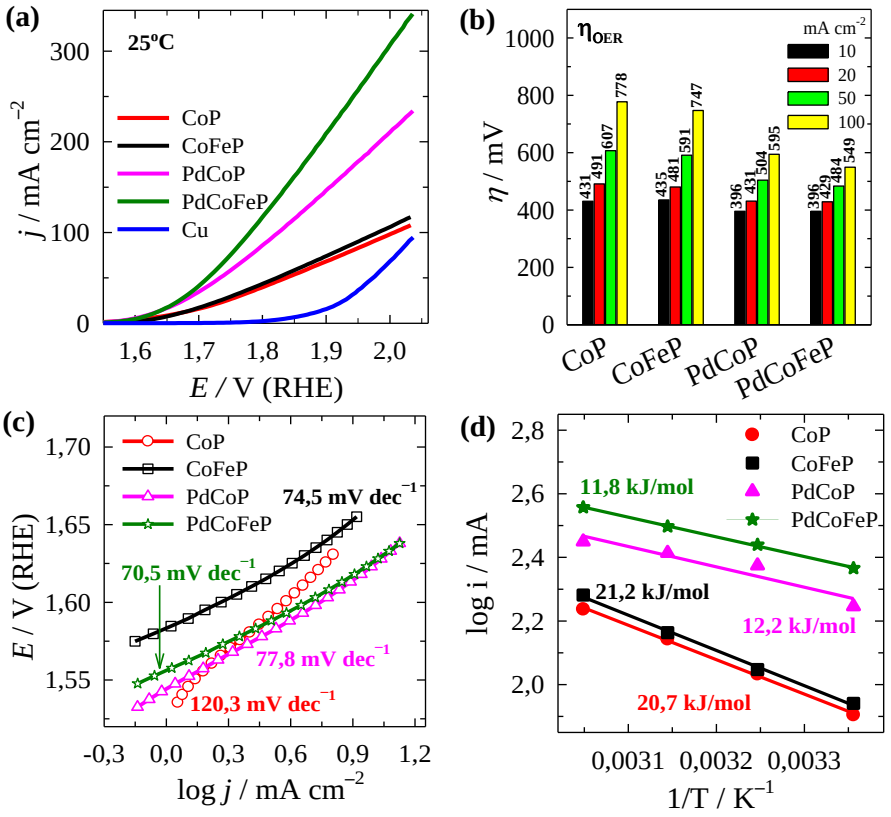

12 pav. (a) OER poliarizacijos kreivės N_2 prisotintame 1 M KOH tirpale, esant 5 mV s^{-1} potencialo skleidimo greičiui ir 25 °C temperatūrai. (b) Stulpelinės diagramos viršįtampio potencialų verčių, esant 10, 20, 50 ir 100 mA cm^{-2} srovės tankiams. (c, d) Atitinkami Tafelio nuolydžiai ir Arrhenius priklausomybės, vaizduojančios log(*i*) priklausomybę nuo 1/T, esant 1,8 V priklausomai nuo RHE kiekvienam katalizatoriui.

8 lentelė. OER katalizatorių elektrocheminės savybės šarminėje terpėje 25 °C temperatūroje.

Pavyzdys	$E_{\text{pradžios}}$*, V	$\eta_{\text{pradžios}}$, mV	E **, V	η_{10} **, mV	Tafelio nuolydis, mV dec^{-1}	E_a, kJ mol^{-1}
CoP	1,5205	290	1,6607	431	120,3	20,7
CoFeP	1,5846	355	1,6650	435	74,5	21,2
PdCoP	1,5426	313	1,6255	396	77,8	12,2
PdCoFeP	1,5577	328	1,6256	396	70,5	11,8
Cu	1,7638	534	1,8750	645	–	–

* Vertės, esant 1 mA cm^{-2}, ** Vertės, esant 10 mA cm^{-2}.

Be to, palyginimo tikslais buvo užregistruota LSV kreivė ant Cu substrato. Palyginti su Cu substratu, didesnės OER srovės tankiai buvo gauti naudojant CoP, CoFeP ir Pd modifikuotus CoP bei CoFeP katalizatorius (12a pav.), o tai rodo, kad jie pasižymėjo dideliu aktyvumu OER metu. Kaip matyti iš minėtų katalizatorių LSV kreivių, užregistruotų 1 M KOH tirpale, mažiausias OER viršįtampio potencialas – 396 mV – buvo pastebėtas Pd modifikuotų CoP ir CoFeP atveju, pasiekus 10 mA cm^{-2} srovės tankį, palyginti su nemodifikuotu CoP (431 mV) ir CoFeP (435 mV), bei Cu (645 mV) (8 lentelė). Palyginti su CoP katalizatoriumi (120,3 mV dec^{-1}), PdCoFeP, CoFeP ir PdCoP katalizatoriams buvo gautos mažesnės Tafelio nuolydžio vertės (nuo 70,5 iki 77,8 mV dec^{-1}). Šie rezultatai rodo geresnę OER kinetiką (8 lentelė). Didesnės OER srovės tankio vertės buvo gautos, naudojant Pd modifikuotus CoP ir CoFeP katalizatorius, palyginti su nemodifikuotais CoP ir CoFeP katalizatoriais (12b pav.).

PdCoFeP virršįtampio vertė, esant 100 mA cm^{-2}, yra 549 mV, o tai yra mažiau nei PdCoP (595 mV), CoFeP (747 mV) ir CoP (778 mV) atveju. Gauti kiekvieno katalizatoriaus OER LSV rodikliai temperatūrų intervale nuo 25 iki 55 °C pateikti 13 paveiksle ir 9 lentelėje. CoP, CoFeP, PdCoP ir PdCoFeP katalizatorių OER aktyvumas taip pat didėja didėjant elektrolito temperatūrai. Temperatūros padidėjimas kiekvienam katalizatoriui taip pat lemia viršįtampio potencialo verčių sumažėjimą, kurios turi pasiekti 10 mA cm^{-2} (9 lentelė).

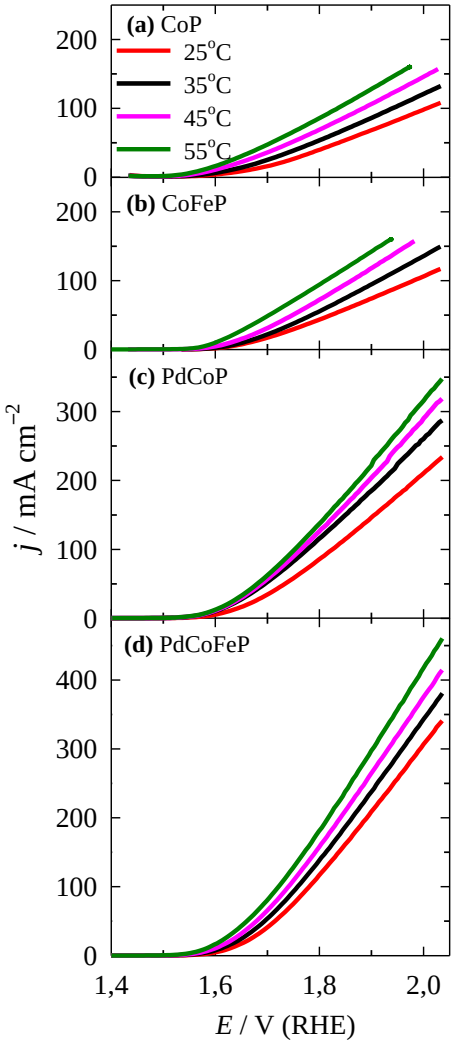

13 pav. OER poliarizacijos kreivės, užregistruotos ant CoP (a), CoFeP (b), PdCoP (c) ir PdCoFeP (d) katalizatorių N_2 prisotintame 1 M KOH tirpale, esant 5 mV s^{-1} potencialo skleidimo greičiui ir temperatūros intervale nuo 25 iki 55 °C.

Gautos Tafelio nuolydžio vertės, kurios taip pat mažėja, didėjant temperatūrai kiekvienam katalizatoriui, svyruoja nuo maždaug 120 iki 95 mV dec^{-1} CoP atveju, nuo 74 iki 60 mV dec^{-1} CoFeP atveju, nuo 78 iki 77 mV dec^{-1} PdCoP atveju, o PdCoFeP – nuo 70 iki 65 mV dec^{-1} esant atitinkamai 25 ir 55 °C temperatūrai (9 lentelė).

9 lentelė. OER katalizatorių elektrocheminės savybės šarminėje terpėje.

Pavyzdys	T, °C	$E_{pradžios}$*, V	$\eta_{pradžios}$, mV	E**, V	η_{10}**, mV	Tafelio nnuolydis, mV dec^{-1}
CoP/Cu	25	1,5205	290,5	1,6607	430,7	120,2
	35	1,5003	270,3	1,6256	395,6	101,5
	45	1,4953	265,3	1,5954	365,5	96,3
	55	1,4802	250,2	1,5729	342,9	95,2
CoFeP/Cu	25	1,5846	354,65	1,6650	435,00	74,5
	35	1,5797	349,73	1,6501	420,08	72,9
	45	1,5603	330,26	1,6306	400,60	71,5
	55	1,5417	311,71	1,5994	369,45	59,6
PdCoP/Cu	25	1,5426	312,6	1,6255	395,5	77,8
	35	1,5224	292,4	1,5979	367,9	75,8
	45	1,5224	292,4	1,5954	365,4	74,9
	55	1,5174	287,4	1,5904	360,4	76,8
PdCoFeP/Cu	25	1,5577	327,7	1,6256	395,6	70,5
	35	1,5426	312,6	1,6080	378,0	69,5
	45	1,5325	302,5	1,5979	367,9	65,2
	55	1,5175	287,5	1,5803	350,3	65,1

* Vertės, esant 1 mA cm^{-2}, ** Vertės, esant 10 mA cm^{-2}.

Norint nustatyti OER E_a, iš LSV profilių buvo išskirtos katalizatorių srovės ir temperatūros vertės esant 1,8 V (vs. RHE) (13 pav.). PdCoFeP, PdCoP, CoP ir CoFeP katalizatorių E_a vertės yra atitinkamai 11,8, 12,2, 20,7 ir 21,2 kJ mol^{-1} (12d pav.). Be to, PdCoFeP katalizatorius turi mažiausią aktyvacijos energiją, t. y. 11,8 kJ mol^{-1}, o tai reiškia, kad jo reakcijos kinetinis barjeras yra mažiausias.

3.2.4. Elektrochemiškai aktyvaus paviršiaus ploto nustatymas

Nemodifikuotų ir Pd modifikuotų CoP bei CoFeP katalizatorių elektrochemiškai aktyvūs paviršiaus plotai (ECSA) buvo nustatyti remiantis elektrocheminės dvigubo sluoksnio talpos (C_{dl}) matavimais. CV kreivės buvo registruojamos, esant skirtingiems skleidimo greičiams nefaradėjinėje potencialų srityje (14a–d pav.), po to buvo apskaičiuotas kreivės nuolydis, gautas atvaizduojant anodinės ir katodinės srovės skirtumus priklausomai nuo skleidimo greičio (14e pav.).

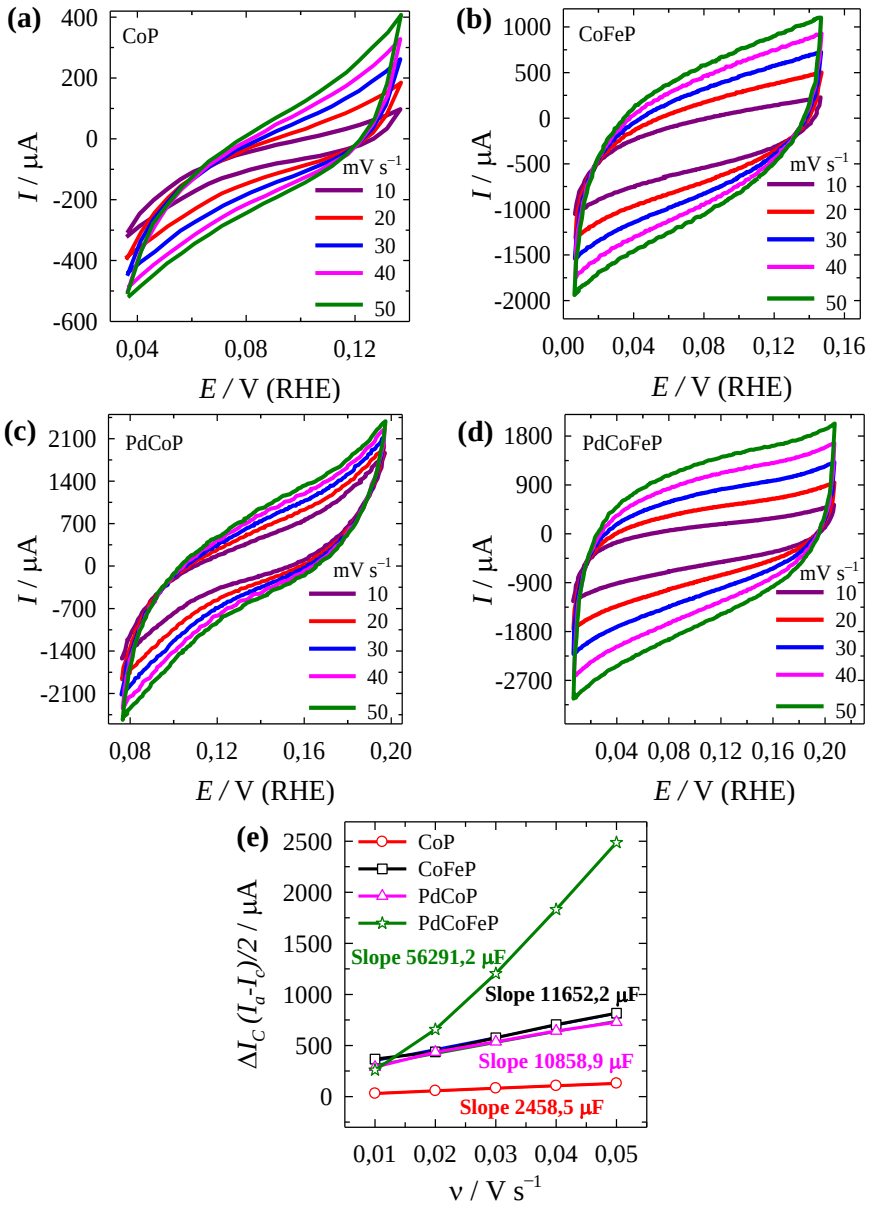

14 pav. (a) CoP, (b) CoFeP, (c) PdCoP ir (d) PdCoFeP CV kreivės N_2 prisotintame 1 M KOH tirpale nefaradėjinėje potencialo srityje, esant skirtingiems skleidimo greičiams (10–50 mV s^{-1}). (e) Įkrovimo srovės priklausomybė nuo skleidimo greičio.

C_{dl} vertės buvo 2458,5, 11 652,2, 10 858,9 ir 56 291,2 μF atitinkamai CoP, CoFeP, PdCoP ir PdCoFeP katalizatoriams (14e pav.), o apskaičiuotos ECSA vertės buvo 61,5, 291,3, 271,5 ir 1407,3 cm^2 atitinkamai CoP, CoFeP, PdCoP ir PdCoFeP atveju.Nustatyta, kad didžiausiu ECSA pasižymi PdCoFeP

katalizatorius. Didesnis aktyvumas OER reakcijai gali būti siejamas su didesniu aktyviųjų vietų skaičiumi. Fe įtraukimas į CoP dangą, po to ją modifikavus Pd kristalitais, leido pasiekti mažiausią OER viršįtampio vertę, Tafelio nuolydį ir E_a, o tai rodo, kad OER aktyvumui turi įtakos ne tik aktyviųjų vietų skaičius, bet ir kiti veiksniai, tokie kaip elektroninė struktūra ir laidumas, taip pat didelė ECSA, taip pat reikšmingai įtakoja katalizatoriaus veikimą. Katalizatorius, kuriame buvo 8,36 at% Pd, pasižymėjo geriausiu aktyvumu OER metu.

3.2.5. PdCoP/Cu ir PdCoFeP/Cu katalizatorių stabilumo tyrimas

Be to, buvo tiriamas perspektyviausių Pd modifikuotų CoP ir CoFeP katalizatorių stabilumas, taikant chronoamperometriją – 10 valandų trukmės chronoamperometrinės kreivės buvo registruojamos ant PdCoP ir PdCoFeP katalizatorių, esant pastoviam –0,26 V potencialui (15 pav.). PdCoFeP/Cu katalizatorius pasižymėjo puikiu stabilumu – per 10 val. srovės išlaikymas siekė 96,02 %, palyginti su PdCoP/Cu katalizatoriumi.

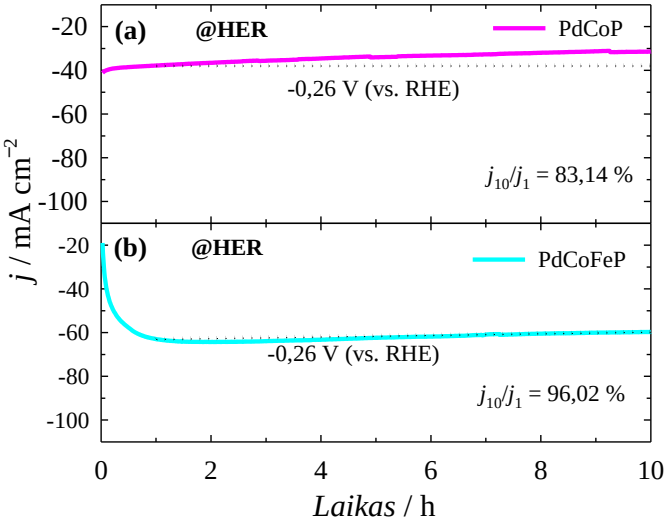

15 pav. Tiriamų PdCoP (a) ir PdCoFeP (b) katalizatorių CA kreivės 1 M KOH tirpale, esant 25 ºC temperatūrai ir –0,26 V potencialui (RHE).

16 paveiksle pateiktos chronopotentiometrinės kreivės, užregistruotos ant PdCoP (a) ir PdCoFeP (b) katalizatorių 1 M KOH tirpale, esant pastoviam srovės tankiui – 10 mA cm^{-2} ir 25 °C temperatūrai. Akivaizdu, kad potencialas, reikalingas pasiekti – 10 mA cm^{-2}, šiek tiek padidėjo nuo –0,1945 V iki –0,2131 V PdCoP atveju (16a pav.) ir nuo –0,1551 V iki –0,1740 V

PdFeCoP atveju (16b pav.) per 10 val., kas rodo abiejų katalizatorių gerą stabilumą.

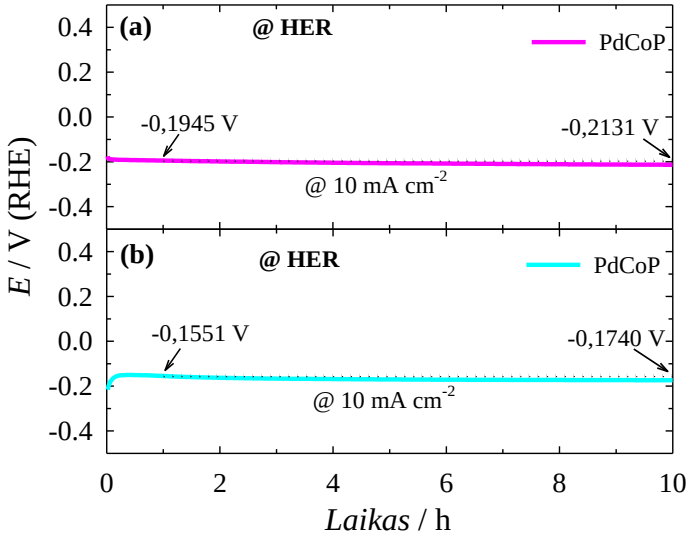

16 pav. Tiriamų PdCoP (a) ir PdCoFeP (b) katalizatorių CP kreivės 1 M KOH tirpale, esant pastoviam srovės tankiui −10 mA cm^{-2} ir 25 ºC temperatūrai.

3.2.6. Vandens skilimo proceso tyrimas, naudojant nemodifikuotus ir Pd-modifikuotus CoP/Cu ir CoFeP/Cu katalizatorius

Siekiant patvirtinti nemodifikuotų ir Pd modifikuotų CoP bei CoFeP katalizatorių bifunkcinį aktyvumą, buvo sukonstruotas dviejų elektrodų vandens elektrolizeris, kuriame kaip anodas ir katodas buvo panaudoti du tokie patys tirti katalizatoriai: CoP‖CoP, CoFeP‖CoFeP, PdCoP‖PdCoP ir PdCoFeP‖PdFeCoP. 17 paveiksle pateikiamos elektrolizerio poliarizacinės kreivės, naudojant tiriamus katalizatorius.

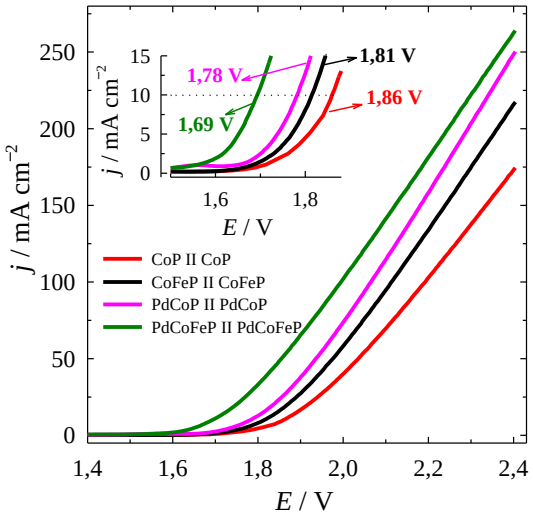

17 pav. CoP, CoFeP, PdCoP ir PdCoFeP katalizatorių, naudotų kaip anodai ir kaip katodai, poliarizacijos kreivės dviejų elektrodų elektrolizeryje, užrašytos, esant 5 mV s^{-1} skleidimo greičiui.

Sukurti CoP, CoFeP, PdCoP ir PdFeCoP elektrodai, esant srovės tankio vertei 10 mA cm^{-2}, parodė atitinkamai 1,86 V, 1,81 V, 1,78 V ir 1,69 V elektrolizerių įtampas (17 pav.). Buvo apskaičiuotas elektrolizerių energijos naudingumas. CoP, CoFeP, PdCoP ir PdCoFeP elektrolizerių energijos naudingumas buvo atitinkamai 66,13 %, 67,96 %, 69,10 % ir 72,78 %. Šie katalizatoriai atrodo esantys perspektyvūs kandidatai praktiniam vandens skilimo taikymui.

3.3. PtCoP/Cu ir PtCoFeP/Cu katalizatorių sintezė ir charakterizavimas

3.3.1. Nemodifikuotų ir Pt-modifikuotų CoP ir CoFeP dangų, mikrostruktūros ir morfologijos tyrimai

Siekiant ištirti cheminio nusodinimo būdu gautų dangų paviršiaus morfologiją ir elementinę sudėtį, buvo atliktos SEM ir EDX analizės. 18 paveiksle pateikti Co pagrindu pagamintų dangų, turinčių skirtingą sudėtį, įskaitant CoP (a), CoFeP (b), PtCoP (c) ir PtCoFeP (d), nusodintų ant Cu pagrindo, SEM vaizdai ir EDX spektrai. Pt, Co, Fe ir P buvimas dangose patvirtintas atitinkamais visų mėginių EDX spektrais. EDX rezultatai pateikti 10 lentelėje; iš jos matyti, kad pagamintų CoP, CoFeP, PtCoP ir PtCoFeP elektrokatalizatorių sudėtyje yra nuo 0,18 iki 5,96 at% Pt, nuo 61,06 iki 90,72 at% Co, nuo 10,31 iki 13,33 at% Fe ir nuo 6,18 iki 22,66 at% P. Taigi

šie rezultatai patvirtina veiksmingą sudėties modifikavimą po Fe įterpimo ir vėlesnio Pt paviršiaus modifikavimo.

10 lentelė. EDX analize nustatyta dangų, nusodintų ant Cu paviršiaus, elementinė sudėtis.

Pavyzdys	Elementas, at%			
	Pt	Co	Fe	P
CoP	–	90,72	–	9,28
CoFeP	–	80,49	13,33	6,18
PtCoP	0,18	90,34	–	9,48
PtCoFeP	5,96	61,06	10,31	22,66

SEM analizė parodė, kad dėl dangų sudėties pokyčių atsirado aiškių morfologinių skirtumų. CoP danga pasižymėjo homogeniška ir kompaktiška, žvynelių pavidalo morfologija, sudaryta iš lapų formos kristalitų, kurie buvo tankiai tarpusavyje susijungę ir tolygiai dengė Cu pagrindą (18a pav.).

Priešingai, CoFeP danga (18b pav.) pasižymėjo šiurkščia, žiedinio kopūsto pavidalo granuliuota morfologija, susidedančia iš susikaupusių nanodydžio grūdelių ir akytų mikrogruodžių, pasiskirsčiusių po visą paviršių. Fe įtraukimas lėmė žymius nusodinimo greičio ir augimo savybių pokyčius, dėl kurių padidėjo paviršiaus šiurkštumas, susiformavo tikslesnis grūdelių pasiskirstymas, taip pat aiškiai nevienalytė akyta struktūra. Įterpus Pt, PtCoP danga (18c pav.) pasižymėjo palyginti didesnių daugiakampių ir briaunų formos mikrogrūdelių susidarymu, kurį lydėjo aiškiai apibrėžtos grūdelių ribos ir lokalizuoti mikroįtrūkimai. Buvo nustatyta, kad paviršius tapo palyginti nelygus ir tankus dėl Pt sukeltos dalelių adhezijos ir kristalų susidarymo, o tai rodo veiksmingą CoP dangos paviršiaus rekonstrukciją. Iš visų mėginių PtCoFeP danga (18d pav.) pasižymėjo ryškiausia ir tekstūruota morfologija, sudaryta iš tolygiai pasiskirsčiusių mazginių nanodalelių, sujungtų į akytą tinklinę struktūrą. Fe ir Pt paviršiaus modifikavimo sinergetinis poveikis sustiprino branduolių susidarymą iš smulkesnių grūdelių nusodinimo metu, o tai lėmė reikšmingą dangos paviršiaus tekstūros ir mikrostruktūros modifikaciją. Gauti rezultatai rodo, kad sudėties pokyčiai daro reikšmingą poveikį cheminio nusodinimo būdu gautų dangų morfologinei evoliucijai.

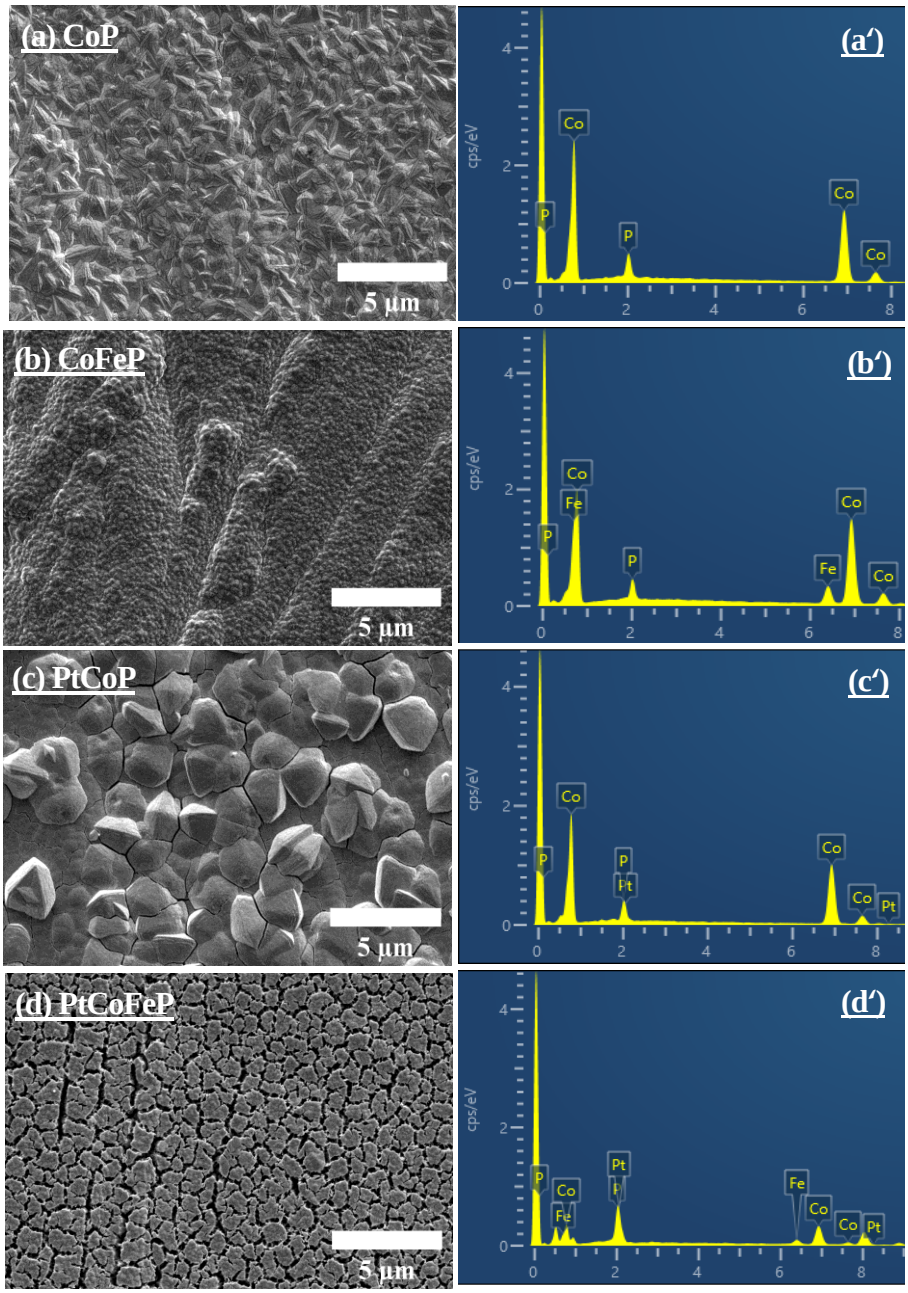

18 pav. Cu paviršiuje nusodintų CoP (a), CoFeP (b), PtCoP (c) ir PtCoFeP (d) SEM vaizdai. (a′–d′) EDX spektrai, atitinkantys minėtus SEM vaizdus.

3.3.2. Nemodifikuotų ir Pt-modifikuotų CoP/Cu ir CoFeP/Cu elektrokatalizinis aktyvumas HER atžvilgiu

Paruoštų katalizatorių elektrokatalizinės savybės HER reakcijoje buvo tiriamos registruojant LSVs 1 M KOH tirpale, esant 5 mV s^{-1} skleidimo greičiui ir 25 °C temperatūrai; gautos poliarizacijos kreivės pateiktos 19a paveiksle.

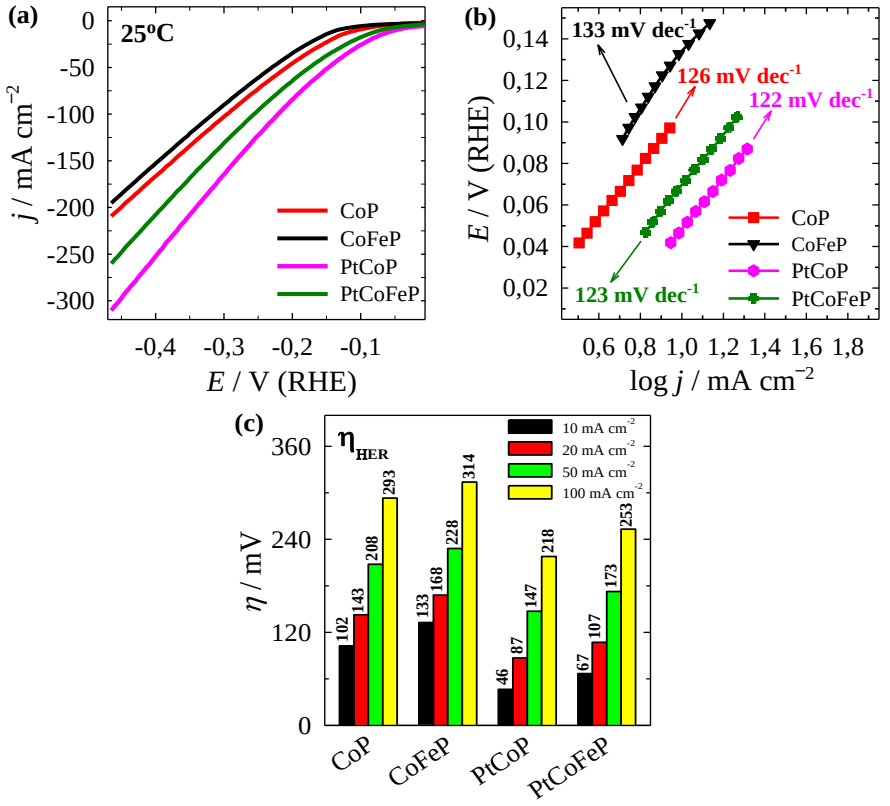

19 pav. (a) HER poliarizacijos kreivės N_2 prisotintame 1 M KOH tirpale, esant 5 mV s^{-1} potencialo skleidimo greičiui ir 25 ºC temperatūrai. (b) Atitinkami Tafelio nuolydžiai. (c) Stulpelinės diagramos, atspindinčios atitinkamus viršįtampio potencialus, esant 10, 20, 50 ir 100 mA cm^{-2} srovės tankio vertėms.

Apibendrinti HER parametrai, gauti ant tiriamų katalizatorių šarminėje terpėje 25 °C temperatūroje, pateikti 11 lentelėje.

11 lentelė. HER parametrų apibendrinimas tiriamuose katalizatoriuose šarminėje terpėje.

Pavyzdys	$E_{\text{pradžios}}$ *, V	η_{10} **, mV	Tafelio nuolydis, mV dec^{-1}
CoP	0,064	102	126
CoFeP	0,069	133	133
PtCoP	0,084	46	122
PtCoFeP	0,049	67	123

* Vertės, esant 1 mA cm^{-2}, ** Vertės, esant 10 mA cm^{-2}.

Atitinkamos viršįtampio potencialo vertės, esant 10, 20, 50 ir 100 mA cm^{-2} srovės tankiams, pateiktos 19c paveiksle. Iš tirtų katalizatorių PtCoP elektrokatalizatorius pasižymėjo geriausiu HER aktyvumu – norint pasiekti 10 mA cm^{-2} srovės tankį, jam reikėjo mažiausio viršįtampio potencialo (46 mV); po jo sekė PtCoFeP (66 mV), CoP (102 mV) ir CoFeP (132 mV), kaip parodyta 19a ir 19c paveiksluose. Be to, esant 100 mA cm^{-2} srovės tankiui, PtCoP parodė mažiausią 217 mV viršįtampio potencialo vertę, palyginti su PtCoFeP (253 mV), CoP (293 mV) ir CoFeP (313 mV), taip patvirtindamas savo pranašesnes katalizinės savybes visame srovės tankio diapazone. Mažesnis PtCoP viršįtampio potencialas liudija apie jo padidėjusį katalizinį aktyvumą vandenilio išsiskyrimo atžvilgiu šarminėje terpėje. Be to, Pt modifikuoti katalizatoriai parodė nuosekliai mažesnius viršįtampio potencialus, palyginti su nemodifikuotais katalizatoriais, taip patvirtindami lemiamą Pt įtraukimo vaidmenį, gerinant HER kinetiką ir didinant bendrą katalizinį efektyvumą. Susintetintų katalizatorių HER kinetika buvo toliau tirta, naudojant atitinkamas Tafelio diagramas, kaip parodyta 19b paveiksle. Tafelio nuolydis, kuris nustatomas pagal viršįtampio potencialo (η) ir logaritminio srovės tankio (log(j) koreliacijos, suteikia svarbių įžvalgų apie reakcijos kinetiką ir galimą HER mechanizmą. Apskaičiuotos Tafelio nuolydžio vertės buvo 126, 133, 122 ir 123 mV dec^{-1} atitinkamai CoP, CoFeP, PtCoP ir PtCoFeP katalizatoriams. Tarp tiriamų katalizatorių mažiausią Tafelio nuolydį parodė PtCoP, o po jo – PtCoFeP. Šis rezultatas rodo palankesnę HER kinetiką ir pagerėjusias krūvio perdavimo charakteristikas po modifikavimo Pt. Mažesnės Pt modifikuotų katalizatorių Tafelio nuolydžio vertės, palyginti su CoP ir CoFeP, suteikia papildomų įrodymų apie palankų Pt vaidmenį palengvinant HER. Gauti Tafelio nuolydžio dydžiai, svyruojantys nuo 122 iki 133 mV dec^{-1}, rodo, kad HER šarminėje terpėje gali vykti pagal Volmerio–Heyrovskio mechanizmą. Šis mechanizmas apima vandenilio tarpinių junginių (H_{ads}) adsorbciją ant katalizatoriaus paviršiaus, po kurios

vyksta jų elektrocheminė desorbcija. Pagerėję PtCoP ir PtCoFeP kinetiniai parametrai yra susiję su sumažėjusiais viršįtampio potencialais ir padidėjusiu HER aktyvumu.

Siekiant geriau suprasti, kaip Pt įtraukimas veikia CoP, CoFeP, PtCoP ir PtCoFeP katalizatorių aktyvumą HER, buvo atlikti elektrocheminės impedanso spektroskopijos (EIS) matavimai. 20 paveiksle pateikti impedansų, gautų esant −150 mV, Nyquisto diagramos.

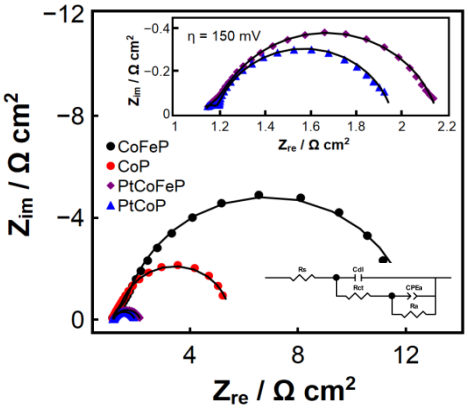

20 pav. Įvairių plėvelių Nyquisto diagramos, gautos esant −150 mV prieš RHE. Įterptame paveikslėlyje pateiktas padidintas Pd turinčių plėvelių EIS spektrų vaizdas.

Šiame potencialo intervale visi spektrai susideda iš neryškaus aukšto dažnio signalo, po kurio seka platus pusapskritimas vidutinių ir žemų dažnių srityje, kurį lemia vandenilio adsorbcija [191]. Remiantis LSV rezultatais, didžiausia impedanso vertė (t. y. mažiausia HER srovė, esant šiam viršįtampio potencialui) stebima CoFeP katalizatoriui, po kurio eina CoP. Pt modifikuoti katalizatoriai pasižymi žymiai mažesnėmis impedanso vertėmis, kaip matyti iš 20 paveikslo intarpe pateiktų Nyquisto diagramų. Spektrai buvo pritaikyti prie ekvivalentinės grandinės, sudarytos iš dviejų lygiagrečiai sujungtų RC elementų, kuri literatūroje dažnai naudojama adsorbcijos pagrįstoms reakcijoms, tokioms kaip HER [191]. Čia C_{dl} ir R_{ct} yra dvigubo sluoksnio talpa ir krūvio perdavimo varža, o C_a ir R_a – vandenilio adsorbcijos pseudotalpa ir su ja susijusi varža. Gauti dydžiai pateikti 12 lentelėje, kurioje matyti, kad Pd modifikuotos plėvelės pasižymi ~10 kartų mažesnėmis R_{ct} vertėmis, o tai rodo žymiai spartesnę HER kinetiką. Be to, įterpiant Pd, R_a vertė smarkiai sumažėja (nuo ~10 – 3,44 Ω cm^2 iki 0,93 – 0,77 Ω cm^2), o tai rodo greitesnę adsorbuotų H* tarpininkų relaksaciją. Kalbant konkrečiai apie PtCoP, didelė C_a vertė (16,8 mF cm^{-2}) greičiausiai yra susijusi su padidėjusiu aktyviųjų vietų, skirtų

vandenilio adsorbcijai ir desorbcijai, skaičiumi. Apskritai EIS rezultatai patvirtina teigiamą Pd įterpimo poveikį HER ir rodo, kad geriausiai veikiantis PtCoP katalizatorius pasižymi mažiausia krūvio perdavimo varža, optimaliu vandenilio ryšio stiprumu adsorbcijai ir desorbcijai bei didžiausia vandenilio adsorbcijos pseudotalpa, o tai rodo, kad jame yra daug aktyvių HER vietų.

12 lentelė. CoP, CoFeP, PtCoP ir PtCoFeP elektrokatalizatorių EIS pritaikymo parametrai HER procesui.

Katalizato-rius	**C_{dl}, mF cm^{-2}**	**R_{ct}, Ω cm^2**	**C_a, mF cm^{-2}**	**R_a, Ω cm^2**
CoP	1,47	0,94	2,01	3,44
CoFeP	1,00	1,01	1,88	9,98
PtCoP	1,13	0,075	16,8	0,77
PtCoFeP	1,95	0,095	5,20	0,93

3.3.3. Nemodifikuotų ir Pt-modifikuotų CoP/Cu ir CoFeP/Cu elektrokatalizinis aktyvumas OER atžvilgiu

Taip pat buvo įvertintos CoP, CoFeP, PtCoP ir PtCoFeP katalizatorių elektrokatalizinės savybės OER, o atitinkamos poliarizacijos kreivės pateiktos 21a paveiksle. Kaip rodo LSV kreivės, užregistruotos CoP, CoFeP, PtCoP ir PtCoFeP katalizatoriams 1 M KOH tirpale 25 °C temperatūroje, iš visų tiriamų mėginių didžiausią OER aktyvumą parodė PtCoFeP. Viršįtampio vertės, reikalingos 10, 20, 50 ir 100 mA cm^{-2} srovės tankiams pasiekti, pateiktos 21c paveiksle. Nustatyta, kad iš tirtų katalizatorių PtCoFeP reikėjo mažiausio viršįtampio potencialo – 322 mV, norint pasiekti 10 mA cm^{-2} srovės tankį; po jo sekė PtCoP (343 mV), CoFeP (373 mV) ir CoP (419 mV). Be to, esant 100 mA cm^{-2} srovės tankiui, PtCoFeP parodė mažiausią 509 mV viršįtampio potencialo vertę, palyginti su PtCoP (534 mV), CoFeP (565 mV) ir CoP (615 mV), o tai rodo jo pagerėjusias OER charakteristikas visame srovės tankio diapazone. Mažesnės PtCoFeP viršįtampio potencialo vertės nuosekliai rodo teigiamą Fe priedo ir dėl to įvykusios Pt paviršiaus modifikacijos poveikį, gerinant OER kinetiką ir bendrą elektrokatalizinį našumą šarminėje terpėje.

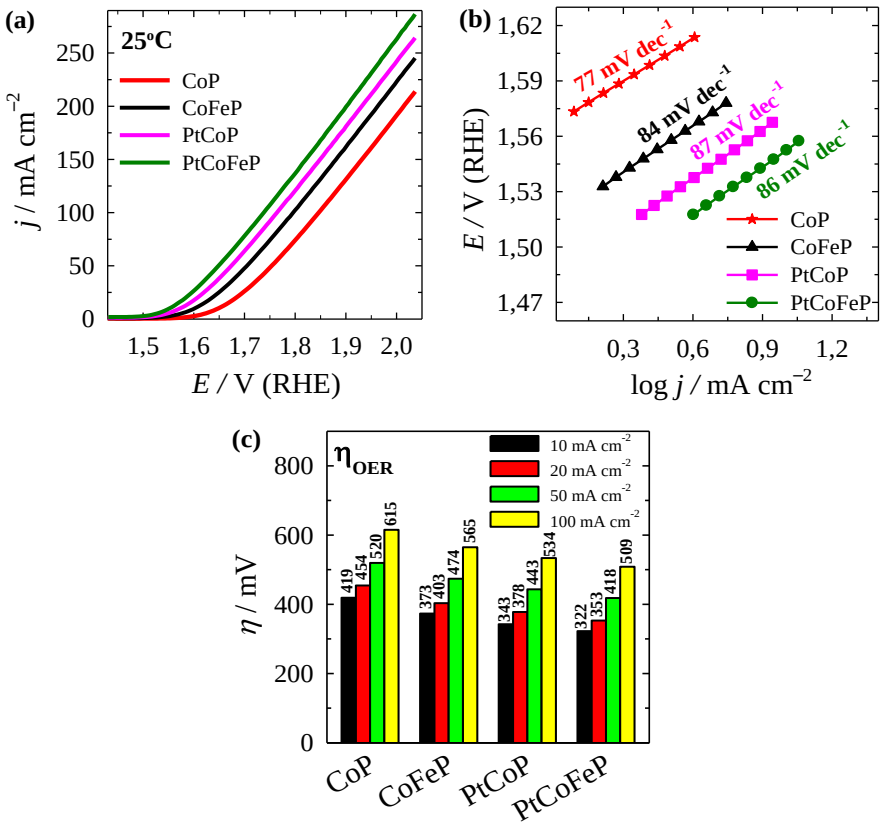

21 pav. (a) OER poliarizacijos kreivės N_2 prisotintame 1 M KOH tirpale, esant 5 mV s^{-1} potencialo skleidimo greičiui ir 25 °C temperatūrai. (b) Atitinkami Tafelio nuolydžiai. (c) Stulpelinės diagramos, atspindinčios atitinkamus viršįtampio potencialus, esant 10, 20, 50 ir 100 mA cm^{-2} srovės tankiams.

13 lentelė. OER katalizatorių elektrocheminės savybės šarminėje terpėje, esant 25 °C temperatūrai.

Pavyzdys	$E_{\text{pradžios}}$ *, **V**	η_{10} **, **mV**	**Tafelio nuolydis, mV dec^{-1}**
CoP	1,568	419	77
CoFeP	1,513	373	84
PtCoP	1,447	343	87
PtCoFeP	1,437	322	86

* Vertės, esant 1 mA cm^{-2}, ** Vertės, esant 10 mA cm^{-2}.

Padidėjęs PtCoFeP aktyvumas tiek esant mažam, tiek dideliam srovės tankiui dar labiau rodo jo išskirtinį gebėjimą skatinti greitą deguonies išsiskyrimą realiomis eksploatavimo sąlygomis. Katalizatorių OER kinetinės savybės buvo toliau tiriamos, naudojant atitinkamas Tafelio diagramas (žr. 21b pav.). Apskaičiuotos Tafelio nuolydžio vertės buvo 77, 84, 87 ir 86 mV dec^{-1} atitinkamai CoP, CoFeP, PtCoP ir PtCoFeP katalizatorių atveju. Tačiau, nepaisant mažiausio Tafelio nuolydžio, CoP reikėjo žymiai didesnių viršįtampio potencialų, kad būtų pasiektas norimas srovės tankis. Tuo tarpu PtCoFeP parodė mažiausias viršįtampio potencialo vertes visame tiriamame srovės tankių diapazone, o tai rodo geresnį OER aktyvumą. Iš eksperimentinių duomenų gautos Tafelio nuolydžio vertės rodo, kad OER vyksta per daugiažengį, su protonais susietą elektronų perdavimo procesą, kuriame dalyvauja deguonies turintys tarpiniai junginiai. Geresnį PtCoFeP aktyvumą OER galima priskirti jo paviršiaus morfologijai ir sudėčiai. Be to, bendras Pt, Co, Fe ir P poveikis gali skatinti krūvio perdavimą ir pagerinti OER kinetiką, taip prisidėdamas prie padidėjusio PtCoFeP OER katalizinio aktyvumo šarminėje terpėje.

3.3.4. PtCoP/Cu ir PtCoFeP/Cu katalizatorių stabilumo tyrimas

PtCoP ir PtCoFeP elektrokatalizatorių ilgalaikis stabilumas HER reakcijoje buvo įvertintas taikant chronopotentiometriją, esant pastoviam srovės tankiui –10 mA cm^{-2} 15 valandų trukmės bandymo metu 1 M KOH tirpale 25 ^{o}C temperatūroje. Atitinkami rezultatai pateikti 22 paveiksle. Pažymėtina, kad potencialas, reikalingas 10 mA cm^{-2} srovei palaikyti, per visą 15 valandų trukmės stabilumo bandymą išliko beveik pastovus. 22a paveiksle matyti, kad PtCoP katalizatorius yra labai stabilus, o potencialas proceso eigoje pakito tik nežymiai – nuo –0,0553 iki –0,0565 V. Panašiai, kaip parodyta 22b paveiksle, PtCoFeP katalizatorius pademonstravo taip pat didelį stabilumą, išlaikydamas santykinai pastovų potencialą per visą matavimo intervalą, o jo pokytis buvo irgi nežymus – nuo –0,0535 iki –0,0550 V. Siekiant išsamiau ištirti katalizatorių paviršiaus morfologiją po ilgalaikio HER veikimo, po 15 val. trukusio chronopotentiometrinio bandymo buvo tirta katalizatorių paviršiaus morfologija, naudojant SEM. Kaip matyti iš 22c ir 22d paveikslų, SEM vaizdai, gauti po stabilumo etapo, parodė, kad tiek PtCoP, tiek PtCoFeP išlaikė savo pradinę paviršiaus morfologiją, be akivaizdžių paviršiaus susidėvėjimo ar struktūrinio pablogėjimo požymių. Nors buvo pastebėta nežymi paviršiaus rekonstrukcija, abiejų katalizatorių bendrosios morfologinės charakteristikos po ilgalaikės elektrolizės išliko nepaprastai gerai išsaugotos.

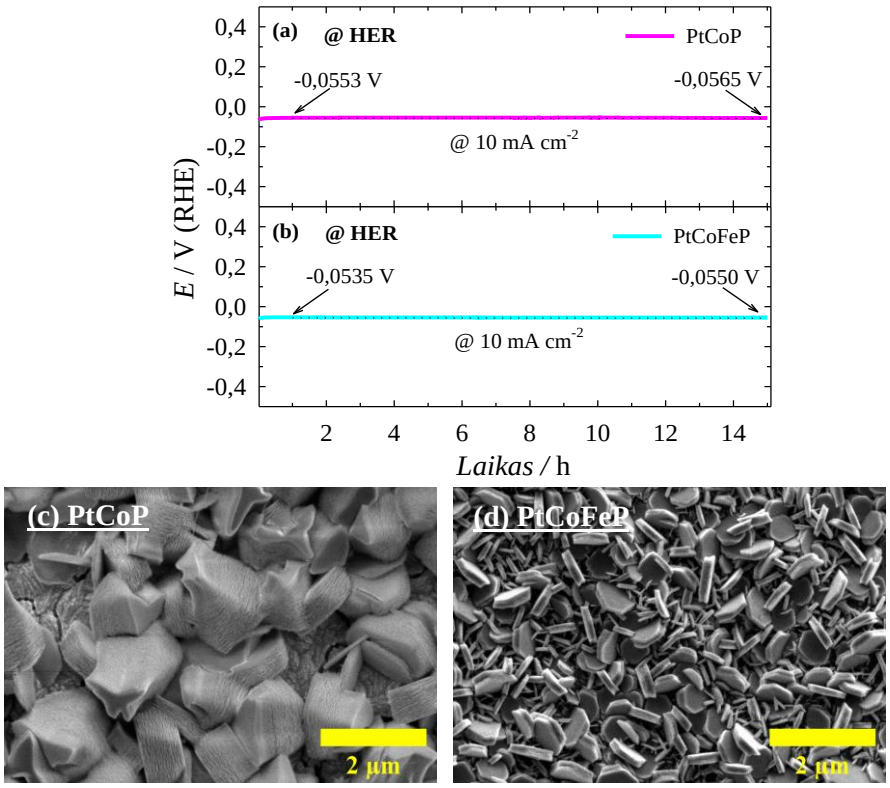

22 pav. Tiriamų PtCoP (a) ir PtCoFeP (b) katalizatorių CP kreivės 1 M KOH tirpale esant pastoviam srovės tankiui 10 mA cm^{-2} ir 25 ^{o}C temperatūrai. Pt-CoP (c) ir Pt-CoFeP (d) SEM analizės vaizdai po stabilumo tyrimo.

3.3.5. Vandens skilimo proceso tyrimas, naudojant nemodifikuotus ir Pt-modifikuotus CoP/Cu ir CoFeP/Cu katalizatorius.

Atsižvelgiant į gautas katalizatorių elektrokatalizines savybes HER ir OER procesams, buvo tiriamas nemodifikuotų ir Pt modifikuotų CoP bei CoFeP katalizatorių bifunkcinis elektrokatalizinis aktyvumas vandens elektrolizės metu, naudojant dviejų elektrodų celę – elektrolizerį šarminėje terpėje, kurioje tiek anodu, tiek katodu buvo naudojamas tas pats katalizatorius. 23a paveiksle pateikiamos išmatuotos elektrolizerių įtampos vertės, kai tiek anodu, tiek katodu naudojami tie patys katalizatoriai: CoP‖CoP, CoFeP‖CoFeP, PtCoP‖PtCoP ir PtCoFeP‖PtFeCoP.

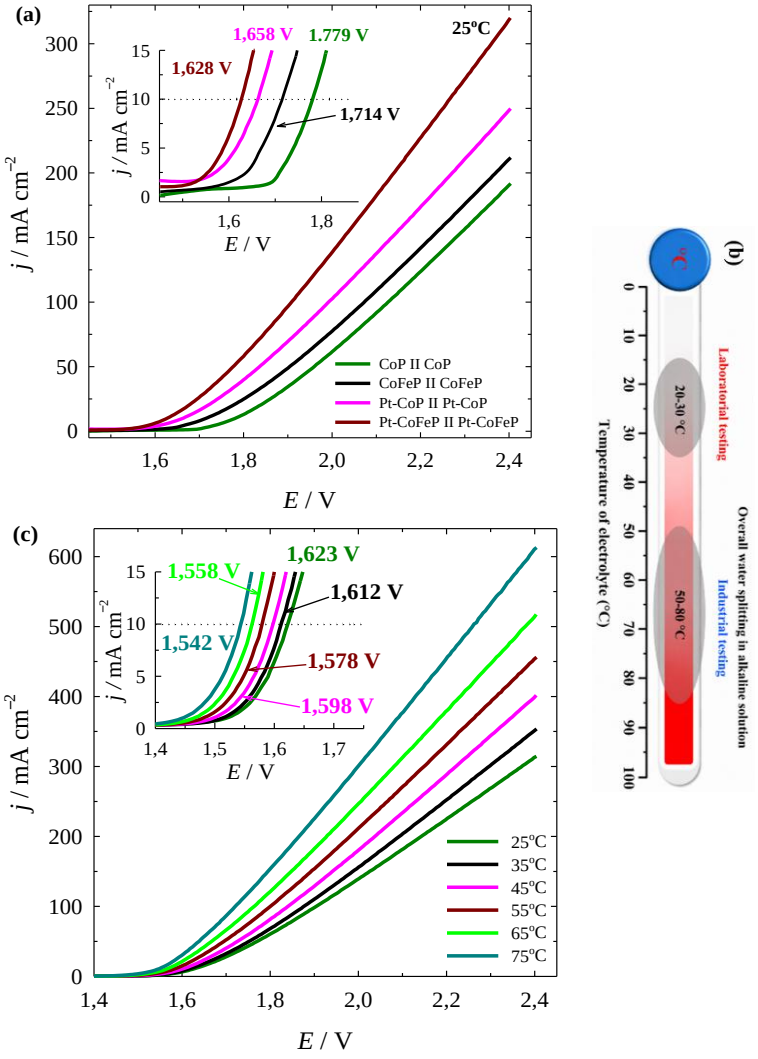

23 pav. Vandens skilimo proceso poliarizacijos kreivės, užrašytos dviejų elektrodų elektrolizeryje, kuriame tiek anodu, tiek katodu naudoti tie patys katalizatoriai, esant 5 mV s^{-1} skleidimo greičiui (a). Laboratorinės ir pramoninės bandymų temperatūros skirtumas (b). Poliarizacijos kreivės, kai katodu naudojamas PtCoP, o anodu – PtCoFeP, esant skirtingoms temperatūroms (25–75 °C) (c).

Bendrą vandens skilimo efektyvumą žymiai lemia katalizatoriaus sudėtis. Tarp tiriamų elektrodų puikų efektyvumą parodė PtCoFeP‖PtCoFeP elektrolizeris, kuriam pasiekti 10 mA cm^{-2} srovės tankį reikėjo tik 1,628 V įtampos. Palyginimui, PtCoP‖PtCoP, CoFeP‖CoFeP ir CoP‖CoP sistemoms

reikėjo atitinkamai 1,658, 1,714 ir 1,779 V įtampos. PtCoFeP‖PtCoFeP sistemoje buvo pastebėtas žymus elementų įtampos sumažėjimas, o tai rodo, kad Fe priedas ir Pt paviršiaus modifikavimas daro teigiamą poveikį bendram vandens skilimo efektyvumui. Šis pagerintas bifunkcinis elektrokatalizinis katalizatorių efektyvumas pirmiausia gali būti priskirtas Pt, Co, Fe ir P sinergijai, kuri skatina krūvio perdavimą ir taip palengvina tiek vandenilio, tiek deguonies išsiskyrimo reakcijas.

Kaip matyti iš 23b paveikslo, tarp vandens elektrolizės laboratorinių bandymų ir pramoninio pritaikymo yra didelis atotrūkis. Laboratorijoje temperatūra paprastai palaikoma 20–30 ^{o}C ribose. Praktiniame pritaikyme bendras vandens skilimo našumas paprastai pasiekiamas esant 50–80 ^{o}C temperatūrai, siekiant sumažinti reikalingą įtampą. Siekiant užpildyti atotrūkį tarp laboratorinių ir pramoninių sąlygų, vandens skilimo elektrolizerio elektrocheminės savybės vertinamos, naudojant pramonines temperatūras. Temperatūros įtaka elektrolizės našumui buvo įvertinta, tiriant dviejų elektrodų elektrolizerio parametrus, kai katodu buvo naudojamas PtCoP katalizatorius, o anodu – iš PtCoFeP, esant temperatūrai nuo 25 iki 75 ^{o}C. Konkrečiame temperatūrų intervale PtCoP‖PtCoFeP poliarizacijos kreivės pateiktos 23b paveiksle. Pastebėta, kad esant tam pačiam srovės tankiui, vandens skilimo įtampa palaipsniui mažėja, didėjant reakcijos temperatūrai. Išmatuotos PtCoP‖PtCoFeP elektrolizerio įtampos vertės yra 1,623, 1,612, 1,598, 1,578, 1,558 ir 1,542 V atitinkamai, esant 25, 35, 45, 55, 65 ir 75 ^{o}C temperatūroms, kad būtų pasiektas 10 mA cm^{-2} srovės tankis. Šie rezultatai rodo, kad PtCoP‖PtCoFeP elektrolizeris turi didelį potencialą pramoniniam vandens elektrolizės taikymui.

APRIBOJIMAI IR TOLESNIO TOBULINIMO PERSPEKTYVOS

Nepaisant to, kad susintetinti CoP_x/Cu, CoFeP/Cu, PdCoP/Cu, PdCoFeP/Cu, PtCoP/Cu ir PtCoFeP/Cu elektrokatalizatoriai pasižymi geru elektrokataliziniu aktyvumu ir stabilumu HER, OER ir bendro vandens skilimo procesuose, yra keletas trūkumų, kuriuos reikia toliau tirti. CoP_x/Cu ir CoFeP/Cu elektrokatalizatoriai, kurių sudėtyje nėra tauriųjų metalų, vis dar pasižymi palyginti didesniais viršįtampiais, ypač OER atveju, palyginti su Pt modifikuotais elektrokatalizatoriais. Tokiu būdu, katalizatorių katalizinį efektyvumą galima dar pagerinti. Be to, nepaisant to, kad Pt ir Pd kiekiai katalizatoriuose yra pakankamai maži, tauriųjų metalų naudojimas tebėra kliūtis katalizatorių gamybai dideliu mastu dėl jų didelės kainos ir retumo. Pagerinti katalizatorių savybes būtų galima, optimizuojant Co/Fe/P sudėtį ir reguliuojant paviršiaus morfologiją, siekiant padidinti aktyviųjų vietų kiekį ir prieinamumą, tuo pačiu mažinant tauriųjų metalų kiekį per kontroliuojamą paviršiaus modifikavimą. Be to, nepaisant gero stabilumo, parodyto šio tyrimo sąlygomis, manoma, kad būtų naudinga atlikti ilgalaikius patvarumo bandymus aukštesnėse temperatūrose ir esant didesniam srovės tankiui, siekiant įvertinti jų praktinį tinkamumą. Toks optimizavimas gali pagerinti sukurtų elektrokatalizatorių bendrą katalizinį našumą, patvarumą ir ekonomiškumą.

IŠVADOS

1. Šiame tyrime sėkmingai sukurti CoP_x/Cu (0,4–11 mas. % P), CoFeP/Cu, PdCoP/Cu, PdCoFeP/Cu, PtCoP/Cu ir PtCoFeP/Cu elektrokatalizatoriai buvo pagaminti, taikant paprastus metodus, apimančius cheminį nusodinimą ir galvaninį pakeitimą. Šie elektrokatalizatoriai parodė puikias savybes HER, OER ir OWS procesuose šarminėje terpėje. HER ir OER katalizinis aktyvumas buvo vertinamas trijų elektrodų celėje, naudojant 1 M KOH, o OWS savybės buvo vertinamos dviejų elektrodų elektrolizeryje tiek laboratorinėmis sąlygomis, tiek pramonėje aktualiose temperatūrose (25–75 ^{o}C).
2. Nustatyta, kad fosforo kiekis yra pagrindinys veiksnys, įtakojantis kobalto fosfido dangų elektrokatalizines savybes. Iš CoP_x katalizatorių CoP_{11}/Cu pasižymėjo geriausiu aktyvumu HER, kai viršįtampio potencialas buvo 98,9 mV, esant 10 mA cm^{-2}, o CoP_8/Cu pasižymėjo efektyviausiu aktyvumu OER, kai viršįtampio vertė buvo 378 mV, esant 10 mA cm^{-2} 1 M KOH tirpale.
3. CoP ir CoFeP katalizatorių elektrokatalizinis aktyvumas buvo žymiai pagerintas, paviršių modifikavus nedideliu Pd kiekiu galvaninio pakeitimo būdu. Tarp Pd modifikuotų katalizatorių didžiausiu HER aktyvumu pasižymėjo PdCoP/Cu, kuriam pasiekti 10 mA cm^{-2} srovės tankį pakako 250 mV viršįtampio vertės. Be to, PdCoP/Cu ir PdCoFeP/Cu parodė padidėjusį OER aktyvumą, kuriam 1 M KOH tirpale 10 mA cm^{-2} srovės tankiui pasiekti reikėjo tik 396 mV viršįtampio. Fe įterpimas į dangas lėmė padidėjusį katalizinį aktyvumą ir stabilumą dėl dangos sudėties ir paviršiaus savybių modifikavimo.
4. Nustatyta, kad CoP ir CoFeP katalizatorių paviršiaus modifikavimas nedideliu Pt kiekiu galvaninio pakeitimo būdu lėmė elektrokatalizinio aktyvumo padidėjimą. PtCoP/Cu pasižymėjo ženkliai didesniu aktyvumu HER, pasiekdamas vos 46 mV viršįtampio vertę, esant 10 mA cm^{-2} srovės tankiui, o PtCoFeP/Cu pademonstravo puikias OER savybes, pasiekdamas 322 mV viršįtampio vertę, esant 10 mA cm^{-2} srovės tankiui, taip patvirtindamas sinergetinį Fe įterpimo ir Pt modifikavimo poveikį elektrokatalizinėms savybėms.
5. Pažymėtina, kad 25 ^{o}C temperatūroje OWS charakteristikos palaipsniui didėjo, pradedant nuo CoP_{11}/Cu pagrindu pagaminto elektrolizerio (1,81 V, esant 10 mA cm^{-2}) iki PdCoFeP/Cu pagrindu pagaminto elektrolizatoriaus (1,69 V, esant 10 mA cm^{-2}). Iš visų surinktų elektrolizerių, išskirtinius OWS parametrus pademonstravo $PtCoFeP_{(+)}$ ‖ $PtCoP_{(-)}$ konfigūracija, kai 10 mA cm^{-2} srovės tankiui

pasiekti 1 M KOH tirpale reikėjo tik 1,63 V įtampos esant 25 ^{o}C temperatūrai ir 1,54 V esant 75 ^{o}C temperatūrai. Šie rezultatai rodo didelį šios konfigūracijos potencialą praktiniam pritaikymui pramoninėje šarminėje vandens elektrolizėje, esant atitinkamoms darbo temperatūroms.

6. Sukurti CoP_{11}/Cu, PdCoP/Cu, PdCoFeP/Cu, PtCoP/Cu ir PtCoFeP/Cu elektrokatalizatoriai pasižymėjo elektrocheminiu stabilumu šarminėse sąlygose. Chronopotentiometriniai tyrimai parodė, kad po 10 valandų PdCoP/Cu ir PdCoFeP/Cu katalizatorių atveju potencialo poslinkiai buvo atitinkamai 18,6 mV ir 18,9 mV, esant 10 mA cm^{-2}. Tuo tarpu PtCoP/Cu ir PtCoFeP/Cu katalizatorių atveju, po 15 valandų potencialo poslinkiai siekė atitinkamai tik 1,2 mV ir 1,5 mV, esant 10 mA cm^{-2}. Be to, PdCoFeP/Cu, esant pastoviam –0,26 V potencialui, pademonstravo įspūdingą 96,02 % pradinės srovės išlaikymą, o CoP_{11}/Cu buvo stabilus 15 valandų bėgyje, esant pastoviai potencialo vetei –0,26 V. Be to, CoP_{11}/Cu pasižymėjo dideliu stabilumu po 1000 pagreitintos degradacijos bandymo ciklų.
7. Optimizuotų CoP_{11}/Cu ir PdCoFeP/Cu elektrokatalizatorių elektrochemiškai aktyvaus paviršiaus ploto (ECSA) vertės buvo atitinkamai 115,6 ir 1407,3 cm^2. Didelės ECSA vertės rodo, kad elektrochemiškai prieinamų aktyviųjų vietų skaičius gali būti didesnis, o tai potencialiai gali lemti didesnį elektrokatalizinį aktyvumą HER ir OER.
8. Apibendrinant galima teigti, kad cheminio nusodinimo ir galvaninio pakeitimo metodai yra nesudėtingi, ekonomiški ir pritaikomi didelio efektyvumo kobalto fosfido pagrindu pagamintų elektrokatalizatorių gamybos būdai. Šios medžiagos turi potencialą tapti efektyviomis kandidatėmis vandenilio gamybai šarminės vandens elektrolizės būdu, ypač pramoninėmis eksploatavimo sąlygomis.

REFERENCES

1. G. Mombekova, M. Nurgabylov, A. Baimbetova, B. Keneshbayev, B. Izatullayeva. The relationship between energy consumption, population, and economic growth in developing countries. *Int. J. Energy Econ. Policy*, 2024, 14, 368–374.

2. A. N. Feltrin. Energy equality and the challenges of population growth. *Relations*, 2018, 6, 313–320.

3. S. A. Olaleru, J. Kirui, F. Elegbeleye, T. Aniyikaiye. Green Technology Solution to Global Climate Change Mitigation. *Energy Environ. Storage J.*, 2021, 1, 26–41.

4. I. Elegbeleye, O. Oguntona, F. Elegbeleye. Green hydrogen: Pathway to net zero green house gas emission and global climate change mitigation. *Hydrogen*, 2025, 6(2), 29.

5. Y. Shi, Z.R. Ma, Y.Y. Xiao, Y.C. Yin, W.M. Huang, Z.C. Huang, Y.Z. Zheng, F.Y. Mu, R. Huang, G.Y. Shi, Y.Y. Sun, X.H. Xia, W. Chen. Electronic metal–support interaction modulates single-atom platinum catalysis for hydrogen evolution reaction. *Nat. Commun.*, 2021, 12(1), 3021.

6. Y. Dou, A. Wang, L. Zhao, X. Yang, Q. Wang, M.S. Sudi, W. Zhu, D. Shang. Boosted hydrogen evolution reaction for a nitrogen-rich azo-bridged metallated porphyrin network. *J. Colloid Interface Sci.*, 2023, 650, 943–950.

7. R. Yao, K. Sun, K. Zhang, Y. Wu, Y. Du, Q. Zhao, G. Liu, C. Chen, Y. Sun, J. Li. Stable hydrogen evolution reaction at high current densities via designing the Ni single atoms and Ru nanoparticles linked by carbon bridges. *Nat. Commun.*, 2024, 15(1), 2218.

8. I.H. Kwak, J.Y. Kim, G.M. Zewdie, J. Yang, K.S. Lee, S.J. Yoo, I.S. Kwon, J. Park, H.S. Kang. Electrocatalytic activation in $ReSe_2$-VSe_2 alloy nanosheets to boost water-splitting hydrogen evolution reaction. *Adv. Mater.*, 2024, 36, 2310769.

9. K.N. Dinh, Y. Sun, Z. Pei, Z. Yuan, A. Suwardi, Q. Huang, X. Liao, Z. Wang, Y. Chen, Q. Yan. Electronic modulation of nickel disulfide toward efficient water electrolysis. *Small*, 2020, 16(17), 1905885.

10. S. Liu, Y. Wei, M. Wang, Y. Shen. The future of alkaline water splitting from the perspective of electrocatalysts-seizing today's opportunities. *Coord. Chem. Rev.*, 2025, 522, 216190.

11. L. Tian, Z. Li, X. Xu, C. Zhang. Advances in noble metal (Ru, Rh, and Ir) doping for boosting water splitting electrocatalysis. *J. Mater. Chem. A*, 2021, 9(23), 13459–13470.

12. H. Yang, H. Wang, H. Cheng, X. Xu, J. Li, X. He, L. Tian, Z. Li. Redox activity of Co species in the active sites of CoN_x/CoO_x facilitates oxygen

electrocatalysis for Zn-air batteries. *Chem. Eur. J.*, 2024, 30(69), e202402972.
13. J. Mei, T. He, J. Bai, D. Qi, A. Du, T. Liao, G.A. Ayoko, Y. Yamauchi, L. Sun, Z. Sun. Surface-dependent intermediate adsorption modulation on iridium-modified black phosphorus electrocatalysts for efficient pH-universal water splitting. *Adv. Mater.*, 2021, 33(49), 2104638.
14. W. Hao, D. Yao, Q. Xu, R. Wang, C. Zhang, Y. Guo, R. Sun, M. Huang, Z. Chen. Highly efficient overall-water splitting enabled via grafting boron-inserted Fe-Ni solid solution nanosheets onto unconventional skeleton. *Appl. Catal. B Environ.*, 2021, 292, 120188.
15. Z. Li, H. Feng, M. Song, C. He, W. Zhuang, L. Tian. Advances in CoP electrocatalysts for water splitting. *Mater. Today Energy*, 2021, 20, 100698.
16. K. Zhang, W. Ma, G. Tan, Z. Cheng, Y. Ma, W. Li, X. Feng, Z. Li. Interfacial engineering of Ru-doped Co_3O_4/CoP nanowires heterostructure as efficient bifunctional electrocatalysts for alkaline water splitting. *Molecular Catalysis*, 2022, 530, 112640.
17. R. Deng, M. Guo, C. Wang, Q. Zhang. Recent advances in cobalt phosphide-based materials for electrocatalytic water splitting: From catalytic mechanism and synthesis method to optimization design. *Nano Materials Science*, 2024, 6(2), pp.139-173.
18. Z. Wei, O. Moyo, J. Yang, Y. Zhang, J. Zhang, H. Sun. Recent Advances in Low-Loading Noble Metal-Promoted Transition Metal Catalysts for Hydrogen Production via Electrochemical Small Molecule Oxidation. *Adv. Funct. Mater.*, 2026, e76158.
19. H. Sun, X. Xu, H. Kim, W. Jung, W. Zhou, Z. Shao. Electrochemical water splitting: Bridging the gaps between fundamental research and industrial applications. *Energy Environ. Mater.*, 2023, 6(5), e12441.
20. E. Worrell, L. Price, N. Martin, C. Hendriks, L.O. Meida. Carbon dioxide emissions from the global cement industry. *Annu. Rev. Energy Environ.*, 2001, 26(1), 303–329.
21. S. Solomon, G.K. Plattner, R. Knutti, P. Friedlingstein, Irreversible climate change due to carbon dioxide emissions. *Proc. Natl. Acad. Sci. U.S.A.*, 2009, 106(6), 1704–1709.
22. Paris Agreement. Paris Agreement to the United Nations Framework Convention on Climate Change. *TIAS*, 2015, 16-1104.
23. Z. Abdin, A. Zafaranloo, A. Rafiee, W. Mérida, W. Lipiński, K.R. Khalilpour. Hydrogen as an energy vector. *Renew. Sustain. Energy Rev.*, 2020, 120, 109620.
24. F. Dawood, M. Anda, G.M. Shafiullah. Hydrogen production for energy: An overview. *Int. J. Hydrogen Energy*, 2020, 45(7), 3847–3869.
25. H. Eric. Hidden hydrogen: Earth may hold vast stores of a renewable,

carbon-free fuel. *Science*, 2023, 379(6633), 630–636.
26. S.S. Araya, X. Cui, N. Li, V. Liso, S.L. Sahlin. Power-to-X: Technology overview, possibilities and challenges. *Chem. Eng. Process. Process Intensif.*, 2022, 23.
27. M. Hermesmann, K. Grübel, L. Scherotzki, T.E. Müller. Promising pathways: The geographic and energetic potential of power-to-X technologies based on regeneratively obtained hydrogen. *Renew. Sustain. Energy Rev.*, 2021, 138, 110644.
28. A. Boretti, B.G. Pollet, Hydrogen economy: Paving the path to a sustainable, low-carbon future. *Int. J. Hydrogen Energy*, 2024, 93, 307–319.
29. International Energy Agency (IEA). *Global Hydrogen Review 2024*. IEA, Paris, 2024. Available at: https://www.iea.org/reports/global-hydrogen-review-2024
30. International Energy Agency (IEA). *Global Hydrogen Review 2025*. IEA, Paris, 2025. Available at: https://www.iea.org/reports/global-hydrogen-review-2025
31. S.O. Jeje, T. Marazani, J.O. Obiko, M.B. Shongwe. Advancing the hydrogen production economy: A comprehensive review of technologies, sustainability, and future prospects. *Int. J. Hydrogen Energy*, 2024, 78, 642–661.
32. J. Oyekale, M. Petrollese, V. Tola, G. Cau. Impacts of renewable energy resources on effectiveness of grid-integrated systems: Succinct review of current challenges and potential solution strategies. *Energies*, 2020, 13(18), 4856.
33. S. Ullah, K.I. Khan, M.R.A. Karim, A. Ahmed. Novel NiCoMn–PDC MOFs: A dual-functional material for electrocatalytic water splitting and hybrid supercapacitor applications. *RSC Adv.*, 2025, 15(54), 46277–46296.
34. W. Zhang, L. Cui, J. Liu. Recent advances in cobalt-based electrocatalysts for hydrogen and oxygen evolution reactions. *J. Alloys Compd.*, 2020, 821, 153542.
35. A.B. Laursen, S. Kegnæs, S. Dahl, I. Chorkendorff. Molybdenum sulfides: Efficient and viable materials for electro- and photoelectrocatalytic hydrogen evolution. *Energy Environ. Sci.*, 2012, 5(2), 5577–5591.
36. A. Li, Y. Sun, T. Yao, H. Han. Earth-abundant transition-metal-based electrocatalysts for water electrolysis to produce renewable hydrogen. *Chem. Eur. J.*, 2018, 24(69), 18334–18355.
37. T. Zhang, Y. Zhu, J.Y. Lee. Unconventional noble metal-free catalysts for oxygen evolution in aqueous systems. *J. Mater. Chem. A*, 2018, 6(18), 8147–8158.
38. X. Shang, J.H. Tang, B. Dong, Y. Sun. Recent advances of nonprecious

and bifunctional electrocatalysts for overall water splitting. *Sustain. Energy Fuels*, 2020, 4(7), 3211–3228.
39. B. A. Oni. A review on electrochemical water splitting electrocatalysts for green H_2 production: Unveiling the fundamentals and recent advances. *Langmuir*, 2025, 41(17), 10742–10767.
40. Giddaerappa, N. Kousar, U. Deshpande, L.K. Sannegowda. Cobalt phthalocyanine based metal–organic framework as an efficient bifunctional electrocatalyst for water electrolysis. *Energy Fuels*, 2024, 38(9), 8249–8261.
41. B. Z. Desalegn, H.S. Jadhav, J.G. Seo. Interface modulation of a layer-by-layer electrodeposited $Fe_xCo_{(1-x)}P$/NiP@CC heterostructure for high-performance oxygen evolution reaction. *Sustain. Energy Fuels*, 2020, 4(4), 1863–1874.
42. Gurudayal, D. Sabba, M.H. Kumar, L.H. Wong, J. Barber, M. Grätzel, N. Mathews. Perovskite–hematite tandem cells for efficient overall solar driven water splitting. *Nano Lett.*, 2015, 15(6), 3833–3839.
43. W. Yang, R. R. Prabhakar, J. Tan, S.D. Tilley, J. Moon. Strategies for enhancing the photocurrent, photovoltage, and stability of photoelectrodes for photoelectrochemical water splitting. *Chem. Soc. Rev.*, 2019, 48(19), 4979–5015.
44. F. Lyu, Q. Wang, S. M. Choi, Y. Yin. Noble-metal-free electrocatalysts for oxygen evolution. *Small*, 2019, 15(1), 1804201.
45. D.V. Esposito, S.T. Hunt, A.L. Stottlemyer, K.D. Dobson, B.E. McCandless, R.W. Birkmire, J.G. Chen, Low-cost hydrogen evolution catalysts based on monolayer platinum on tungsten monocarbide substrates. *Angew. Chem. Int. Ed.*, 2010, 49(51), 9859–9862.
46. X. Huang, Z. Zeng, S. Bao, M. Wang, X. Qi, Z. Fan, H. Zhang. Solution-phase epitaxial growth of noble metal nanostructures on dispersible single-layer molybdenum disulfide nanosheets. *Nat. Commun.*, 2013, 4(1), 1444.
47. X. Li, G. Chen, Y. Liu, R. Lu, C. Ma, Z. Wang, Y. Han, D. Wang. Optimal selection of RuO_2 for durable oxygen evolution reactions in acidic media by continuous regulation of Ru–O covalency. *Energy Environ. Sci.*, 2025, 18(9), 4200–4209.
48. L. Li, B. Wang, G. Zhang, G. Yang, T. Yang, S. Yang, S. Yang. Electrochemically modifying the electronic structure of IrO_2 nanoparticles for overall electrochemical water splitting with extensive adaptability. *Adv. Energy Mater.*, 2020, 10(30), 2001600.
49. M. Lan, R.M. Guo, Y. Dou, J. Zhou, A. Zhou, J.R. Li. Fabrication of porous Pt doping heterojunctions by using bimetallic MOF template for photocatalytic hydrogen generation. *Nano Energy*, 2017, 33, 238–246.
50. Z. Yan, G. He, P.K. Shen, Z. Luo, J. Xie, M. Chen. MoC–graphite

composite as a Pt electrocatalyst support for highly active methanol oxidation and oxygen reduction reaction. *J. Mater. Chem. A*, 2014, 2(11), 4014–4022.
51. H. Zhang, Y. Liu, H. Wu, W. Zhou, Z. Kou, S.J. Pennycook, J. Xie, C. Guan, J. Wang. Open hollow Co–Pt clusters embedded in carbon nanoflake arrays for highly efficient alkaline water splitting. *J. Mater. Chem. A*, 2018, 6(41), 20214–20223.
52. Y. Wang, B. Kong, D. Zhao, H. Wang, C. Selomulya. Strategies for developing transition metal phosphides as heterogeneous electrocatalysts for water splitting. *Nano Today*, 2017, 15, 26–55.
53. J. Fan, K. Qi, L. Zhang, H. Zhang, S. Yu, X. Cui. Engineering Pt/Pd interfacial electronic structures for highly efficient hydrogen evolution and alcohol oxidation. *ACS Appl. Mater. Interfaces*, 2017, 9(21), 18008–18014.
54. J.M.V. Nsanzimana, Y. Peng, Y.Y. Xu, L. Thia, C. Wang, B.Y. Xia, X. Wang, An efficient and earth-abundant oxygen-evolving electrocatalyst based on amorphous metal borides. *Adv. Energy Mater.*, 2018, 8(1), 1701475.
55. X. Shang, X.Y. Zhang, J.Y. Xie, B. Dong, J.Q. Chi, B.Y. Guo, M. Yang, Y.M. Chai, C.G. Liu. Double-catalytic-site engineering of nickel-based electrocatalysts by group VB metals doping coupling with in-situ cathodic activation for hydrogen evolution. *Appl. Catal. B Environ.*, 2019, 258, 117984.
56. C.F. Du, Q. Liang, R. Dangol, J. Zhao, H. Ren, S. Madhavi, Q. Yan. Layered trichalcogenidophosphate: A new catalyst family for water splitting. *Nano-Micro Lett.*, 2018, 10(4), 67.
57. S. Anantharaj, S.R. Ede, K. Sakthikumar, K. Karthick, S. Mishra, S. Kundu. Recent trends and perspectives in electrochemical water splitting with an emphasis on sulfide, selenide, and phosphide catalysts of Fe, Co, and Ni: A review. *ACS Catal.*, 2016, 6(12), 8069–8097.
58. C. Huang, P. Qin, Y. Luo, Q. Ruan, L. Liu, Y. Wu, Q. Li, Y. Xu, R. Liu, P.K. Chu. Recent progress and perspective of cobalt-based catalysts for water splitting: Design and nanoarchitectonics. *Mater. Today Energy*, 2022, 23, 100911.
59. F. Li, J. Li, X. Lin, X. Li, Y. Fang, L. Jiao, X. An, Y. Fu, J. Jin, R. Li. Designed synthesis of multi-walled carbon nanotubes@Cu@MoS_2 hybrid as advanced electrocatalyst for highly efficient hydrogen evolution reaction. *J. Power Sources*, 2015, 300, 301–308.
60. K. Lan, X. Wang, H. Yang, K. Iqbal, Y. Zhu, P. Jiang, Y. Tang, Y. Yang, W. Gao, R. Li. Ultrafine MoP nanoparticles well embedded in carbon nanosheets as electrocatalyst with high active site density for hydrogen evolution. *ChemElectroChem*, 2018, 5(16), 2256–2262.
61. X. Wang, X. Huang, W. Gao, Y. Tang, P. Jiang, K. Lan, R. Yang, B. Wang,

R. Li. Metal–organic framework derived $CoTe_2$ encapsulated in nitrogen-doped carbon nanotube frameworks: A high-efficiency bifunctional electrocatalyst for overall water splitting. *J. Mater. Chem. A*, 2018, 6(8), 3684–3691.
62. Y. Guo, D. Guo, F. Ye, K. Wang, Z. Shi. Synthesis of lawn-like NiS_2 nanowires on carbon fiber paper as bifunctional electrodes for water splitting. *Int. J. Hydrogen Energy*, 2017, 42(27), 17038–17048.
63. Y. Liu, X. Xie, G. Zhu, Y. Mao, Y. Yu, S. Ju, X. Shen, H. Pang. Small sized Fe–Co sulfide nanoclusters anchored on carbon for oxygen evolution. *J. Mater. Chem. A*, 2019, 7(26), 15851–15861.
64. F. Li, L. Zhang, J. Li, X. Lin, X. Li, Y. Fang, J. Huang, W. Li, M. Tian, J. Jin, R. Li. Synthesis of Cu–MoS_2/rGO hybrid as non-noble metal electrocatalysts for the hydrogen evolution reaction. *J. Power Sources*, 2015, 292, 15–22.
65. S. Gupta, N. Patel, R. Fernandes, R. Kadrekar, A. Dashora, A.K. Yadav, D. Bhattacharyya, S.N. Jha, A. Miotello, D.C. Kothari. Co–Ni–B nanocatalyst for efficient hydrogen evolution reaction in wide pH range. *Appl. Catal. B Environ.*, 2016, 192, 126–133.
66. M. Chen, Y. Xie, J.X. Wu, H. Huang, J. Teng, D. Wang, Y. Fan, J.J. Jiang, H.P. Wang, C.Y. Su. Cobalt (oxy) hydroxide nanosheet arrays with exceptional porosity and rich defects as a highly efficient oxygen evolution electrocatalyst under neutral conditions. *J. Mater. Chem. A*, 2019, 7(17), 10217–10224.
67. P. Babar, A. Lokhande, H.H. Shin, B. Pawar, M.G. Gang, S. Pawar, J.H. Kim. Cobalt iron hydroxide as a precious metal-free bifunctional electrocatalyst for efficient overall water splitting. *Small*, 2018, 14(7), 1702568.
68. W. Liu, H. Liu, L. Dang, H. Zhang, X. Wu, B. Yang, Z. Li, X. Zhang, L. Lei, S. Jin. Amorphous cobalt–iron hydroxide nanosheet electrocatalyst for efficient electrochemical and photo-electrochemical oxygen evolution. *Adv. Funct. Mater.*, 2017, 27(14), 1603904.
69. K. Wang, X. She, S. Chen, H. Liu, D. Li, Y. Wang, H. Zhang, D. Yang, X. Yao. Boosting hydrogen evolution via optimized hydrogen adsorption at the interface of CoP_3 and Ni_2P. *J. Mater. Chem. A*, 2018, 6(14), 5560–5565.
70. R. Beltrán-Suito, P.W. Menezes, M. Driess. Amorphous outperforms crystalline nanomaterials: Surface modifications of molecularly derived CoP electro(pre)catalysts for efficient water-splitting. *J. Mater. Chem. A*, 2019, 7(26), 15749–15756.
71. W. Ou, L. Li, W. Zhou, M. Chen, C. Zhu, X. Zhu, K. Yuan. Developing a cobalt phosphide catalyst with combined cobalt defects and phosphorus

vacancies to boost oxygen evolution reaction. *Materials*, 2024, 17(18), 4647.
72. Y. Du, Z. Zhong, L. Zhou, W. Chen, Z. Shi, P. Song, Y. Liu, Y. Yao, Y. Liu, S.H. Dou, Y. Xiao. Coordination polymer derived transition metal phosphide/carbon composites for bifunctional oxygen electrocatalyst. *J. Mater. Sci. Technol.*, 2025, 222, 142–151.
73. T. Zhang, J. Zhong, W. Gao, Y. Wang. Interface engineering induced N, P doped carbon shell encapsulated FeP/NiP_2/Ni_5P_4/NiP nanoparticles for highly efficient hydrogen evolution reaction. *Coatings*, 2024, 14(7), 817.
74. A. Yadav, M.R. Das, S. Deka. Fine tuning of torus shaped Mo doped Ni_2P nanorings for enhanced seawater electrolysis. *Small*, 2025, 21(3), 2408036.
75. T. Parvanova-Mancheva, V. Chakarova, M. Gabrovska, S. Atanasova-Vladimirova, A. Baeva, R. Andreeva, F. Hodzhaoglu, D. Nikolova. Evaluating the bifunctional properties towards HER and OER of NiCo electrodeposited coatings: Combined influence of support, Ni/Co ratio, and phosphorus doping. *Catal. Today*, 2025, 460, 115495.
76. P. Ren, R. Wang, Y. Yang, T. Wang, Y. Hong, Y. Zheng, X. Ren, Z. Jia. Facile synthesis of MoP and its composite structure with Ru as an efficient electrocatalyst for hydrogen evolution reaction in both acidic and alkaline conditions. *Materials*, 2025, 18(5), 1184.
77. L. Xiao, W. Bao, J. Zhang, C. Yang, T. Ai, Y. Li, X. Wei, P. Jiang, L. Kou. Interfacial interaction between NiMoP and NiFe-LDH to regulate the electronic structure toward high-efficiency electrocatalytic oxygen evolution reaction. *Int. J. Hydrogen Energy*, 2022, 47(15), 9230–9238.
78. M. Jiang, J. Li, J. Li, Y. Zhao, L. Pan, Q. Cao, D. Wang, Y. Du. Two-dimensional bimetallic phosphide ultrathin nanosheets as non-noble electrocatalysts for a highly efficient oxygen evolution reaction. *Nanoscale*, 2019, 11(19), 9654–9660.
79. J. Kibsgaard, C. Tsai, K. Chan, J.D. Benck, J.K. Nørskov, F. Abild-Pedersen, T.F. Jaramillo. Designing an improved transition metal phosphide catalyst for hydrogen evolution using experimental and theoretical trends. *Energy Environ. Sci.*, 2015, 8(10), 3022–3029.
80. Z. Liu, X. Yu, H. Xue, L. Feng. A nitrogen-doped CoP nanoarray over 3D porous Co foam as an efficient bifunctional electrocatalyst for overall water splitting. *J. Mater. Chem. A*, 2019, 7(21), 13242–13248.
81. Z. Wu, D. Nie, M. Song, T. Jiao, G. Fu, X. Liu. Facile synthesis of Co–Fe–B–P nanochains as an efficient bifunctional electrocatalyst for overall water-splitting. *Nanoscale*, 2019, 11(15), 7506–7512.
82. X. Huang, L. Gong, H. Xu, J. Qin, P. Ma, M. Yang, K. Wang, L. Ma, X. Mu, R. Li. Hierarchical iron-doped CoP heterostructures self-assembled on copper foam as a bifunctional electrocatalyst for efficient overall water

splitting. *J. Colloid Interface Sci.*, 2020, 569, 140–149.
83. C. Yang, T. He, W. Zhou, R. Deng, Q. Zhang. Iron-tuned 3D cobalt–phosphate catalysts for efficient hydrogen and oxygen evolution reactions over a wide pH range. *ACS Sustainable Chem. Eng.*, 2020, 8(36), 13793–13804.
84. K. Sun, K. Wang, T. Yu, X. Liu, G. Wang, L. Jiang, Y. Bu, G. Xie. High-performance FeCoP alloy catalysts by electroless deposition for overall water splitting. *Int. J. Hydrogen Energy*, 2019, 44(3), 1328–1335.
85. M. Guan, S. Fu, F. Qin, P. Zuo, W. Shen. Urchin-like bifunctional CoP/FeP electrocatalyst for overall water splitting. *Int. J. Hydrogen Energy*, 2024, 93, 147–157.
86. D. Duan, D. Guo, J. Gao, S. Liu, Y. Wang. Electrodeposition of cobalt-iron bimetal phosphide on Ni foam as a bifunctional electrocatalyst for efficient overall water splitting. *J. Colloid Interface Sci.*, 2022, 622, 250–260.
87. Y. Yang, J. Yang, C. Kong, Q. Zhou, D. Qian, Y. Xiong, Z. Hu. Heterogeneous cobalt-iron phosphide nanosheets formed by *in situ* phosphating of hydroxide for efficient overall water splitting. *J. Alloys Compd.*, 2022, 926, 166930.
88. Y. Lian, H. Sun, X. Wang, P. Qi, Q. Mu, Y. Chen, J. Ye, X. Zhao, Z. Deng, Y. Peng. Carved nanoframes of cobalt–iron bimetal phosphide as a bifunctional electrocatalyst for efficient overall water splitting. *Chem. Sci.*, 2019, 10(2), 464–474.
89. X. Liu, Y. Yao, H. Zhang, L. Pan, C. Shi, X. Zhang, Z.F. Huang, J.J. Zou. *In situ*-grown cobalt–iron phosphide-based integrated electrode for long-term water splitting under a large current density at the industrial electrolysis temperature. *ACS Sustainable Chem. Eng.*, 2020, 8(48), 17828–17838.
90. Y. Zhang, X. Gao, L. Lv, J. Xu, H. Lin, Y. Ding, C. Wang. Tailoring π-symmetry electrons in cobalt-iron phosphide for highly efficient oxygen evolution. *Electrochim. Acta*, 2020, 341, 136029.
91. X. Ding, H. Huang, Q. Wan, X. Guan, Y. Fang, S. Lin, D. Chen, Z. Xie. Self-template synthesis of hollow Fe-doped CoP prisms with enhanced oxygen evolution reaction activity. *J. Energy Chem.*, 2021, 62, 415–422.
92. Z. Jiang, J. Ren, Y. Li, X. Zhang, P. Zhang, J. Huang, C. Du, J. Chen. Low-cost high-performance hydrogen evolution electrocatalysts based on Pt-CoP polyhedra with low Pt loading in both alkaline and neutral media. *Dalton Trans.*, 2019, 48(24), 8920–8930.
93. W. Yang, P. Cheng, Z. Li, Y. Lin, M. Li, J. Zi, H. Shi, G. Li, Z. Lian, H. Li. Tuning the cobalt–platinum alloy regulating single-atom platinum for highly efficient hydrogen evolution reaction. *Adv. Funct. Mater.*, 2022, 32(29), 2205920.

94. F. Nichols, Q. Liu, J. Sandhu, Z. Azhar, R. Cazares, R. Mercado, F. Bridges, S. Chen. Platinum-complexed phosphorous-doped carbon nitride for electrocatalytic hydrogen evolution. *J. Mater. Chem. A*, 2022, 10(11), 5962–5970.
95. Y. Yan, J. Lin, T. Xu, B. Liu, K. Huang, L. Qiao, S. Liu, J. Cao, S.C. Jun, Y. Yamauchi, J. Qi. Atomic-level platinum filling into Ni-vacancies of dual-deficient NiO for boosting electrocatalytic hydrogen evolution. *Adv. Energy Mater.*, 2022, 12(24), 2200434.
96. J. Chen, M. Qin, S. Ma, R. Fan, X. Zheng, S. Mao, C. Chen, Y. Wang. Rational construction of Pt/$PtTe_x$ interface with optimal intermediate adsorption energy for efficient hydrogen evolution reaction. *Appl. Catal. B Environ.*, 2021, 299, 120640.
97. L. Yang, M. Wang, H. Shan, Y. Ma, Y. Peng, K. Hu, C. Deng, H. Yu, J. Lv. Generic heterostructure interfaces bound to Co_9S_8 for efficient overall water splitting supported by photothermal. *J. Colloid Interface Sci.*, 2024, 662, 748–759.
98. J. Yin, C. Wang, J. Li, S. Yu, Z. Wu, Y. Zhang, Y. Du. *In situ* electrodeposition of ultralow Pt into NiFe-metal-organic framework/nickel foam nanosheet arrays as a bifunctional catalyst for overall water splitting. *Inorg. Chem.*, 2024, 63(11), 5167–5174.
99. Y. Yang, H. Meng, C. Kong, S. Yan, W. Ma, H. Zhu, F. Ma, C. Wang, Z. Hu. Heterogeneous Ni_3S_2@$FeNi_2S_4$@NF nanosheet arrays directly used as high efficiency bifunctional electrocatalyst for water decomposition. *J. Colloid Interface Sci.*, 2021, 599, 300–312.
100. G.H. Gao, R.Z. Zhao, Y.J. Wang, X. Ma, Y. Li, J. Zhang, J.S. Li. Core-shell heterostructure engineering of CoP nanowires coupled NiFe LDH nanosheets for highly efficient water/seawater oxidation. *Chin. Chem. Lett.*, 2024, 35(8), 109181.
101. W. Cheng, Z. Cui, S. Xu, S. Cheng, N. Gao, M. Yang, H. Li. Pt doped $NiCo_2$ electrolysis for achieving highly efficient overall water splitting in alkaline condition. *J. Power Sources*, 2025, 641, 236891.
102. Y. Jia, T.H. Huang, S. Lin, L. Guo, Y.M. Yu, J.H. Wang, K.W. Wang, S. Dai. Stable Pd–Cu hydride catalyst for efficient hydrogen evolution. *Nano Lett.*, 2022, 22(3), 1391–1397.
103. D. Kaya, H.H. Isik, I.B. Isik, G. Sigircik, T. Tuken, F. Karadag, A. Ekicibil. Electrocatalytic hydrogen evolution on metallic and bimetallic Pd–Co alloy nanoparticles. *Int. J. Hydrogen Energy*, 2023, 48(39), 14633–14641.
104. M. Zhong, L. Li, K. Zhao, F. He, B. Su, D. Wang. PdCo alloys@N-doped porous carbon supported on reduced graphene oxide as a highly efficient electrocatalyst for hydrogen evolution reaction. *J. Mater. Sci.*, 2021, 56(25),

14222–14233.
105. Y. Du, B. Li, G. Xu, L. Wang. Recent advances in interface engineering strategy for highly-efficient electrocatalytic water splitting. *InfoMat*, 2023, 5(1), e12377.
106. N.K. Kim, S.M. Kang, T. Kim, S. Kim, G.H. Kim. Electroless plating on polymer surfaces: Comprehensive review of mechanism, process, analysis, and future applications. *Adv. Mater. Interfaces*, 2025, 12, 2400931.
107. M. Molaei, M. Atapour. Nickel-based coatings as highly active electrocatalysts for hydrogen evolution reaction: A review on electroless plating cost-effective technique. *Sustain. Mater. Technol.*, 2024, 40, e00991.
108. A. Sharma, C.S. Cheon, J.P. Jung. Recent progress in electroless plating of copper. *J. Microelectron. Packag. Soc.*, 2016, 23(4), 1–6.
109. M. Schlesinger. Electroless and electrodeposition of silver. *Modern Electroplating*, 2010, 131-138.
110. T. Fujimura, M. Kunimoto, Y. Fukunaka, H. Ito, T. Homma. Direct formation of metal layer on anion exchange membrane using electroless deposition process. *Electrochemistry*, 2021, 89(2), 192–196.
111. W. Hao, H. Huang, Z. Chen, L. Wang, X. Ma, M. Huang, X. Ou, Y. Guo. Electroless plating-induced morphology self-assembly of free-standing Co–P–B enabling efficient overall water splitting. *Electrochim. Acta*, 2020, 354, 136645.
112. A. Papaderakis, I. Mintsouli, J. Georgieva, S. Sotiropoulos. Electrocatalysts prepared by galvanic replacement. *Catalysts*, 2017, 7(3), 80.
113. D. Kunces. Chemical deposition of metallic films from aqueous solutions. *Electroless Plating: Fundamentals and Applications, 1st ed.; G.O. Mallory and J.B. Hajdu, Eds.*, 1990, 511–517.
114. G.D. Moon, S. Ko, Y. Min, J. Zeng, Y. Xia, U. Jeong. Chemical transformations of nanostructured materials. *Nano Today*, 2011, 6(2), 186–203.
115. R. Zahra, E. Pervaiz, M.M. Baig, O. Rabi. Three-dimensional hierarchical flowers-like cobalt-nickel sulfide constructed on graphitic carbon nitride: Bifunctional non-noble electrocatalyst for overall water splitting. *Electrochim. Acta*, 2022, 418, 140346.
116. T. Niyitanga, H. Kim. Time-dependent oxidation of graphite and cobalt oxide nanoparticles as electrocatalysts for the oxygen evolution reaction. *J. Electroanal. Chem.*, 2022, 914, 116297.
117. W. Luo, Y. Wang, C. Cheng. Ru-based electrocatalysts for hydrogen evolution reaction: Recent research advances and perspectives. *Mater. Today Phys.*, 2020, 15, 100274.
118. E. Cossar, M.S.E. Houache, Z. Zhang, E.A. Baranova. Comparison of

electrochemical active surface area methods for various nickel nanostructures. *J. Electroanal. Chem.*, 2020, 870, 114246.
119. T. Zhou, Z. Cao, P. Zhang, H. Ma, Z. Gao, H. Wang, Y. Lu, J. He, Y. Zhao. Transition metal ions regulated oxygen evolution reaction performance of Ni-based hydroxides hierarchical nanoarrays. *Sci. Rep.*, 2017, 7(1), 46154.
120. F. Kong, W. Zhang, L. Sun, L. Huo, H. Zhao. Interface electronic coupling in hierarchical FeLDH(FeCo)/$Co(OH)_2$ arrays for efficient electrocatalytic oxygen evolution. *ChemSusChem*, 2019, 12(15), 3592–3601.
121. S.F. Zai, Y.T. Zhou, C.C. Yang, Q. Jiang, Al. Fe-codoped CoP nanoparticles anchored on reduced graphene oxide as bifunctional catalysts to enhance overall water splitting. *Chem. Eng. J.*, 2021, 421, 127856.
122. M. Liu, J. Li. Cobalt phosphide hollow polyhedron as efficient bifunctional electrocatalysts for the evolution reaction of hydrogen and oxygen. *ACS Appl. Mater. Interfaces*, 2016, 8(3), 2158–2165.
123. H. Sun, X. Xu, Z. Yan, X. Chen, L. Jiao, F. Cheng, J. Chen. Superhydrophilic amorphous Co–B–P nanosheet electrocatalysts with Pt-like activity and durability for the hydrogen evolution reaction. *J. Mater. Chem. A*, 2018, 6(44), 22062–22069.
124. C. Tang, A.M. Asiri, Y. Luo, X. Sun. Electrodeposited Ni-P alloy nanoparticle films for efficiently catalyzing hydrogen- and oxygen-evolution reactions. *ChemNanoMat*, 2015, 1(8), 558–561.
125. N. Jiang, B. You, M. Sheng, Y. Sun. Electrodeposited cobalt-phosphorous-derived films as competent bifunctional catalysts for overall water splitting. *Angew. Chem. Int. Ed.*, 2015, 54(21), 6251–6254.
126. G. Huang, W. Liang, Y. Wu, J. Li, Y.Q. Jin, H. Zeng, H. Zhang, F. Xie, J. Chen, N. Wang, Y. Jin, H. Meng. Co_2P/CoP hybrid as a reversible electrocatalyst for hydrogen oxidation/evolution reactions in alkaline medium. *J. Catal.*, 2020, 390, 23–29.
127. X. Wang, X. Xiao, H. Yan, C. Chen, D. Zhang, D. Sun, X. Xu. The defect-rich porous CoP_4/Co_4S_3 microcubes as robust electrocatalyst for clean H_2 energy production via alkaline overall water splitting. *Appl. Catal. A Gen.*, 2023, 668, 119461.
128. G. Hu, Q. Tang, D.E. Jiang. CoP for hydrogen evolution: Implications from hydrogen adsorption. *Phys. Chem. Chem. Phys.*, 2016, 18(34), 23864–23871.
129. J.F. Qin, J.H. Lin, T.S. Chen, D.P. Liu, J.Y. Xie, B.Y. Guo, L. Wang, Y.M. Chai, B. Dong. Facile synthesis of V-doped CoP nanoparticles as bifunctional electrocatalyst for efficient water splitting. *J. Energy Chem.*, 2019, 39, 182–187.
130. Y. Jiang, Y. Lu, J. Lin, X. Wang, Z. Shen. A hierarchical MoP nanoflake

array supported on Ni foam: A bifunctional electrocatalyst for overall water splitting. *Small Methods*, 2018, 2(5), 1700369.
131. H. Zhang, X. Li, A. Hähnel, V. Naumann, C. Lin, S. Azimi, S.L. Schweizer, A.W. Maijenburg, R.B. Wehrspohn. Bifunctional heterostructure assembly of NiFe LDH nanosheets on NiCoP nanowires for highly efficient and stable overall water splitting. *Adv. Funct. Mater.*, 2018, 28(14), 1706847.
132. D.H. Ha, B. Han, M. Risch, L. Giordano, K.P. Yao, P. Karayaylali, Y. Shao-Horn. Activity and stability of cobalt phosphides for hydrogen evolution upon water splitting. *Nano Energy*, 2016, 29, 37–45.
133. C. Yu, F. Xu, L. Luo, H.S. Abbo, S.J. Titinchi, P.K. Shen, P. Tsiakaras, S. Yin. Bimetallic Ni–Co phosphide nanosheets self-supported on nickel foam as high-performance electrocatalyst for hydrogen evolution reaction. *Electrochim. Acta*, 2019, 317, 191–198.
134. Y. Liang, Q. Liu, A.M. Asiri, X. Sun, Y. Luo. Self-supported FeP nanorod arrays: A cost-effective 3D hydrogen evolution cathode with high catalytic activity. *ACS Catal.*, 2014, 4(11), 4065–4069.
135. C. Tang, R. Zhang, W. Lu, L. He, X. Jiang, A.M. Asiri, X. Sun. Fe-doped CoP nanoarray: A monolithic multifunctional catalyst for highly efficient hydrogen generation. *Adv. Mater.*, 2017, 29(2), 1602441.
136. J. Chang, L. Liang, C. Li, M. Wang, J. Ge, C. Liu, W. Xing. Ultrathin cobalt phosphide nanosheets as efficient bifunctional catalysts for a water electrolysis cell and the origin for cell performance degradation. *Green Chem.*, 2016, 18(8), 2287–2295.
137. M.A.R. Anjum, M.S. Okyay, M. Kim, M.H. Lee, N. Park, J.S. Lee. Bifunctional sulfur-doped cobalt phosphide electrocatalyst outperforms all-noble-metal electrocatalysts in alkaline electrolyzer for overall water splitting. *Nano Energy*, 2018, 53, 286–295.
138. Y.P. Zhu, Y.P. Liu, T.Z. Ren, Z.Y. Yuan. Self-supported cobalt phosphide mesoporous nanorod arrays: A flexible and bifunctional electrode for highly active electrocatalytic water reduction and oxidation. *Adv. Funct. Mater.*, 2015, 25(47), 7337–7347.
139. H. Tabassum, W. Guo, W. Meng, A. Mahmood, R. Zhao, Q. Wang, R. Zou. Metal-organic frameworks derived cobalt phosphide architecture encapsulated into B/N Co-doped graphene nanotubes for all pH value electrochemical hydrogen evolution. *Adv. Energy Mater.*, 2017, 7(9), 1601671.
140. J.A. Vigil, T.N. Lambert, B.T. Christensen. Cobalt phosphide-based nanoparticles as bifunctional electrocatalysts for alkaline water splitting. *J. Mater. Chem. A*, 2016, 4(20), 7549–7554.
141. W. Li, S. Zhang, Q. Fan, F. Zhang, S. Xu. Hierarchically scaffolded

CoP/CoP_2 nanoparticles: Controllable synthesis and their application as a well-matched bifunctional electrocatalyst for overall water splitting. *Nanoscale*, 2017, 9(17), 5677–5685.
142. M. Zhang, S. Ci, H. Li, P. Cai, H. Xu, Z. Wen. Highly defective porous CoP nanowire as electrocatalyst for full water splitting. *Int. J. Hydrogen Energy*, 2017, 42(49), 29080–29090.
143. K. Xu, H. Ding, M. Zhang, M. Chen, Z. Hao, L. Zhang, C. Wu, Y. Xie. Regulating water-reduction kinetics in cobalt phosphide for enhancing HER catalytic activity in alkaline solution. *Adv. Mater.*, 2017, 29(28), 1606980.
144. Y. Feng, X.Y. Yu, U. Paik. Nickel cobalt phosphides quasi-hollow nanocubes as an efficient electrocatalyst for hydrogen evolution in alkaline solution. *Chem. Commun.*, 2016, 52(8), 1633–1636.
145. M.R. Liu, Q.L. Hong, Q.H. Li, Y. Du, H.X. Zhang, S. Chen, T. Zhou, J. Zhang. Cobalt boron imidazolate framework derived cobalt nanoparticles encapsulated in B/N codoped nanocarbon as efficient bifunctional electrocatalysts for overall water splitting. *Adv. Funct. Mater.*, 2018, 28(26), 1801136.
146. X. Yu, S. Zhang, C. Li, C. Zhu, Y. Chen, P. Gao, L. Qi, X. Zhang. Hollow CoP nanoparticle/N-doped graphene hybrids as highly active and stable bifunctional catalysts for full water splitting. *Nanoscale*, 2016, 8(21), 10902–10907.
147. Z. Peng, Y. Yu, D. Jiang, Y. Wu, B.Y. Xia, Z. Dong. N-doped carbon shell coated CoP nanocrystals encapsulated in porous N-doped carbon substrate as efficient electrocatalyst of water splitting. *Carbon*, 2019, 144, 464–471.
148. X. Zhang, F. Wang, Y. Zhou, A. Liang, J. Zhang. Aluminum-induced direct electroless deposition of Co and Co-P coatings on copper and their catalytic performance for electrochemical water splitting. *Surf. Coat. Technol.*, 2018, 352, 42–48.
149. J. Chang, Y. Xiao, M. Xiao, J. Ge, C. Liu, X. Han, C. Zhong, W. Hu, W. Xing. Surface oxidized cobalt-phosphide nanorods as an advanced oxygen evolution catalyst in alkaline solution. *ACS Catal.*, 2015, 5(11), 6874–6878.
150. M. Song, Y. He, M. Zhang, X. Zheng, Y. Wang, J. Zhang, X. Han, C. Zhong, W. Hu, Y. Deng. Controllable synthesis of Co_2P nanorods as high-efficiency bifunctional electrocatalyst for overall water splitting. *J. Power Sources*, 2018, 402, 345–352.
151. S. Zhao, C. Li, H. Huang, Y. Liu, Z. Kang. Carbon nanodots modified cobalt phosphate as efficient electrocatalyst for water oxidation. *J. Mater.*, 2015, 1(3), 236–244.
152. C. Guan, W. Xiao, H. Wu, X. Liu, W. Zang, H. Zhang, J. Ding, Y.P.

Feng, S.J. Pennycook, J. Wang. Hollow Mo-doped CoP nanoarrays for efficient overall water splitting. *Nano Energy*, 2018, 48, 73–80.
153. Y. Yang, H. Fei, G. Ruan, J.M. Tour. Porous cobalt-based thin film as a bifunctional catalyst for hydrogen generation and oxygen generation. *Adv. Mater.*, 2015, 27(20), 3175–3180.
154. Y. Wang, T. Zhou, K. Jiang, P. Da, Z. Peng, J. Tang, B. Kong, W.B. Cai, Z. Yang, G. Zheng. Reduced mesoporous Co_3O_4 nanowires as efficient water oxidation electrocatalysts and supercapacitor electrodes. *Adv. Energy Mater.*, 2014, 4(16), 1400696.
155. Y. Chang, N.E. Shi, S. Zhao, D. Xu, C. Liu, Y.J. Tang, Z. Dai, Y.Q. Lan, M. Han, J. Bao. Coralloid $Co_2P_2O_7$ nanocrystals encapsulated by thin carbon shells for enhanced electrochemical water oxidation. *ACS Appl. Mater. Interfaces*, 2016, 8(34), 22534–22544.
156. Y. Zhang, J. Shi, Y. Hu, Z. Huang, L. Guo. $Co_3(OH)_2(HPO_4)_2$ as a novel photocatalyst for O_2 evolution under visible-light irradiation. *Catal. Sci. Technol.*, 2016, 6(22), 8080–8088.
157. C. Ding, Y. Yu, Y. Wang, Y. Mu, X. Dong, C. Meng, C. Huang, Y. Zhang. Phosphate-modified cobalt silicate hydroxide with improved oxygen evolution reaction. *J. Colloid Interface Sci.*, 2023, 648, 251–258.
158. J. Masa, P. Weide, D. Peeters, I. Sinev, W. Xia, Z. Sun, C. Somsen, M. Muhler, W. Schuhmann. Amorphous cobalt boride (Co_2B) as a highly efficient nonprecious catalyst for electrochemical water splitting: Oxygen and hydrogen evolution. *Adv. Energy Mater.*, 2016, 6(6), 1502313.
159. B.Y. Guan, L. Yu, X.W. Lou. General synthesis of multishell mixed-metal oxyphosphide particles with enhanced electrocatalytic activity in the oxygen evolution reaction. *Angew. Chem. Int. Ed.*, 2017, 129(9), 2426–2429.
160. P. He, X.Y. Yu, X.W. Lou. Carbon-incorporated nickel–cobalt mixed metal phosphide nanoboxes with enhanced electrocatalytic activity for oxygen evolution. *Angew. Chem. Int. Ed.*, 2017, 129(14), 3955–3958.
161. G. Zhou, M. Li, Y. Li, H. Dong, D. Sun, X. Liu, L. Xu, Z. Tian, Y. Tang. Regulating the electronic structure of CoP nanosheets by O incorporation for high-efficiency electrochemical overall water splitting. *Adv. Funct. Mater.*, 2020, 30(7), 1905252.
162. Y. Liu, N. Ran, R. Ge, J. Liu, W. Li, Y. Chen, L. Feng, R. Che. Porous Mn-doped cobalt phosphide nanosheets as highly active electrocatalysts for oxygen evolution reaction. *Chem. Eng. J.*, 2021, 425, 131642.
163. X. Liu, J. Huang, T. Li, W. Chen, G. Chen, L. Han, K.K. Ostrikov. High-efficiency oxygen evolution catalyzed by Sn–Co–Ni phosphide with oriented crystal phases. *J. Mater. Chem. A*, 2022, 10(25), 13448–13455.
164. X.Y. Yu, Y. Feng, B. Guan, X.W.D. Lou, U. Paik. Carbon coated porous

nickel phosphides nanoplates for highly efficient oxygen evolution reaction. *Energy Environ. Sci.*, 2016, 9(4), 1246–1250.
165. P.K. Katkar, S.J. Marje, S.B. Kale, A.C. Lokhande, C.D. Lokhande, U.M. Patil. Synthesis of hydrous cobalt phosphate electro-catalysts by a facile hydrothermal method for enhanced oxygen evolution reaction: Effect of urea variation. *CrystEngComm*, 2019, 21(5), 884–893.
166. L. Su, X. Cui, T. He, L. Zeng, H. Tian, Y. Song, K. Qi, B.Y. Xia. Surface reconstruction of cobalt phosphide nanosheets by electrochemical activation for enhanced hydrogen evolution in alkaline solution. *Chem. Sci.*, 2019, 10(7), 2019–2024.
167. H. Liu, S. Hu, B. Long, H. Dai, Y. Yang, M. Yang, Q. Zhang, Z. Ke, W. Li, D. He, Z. Wang, X. Xiao. In Situ Unraveling Surface Reconstruction of Ni-CoP Nanowire for Excellent Alkaline Water Electrolysis. *Energy Environ. Mater.*, 2025, 8(2), e12834.
168. L. Jiao, Y.X. Zhou, H.L. Jiang. Metal-organic framework-based CoP/reduced graphene oxide: High-performance bifunctional electrocatalyst for overall water splitting. *Chem. Sci.*, 2016, 7(3), 1690–1695.
169. X. Liu, J. Dong, B. You, Y. Sun. Competent overall water-splitting electrocatalysts derived from ZIF-67 grown on carbon cloth. *RSC Adv.*, 2016, 6(77), 73336–73342.
170. Y. Li, Y. Liu, Q. Qian, G. Wang, G. Zhang. Supramolecular assisted one-pot synthesis of donut-shaped CoP@PNC hybrid nanostructures as multifunctional electrocatalysts for rechargeable Zn-air batteries and self-powered hydrogen production. *Energy Storage Mater.*, 2020, 28, 27–36.
171. P. Guo, J. Wu, X.B. Li, J. Luo, W.M. Lau, H. Liu, X.L. Sun, L.M. Liu. A highly stable bifunctional catalyst based on 3D $Co(OH)_2$@NCNTs@NF towards overall water-splitting. *Nano Energy*, 2018, 47, 96–104.
172. T. Liu, L. Xie, J. Yang, R. Kong, G. Du, A.M. Asiri, X. Sun, L. Chen. Self-standing CoP nanosheets array: A three-dimensional bifunctional catalyst electrode for overall water splitting in both neutral and alkaline media. *ChemElectroChem*, 2017, 4(8), 1840–1845.
173. Y. Zhang, B. Ouyang, J. Xu, G. Jia, S. Chen, R.S. Rawat, H.J. Fan. Rapid synthesis of cobalt nitride nanowires: Highly efficient and low-cost catalysts for oxygen evolution. *Angew. Chem.*, 2016, 55(30), 8670–8674.
174. Y. Du, H. Qu, Y. Liu, Y. Han, L. Wang, B. Dong. Bimetallic CoFeP hollow microspheres as highly efficient bifunctional electrocatalysts for overall water splitting in alkaline media. *Appl. Surf. Sci.*, 2019, 465, 816–823.
175. A. Goryachev, L. Gao, Y. Zhang, R.Y. Rohling, R.H.J. Vervuurt, A.A. Bol, J.P. Hofmann, E.J.M. Hensen. Stability of CoP_x electrocatalysts in continuous and interrupted acidic electrolysis of water. *ChemElectroChem*,

2018, 5(8), 1230–1239.
176. C. Li, Z. Peng, J. Huang. Impedance response of electrochemical interfaces: Part IV–Low-frequency inductive loop for a single-electron reaction. *J. Phys. Chem. C*, 2023, 127(33), 16367–16373.
177. R. Levinas, N. Tsyntsaru, M. Lelis, H. Cesiulis. Synthesis, electrochemical impedance spectroscopy study and photoelectrochemical behaviour of as-deposited and annealed WO_3 films. *Electrochim. Acta*, 2017, 225, 29–38.
178. G.J. Brug, A.L.G. van den Eeden, M. Sluyters-Rehbach, J.H. Sluyters. The analysis of electrode impedances complicated by the presence of a constant phase element. *J. Electroanal. Chem. Interfacial Electrochem.*, 1984, 176(1-2), 275–295.
179. L. Trotochaud, J.K. Ranney, K.N. Williams, S.W. Boettcher. Solution-cast metal oxide thin film electrocatalysts for oxygen evolution. *J. Am. Chem. Soc.*, 2012, 134(41), 17253–17261.
180. Y. Chang, N.E. Shi, S. Zhao, D. Xu, C. Liu, Y.J. Tang, Z. Dai, Y.Q. Lan, M. Han, J. Bao. Coralloid $Co_2P_2O_7$ nanocrystals encapsulated by thin carbon shells for enhanced electrochemical water oxidation. *ACS Appl. Mater. Interfaces*, 2016, 8(34), 22534–22544.
181. C. Ding, Y. Yu, Y. Wang, Y. Mu, X. Dong, C. Meng, C. Huang, Y. Zhang. Phosphate-modified cobalt silicate hydroxide with improved oxygen evolution reaction. *J. Colloid Interface Sci.*, 2023, 648, 251–258.
182. Y. Liu, N. Ran, R. Ge, J. Liu, W. Li, Y. Chen, L. Feng, R. Che. Porous Mn-doped cobalt phosphide nanosheets as highly active electrocatalysts for oxygen evolution reaction. *Chem. Eng. J.*, 2021, 425, 131642.
183. L. Yang, L. Li. Synthesis of uniformly dispersed NiCoFe trimetallic phosphide for efficient overall water splitting. *J. Phys. Chem. Solids*, 2025, 207, 112926.
184. S. Jiang, Q. Li, Q. Zhao, L. Cheng, T. Jiang. A hierarchical core shell CuO@FeCoP/CF heterostructure for efficient overall water splitting in alkaline media. *J. Alloys Compd.*, 2024, 1010, 177291.
185. J. Luo, Y. Tuo, J. Zhang, W. Li, S. Wang, Y. Li, Y. Pan, Y. Zhou, J. Zhang. Carbon confined Mo doped CoP for alkali overall water splitting with enhanced catalytic activity and durability. *Chem. Eng. J.*, 2025, 510, 161519.
186. Z. Yang, K. Li, D. Zhang, H. Yang. The synergistic effect of hard magnetic Co_2C and soft magnetic CoFe improves electrocatalytic overall water splitting performance. *J. Alloys Compd.*, 2025, 1036, 181593.
187. M.I. Díez-García, G. Montaña-Mora, M. Botifoll, A. Cabot, J. Arbiol, M. Qamar, J.R. Morante. Cobalt–Iron Oxyhydroxide Obtained from the Metal Phosphide: A Highly Effective Electrocatalyst for the Oxygen Evolution

Reaction at High Current Densities. *ACS Appl. Energy Mater.*, 2023, 6(11), 5690–5699.
188. L. Jiao, Y.X. Zhou, H.L. Jiang. Metal-organic framework-based CoP/reduced graphene oxide: High-performance bifunctional electrocatalyst for overall water splitting. *Chem. Sci.*, 2016, 7(3), 1690–1695.
189. P. Guo, J. Wu, X.B. Li, J. Luo, W.M. Lau, H. Liu, X.L. Sun, L.M. Liu. A highly stable bifunctional catalyst based on 3D $Co(OH)_2$@NCNTs@NF towards overall water-splitting. *Nano Energy*, 2018, 47, 96–104.
190. X. Liu, J. Dong, B. You, Y. Sun. Competent overall water-splitting electrocatalysts derived from ZIF-67 grown on carbon cloth. *RSC Adv.*, 2016, 6(77), 73336–73342.
191. A. Lasia. Electrochemical impedance spectroscopy and its applications. *Springer New York*, 2014.
192. X. Chang, J. Yan, X. Ding, Y. Jia, S. Li, M. Zhang. One-dimensional CoMoP nanostructures as bifunctional electrodes for overall water splitting. *Nanomaterials*, 2022, 12(21), 3886.
193. Z.H. Zhang, Y. Zhang, A. Barras, A. Addad, P. Roussel, L.C. Tang, M.A. Amin, S. Szunerits, R. Boukherroub. Preparation of flower-shaped Co-Fe layered double hydroxide nanosheets loaded with Pt nanoparticles by corrosion engineering for efficient electrocatalytic water splitting. *ACS Appl. Energy Mater.*, 2022, 5(12), 15269–15281.
194. Y. Zhao, Y. Gao, Z. Chen, Z. Li, T. Ma, Z. Wu, L. Wang. Trifle Pt coupled with NiFe hydroxide synthesized via corrosion engineering to boost the cleavage of water molecule for alkaline water-splitting. *Appl. Catal. B Environ.*, 2021, 297, 120395.
195. Y. Wang, B. Ma, Y. Chen. Iron phosphides supported on three-dimensional iron foam as an efficient electrocatalyst for water splitting reactions. *J. Mater. Sci.*, 2019, 54(24), 14872–14883.
196. H.K. Basak, M.K. Adak, A. Rajput, B. Chakraborty. Low Pt loading on wolframite-type $NiWO_4$ to excel the electrocatalytic water splitting and ammonia oxidation reaction. *ACS Appl. Mater. Interfaces*, 2025, 17(7), 9391–9406.
197. C. Zeng, Q. Li, Y. You, L. Sun, W. Cheng, X. Zheng, S. Liu, Q. Wang. Structural regulation of Fe–Co Prussian blue analogues by incorporation of Pt for enhanced electrocatalytic overall water splitting. *Int. J. Hydrogen Energy*, 2022, 47(83), 35149–35155.

LIST OF PUBLICATIONS

1. **H. Amber**, A. Balčiūnaitė, Z. Sukackienė, L. Tamašauskaitė-Tamašiūnaitė, and E. Norkus. *Electrolessly Deposited Cobalt–Phosphorus Coatings for Efficient Hydrogen and Oxygen Evolution Reactions. Catalysts*, 2024, 15(1), 8. https://doi.org/10.3390/catal15010008
2. **H. Amber**, A. Balčiūnaitė, V. Kepeniene, G. Stalnionis, Z. Mockus, L. Tamašauskaitė-Tamašiūnaitė, and E. Norkus. *Pd-Modified CoP and CoFeP Catalysts as Efficient Bifunctional Catalysts for Water Splitting*. *Catalysts*, 2025, 15(11), 1035. https://doi.org/10.3390/catal15111035
3. **H. Amber**, L. Tamašauskaitė-Tamašiūnaitė, D. Shyshkin, G. Stalnionis, R. Levinas, and E. Norkus. *Pt-Modified CoP and CoFeP Bifunctional Electrocatalysts for Efficient Overall Water Splitting at Industrial Temperatures* (Manuscript in preparation).

LIST OF CONFERENCE PRESENTATIONS

The results obtained during the doctoral studies were presented at national and international scientific conferences:

1. **H. Amber**, L. Tamašauskaitė-Tamašiūnaitė and E. Norkus, *Hydrogen Evolution Reaction Evaluated on Cobalt Phosphorus Catalysts Prepared by Electroless Metal Plating*. 12th Young Scientists' Conference "Interdisciplinary Research in Physical Sciences and Technology", 14th May, 2024, Lithuanian Academy of Sciences, Vilnius, Lithuania. (Poster Presentation).
2. **H. Amber**, L. Tamašauskaitė-Tamašiūnaitė and E. Norkus, *Electrolessly Deposited Cobalt-Phosphorus Catalysts for Hydrogen and Oxygen Evolution Reactions*. 38th Topical Meeting of the International Society of Electrochemistry (ISE), 8th–11th September, 2024, Manchester, UK. (Poster Presentation).
3. **H. Amber**, L. Tamašauskaitė-Tamašiūnaitė, *Electrocatalytic Performance of Cobalt-Phosphorus Catalyst for Overall Water Splitting in Alkaline Media*. 14th Conference of Doctoral Students and Young Scientists "FizTeCh 2024", 15th–17th October, 2024, Vilnius, Lithuania. (Oral Presentation).
4. **H. Amber**, A. Balčiūnaitė, Z. Sukackienė, L. Tamašauskaitė-Tamašiūnaitė and E. Norkus, *Cobalt-Based Alloys as Advanced Electrocatalysts for Efficient Water Splitting and Energy Storage*. 13th Young Scientists' Conference "Interdisciplinary Research in Physical Sciences and Technology", 11th April, 2025, Vilnius, Lithuania. (Poster Presentation).
5. **H. Amber**, A. Balčiūnaitė, L. Tamašauskaitė-Tamašiūnaitė, Z. Sukackienė, J. Vaičiūnienė and E. Norkus, *Cobalt-Based Electrocatalysts: A Pathway Toward Cost-Effective and High-Performance Energy Conversion*. "IECME 2025", 5th–7th May, 2025, Online. (Poster Presentation).
6. **H. Amber**, A. Balčiūnaitė, L. Tamašauskaitė-Tamašiūnaitė, J. Vaičiūnienė and E. Norkus, *Non-Precious Metal Electrocatalysts for the Overall Water Splitting: Synthesis, Characterization and Properties*. 68th International Conference for Students of Physics and Natural Sciences "Open Readings 2025", 13th–16th May, 2025, Vilnius, Lithuania. (Poster Presentation).

7. **H. Amber**, A. Balčiūnaitė, L. Tamašauskaitė-Tamašiūnaitė, Z. Sukackienė, J. Vaičiūnienė and E. Norkus, *Efficient Overall Water Splitting in an Alkaline Medium Using Palladium-Enhanced Cobalt-Based Coatings on Flexible Copper-Coated Polyimide Surface*. "Grotthuss 2025 Conference", 4th–6th June, 2025, Vilnius, Lithuania. (Poster Presentation).
8. **H. Amber**, L. Tamašauskaitė-Tamašiūnaitė, A. Balčiūnaitė, Z. Sukackienė and E. Norkus, *Platinum-Decorated Transition Metal Phosphides for High-Efficiency Renewable Hydrogen Production*. "IOCN 2025", 22nd–24th September, 2025, Online. (Poster Presentation).
9. **H. Amber**, A. Balčiūnaitė, Z. Sukackienė, L. Tamašauskaitė-Tamašiūnaitė and E. Norkus, *Cobalt-Based Electrocatalysts: A Pathway Toward Cost-Effective and High-Performance Water Splitting*. 15th FizTeCh, 14th–16th October, 2025, Vilnius, Lithuania. (Oral Presentation).
10. **H. Amber**, A. Balčiūnaitė, Z. Sukackienė, L. Tamašauskaitė-Tamašiūnaitė and E. Norkus, *Phosphorus-Tuned Co-P Alloy Coatings for High-Performance Water Splitting and Hydrogen Production*. "ASEC 2025", 9th–11th December, 2025, Online. (Poster Presentation).
11. **H. Amber**, D. Shyshkin, L. Tamašauskaitė-Tamašiūnaitė and E. Norkus, *Platinum-Modified Cobalt-Iron Phosphide Electrocatalysts for Efficient Overall Water Splitting at Industrial Temperatures*. 69th International Conference for Students of Physics and Natural Sciences "Open Readings 2026", 27th–30th April, 2026, Vilnius, Lithuania. (Poster Presentation).
12. **H. Amber**, D. Shyshkin, L. Tamašauskaitė-Tamašiūnaitė and E. Norkus, *Highly Efficient PtNPs-Decorated CoP and CoFeP Bifunctional Electrocatalysts for Overall Water Splitting*. 42nd Topical Meeting of the International Society of Electrochemistry (ISE), 23rd–26th June, 2026, Helsinki, Finland. (Poster Presentation).

Conferences where the doctoral student was a co-author:

1. E. Norkus, **H. Amber**, K. Vjunova, Z. Sukackienė, B. Šimkūnaitė-Stanynienė, J. Vaičiūnienė and L. Tamašauskaitė-Tamašiūnaitė, *Cobalt-Iron-Phosphorus Catalysts for Hydrogen and Oxygen Evolution*. 10th International Congress on Energy Efficiency and Energy Related Materials "ENEFM 2024", 8th–11th October, 2024, Ölüdeniz, Turkey. (Poster Presentation).

2. **H. Amber**, L. Tamasauskaite-Tamasiunaite, K. Vjunova, Z. Sukackiene, D. Simkunaite, J. Vaiciuniene, E. Norkus, *Study of oxygen reduction and evolution on palladium-modified cobalt-phosphorus and cobalt-iron-phosphorus coatings*.10th International Congress on Energy Efficiency and Energy Related Materials “ENEFM 2024”, 8th–11th October, 2024, Ölüdeniz, Turkey. (Poster Presentation).
3. A. Degollado-Vasalauskas, **H. Amber**, A. Balčiūnaitė, L. Tamašauskaitė-Tamašiūnaitė, Z. Sukackienė, D. Šimkūnaitė, J. Vaičiūnienė and E. Norkus, *Palladium-Modified Cobalt Phosphorus and Cobalt-Iron-Phosphorus Coatings for Oxygen Evolution Reaction*. 14th Conference of Doctoral Students and Young Scientists “FizTeCh 2024”, 15th–17th October, 2024, Vilnius, Lithuania. (Poster Presentation).
4. D. Shyshkin, **H. Amber**, *Highly Efficient Bifunctional Pt/Au-CoFeP and CoP Electrocatalysts for Overall Water Splitting Toward Green Hydrogen Production*. Conference “Summer of Science with LMT”, 26th August, 2025, Vilnius, Lithuania. (Poster Presentation).

LIST OF AWARDS

1. Best Poster Presentation Award in the 68th International Conference for Students of Physics and Natural Sciences **"Open Readings 2025"**.
2. Best Poster Presentation Award in the 24th Biennial Conference **"EcoBalt 2025"**.
3. Best Poster Presentation Award in the **"ECCS 2025"**.
4. Best Poster Presentation Award in the **"IECME 2025"**.
5. Mobility Fund from the Research Council of Lithuania to participate in an international conference in Nürnberg, Germany **(P-DAK-24-42)**.
6. Financial Grant for study results from the Research Council of Lithuania **(P-DAP-25-239)**.
7. Mobility Fund from the Research Council of Lithuania to participate in an international conference in Mainz, Germany **(P-DAK-25-134)**.
8. Mobility Fund from the Research Council of Lithuania to participate in an international conference in Helsinki, Finland **(P-DAK-26-71)**.
9. Financial Grant for study results from the Research Council of Lithuania **(P-DAP-26-268)**.
10. Grant by LMT Student Summer Internship (research internship project) 2025 **(P-SV3-25-715)**.

CURRICULUM VITAE

Personal Information	
Name, Surname	Huma Amber
Nationality	Pakistani
Education	
2012 - 2016	Bachelor's Degree in Chemistry, Government College University Faisalabad, Pakistan
2016 – 2018	Master's Degree in Inorganic Chemistry, Government College University Faisalabad, Pakistan
2022 – 2026	PhD studies at the Department of Catalysis, Center for Physical Sciences and Technology
Work Experience	
2023– 2024	Senior Engineer, Department of Catalysis, Center for Physical Sciences and Technology
2024– Present	Junior Researcher, Department of Catalysis, Center for Physical Sciences and Technology
Participation in Scientific Projects	
2024-01 – 2024-12	LMT MIP Project “Novel Materials for Flexible Fuel Cells”, PI: Dr. Loreta Tamašauskaitė Tamašiūnaitė, reg. No. P-MIP-23-467
2024-10 – 2025-12	LMT MIP project “Electroless deposition of binary and ternary alloys and their application for green energy conversion (BITECAT)”, PI: Prof. Habil. Dr. Eugenijus Norkus, reg. No. MIP-24-653
Publications and Conferences	
1. 6 research articles published during PhD studies, all indexed in the Clarivate Analytics Web of Science database.	

2. 38 conference presentations during PhD studies, including 27 international and 11 national conferences.

Experiences in Other Foundations

1. Peer Reviewer: Springer journals – 2 manuscript reviews

2. Professional Membership: International Society of Electrochemistry (ISE) member

FOR NOTES

FOR NOTES

FOR NOTES

Vilniaus universiteto leidykla
Saulėtekio al. 9, III rūmai, LT-10222 Vilnius
El. p. info@leidykla.vu.lt, www.leidykla.vu.lt
bookshop.vu.lt, journals.vu.lt
Tiražas 26 egz.